

# A Lagrangian Perspective on the Lifecycle and Radiative Effect of Deep Convective Clouds



William Kenneth Jones

Wolfson College

University of Oxford

A thesis submitted for the degree of

*Doctor of Philosophy*

2024

*“One of the most fascinating things about clouds  
is that they are not all the same”*

Robert A. Houze, Jr.

## Acknowledgements

I would like to begin by thanking my supervisor, Philip Stier, for his excellent mentorship and allowing me the freedom to explore the many aspects of cloud and storm physics. The path to writing this thesis has been far from the easiest one, and I would not have made it without such a supportive supervisor.

I would also like to thank Matt Christensen, my co-advisor, for his support and for first getting me interested in the study of clouds through the lens of satellite observations.

The *tobac* development team, including, but not limited to, Max Heikenfeld, Fabian Senf, Sean Freeman, Julia Kukulies and Kelcy Brunner have greatly helped shape the development of the approaches used within the study the properties of deep convective clouds.

I would like to thank Sue van den Heever and Graeme Stephens for many insightful discussions on the behaviour of deep convection, which in particular inspired the contents of chapter 4.

I thank Martin Stengel and the ESA Cloud-CCI+ team for providing the cloud retrievals that made chapter 5 possible.

I am very grateful to Don Grainger and Johannes Quaas for volunteering their time as my examiners.

I give thanks to my parents, Rosie and Stephen, for their continued guidance, love and support, even if they couldn't convince me that there were options other than Physics.

Finally, but most importantly, I would like to thank my partner Cat for her love and support during times both happy and difficult. Let's hope that the stormy skies are behind us now.

## Statement of Originality

I hereby declare that, to the best of my knowledge, all work contained in this thesis is my own, original contribution, unless otherwise stated.

Chapter 2 is adapted from the article “A semi-Lagrangian method for detecting and tracking deep convective clouds in geostationary satellite observations” [Jones et al., 2023a]. In this article, I (William Jones) led the development of the detection and tracking framework, data analysis and validation, and wrote the paper with contributions from Matthew Christensen and Philip Stier.

Chapter 5 is adapted from the article “A Lagrangian Perspective on the Lifecycle and Cloud Radiative Effect of Deep Convective Clouds Over Africa” [Jones et al., 2023b, accepted]. In this article, I (William Jones) designed the study. Martin Stengel provided the retrieved cloud properties and radiative fluxes from Meteosat SEVIRI data. I performed the detection and tracking and the data analysis, and wrote the paper with contributions from Martin Stengel and Philip Stier.

## Abstract

Deep Convective Clouds (DCCs) are responsible for a wide range of extreme weather, and play key roles in the general circulation of the atmosphere, and the radiative balance of the troposphere. Perturbations in the properties of DCCs due to climate change have feedbacks via the anvil cloud radiative effects. While these feedbacks have traditionally understood in terms of the anvil height and area responses, more recent research has highlighted the important of optical properties, anvil structure and lifecycle. Reducing the uncertainties in the response of DCCs to changes in convective processes is vital to better understanding both the sensitivity of climate change and its impact upon society. Geostationary satellite observations offer a unique capability to observe the entire extent and lifecycle of DCCs. By developing novel cloud tracking algorithms, we can make full use of the capability of these instruments to observe the behaviour of DCCs in a Lagrangian framework. We use these new methods to investigate two aspects of DCC behaviour; the impact of convective processes on anvil structure, and the impact of the diurnal cycle on anvil radiative effect. We find that different convective processes on anvil structure, and that these changes impact DCCs at different points in their lifecycle. We also show that, despite the near neutral average radiative effect of anvil clouds, they exhibit wide variance across the diurnal cycle and it is only through the balance of day- and night-time convection that the net effect is achieved. In particular, we find that smaller, isolated DCCs may be more sensitive, and have a greater importance than previously thought. Overall, understanding the interplay between convective processes and the evolution of anvils across their entire lifecycle is vital to understanding the impact of DCCs on the climate, and cloud tracking provides a powerful tool to approach this. Future work should focus on closing the loop between the diurnal cycle, convective processes, anvil structure and cloud radiative effect, and establish whether these changes are expected to warm or cool the climate.

# Contents

<b>List of Figures</b>	<b>iv</b>
<b>List of Tables</b>	<b>ix</b>
<b>List of Acronyms and Symbols</b>	<b>x</b>
<b>1 Introduction</b>	<b>1</b>
1.1 Motivation . . . . .	1
1.2 Physical properties of DCCs . . . . .	5
1.2.1 Cloud microphysical properties . . . . .	5
1.2.2 Cloud radiative properties . . . . .	9
1.2.3 Thermodynamics of deep convection . . . . .	10
1.2.4 Lifecycle and structure of DCCs . . . . .	15
1.2.5 Convective organisation . . . . .	19
1.3 Anvil Radiative Feedbacks . . . . .	22
1.4 Detection and tracking of deep convection . . . . .	25
1.5 Structure of the thesis . . . . .	32
1.5.1 Can we harness new geostationary satellite measurements to track DCCs across all scales? . . . . .	32
1.5.2 How do the spatial distribution, properties and diurnal cycle of convective cores and anvils relate to each other? . . . . .	33
1.5.3 How do convective processes affect the structure and lifecycle of anvil clouds? . . . . .	33
1.5.4 How does the diurnal cycle influence the CRE of tropical anvil clouds? . . . . .	34
<b>2 A Semi-Lagrangian Method for Detecting and Tracking DCCs in Geostationary Satellite Observations</b>	<b>36</b>
2.1 Introduction . . . . .	36

2.2	Data . . . . .	42
2.2.1	Advanced Baseline Imager . . . . .	42
2.2.1.1	Selection of ABI Channels and Channel Combinations	44
2.2.2	Geostationary Lightning Mapper . . . . .	47
2.2.3	Next Generation Radar . . . . .	48
2.3	Theory . . . . .	49
2.3.1	Observing growing convective cores . . . . .	50
2.3.2	Observing anvil clouds . . . . .	52
2.4	Method . . . . .	55
2.4.1	Estimation of cloud motion vectors using optical flow . . . . .	56
2.4.1.1	Evaluation of Optical Flow Methods . . . . .	57
2.4.2	A Semi-Lagrangian Framework for Morphological Image Processing . . . . .	66
2.4.3	Detection of Growing Deep Convection . . . . .	68
2.4.4	Detection of Anvil Clouds . . . . .	69
2.5	Evaluation . . . . .	74
2.6	Summary . . . . .	77
<b>3</b>	<b>Linking the Properties of Deep Convective Cores and their Associated Anvil Clouds Observed over North America</b>	<b>79</b>
3.1	Introduction . . . . .	79
3.2	Data . . . . .	82
3.3	Method . . . . .	83
3.4	Results . . . . .	88
3.4.1	Distributions and properties of developing convective cores . . . . .	88
3.4.2	Diurnal cycle of convective cores . . . . .	97
3.4.3	Distributions and properties of observed anvil clouds . . . . .	102
3.4.4	Diurnal cycle of anvils . . . . .	111
3.5	Summary . . . . .	116
<b>4</b>	<b>Contrasting effects of convective intensity and organisation on the structure and lifecycle of DCCs</b>	<b>118</b>
4.1	Introduction . . . . .	118
4.2	Data . . . . .	120
4.3	Method . . . . .	122
4.3.1	Detection of thick and thin anvils . . . . .	122
4.3.2	Estimation of convective intensity and organisation . . . . .	124

4.3.3	Lifecycle analysis . . . . .	125
4.3.4	Composite analysis . . . . .	127
4.4	Results . . . . .	129
4.4.1	Change in thin anvil fraction with intensity and organisation .	129
4.4.2	Impact of intensity and organisation on DCC properties . . .	132
4.4.3	Changes in DCC lifecycle with intensity and organisation . . .	137
4.4.4	Changes in thin anvil fraction over DCC lifecycle . . . . .	142
4.5	Summary . . . . .	145
<b>5</b>	<b>The Lifecycle and Cloud Radiative Effect of Deep Convective Clouds Over Africa</b>	<b>148</b>
5.1	Introduction . . . . .	148
5.2	Data . . . . .	150
5.3	Method . . . . .	156
5.4	Results . . . . .	162
5.4.1	Spatial and temporal distributions . . . . .	162
5.4.2	Anvil Cloud Properties . . . . .	165
5.4.3	Anvil CRE . . . . .	169
5.5	Summary . . . . .	175
<b>6</b>	<b>Conclusion</b>	<b>179</b>
6.1	Summary . . . . .	179
6.1.1	Chapter 2: harnessing new geostationary satellite measurements to track DCCs across all scales . . . . .	180
6.1.2	Chapter 3: relating the spatial distribution, properties and diurnal cycle of convective cores and anvils . . . . .	181
6.1.3	Chapter 4: the effect of convective processes on the structure and lifecycle of anvil clouds . . . . .	182
6.1.4	Chapter 5: the influence of the diurnal cycle on the CRE of tropical anvil clouds . . . . .	184
6.2	Discussion & Future work . . . . .	186
6.3	Concluding remarks . . . . .	189
<b>Bibliography</b>		<b>191</b>

# List of Figures

1.1	A photograph of a DCC seen over Africa from the ISS . . . . .	2
1.2	An illustration of parcel ascent on a tephigram for a sounding taken on 2018-06-20 00:00 UTC at Jacksonville, Florida . . . . .	13
2.1	Observations of a cluster of DCCs over North-West Florida throughout three stages of their lifecycle . . . . .	38
2.2	Cross sections of the DCC observed in figure 2.1 as they develop over time . . . . .	40
2.3	ABI channels and channel differences used with the detection and tracking algorithm . . . . .	45
2.4	Clear sky vertical weighting functions for the 6.2, 7.3, 10.4 and 12.4 $\mu\text{m}$ ABI channels . . . . .	47
2.5	ToA BT spectra for a simulated cloud representing a DCC core at heights between 1 and 15 km . . . . .	51
2.6	Simulated observations of the 6.2, 7.3, 10.4 and 12.4 $\mu\text{m}$ ABI channels, WVD and SWD for a DCC core of increasing height . . . . .	52
2.7	Simulated observed cooling rates of the 10.4 $\mu\text{m}$ ABI channels and the WVD combination for a convective core growing at a rate of $1 \text{ ms}^{-1}$ .	53
2.8	ToA BT spectra for a simulated anvil cloud with optical thickness between 0 and 10 . . . . .	54
2.9	Simulated ABI BT observations for a DCC anvil of decreasing optical depth . . . . .	55
2.10	A comparison of the motion vector fields generated by different optical flow methods . . . . .	60
2.11	The difference in BT between subsequent ABI observations when tak- ing into account the cloud motion predicted by the different optical flow algorithms. . . . .	61
2.12	A comparison of the BT difference and residual vector magnitude MSE for each of the optical flow algorithms . . . . .	63

2.13	A comparison of the computational performance of each optical flow method . . . . .	64
2.14	An example of the motion vectors and their residual errors calculated using the Farneb��k algorithm . . . . .	65
2.15	A comparison of convolution stencils with square connectivity in Eulerian and Lagrangian frameworks. . . . .	67
2.16	Detection of growing DCC using NEXRAD column radar reflectivity, 10.4 µm BT and WVD growth rates . . . . .	70
2.17	Detection of anvil cloud extent for the mature DCC cluster in 2.1 using the edge gradient method . . . . .	72
2.18	Detected regions of thin anvil cloud, thick anvil cloud , and developing cores through the growing, mature and dissipating phases of the DCC lifecycle . . . . .	73
3.1	The sensor zenith angle of GOES-16 ABI observations across the CONUS domain . . . . .	83
3.2	Detected cores and anvils from a snapshot of GOES-16 CONUS domain observations . . . . .	87
3.3	The spatial distribution of observed cores by season . . . . .	89
3.4	Monthly distributions of the proportion of cores detected each month over land, sea, tropics and mid-latitudes . . . . .	90
3.5	The average speed and direction of propagation of cores . . . . .	91
3.6	A map showing the mean lifetime in minutes of cores within each 1×1 ° grid box . . . . .	91
3.7	A map of the average maximum core cooling rate for each 1×1 ° grid box . . . . .	92
3.8	Histograms showing the distributions of observed core lifetimes, maximum areas, cooling rates and BT . . . . .	93
3.9	The mean observed lifetimes, maximum areas, cooling rates and BT for cores detected over land, sea, tropics and mid-latitudes . . . . .	95
3.10	Average core lifetime and minimum BT with increasing core cooling rate . . . . .	96
3.11	A map of average time of day of initiation of detected cores . . . . .	97
3.12	The diurnal distributions of the local time of detection for cores detected over land, sea, tropics and mid-latitudes . . . . .	98
3.13	The diurnal distribution of cores detected in the NGP region . . . . .	99

3.14	The change in average time of core detection with distance from the coastline . . . . .	100
3.15	The diurnal cycle of the maximum cooling rate of cores detected over land, sea, tropics and mid-latitudes . . . . .	101
3.16	Maps showing the spatial distribution of observed anvils by season .	102
3.17	Monthly distributions of the proportion of cores detected each month over land, sea, tropics and mid-latitudes . . . . .	103
3.18	The average speed and direction of propagation of anvils . . . . .	104
3.19	Maps showing the spatial changes in the averages of anvil maximum area, lifetime, BT and number of cores . . . . .	105
3.20	Histograms showing the distribution of observed anvil properties . .	107
3.21	The change in the average area and lifetime of anvils with different number of cores, and their total area coverage. . . . .	108
3.22	The change in the average areas, lifetimes, BT and number of cores of anvils observed over sea, land, tropics and mid-latitudes. . . . .	110
3.23	The average time of detection of anvils . . . . .	111
3.24	The diurnal distributions of the local time of detection for anvils detected over sea, land, tropics and mid-latitudes . . . . .	112
3.25	A map showing the average time of observation of anvils . . . . .	113
3.26	The diurnal distributions of the local time of observation for anvils detected over sea, land, tropics and mid-latitudes . . . . .	114
3.27	The average age of anvils observed over sea, land, tropics and mid-latitudes throughout the diurnal cycle. . . . .	115
4.1	Simulated ABI BT observations of DCC anvils at a range of heights and optical depths for detection of thick and thin anvil detection . .	123
4.2	Definition of anvil lifecycle stages based on the method of Futyana and Del Genio [2007] . . . . .	126
4.3	The average evolution of composites of cores (red), thick anvils (orange) and thin anvils (blue) over their normalised lifetimes . . . . .	128
4.4	Thin anvil proportion of anvils categorised by mean anvil BT, initial core cooling rate and number of cores . . . . .	130
4.5	A comparison of the change in thin anvil proportion with maximum core cooling rate and number of cores for four different regions . .	131
4.6	The effect of initial core cooling rate on maximum anvil area, anvil lifetime, and mean and minimum BT . . . . .	134

4.7	The effect of the number of cores on maximum anvil area, anvil lifetime, and mean and minimum BT . . . . .	135
4.8	A comparison of the proportion of thin anvil measured at the time of maximum anvil area, and the proportional difference in lifetime, compared to the overall thin anvil proportion. . . . .	136
4.9	The average lifetime of each lifecycle stage for anvils categorised by initial core cooling rate . . . . .	138
4.10	The average fraction of anvil lifetime of each lifecycle stage for anvils categorised by initial core cooling rate . . . . .	139
4.11	The average lifetime of each lifecycle stage for anvils categorised by number of cores . . . . .	140
4.12	The average fraction of anvil lifetime of each lifecycle stage for anvils categorised by number of cores . . . . .	141
4.13	Mean thin anvil proportion for composites of anvil area of normalised lifetime categorised by the cooling rate of their initial cores. . . . .	143
4.14	Mean thin anvil proportion for composites of anvil area of normalised lifetime categorised by the number of cores . . . . .	144
5.1	Example observations from the Meteosat SEVIRI instrument at 15:00:00 UTC on 2016/6/01 . . . . .	152
5.2	An example of the ToA CRE derived using the radiative flux model . . . . .	153
5.3	Validation of derived broadband fluxes against monthly CERES-EBAF CRE . . . . .	155
5.4	Simulated sensitivity of the SEVIRI 10.8 $\mu\text{m}$ BT (top) and WVD minus SWD (bottom) to anvil clouds of varying optical thickness at heights of 10, 12 and 14 km . . . . .	158
5.5	Comparison of the relative spectral response (RSR) functions for the GOES-16 ABI and Meteosat-11 SEVIRI thermal IR channels . . . . .	160
5.6	Comparison of the sensitivities of ABI (dashed lines) and SEVIRI (solid lines) to anvil clouds of different optical thickness . . . . .	161
5.7	An example of the cores and anvils (detected by tobac-flow, shown at 3-hour time intervals . . . . .	162
5.8	Number of detected cores and average hour of core detection . . . . .	164
5.9	Anvil statistics by number of associated cores for average maximum area, average lifetime, occurrence of anvils by number of cores, and percentage of total anvil coverage . . . . .	166

5.10 Anvil statistics by number of cores for average anvil CTT and average minimum anvil temperature . . . . .	168
5.11 The distribution of time to coldest mean anvil CTT, largest anvil area and time of anvil dissipation . . . . .	169
5.12 The proportion of anvil lifetime spent in the growing, mature and dissipating phase . . . . .	170
5.13 Anvil net, LW, and SW CRE, cumulative mean CRE over anvil lifetime	171
5.14 The distribution of lifetime anvil CRE for all observed anvils . . . . .	173
5.15 The distributions of mean anvil SW CRE and LW CRE . . . . .	174
5.16 Average anvil CRE binned by the time of detection (local time) and mean anvil CTT . . . . .	175
5.17 The contribution to the net CRE for anvils with differing numbers of cores . . . . .	177

# List of Tables

2.1	Comparison of data from ABI to that from older geostationary instruments	44
2.2	Selected options for the libRadTran simulations	49
2.3	POD, FAR and F <sub>1</sub> -score for three different detection methods validated against observed GLM flashes	76
3.1	Validity criteria for detected cores	84
3.2	Validity criteria for detected anvils	85
5.1	SEVIRI channels and their use in the DCC tracking algorithm and cloud properties retrieval.	150

# List of Acronyms and Symbols

- A-train** Afternoon train. 188, 189
- ABI** Advanced Baseline Imager. ii, iv–vii, ix, 37, 38, 40, 42–53, 55, 56, 58, 61, 63, 64, 69, 70, 73, 75, 79, 82–85, 116, 122, 123, 159–161, 181, 188
- AHI** Advanced Himawari Imager. 188
- AMV** Atmospheric Motion Vector. 4, 25, 26, 29, 56, 57
- AOS** Atmosphere Observing System. 189
- BoA** Bottom-of-Atmosphere. 152
- BT** Brightness Temperature. iv–vii, 26–31, 37–41, 43–46, 49–55, 58, 59, 61–65, 67–70, 73, 84, 86, 87, 92–97, 105–107, 109, 110, 116, 119–127, 129, 130, 132–135, 138, 150–152, 157, 158, 161, 181, 184, 185, 187
- CALIOP** Cloud-Aerosol Lidar with Orthogonal Polarization. 188
- CAPE** Convective Available Potential Energy. 11–15, 81, 92
- CC4CL** Community Cloud Retrieval for Climate. 152
- CCI** Climate Change Initiative. 150
- CCN** Cloud Condensation Nuclei. 6, 7
- CERES** Clouds and the Earth’s Radiant Energy System. vii, 153–155
- CIN** Convective Inhibition. 11–14, 16, 17
- CONUS** Continental United States. v, 43, 44, 48, 56, 75, 78, 79, 82, 83, 86, 87, 116, 124
- CPR** Cloud Profiling Radar. 119, 188
- CRE** Cloud Radiative Effect. i, iii, vii, viii, 4, 5, 9, 10, 22, 24, 25, 34, 35, 140, 145, 147–150, 153–155, 159, 160, 168–178, 184–188, 190
- CTH** Cloud Top Height. 50, 52, 97
- CTT** Cloud Top Temperature. viii, 23, 24, 50, 53, 59, 62, 97, 121, 152, 167–169, 172–175, 184–186
- DCC** Deep Convective Cloud. i–vi, ix, 1–6, 10, 14–21, 23–46, 48–52, 55–57, 63–67, 69–86, 88, 93, 94, 106, 109, 110, 112, 113, 116–127, 129, 132, 133, 136–151, 155–157, 159–161, 164, 165, 167–190

- DIS** Deep Inverse Search. 58–60, 62
- Dual TV-L<sup>1</sup>** Dual Total Variation Regularisation & Robust L<sup>1</sup> Norm. 58–60, 62, 63
- EarthCARE** Earth Cloud Aerosol and Radiation Explorer. 188
- EBAF** Energy Balanced and Filled. vii, 153, 155
- ESA** European Space Agency. 150, 188
- EUMETSAT** European Organisation for the Exploitation of Meteorological Satellites. 3
- FAR** False Alarm Rate. ix, 75–77
- FAT** Fixed Anvil Temperature. 23, 186
- FCI** Flexible Combined Imager. 188
- GCM** Global Climate Model. 10, 28, 30
- GLM** Geostationary Lightning Mapper. ix, 37, 38, 40, 42, 47, 48, 74–76
- GOES** Geostationary Operational Environment Satellite. v, vii, 3, 26, 33, 37, 42, 44, 47, 49, 56, 73, 75, 79, 82, 83, 87, 116, 159, 160
- INCUS** Investigation into Convective Updrafts. 188, 189
- INP** Ice Nucleating Particle. 8
- IR** Infrared. vii, 26, 29, 36, 39, 42–44, 46, 49, 50, 55, 119, 151, 160
- ITCZ** Inter-Tropical Convergence Zone. 162, 176
- IWC** Ice Water Content. 24
- JMA** Japanese Meteorological Agency. 3
- LCL** Lifted Condensation Level. 10, 12–14
- LFC** Level of Free Convection. 10–14
- LNB** Level of Neutral Buoyancy. 11–15, 18
- LW** Longwave. viii, 4, 5, 9, 10, 15, 22–24, 26, 34, 43–46, 51, 53, 55, 118, 121, 145, 147–150, 152–155, 159, 160, 168–176, 181, 184–186
- LWC** Liquid Water Content. 50
- MCMIP** Multi-channel Cloud and Moisture Imagery Product. 43, 82
- MCS** Mesoscale Convective System. 19–22, 27–32, 79–81, 105, 106, 111, 125, 147, 148, 156, 165, 167, 176, 180, 184–186
- MSE** Mean Square Error. iv, 62, 63
- MSG** Meteosat Second Generation. 150

- NASA** National Aeronautics and Space Administration. 2, 188, 189
- NEXRAD** Next Generation (Weather) Radar. v, 37, 38, 40, 42, 48, 69, 70
- NGP** Northern Great Plains. v, 99, 100, 111
- NIR** Near Infrared. 9, 37, 38, 43, 45, 47, 150, 151
- NOAA** National Oceanic and Atmospheric Administration. 3, 44
- OD** Optical Depth. 52–54, 122–124
- PBL** Planetary Boundary Layer. 5, 14, 15
- PCA** Principle Component Analysis. 58, 60, 62
- POD** Probability of Detection. ix, 74–77
- r<sub>e</sub>** Effective Radius. 50, 52, 53
- RGB** Red, Green, Blue. 37, 151, 152
- SEVIRI** Spinning Enhanced Visible Infra-Red Imager. vii, ix, 24, 29, 35, 44, 150–153, 155, 157–162, 178, 184
- SW** Shortwave. viii, 4, 9, 10, 15, 16, 22, 24, 34, 115, 118, 140, 145, 147–150, 152–155, 169–174, 176, 177, 182, 184–186
- SWD** Split Window Difference. iv, vii, 45, 46, 50, 52–55, 69, 71, 72, 123, 124, 151, 152, 157–159, 161, 181
- ToA** Top-of-Atmosphere. iv, vii, 9, 22, 24, 33, 49, 51, 54, 118, 145, 147, 152–155, 169
- USA** United States of America. 80, 81, 88
- UTC** Universal Co-ordinated Time. iv, vii, 13, 38, 40, 44, 46, 47, 58–61, 65, 83, 151–153, 162
- WSR-88D** Weather Surveillance Radar, 1988, Doppler. 48
- WV** Water Vapour. 43–46, 50, 53, 55, 71, 150, 185
- WVD** Water Vapour Difference. iv, v, vii, 45, 46, 50–55, 68–72, 76, 77, 123, 124, 151, 152, 157–159, 161, 181

# Chapter 1

## Introduction

### 1.1 Motivation

Deep Convective Clouds (DCCs)—also known as cumulonimbus (*'heaped raincloud'*)  
or thunderstorms—are dynamical atmospheric phenomena resulting from instability  
in the troposphere. DCCs consists of tall, central ‘cores’ surrounded by a large,  
detained cirrus ‘anvil’ (fig. 1.1). The central cores of DCCs form around intense  
convective updrafts that transport water from near the surface to the upper tropo-  
sphere. At the top of these updrafts, the divergence of the cloudy airmass leads to  
the formation of a large area of detained anvil that extends beyond the footprint of  
the core. With heights in excess of 10 km tall, and anvils that measure hundreds or  
thousands of km in extent, DCCs form some of the most physically imposing objects  
in the atmosphere, and have important impacts on weather and climate.

First identified as a unique cloud type in the late 19<sup>th</sup> century by Abercromby  
[1887] and Hildebrandsson [1887], DCCs have been a focus of scientific investigation  
ever since. DCCs are the source of many severe weather events, including heavy pre-  
cipitation, lightning, hail, flooding, tornadoes and tropical cyclones [Westra et al.,  
2014; Houze, 2014; Williams et al., 1992; Bruning and MacGorman, 2013; Punge and  
Kunz, 2016; Matsudo and Salio, 2011]. DCCs play an important role in weather and  
climate beyond extreme weather events. In the tropics, deep convection forms the  
ascending branch of the Hadley cell [Riehl and Malkus, 1958], and in doing so begins



Figure 1.1: A photograph of a DCC seen over Africa from the International Space Station on 5th February 2008. The main convective core can be seen in the centre of the image as the turbulent, textured region emerging through the wide, flat anvil that surrounds it. On the right-hand side of the image a new core can be seen developing that is about to make contact with the anvil of the original core. Image credit: NASA Image and Video Library, iss016e027426.

the transport of energy through the atmosphere from the equator to the poles. In many regions of the world, from tropical Africa to the Great Plains of North America, DCCs provide the majority of precipitation [Feng et al., 2021], and while too much convection means flooding, too little means drought and crop failure. The large anvil clouds of DCCs have a mediating effect on the radiative heating of the climate, reflecting incoming sunlight and trapping outgoing longwave radiation in equal amounts [Ramanathan et al., 1989; Hartmann et al., 1992; Hartmann, 2016]. Anthropogenic influences on the atmosphere and climate—including global warming as a result of greenhouse gasses, aerosol radiation interactions and aerosol-cloud interactions—are expected to affect DCCs by increasing the amount of heavy precipitation and related

severe weather [e.g. Allen and Ingram, 2002; Trenberth et al., 2003; Held and Soden, 2006; Khain et al., 2005; Koren et al., 2008; Rosenfeld et al., 2008; Fan et al., 2013, 2016]. However, our ability to observe anthropogenic impacts on DCCs is difficult 35 due to the complex nature of the interactions between DCCs and the environment. Understanding the behaviour, interactions and feedbacks of DCCs is therefore vital for understanding both our present-day climate and its response in a changing world [Bony et al., 2015; Sherwood et al., 2020].

The study of DCCs is made difficult by the range of scales over which they occur. 40 The processes of individual DCCs span a scale from single kilometres and minutes, to hundreds of km and multiple days. When considering their dynamic and stochastic nature and coupling with synoptic scale atmospheric effects, the adequate length and time scales may extend to thousands of km and multiple years, all while maintaining the resolution of the smallest scales. Geostationary weather satellites, such as the National Oceanic and Atmospheric Administration (NOAA) Geostationary Operational Environment Satellite (GOES) series, the European Organisation for the Exploitation of Meteorological Satellites (EUMETSAT) Meteosat series, and the Japanese Meteorological Agency Himawari series, have provided imagery of DCCs over many decades for the purpose of monitoring and predicting the weather. However, these 45 instruments have not traditionally supported the accuracy required for scientific studies, and it is only with the latest generation that the capability of this imagery for studying the behaviour of deep convection is being fully realised.

50

The study of DCCs is made difficult by their dynamic and stochastic nature. Many techniques used to study more slowly varying or spatially uniform atmospheric 55 phenomena (including other cloud types, such as stratus and cumulostratus regions) cannot fully capture the complexity of DCCs. Even snapshot observations, such as those made by polar-orbiting earth observation satellites, cannot fully characterise DCC behaviour, no matter how detailed they are, due to the rapid changes in the

properties of DCCs over their lifetimes. Lagrangian methods—those which follow  
60 the DCCs' motion—provide vital observations of DCC properties over their lifecycle. While particle trajectory models have been successfully utilised to study boundary layer clouds from a Lagrangian perspective [e.g Eastman and Wood, 2018; Christensen et al., 2020], these techniques are not easily applicable due to the complex wind environment of DCCs, and the low accuracy of reanalysis models and derived  
65 Atmospheric Motion Vectors (AMVs) in these environments. Instead, image processing methods that detect and track DCCs are used to study their behaviour from a Lagrangian perspective. Traditionally developed for the purpose of forecasting convective development, these methods have seen a renaissance in recent years for in a wide range of applications for studying deep convection, including convective resolv-  
70 ing models, weather radars and geostationary satellite imagery. There are however a number of limitations in existing tracking models, and so the development of novel techniques is required to better understand the full spectrum of DCCs.

In this introductory chapter, we will explore a range of topics regarding the behaviour of DCCs and their further impacts. We will begin with a description of the  
75 dynamical and microphysical properties of clouds, with a focus on DCCs. We will investigate the lifecycle of deep convective clouds, including their initiation, growth and dissipation, and how these stages change with difficult scales of DCCs. We will look into the relationship between DCCs and radiation, including both the role of Shortwave (SW) heating and Longwave (LW) cooling in the development of deep  
80 convection, the Cloud Radiative Effect (CRE) of anvil clouds, and the interactions between radiation, the diurnal cycle and the lifecycle of DCCs. Moving on, we will provide an overview of the theorised feedbacks mechanisms of DCCs in a changing climate, with a particular focus on the DCC CRE feedback. We will provide an overview of the use of various satellite observations for the study of DCCs, including  
85 both active and passive instruments. Finally, we will describe the development and

applications of detection and tracking models for the study of deep convection, and highlight where further development is needed to better understand the behaviour of DCCs across a wide range of scales. We will also provide an overview of the structure of this thesis, in which we lay out how, through the use of novel cloud tracking methodology applied to geostationary satellite imagery, it aims to better characterise the lifecycle and CRE of DCCs.

## 1.2 Physical properties of DCCs

The physical nature of a DCC can be viewed through several lenses: as a cloud system, consisting of a multitude of liquid and ice water cloud particles along with several kinds of precipitation; a thermodynamic system in which moisture and energy are transformed into intense vertical motion and circulations across several scales; and a radiative system in which the large anvil reflects sunlight and absorbs LW radiation, both heating and cooling the atmosphere within and below it. These processes are not independent and interact with each other in numerous ways. As a result, understanding each of them is important to understanding the behaviour of DCCs.

### 1.2.1 Cloud microphysical properties

DCCs, like any other cloud, are formed from a great number of water and ice particles suspended in the atmosphere. DCCs consist of a vertically growing core spanning from the Planetary Boundary Layer (PBL) to the tropopause, a distance often exceeding 10 km, with a diameter of 10 km and updraught velocities of around  $10 \text{ ms}^{-1}$  [Weisman, 2015], and a surrounding anvil cloud formed due to horizontal divergence of cloud droplets lifted to the level of neutral buoyancy [Houze, 2014]. While the anvil cirrus of a DCC consists of ice particles, many of these particles form in the liquid phase within the core, before freezing as they are lifted vertically and then detrained horizontally.

As a result, unlike cirrus clouds which form *in situ* at high altitudes, liquid-phase microphysics are also important to the properties of DCC anvils.

---

**Equation 1.1** The Clausius–Clapeyron relation for saturation vapour pressure, where  $e_s$  is the saturation vapour pressure,  $T$  is the parcel temperature,  $L$  is the latent heat of vaporisation (or sublimation, for ice particles), and  $R_v$  is the gas constant of water vapour. While this can be solved analytically, a more accurate solution can be found empirically which is shown in eq. 1.2 [Alduchov and Eskridge, 1997].

---

$$\frac{1}{e_s} \frac{de_s}{dT} \cong \frac{L}{R_v T^2} \quad (1.1)$$

$$e_s(T) \cong 6.1094 \left( \frac{17.625 \cdot T}{T + 243.04} \right) \quad (1.2)$$


---

When an airmass containing water vapour is lifted it expands and cools. In doing so, saturation vapour pressure decreases—in accordance with the Clausius–Clapeyron relation (eq. 1.1)—at a faster rate than the specific vapour pressure of the airmass. If the vapour pressure exceeds the saturation vapour pressure the result is a supersaturated airmass, which can condense to form cloud droplets. It is very difficult, however, for water droplets to form in a perfectly clean atmosphere, and so for this to happen supersaturation of several hundred percent would be required. Instead, aerosol particles in the supersaturated airmass become the surface on which cloud droplets form, a process known as Cloud Condensation Nuclei (CCN) activation [V. Hobbs, 1993]. The conditions under which aerosols can be activated as CCN are given by the Köhler curves, which combine the competing effects of Kelvin’s equation and Raoult’s law on the equilibrium vapour pressure above the surface of a droplet. Kelvin’s equation defines how the equilibrium vapour pressure increases as the radius of curvature decreases, therefore requiring a higher supersaturation for the activation of smaller droplets. Raoult’s law regards the effect of soluble ions on the equilibrium vapour pressure: a larger amount of solute within the droplet reduces the required super-

saturation. The resulting curve has a peak supersaturation requirement at a certain  
130 droplet radius. For an aerosol particle to be activated and grow into a cloud droplet it must either be larger than this radius and large enough that water can condense on it at the current supersaturation, or contain enough soluble ions that the peak supersaturation of the Köhler curve is less than the airmass supersaturation. As a result, aerosol particles with high solubility—including in particular sulphate and  
135 nitrate aerosols, volatile organic compounds and sea salt—form the majority of CCN.

Activated cloud droplets grow through two processes: condensation and coalescence. Condensation growth is most effective on small droplets as they have the largest surface area to volume ratio, and is responsible for the growth of cloud droplets from the radius of CCN (on the order of  $0.1\text{ }\mu\text{m}$ ) to that of a typical cloud droplet of  
140 around  $10\text{ }\mu\text{m}$  [Rogers, 1979]. This process also results in a narrowing of the cloud droplet size distribution. Coalescence growth occurs through either the merging of cloud droplets due to collision, or the collection of cloud droplets by rain droplets as the fall (accretion). It becomes effective for larger cloud droplets beginning with radii of around  $20\text{ }\mu\text{m}$  and is responsible for their growth into rain droplets [Rogers,  
145 1979]. However, growth through condensation is very slow to reach the droplet sizes required for coalescence growth, and instead stochastic variability and the activation of giant CCN [Feingold et al., 1999] are required for rain droplets to form. On average, only about 30% of the condensed water within a cloud will become rain droplets [Trenberth et al., 2003].

150 Ice clouds have important and complex microphysics. Ice cloud particles may be formed either through direct deposition of water vapour into ice, or through the freezing of liquid cloud droplets. Liquid water will not, however, freeze immediately below the freezing point due to the freezing energy barrier [Heymsfield and Miloshevich,  
155 1993]. Instead, liquid cloud droplets may exist in a super-cooled state, which may be frozen by one of two processes. Homogeneous freezing occurs at temperatures below

–38 °C, allowing liquid droplets to freeze without external interactions [Koop et al., 2000]. As a result, homogeneous freezing of liquid cloud droplets tends to result in a larger number of smaller ice particles [Kärcher and Lohmann, 2002; Ickes et al., 2015]. Heterogeneous freezing occurs due to the presence of Ice Nucleating Particles (INPs) [Kanji et al., 2017]. INPs reduce the freezing energy barrier due to having similar structures to ice crystals [Hoose and Möhler, 2012], and so allow freezing at warmer temperatures [Kärcher and Ström, 2003]. However, INPs are somewhat rare in the atmosphere [Burrows et al., 2022], and so heterogeneous freezing tends to result in fewer ice cloud particles, and, in some cases, mixed-phase clouds which consist of both ice and liquid droplets.

Ice particles may grow through deposition; the direct freezing of water vapour onto the surface of the crystal. Similarly, ice crystals may lose mass due to sublimation, however due to the low saturation vapour pressures in cold temperatures this process is slow at high altitudes [Seeley et al., 2019a]. Ice crystals may grow through aggregation, where multiple crystals join together, or through riming, where super-cooled water droplets freeze on contact with an ice crystal [Taylor et al., 2016]. Additional, smaller ice crystals are produced through secondary ice production processes including rime-splintering, droplet shattering and collision fragmentation [Field et al., 2017]. Ice crystals are commonly removed from the atmosphere via sedimentation, which plays an important role in precipitation [Mülmenstädt et al., 2015].

Overall, ice cloud microphysics has complex dependencies on a wide range of factors. In addition, these complex processes lead to a wide variety of shapes and sizes of ice particles, including both regular and irregular shapes [Waitz et al., 2022], which adds further variance to ice crystal interactions. The understanding of ice cloud microphysics, along with its parameterisations in climate models, is a large and important source of uncertainty in understanding clouds and future climate change [Sullivan and Voigt, 2021; Gasparini et al., 2023].

### 1.2.2 Cloud radiative properties

Cloud droplets interact through radiation both through the reflectance and scattering  
185 of solar visible and Near Infrared (NIR) radiation, and also through the absorbance and emission in the LW spectrum. While the reflection of incoming radiation has a cooling effect on the Top-of-Atmosphere (ToA) atmospheric energy balance, the LW effect of cloud is warming. As a result, a cloud may have a net warming or cooling effect depending on the balance of these two factors. The difference between the ToA  
190 radiative flux with clouds versus that for a clear sky is referred to as the CRE.

The SW reflectance of a cloud depends upon both the microphysics and the number of cloud droplets. The impact of cloud microphysics can be reduced to a single variable, effective radius, which is the average radius of the extinction cross-section for the droplets [Liou, 1992]. While this is relatively straightforward for liquid cloud  
195 droplets, for ice clouds this is complicated by their non-spherical geometries [Wyser, 1998]. By combining the effective radius with the cloud liquid water path or ice water path, the optical thickness of the cloud can be calculated, which represents the amount of transmittance that is blocked by the cloud. Clouds with high optical thickness reflect more SW radiation, and vice versa.

On the other hand, the LW effect depends more upon the temperature (and hence height) of the cloud than its microphysics. High-altitude clouds with a large temperature difference to the surface will emit less LW radiation than they absorb and hence have a warming effect. As the absorption of LW radiation by cloud droplets is typically greater than their SW reflectivity, thin clouds will tend to have a greater  
205 LW effect than SW.

Thick, low-level clouds, such as cumulus, stratocumulus and stratus have an overall cooling effect as they reflect a large proportion of incoming solar radiation but emit in the LW at a similar temperature to the surface. On the contrary, high, thin, cirrus clouds have a strong warming effect as they transmit the majority of incoming solar

<sup>210</sup> radiation but emit at a much lower temperature than the surface. DCC anvils, being both thick and at a high altitude, tend to have a balanced effect within  $10 \text{ W m}^{-2}$  of neutral [Ramanathan et al., 1989; Hartmann et al., 1992; Hartmann, 2016], however their SW and LW CRE both have large magnitudes. Overall, CRE has a cooling effect on the climate, but displays a positive feedback to global warming. This feedback is <sup>215</sup> one of the largest uncertainties in future climate change [Sherwood et al., 2020], and recent research has found that this uncertainty may be underestimated by current Global Climate Models (GCMs) [Hill et al., 2023].

### 1.2.3 Thermodynamics of deep convection

<sup>220</sup> Deep convection requires three ingredients to occur [Brooks et al., 2019]:. First, a build-up of conditional instability throughout the troposphere. Second, a source of moisture in the lower troposphere. Third, a buoyancy perturbation or vertical motion which lifts a parcel of moist, low-level air above the Lifted Condensation Level (LCL) and the Level of Free Convection (LFC).

---

**Equation 1.3** The full buoyancy equation for an air parcel perturbed from the surrounding environment. The buoyant acceleration,  $B$ , is approximately equal to gravitational acceleration times four terms, from left the right: the temperature term, the vapour term, where  $q_v$  is the mixing ratio of water vapour, the pressure perturbation term, and the hydrometeor drag, where  $q_h$  is the mixing ratio of hydrometeors. Variables with bars represent the background state.

---

$$B \approx g \left( \frac{T - \bar{T}}{\bar{T}} + 0.61 \frac{q_v - \bar{q}_v}{\bar{q}_v} - \frac{p - \bar{p}}{\bar{p}} - q_h \right) \quad (1.3)$$


---

<sup>225</sup> Conditional instability refers to a situation in which the decrease in temperature with height in an atmospheric column is greater than the moist pseudo-adiabatic lapse rate, but less than that of the dry adiabatic lapse rate. Whereas unconditional instability (where the temperature lapse rate is greater than the dry adiabatic lapse rate) is quickly stabilised through dry convection, conditional instability can continue

to build until a convective cloud is formed. When water condenses, the latent heat  
230 released results in a positive buoyancy force (eq. 1.3 which accelerates the parcel upwards leading to large vertical velocities. The build-up of instability is measured as the Convective Available Potential Energy (CAPE) of an air parcel (eq. 1.5), which represents the potential kinetic energy provided by the buoyancy of a parcel lifted above the LFC. The work required to lift the parcel to the LFC is measured as the  
235 Convective Inhibition (CIN) (eq. 1.6). High values of CAPE are associated with intense convection.

---

**Equation 1.4** By ignoring the pressure, vapour and hydrometeor terms of eq. 1.3 we can rewrite the buoyancy equation in terms of the vertical velocity,  $w$ , the height  $z$  and temperature. CAPE is calculated by integrating the right-hand side of the equation over height between the LFC and the Level of Neutral Buoyancy (LNB) (eq. 1.5). CIN is calculated by integrating the negative buoyancy between the initial position of the parcel and the LFC (eq 1.6).

---

$$\frac{D}{Dz} \left( \frac{w^2}{2} \right) = g \left( \frac{T - \bar{T}}{\bar{T}} \right) \quad (1.4)$$

$$\text{CAPE} = g \int_{\text{LFC}}^{\text{LNB}} \left( \frac{T - \bar{T}}{\bar{T}} \right) dz \quad (1.5)$$

$$\text{CIN} = -g \int_{z_0}^{\text{LFC}} \left( \frac{T - \bar{T}}{\bar{T}} \right) dz \quad (1.6)$$


---

The properties of a convective airmass are commonly derived using parcel theory [Stull, 2016]. This approach approximates the air parcel as undergoing adiabatic processes while it is lifted from the lower to the upper troposphere. The buoyancy of  
240 the air parcel along this trajectory is dependent on the initial height and moisture content of the parcel as well as the temperature profile of the environment it exists in. Analysis of these trajectories can be performed by plotting them on a thermodynamic

diagram. An example of a tephigram, which plots the ascent of a parcel on axes of temperature and potential temperature which are skewed by 45 degrees, is shown in  
245 fig. 1.2. The tephigram has advantages over other thermodynamic diagrams commonly used in meteorology, such as the T–logP diagram, as its axes are orthogonal to each other and therefore thermodynamic properties such as CAPE and CIN are accurately represented by their areas.

From its initial position, the parcel is assumed to undergo adiabatic cooling as  
250 it is lifted until its temperature reaches that of the dew point of the initial airmass. At this point, the LCL, the saturation of the airmass reaches 100%, condensation occurs and the cloud begins to form. Beyond this point, the temperature of the parcel is assumed to follow the moist pseudo-adiabatic lapse rate. As this lapse rate is less than that of an environment with conditional instability, as the parcel  
255 continues to rise it will reach a point where its temperature is greater than that of the surrounding environment referred to as the LFC. Above the LFC the parcel will experience positive buoyancy until it reaches a more stable layer of the atmosphere. As the moist adiabatic lapse rate approaches that of the dry adiabatic lapse rate at low temperature and humidity (and hence at higher altitudes), and the environmental  
260 lapse rate reduces as it approaches the tropopause layer [Fueglistaler et al., 2009], the parcel will cool below the temperature of the surrounding environment. The point at which the temperature profile of the parcel again crosses that of the environment is called the Level of Neutral Buoyancy (LNB). Although the air parcel may continue to rise above this point due to its momentum, negative buoyancy will act to halt its  
265 ascent.

Two further properties related to convection are also shown on the tephigram. CAPE can be calculated as the area between the parcel temperature profile and the environment profile between the LFC and the LNB, showing clearly how CAPE is the total work exerted by positive buoyancy forces between these two levels. From this,

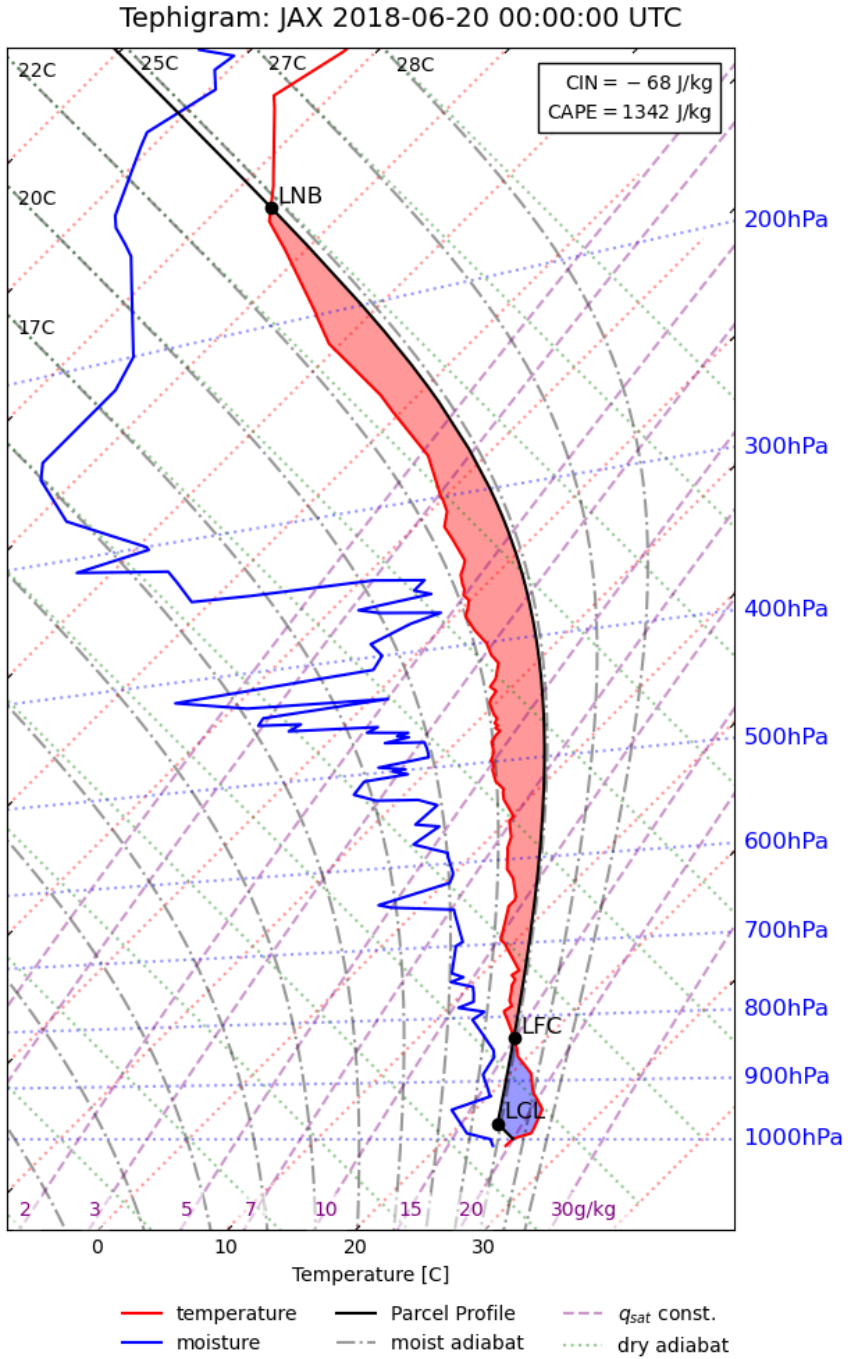


Figure 1.2: An illustration of parcel ascent on a tephigram for a sounding taken on 2018-06-20 00:00 UTC at Jacksonville, Florida. The environmental temperature profile is shown by the red line, and the dewpoint temperature by the blue line. The path of the parcel, which starts near the surface, is shown by the black line. Points marking the LCL, LFC and LNB are shown. The CAPE and CIN are shown by the red and blue areas respectively.

270 CAPE can be used to calculate the theoretical maximum updraft velocity if all CAPE  
is converted to kinetic energy, although typical observed maximum updraft velocities  
are half of this amount. Similarly, Convective Inhibition (CIN) can be calculated  
as the area between the temperature profiles between the initial parcel location and  
the LFC. CIN measures the work required to lift the parcel, overcoming negative  
275 buoyancy forces, in order to reach the LFC.

There are a number of caveats with the parcel approach for deep convection that  
must be considered. The convective profile of a parcel depends upon its starting  
conditions including initial height, temperature and humidity. As a result, for even  
a single atmospheric column, a whole ensemble of parcels initialised at different lo-  
280 cations within the PBL can be considered, each with different values of LCL, LFC,  
LNB, CAPE and CIN. To account for this, the mixed-layer CAPE is often calculated  
from the average for parcels initiated in the PBL [Stull, 2016]. In addition, the prop-  
erties of the most unstable parcel may also be found in the same manner, which may  
provide useful information for predicting convective initiation.

285 Secondly, it is generally assumed that above the LCL the parcel follows the moist  
pseudo-adiabat [Peters et al., 2022], which approximates that all condensed water is  
removed from the parcel immediately via precipitation [Emanuel, 1994]. Although  
this approximation may seem to agree with the high precipitation rates of DCCs,  
observed profiles of convective updrafts more closely match the moist adiabatic lapse  
290 rate (which assumes that all condensed water remains within the parcel) [Xu and  
Emanuel, 1989]. In addition, it is often considered that MSE is conserved in convective  
processes, however this is only correct in the case of environments in hydrostatic  
balance [Peters and Chavas, 2021]. In deep convection, where this is not the case, it  
is a better approximation that MSE minus CAPE is conserved [Romps, 2015].

295 Finally, and arguably most importantly, is that the parcel model assumes that  
there is no mixing between the air parcel and the surrounding environment, a state

that is referred to as undiluted. In the dynamic and turbulent environment of deep convection mixing does occur, however, and it is very rare for an undiluted state to occur [Romps and Kuang, 2010]. The entrainment of dry air into convective updrafts  
300 due to mixing reduces both CAPE [Zhang, 2009] and the LNB [Masunaga and Luo, 2016] as it adjusts the parcel profile closer to the background temperature profile, reducing the buoyancy forces. Observations of DCCs have shown that while the highest cloud tops of DCCs reach or even exceed the LNB, the majority of the anvil cloud is detrained at a level substantially below the LNB [Takahashi and Luo, 2012;  
305 Takahashi et al., 2017a].

An additional factor not considered by the parcel model is the impact of circulation on instability. Low-level convergence may transport additional heat and moisture to the base of the profile, increasing the potential for convection. Wind shear—change in the speed and/or direction of wind with height—may also increase instability by  
310 transporting a colder airmass over a warmer boundary layer. Wind shear plays an important role in the behaviour of DCCs which will be explored in the following section.

#### 1.2.4 Lifecycle and structure of DCCs

The lifecycle of deep convection begins with the development of instability throughout  
315 the troposphere. The primary driver of instability is LW cooling of the troposphere (mainly through water vapour emissions), which cools at around 2K per day [Jeevanjee and Fueglistaler, 2020]. SW heating also affects instability which leads to diurnal differences, however there is also a land–sea contrast in this effect. Over land, SW absorption warms the surface during the daytime, which sensible heating transfers to  
320 the lower troposphere. This SW heating leads to an increase in CAPE throughout the day, and, in particular, a peak in convective initiation in the afternoon due to surface heating and the resulting enthalpy flux into the PBL. On the contrary, over

the ocean, SW heating has less of an effect on the surface due to the greater heat capacity of water and the mixing of the ocean surface. Instead, a peak in instability 325 is seen during the night and early morning, which is believed to be due to the effects of SW heating on the mid and upper troposphere during the day [Wall et al., 2018]. The diurnal cycle of instability is much less pronounced over the ocean than over land, however [Taylor et al., 2017].

Instability can also be driven by the relative motion of air masses. Over the great 330 plains of North America, warm, moist air is transported northward from the Gulf of Mexico which leads to instability as it moves under colder air [Walters and Winkler, 2001]. Polar lows, on the other hand, are linked to the transport of cold air from polar land regions over a relatively warm ocean surface [Moreno-Ibáñez et al., 2021].

Once sufficient instability has built up throughout the troposphere for deep convection to occur, a lifting action or buoyancy perturbation must occur to overcome 335 CIN and initiate the formation of a DCC. This initiating process is referred to as the ‘triggering’ of convection. Triggering can occur through perturbations of the first three terms in the buoyancy equation (eq. 1.3). SW heating of the surface can cause an increase in surface air temperature through sensible heat fluxes, leading to dry 340 convection and convective initiation. Surface heating also causes latent heat fluxes, increasing the enthalpy and moisture content of the boundary layer. In addition, the convergence of air masses within the boundary layer can also increase buoyancy by convergences of moisture and positive pressure perturbations. A number of mechanical lifting mechanisms are also involved in the initiation of convection. Orographic 345 lifting can occur when warm, moist air is blown towards mountains and cools as it ascends [Hodges and Thorncroft, 1997]. Gust fronts of cold, dense air may also act to lift warmer, moist air masses above them. These gust fronts may be caused by a number of processes, including synoptic frontal systems [Wilson and Schreiber, 1986; Jirak and Cotton, 2007], sea breeze [Tripoli and Cotton, 1979; Park et al., 2020], and

<sup>350</sup> cold pools caused by precipitation [Grant and van den Heever, 2016].

The occurrence of cumulus and cumulus congestus clouds (convective clouds in the low- and mid-troposphere [Johnson et al., 1999]) may also lead to deep convection. These lower-level convective clouds cause convergences of warm, moist air near the surface, building instability, and may also act to ‘condition’ the lower troposphere to <sup>355</sup> convection by adjusting the environmental temperature profile closer to that of an ascending air parcel and hence reducing CIN [Masunaga and L’Ecuyer, 2014; Schulz and Stevens, 2018].

Once initiated, the lifecycle of DCCs can be separated into three sections: a growing phase, where the core develops vertically; a mature phase in which the anvil cloud <sup>360</sup> develops horizontally while convection continues within the core; and a dissipating phase in which the anvil cloud dissipates after convective activity ceases within the core [Wall et al., 2018]. For isolated DCCs (those consisting of a single core) the overall lifecycle typically spans 1-3 hours [Chen and Houze, 1997]. However, DCCs may also form with multiple cores feeding a single anvil cloud [Roca et al., 2017], and <sup>365</sup> in these cases may span areas several orders of magnitude larger [Houze, 2004], and exist for 10-20 hours or longer [Chen and Houze, 1997].

The initiation stage occurs between the point of initiation and the time at which the top of the convective core stops growing upwards. During this stage precipitation may occur in both the warm and ice phases, and the horizontal growth of the cloud <sup>370</sup> is small in comparison to the vertical growth. The initiation stage can be further broken down into the periods before and after the onset of freezing. Freezing releases additional latent heat of fusion, however this may not contribute additional buoyancy as it is compensated for by the environment [Seeley and Romps, 2016].

Due to the large vertical velocities and high supersaturation present in deep con-<sup>375</sup> vective updrafts, freezing is dominated by homogeneous freezing processes. Furthermore, the intense dynamics result in a high rate of secondary ice production through

the collision of droplets. As a result, DCCs tend to form with a large number of small ice particles.

In convective updrafts with large vertical velocity, the momentum of the growing cloud may propel it above the LNB. This produces a phenomenon known as an overshooting top. As the cloud will continue to cool adiabatically as they rise, the tops of these updrafts can reach substantially colder temperatures than the surrounding environment [Proud and Bachmeier, 2021].

The mature stage occurs after the top of the DCC has reached the level of neutral buoyancy. The heaviest rates of convective precipitation occur during this stage, and the anvil cloud is formed [Houze, 2014]. The occurrence of heavy precipitation suppresses the convective core both through the generation of downdrafts and through the stabilisation effect of evaporating rain droplets. This process will eventually weaken and dissipate the convective core of the DCC unless the wind shear is large enough to advect the convective rainfall away from the convective core.

Furthermore, the evaporation of falling precipitation leads to the divergence of cold, dense air near the surface. These cold pools may suppress further convective activity, however their gust fronts may also trigger new convective cores.

The final stage of the DCC lifecycle occurs after the convective core has dissipated and convective rainfall has stopped, and is referred to as the dissipating phase. During this phase, the anvil cloud may continue to expand, with maximum anvil cloud extent occurring much later than maximum convective intensity. Additional, stratiform, precipitation may occur throughout the anvil cloud, but this will not be as intense as the earlier convective precipitation [Houze, 2014]. The dissipating stage may also be split into two separate periods; those before and after the end of stratiform precipitation [Wall et al., 2018].

DCCs can also be categorised spatially into three components. Firstly, the core region, in which the convective updraught and convective precipitation occur. Secondly,

the anvil or cloud shield, which consists of a large area of thick cloud surrounding the  
405 core at the level of neutral buoyancy, and within which stratiform precipitation may occur. Finally, the area of cirrus outflow, where thin ice cloud extends beyond the edge of the anvil cloud, particularly within the dissipating phase [Lilly, 1988].

Radiative heating of the anvil cloud base and cooling of the anvil cloud top causes two regions of instability to occur. These unstable profiles drive circulations at the  
410 cloud base and top which increase the entrainment of dry air into the anvil while also lifting the anvil higher in the troposphere. While SW heating during the daytime reduces the instability at the cloud top, the greater LW heating at the cloud base results in a greater net dissipation of anvil during the daytime [Sokol and Hartmann, 2020]. As the anvil cloud thins, these two regions of instability join into a single lapse  
415 rate. This state drives two circulations within the anvil cloud [Gasparini et al., 2023]. The first exists within the anvil cloud and causes updrafts which lift ice particles, reducing sedimentation and increasing particle growth through sedimentation. The second circulation acts horizontally between the anvil cloud and surrounding clear sky regions, and transports additional moisture into the anvil cloud. The combined  
420 effect of these circulations prolongs the lifetime of the thin anvil cloud [Sokol and Hartmann, 2020]. Further thinning of the cirrus anvil results in uniform radiative heating throughout the anvil, ending the circulation and leading to complete dissipation of the anvil cloud.

### 1.2.5 Convective organisation

425 While the majority of DCCs form as isolated storms, with a single convective core that detrains its own anvil cloud. In other cases, DCCs exist with multiple convective cores feeding a single anvil cloud. At the largest end of this progression are Mesoscale Convective Systems (MCSs), which occur when a cluster of deep convective cores form a single large area of anvil referred to as a cloud shield [Roca et al., 2017]. These

<sup>430</sup> MCS cloud shields can cover an area of greater than 10,000 km<sup>2</sup>, several orders of magnitude greater than that of individual DCCs [Houze, 2004].

The convective cores that form MCSs do not group together at random, but are instead clustered by a complex group of processes that are referred to as convective organisation. In general, these processes tend to lead to the triggering of new <sup>435</sup> convective cores that feed the same cloud shield, expanding and extending the life of the system as they do. MCSs occur in a number of shapes and sizes, including mesoscale convective complexes, squall lines and tropical cloud clusters [Tsakraklides and Evans, 2003] which each have their own unique properties. However, all MCSs display large-scale processes that initiate new cores, and increase the size and lifetime <sup>440</sup> of the anvil

The lifecycle of MCSs can be described similarly to that of isolated DCCs through the three-phase growing, mature, dissipating structure [Futyan and Del Genio, 2007]. It should be kept in mind however that when applied to MCSs, these lifecycle stages do not represent the changes in convective processes as described for isolated DCCs, <sup>445</sup> but the mesoscale development and decay of the entire system. The lifetime of these systems is substantially lengthened, with typical MCSs lasting for 10 to 20 hours or longer [Chen and Houze, 1997]. In particular, there is an increase in the lengths of the initiation and mature phases compared to isolated DCCs [Wall et al., 2018] due to the continuous development of new cores throughout the active lifetime of the MCS. The <sup>450</sup> total lifetime of MCSs is determined by the rate at which new cores are triggered, and observations have shown that they tend to decay once the area of convective cores falls below 10% of the total anvil area [Elsaesser et al., 2022].

A key feature that distinguishes MCSs from smaller DCCs is the development of a large, mesoscale circulation that occurs on a larger scale than the individual <sup>455</sup> convective cores. As well as the convergence of heat and moisture at low levels due to the convective cores, this mesoscale circulation draws in additional air from the sur-

rounding areas at the mid-levels of the atmosphere. This mid-level air does enter the cloud shield through the convective cores, but instead condenses at higher altitudes, leading to a top-heavy latent heating profile within the cloud shield [Schumacher et al., 2004]. These organised convective cloud systems have thermodynamic impacts on the environment to a much greater extent than isolated DCCs. The large cloud shields of the MCSs result in much larger amounts of stratiform precipitation than individual DCCs, which is distributed over a much wider area [Houze, 2014]. These organised convective cloud systems have thermodynamic impacts on the environment to a much greater extent than isolated DCCs, with idealised simulations showing that the thermodynamic interactions of organised convective systems can propagate thousands of kilometres within the troposphere [Beucler and Cronin, 2019]. Over time, the mesoscale circulation results in a moistening of the convective system and a drying of the surrounding atmosphere, creating a sharp contrast between the two regions [Bretherton et al., 2005].

MCSs are also characterised by both high rates and large volumes of precipitation, providing the majority of precipitation throughout the tropics as well as in many other regions [Feng et al., 2021]. Unlike isolated DCCs, much of the precipitation occurs not as convective rainfall, but as stratiform rain from the cloud shield [Schumacher and Houze, 2003]. As much as 70 % of the total precipitation of an MCS can come from the stratiform rain, with a higher proportion observed over the ocean than in MCSs over land. Much of this stratiform precipitation can be attributed to the mid-level, mesoscale inflow to the cloud shield as well as the top-heavy latent heating profile.

The processes through which MCSs form in the first place are still uncertain, however [Houze, 2018]. Convective organisation processes have been observed in satellite remote sensing, radiative-convective equilibrium models and cloud-resolving models [Holloway et al., 2017]. The formation and lifetime of MCSs are strongly linked to the dynamics of the surrounding environment through the convergence of

moist, low-level air and the divergence of air at the top of the MCS [Houze, 2014].  
485 Cold pools have a strong influence on the organisation of convective cores, and set the scales over which organisation occurs [Jeevanjee and Romps, 2013], as their gust fronts, transport of moisture and collisions are vital to triggering new convection within MCSs [Feng et al., 2015].

MCSs are, in general, poorly represented in large-scale climate models due to the  
490 inability of the parameterised convection to organise between grid squares [Houze, 2018]. While convective resolving models have been proposed as a solution to this issue [Stevens et al., 2020], these models still do not represent MCSs accurately with a tendency towards too little organisation [Prein et al., 2021]. Gaining a better understanding of the properties and processes of MCS, both in observations and models,  
495 is vital therefore for improving their representation [Feng et al., 2023b]. Changes in convective organisation have important effects on the global climate, with increases in organisation correlated with domain-wide ToA cooling in satellite observations [Bony et al., 2020], and so future changes in organisation may have a large influence on the equilibrium climate sensitivity.

### 500 **1.3 Anvil Radiative Feedbacks**

There are a number of hypotheses regarding the CRE of tropical anvil clouds that consider whether the neutral CRE of tropical anvils is the result of a feedback mechanism. Ramanathan et al. [1989] proposed the thermostat hypothesis in which, in response to a warming environment, anvil clouds produce thicker cirrus which acts to  
505 cool the tropics through increased SW reflectance. The Iris hypothesis proposes that anvil cirrus will decrease in area, resulting in greater LW emission from the surrounding clear-sky regions. Lindzen et al. [2001] first proposed this as a result of increased precipitation efficiency, however evidence for this effect is disputed [Del Genio and Kovari, 2002; Lin et al., 2004]. Bony et al. [2016] proposed a ‘stability iris’ feedback,

510 in which the established trends of increased dry static stability [Held and Soden, 2006] and a reduction in the tropical overturning circulation [Vecchi and Soden, 2007] reduce the detrainment of anvil cirrus. Although the anvil cloud response is generally considered to be a negative climate feedback, the predicted magnitude varies widely and it represents the greatest uncertainty among all cloud feedbacks [Sherwood et al.,  
515 2020].

On the other hand, the Fixed Anvil Temperature (FAT) hypothesis argues that the anvil Cloud Top Temperature (CTT) remains constant in a warming climate, and the greater difference between anvil and surface temperature results in a positive LW feedback [Hartmann and Larson, 2002]. The basis for Fixed Anvil Temperature  
520 (FAT) is that LW cooling of the troposphere due to water vapour becomes inefficient below 220 K [Jeevanjee and Fueglistaler, 2020], which, if relative humidity remains constant, fixes the top of the convectively active troposphere at this isotherm. While there is evidence that this is the case for the largest DCC anvils, the increase in static stability may result in a reduced positive feedback due to a ‘proportionally higher’  
525 anvil temperature [Zelinka and Hartmann, 2010] which more closely matches the LW response of tropical clouds in global climate models. While satellite observations have shown a trend in anvil cloud height [Norris et al., 2016], there is not yet sufficient evidence to distinguish this from inter-annual variability [Takahashi et al., 2019]. Seeley et al. [2019b], argued that FAT is a weak constraint on anvil temperature  
530 as while the radiative tropopause temperature remains fixed, the temperature of the tropopause lapse rate inversion can vary widely. Furthermore, as anvils tend to detrain below the tropopause, [Takahashi et al., 2017a; Wang et al., 2020], anvil temperature and the tropopause temperature may only be weakly connected. Seidel and Yang [2022] however found the inclusion of CO<sub>2</sub> radiative heating produces anvil  
535 temperatures consistent with FAT.

While the iris and FAT feedbacks may act to cancel each other out, and hence

maintain the neutral CRE of tropical anvil clouds, there are other potential feedback mechanisms that may influence this balance. Hill et al. [2023] showed recently that climate models underestimate dynamically driven cloud feedbacks. Furthermore, convective instability is expected to scale with temperature in the same manner as the Clausius-Clapeyron relation [Seeley and Romps, 2015b; Agard and Emanuel, 2017], and some observations of tropical anvil clouds have instead suggested that warming of the surface invigorates convection [Igel et al., 2014]. This invigoration effect may result in colder anvil Cloud Top Temperature (CTT), and hence a stronger warming feedback. Multi-decadal satellite observations have shown a cooling of upper tropospheric cloud temperature over land [Liu et al., 2023], indicating that changes in convective processes may lead to stronger cooling feedbacks.

A recent criticism of the Sherwood et al. [2020] decomposition of anvil feedbacks into the area response and the height response is that, by ignoring changes in the optical properties and structure of anvil clouds, these feedbacks are merged into the calculated iris effect, increasing its uncertainty [Raghuraman et al., 2024]. If we extrapolate from the reasoning of McKim et al. [2024], we find that the anvil area feedback of  $-0.40 \text{ Wm}^{-2}\text{K}^{-1}$  from Sherwood et al. [2020] would require an unrealistic anvil area change of  $-20\% \text{ K}^{-1}$ . Recent work has proposed that the anvil cloud response reduces the area of thicker anvils with high IWC, but not thinner cirrus, resulting in a much smaller overall feedback [McKim et al., 2024; Sokol et al., 2024].

Changes to the lifecycle and diurnal cycle of deep convection may also be an important factor, particularly when considering the SW feedback. Nowicki and Merchant [2004] used estimates of Top-of-Atmosphere (ToA) LW and SW radiative fluxes from Spinning Enhanced Visible Infra-Red Imager (SEVIRI) observations to estimate the diurnal cycle of anvil CRE over equatorial Africa and the equatorial Atlantic. They found that shifting the diurnal cycle of deep convection in these regions could change the CRE by  $\pm 10 \text{ Wm}^{-2}$ , but did not track the properties of individual DCCs. Bouniol

et al. [2016] compared CRE and cloud radiative heating rates to anvil cloud properties  
565 to investigate how radiative heating affects the anvil cloud evolution. These observations were made with polar orbiting instruments however, and they highlighted the need for geostationary observations to characterise the evolution of individual anvil clouds. Subsequent research used DCC tracking methods to better characterise the lifecycle of observed anvil clouds [Bouniol et al., 2021], but as the radiative flux data  
570 was provided by polar-orbiting satellites the CRE could not be measured over the lifetime of the DCC.

## 1.4 Detection and tracking of deep convection

The detection and tracking of clouds has been performed since the earliest sequences of remote sensing imagery from weather radar and geostationary satellites [Menzel,  
575 2001]. Fujita et al. [1968] compared sequences of images observed by the first geostationary weather satellite to those taken using an all-sky camera, and found that by comparing subsequent observations from the satellite one could calculate AMVs similar to those observed on the ground. This tracking of cloud position was performed by hand, and subsequently a plastic stencil ‘computer’ was designed to calculate cloud  
580 velocities taking into account the satellite viewing geometry [Fujita, 1969]. While these early methods compared print-outs of satellite imagery by hand, shortly after a digital computer system was developed to show sequences of images [Chang et al.,  
1973]. Although detection and tracking was still performed manually (albeit with the user selecting cloud positions in subsequent images using the cursor), velocity calculation  
585 was performed automatically. Wider adoption of this technology was applied to produce AMVs during field campaigns in the mid- to late-1970s [Tecson and Fujita, 1975].

There was, however, concern regarding the manual tracking of cloud velocity. This task was both time consuming and also open to subjective judgement which made

590 uncertainties hard to estimate. Fujita et al. [1975] found large variations in AMVs produced using these methods. Early efforts at automation applied cross-correlation techniques, previously used with weather radar, to estimate AMVs in geostationary satellite imagery [Leese et al., 1970]. Endlich et al. [1971] applied a pattern matching technique to ‘brightness centres’ in visible satellite imagery to estimate cloud motion.

595 Rinehart and Garvey [1978] produced a cross-correlation algorithm for the estimation of convective cell motion in 3-d weather radar observations. While these automated methods provided more accurate motion estimate than humans, they were less capable of detecting independent cloud motions both due to errors introduced by noise, and also due to the visible imagery provided by early geostationary satellites meaning it

600 was difficult to distinguish clouds at different altitudes.

Automatic methods for the detection and tracking of DCCs were developed for both radar reflectivity [Crane, 1979] and geostationary satellite LW Infrared (IR) Brightness Temperature (BT) [Endlich and Wolf, 1981]. Both of these methods detected DCC features by labelling the area surrounding local extrema (maxima for 605 radar reflectivity, minima for BT) in individual images. The addition of 11  $\mu\text{m}$  IR-window BT channels to the first operational GOES and Meteosat weather satellites allowed DCCs to be distinguished from low clouds. The centroids (the location of the feature represented as a single point) of these detected features were then linked to create DCC tracks through the use of cost-minimisation algorithms with sought 610 to find the best match between pairs of features detected at subsequent time steps. By explicitly detecting features to track, these algorithms both improved upon the weakness of previous algorithms, but also allowed the properties of tracked objects to be studied beyond their motion vectors.

The development of DCC detection and tracking algorithms continued in parallel 615 for both radar and satellite observations. Rosenfeld [1987] and Williams and Houze [1987] both developed overlap tracking techniques for radar reflectivity and satellite

BT observations respectively. Unlike the prior centroid-based tracking methods, these overlap methods took into account the spatial extent of detected features by linking subsequent pairs of features based on those which shared the largest overlapping area.

620 By removing the approximation of a point-like feature, the overlap techniques better handled cases of DCCs with larger, more complex shapes. The downside to this approach, however, is that, unless the spatial extent of the DCC is propagated using an estimate of the storm motion, it requires that the detected features do not move further than their diameter between subsequent observations. As a result, for small,

625 fast-moving objects (such as convective cells), or observations that are more widely spaced, overlap methods perform poorly.

Early detection and tracking algorithms were strongly limited by the available computational power which restricted tracking to only a small number of DCCs. Furthermore, the accuracy of early algorithms was such that human verification of

630 tracked objects was still required. The majority of algorithms were designed with only a single source of observations, which, in particular for weather radars, reduced the area over which tracking could be performed. While geostationary satellites provided larger areas of observations, the low spatial and temporal resolution of early sensors to only large and long-lived DCCs such as MCSs. Maddox [1980a] tracked mesoscale

635 convective complexes over the US, and subsequent studies showed their distributions globally [Laing and Michael Fritsch, 1997].

Subsequent development produced trends in both those algorithms used to track DCCs in satellite imagery, and those using weather radar. Algorithms using geostationary satellite imagery focused on the study of MCSs, and tended to use overlap-based tracking methods [Arnaud et al., 1992; Evans and Shemo, 1996; Carvalho and Jones, 2001; Morel and Senesi, 2002]. On the other hand, tracking algorithms using radar reflectivity tended to focus on the tracking of convective cells, and favoured centroid-based tracking approaches [Dixon and Wiener, 1993; Johnson et al., 1998;

Handwerker, 2002]. Across both sets of algorithms, the use of fixed thresholds rather than extrema for locating features became favoured both due to the low computational cost, ease of customisation and resilience to noise [Augustine and Howard, 1988]. While the majority of approaches used a single threshold, a number of algorithms introduced the use of multiple threshold to better characterise the detected features of DCCs. Johnson et al. [1998] used a sequence of increasingly larger thresholds to better distinguish individual convective cells, and classify them according the intensity. For MCS detection, the ‘detect-and-spread’ approach was used by Evans and Shemo [1996] and Boer and Ramanathan [1997] to better measure the area of MCSs by first detecting the ‘core’ using a cold BT threshold and then detecting the surrounding cloud area using a warmer threshold. It should be noted however that Augustine and Howard [1988] argued that the area estimated by the approach is highly subjective.

Hodges [1994] developed a more general algorithm for use with multiple gridded datasets, including model data, and subsequently expanded this approach to consider detection and tracking on a sphere for use with GCMs [Hodges, 1995]. The low spatial and temporal resolution of GCMs at the time however meant that detection and tracking of individual DCCs was not possible. Other data, such as rainfall measurements and lightning flash observations, were also used to develop detection and tracking algorithms [Steinacker et al., 2000], however the vast majority of algorithms continued to use either radar reflectivity or geostationary satellite BT observations.

The development of radar detection and tracking algorithms was strongly driven by the needs for nowcasting (short-term, 30- to 60-minute forecasts) of convective activity [Wilson et al., 1998]. As these algorithms are required to predict the future motion of observed DCCs, good estimates of the storm motion, including growth and decay, are required. Development of these algorithms, therefore, focused primarily on the tracking aspect rather than the detection of DCCs [Lakshmanan and Smith,

2010]. The Sydney 2000 Olympics provided both a demonstration of, and comparison between, the capabilities of multiple tracking algorithms [Keenan et al., 2003]. The study into the performance of these algorithms found that no particular tracking approach worked best overall, and that each had strengths and weaknesses in different situations [Wilson et al., 2004]. In response, subsequent algorithms used hybrid approaches which combined multiple tracking methods to provide better performance over a range of scenarios [Lakshmanan et al., 2007; Han et al., 2009].

The second generation of geostationary weather satellites provided greater capability to track individual DCCs due to both their higher spatial and temporal resolutions and increased number of channels across the visible and IR spectrum. Roberts and Rutledge [2003] showed that these observations could be used to detect initiating DCCs up to 30 minutes before they appearing in weather radar observations. Because of their use of a single BT threshold, existing methods could only track DCCs once they had matured. While this was generally acceptable for tracking MCSs, this limited their capability for tracking isolated DCCs. Mecikalski and Bedka [2006] developed an algorithm which combined visible imagery, estimates of BT cooling rate over multiple observations and AMVs to indicate convective initiation. Zinner et al. [2008] used multiple IR BT channels from the Meteosat SEVIRI imager, along with the high resolution visible channel and motion vectors derived using a pyramidal matching algorithm to detect and track developing DCCs over multiple stages from initiation to maturity.

A common theme throughout all the algorithms described so far is the separation of feature detection and tracking into separate procedures, with features detected independently at each time step. While this allows for simplification of the overall process, the independent detection of features at each time step introduces a large degree of inconsistency in the area and location of features detected over time. Furthermore, when using a fixed threshold, this also prevents the detection of features

before or after they reach the threshold, limiting the detection of growing or decaying DCCs. A number of recent algorithms have sought to address this by combining both  
700 feature detection and tracking into a single process. Fiolleau and Roca [2013] applied the ‘detect-and-spread’ approach to a ‘3-D’ stack of images over time. By first detecting the core region using a cold BT threshold, and then detecting the surrounding cloud volume using a warmer threshold, the algorithm is better able to detect the growing and decaying phases of DCCs without erroneously detecting warmer clouds.  
705 However, the algorithm does not consider the motion of the tracked objects in any manner, and so is only suitable for detecting MCSs whose areas are large compared to the distance moved between observations. Thomas et al. [2010] used a variational-data-assimilation model to both detect and track DCCs in geostationary satellite images. This approach not only allowed detection and tracking in a single step, but  
710 was also resilient to cases of noisy or missing data.

Improvements in climate modelling have led to new applications of cloud detection and tracking algorithms in cloud-resolving models [Plant, 2009], large eddy simulations [Dawe and Austin, 2012; Heus and Seifert, 2013] and for the evaluation of GCMs [Clark et al., 2014]. A wide range of modern algorithms have been developed specifically  
715 for general application to radar, satellite and model data [Heikenfeld et al., 2019; Ullrich and Zarzycki, 2017; Ullrich et al., 2021; Raut et al., 2021; Feng et al., 2023a]. These new methods have allowed studies into the differences in DCCs between observations and models, as well as the response of DCCs to perturbations across multiple models [Marinescu et al., 2021; Feng et al., 2023b]. Furthermore, the flexibility of  
720 these general purpose approaches has allowed their application for the detection and tracking of atmospheric phenomena beyond DCCs [Bukowski and van den Heever, 2021; Zhang et al., 2023].

A further focus of modern algorithm development has been for studying trends in the behaviour of DCCs observed in long time series of observations, with techniques

725 optimised to these problems [Núñez Ocasio et al., 2020; Hayden et al., 2021]. Overall, these developments have allowed cloud tracking studies to move from smaller cases to large data problems involving the properties of tens, if not hundreds of thousands of DCCs.

DCC detection and algorithms have made vast advances since the earliest approaches that supplanted human tracking. Through this development process, the requirements for a successful algorithm have become apparent. The detection process needs to accurately distinguish between DCCs and other clouds, while also detecting the largest possible extent and proportion of the DCC lifetime, while being consistent between time steps and resilient to noise. The first two aspects pose a challenge, 730 as in general improving one of these sensitivities means worsening the other. The tracking approach needs to then accurately connect these features without mistakenly connecting or failing to track storms, taking into account the motion of each DCC as well as splits and merges. Many modern algorithm developments have only focused on addressing a few of these concerns, without taking into account developments 735 made by other algorithms. Many of the same issues from older algorithms still exist. For example, many modern detection approaches using satellite BT only use a single 11  $\mu\text{m}$  channel, despite the availability of many different channels providing additional information about DCC properties from modern imagers.

One of the key remaining challenges is the split in algorithms designed to track 745 MCSs and those designed to track individual DCCs. The gap in capabilities between these two approaches makes it challenging, if not impossible, to study the behaviour of DCCs across a wide range of scales. Investigating these properties, therefore, will require further developments on top of those already made on DCC detection and tracking.

## 750 1.5 Structure of the thesis

Improving our knowledge of the processes influencing DCCs is vital to better understanding of their response to a warming world. Recent research has highlighted the need to study the optical properties and structure of DCCs, and improve the connections between convective processes and anvil properties [Gasparini et al., 2023]. In 755 addition, understanding how these properties change over the evolution of the anvil clouds has become an increasing focus of studies [Sokol and Hartmann, 2020; Wall et al., 2018; Bouniol et al., 2021]. The body of this thesis consists of four major chapters, through which we aim to answer four questions about the study and behaviour of DCCs:

### 760 1.5.1 Can we harness new geostationary satellite measurements to track DCCs across all scales?

Automated methods for the detection and tracking of deep convective storms in geostationary satellite imagery have a vital role in both the forecasting of severe storms and research into their behaviour. Studying the interactions and feedbacks between 765 multiple DCCs, however, poses a challenge for existing algorithms due to the necessary compromise between false detection and missed detection errors. In addition, existing approaches to tracking convection tend to be optimised for tracking either individual convective cores or MCSs, and therefore cannot capture the full range of DCCs. A key challenge in tracking DCCs of different sizes is how the algorithm handles 770 the motion of different DCCs, which, in relation to their size and shape, sets a scale dependence on the capabilities of existing algorithms.

In chapter 2, we will develop a novel cloud tracking approach that takes advantage of the latest generation of geostationary weather satellite observations as well as modern computer vision techniques. We will explain the theory, implementation and 775 validation of this new algorithm, and demonstrate its ability to track DCCs across a

wide range of scales. This algorithm will then be implemented in each of the following chapters of the thesis.

### **1.5.2 How do the spatial distribution, properties and diurnal cycle of convective cores and anvils relate to each other?**

780

A major limitation of observational studies into the behaviour of DCCs is the lack of large datasets relating the properties of convective cores and anvils [Gasparini et al., 2023]. In chapter 3, we apply the tracking approach developed in chapter 2 to five years of observations from GOES-16 to study the behaviour of DCC cores and 785 anvils over North America. Using this dataset, we investigate the spatial, diurnal and seasonal distributions of both cores and anvils and their properties. We show that, using high temporal resolution data, a sufficient number of observations of developing cores can be made before they are masked by the development of the anvil cloud, allowing the behaviour of the growing core during this early stage to be linked to the 790 subsequent evolution of the DCC. In addition, we show that the coupling between the diurnal cycle of convection over land and the overpass time of sun-synchronous satellite instruments can cause large selection bias in their observations of DCCs. At certain times, this can occur to such an extent that the comparison between land and sea DCC properties is reversed when compared to their properties measured across 795 the diurnal cycle.

### **1.5.3 How do convective processes affect the structure and lifecycle of anvil clouds?**

The structure of anvil clouds show large variance across their extent and lifetime, with the thick, early cirrus near the core having a ToA cooling effect, and the thin, 800 detrained cirrus having a warming effect [Berry and Mace, 2014]. Despite this, the current decomposition of anvil-climate feedbacks considers these anvils as homogeneous

objects and ignores changes in anvil structure and optical properties [Sherwood et al., 2020], despite the increasingly apparent importance of these properties [Raghuraman et al., 2024]. Recent research into the response of anvil structure to global warming  
805 has highlighted the importance of this process for reducing uncertainty in the anvil area feedback [McKim et al., 2024] and equilibrium climate sensitivity [Sokol et al., 2024]. Previous studies have shown a connection between convective processes in anvil structure in satellite observations [Protopapadaki et al., 2017; Takahashi et al., 2017b], but lack the Lagrangian framework to investigate changes over DCC lifetime  
810 and the diurnal cycle.

Using the dataset of tracked convective cores and anvils produced in chapter 3, we investigate the impact of convective intensity and organisation on anvil structure. We find a clear contrast between these two processes on the development of the anvil clouds, not only in terms of the anvil area but also in their lifetime. Furthermore, by  
815 resolving these changes over time, we can highlight differences in their effect on the DCC lifecycle and the timing of the structural changes. These results highlight the utility of the Lagrangian approach, allowing us both to provide observational evidence of changes seen in idealised simulations, but also make direct deductions about how different processes affect anvil clouds in satellite images.

#### 820 **1.5.4 How does the diurnal cycle influence the CRE of tropical anvil clouds?**

Deep convection displays a prominent diurnal cycle, particularly over land. Due to the balance between the large magnitudes of LW and SW CRE [Hartmann, 2016], small changes in the diurnal cycle of convection have the potential to cause large  
825 radiative feedbacks [Nowicki and Merchant, 2004]. Previous studies into the interaction between the diurnal cycle and anvil CRE have been limited by a lack of Lagrangian data [Bouniol et al., 2016] and a lack of CRE retrievals throughout the diurnal cycle [Bouniol et al., 2021].

In this chapter, we apply the *tobac-flow* algorithm developed in chapter 2 to a  
830 case study over sub-Saharan Africa. Although the older SEVIRI instrument places  
limitations on our ability to detect the evolution of the developing cores and thin anvil,  
we are able to produce a new dataset of tracked DCCs which capture their diurnal  
cycle and organisation. Using cloud property retrievals and derived broadband fluxes  
produced using geostationary satellite data [Sus et al., 2018; McGarragh et al., 2018],  
835 we investigate how these properties change throughout the diurnal cycle, and their  
sensitivity to organisation. We find that the near-zero net CRE of anvils belies a  
complex bimodal distribution of anvil CRE. In particular, we find that isolated DCCs  
are both more sensitive to changes in the timing of the diurnal cycle, and have an  
outsize effect on the net CRE, highlighting the importance of convection across all  
840 scales to the climate.

Through answering these questions, we aim to address gaps in the observational  
study of DCCs. While we cannot hope to “solve” the response of DCCs to warming, by  
answering these questions we can provide novel, key insights into poorly understood  
convective processes and their importance for climate change.

845 **Chapter 2**

# A Semi-Lagrangian Method for Detecting and Tracking DCCs in Geostationary Satellite Observations

850 **2.1 Introduction**

Sequences of images from satellite instruments have been used to detect and track the motion of DCCs and tropical storms since the earliest geostationary weather satellites [Menzel, 2001]. Whereas early detection and tracking were performed by hand, numerous algorithms have been developed for the purpose of performing this task automatically, and are widely used for both forecasting and research purposes [e.g. Mecikalski et al., 2011; Senf et al., 2015; Senf and Deneke, 2017; Feng et al., 2012, 2019; Zinner et al., 2008]. There is a continual effort both to improve existing algorithms and develop new methods to support these activities. However, it is important to understand the differences in observations of DCCs from satellite imagery to those of other sources, particularly radar and lightning observations.

Visible and IR imagery from modern geostationary weather satellite instruments provide unique observations of DCCs and their surrounding environment. Figure 2.1 compares observations of DCCs throughout three different stages of their lifecycle between satellite visible and IR imagery, doppler cloud radar and lightning flash

865 observations. Composite Red, Green, Blue (RGB) images from a combination of visible and NIR channels aboard the ABI show a.: small, isolated cores during the growing phase; b.: a large area of optically thick anvil during the mature phase, and c.: a large area of optically thin anvil cloud during the dissipating phase. BT imagery from the ABI 10.4  $\mu\text{m}$  channel displays d.: cold, small, developing cores; e.: a large, 870 cold anvil cloud, and f.: warmer BTs caused by thermal radiation from the surface penetrating the optically thin dissipating anvil. Lightning flash locations observed by the Geostationary Lightning Mapper (GLM) aboard GOES-16 show g.: low frequency during the growing phase; h.: high frequency during the mature phase, and i.: no lightning activity in the dissipating phase. Column mean radar reflectivity observed 875 by Next Generation (Weather) Radar (NEXRAD) doppler cloud radar shows high radar reflectivity in the convective cores during the j. growing and k. mature phases, and no area of high radar reflectivity during the dissipating phase. The outline of the region of BTs below 270 K observed by ABI is shown by the orange dashed contour over the GLM flash locations and NEXRAD radar reflectivity to indicate 880 their observations relative to the anvil cloud.

These instruments are capable of observing the extent of the anvil clouds associated with DCCs over their entire lifecycle, even after convective activity has ceased (fig. 2.1f). This is of particular importance due to the influence of anvil cloud radiative forcing on the climate, their response to temperature change [Bony et al., 2016; 885 Hartmann, 2016; Ceppi et al., 2017; Gasparini et al., 2019] and possible feedbacks on subsequent convective activity. The newest generation of geostationary imaging satellites offers greater opportunities for the study of DCCs due to their high spatial and temporal resolution – allowing the detection and tracking of individual convective cores [Heikenfeld et al., 2019] – and also due to their high signal-to-noise ratio 890 allowing research quality observations [Iacovazzi and Wu, 2020].

The detection and tracking of DCCs from satellite imagery remains challenging

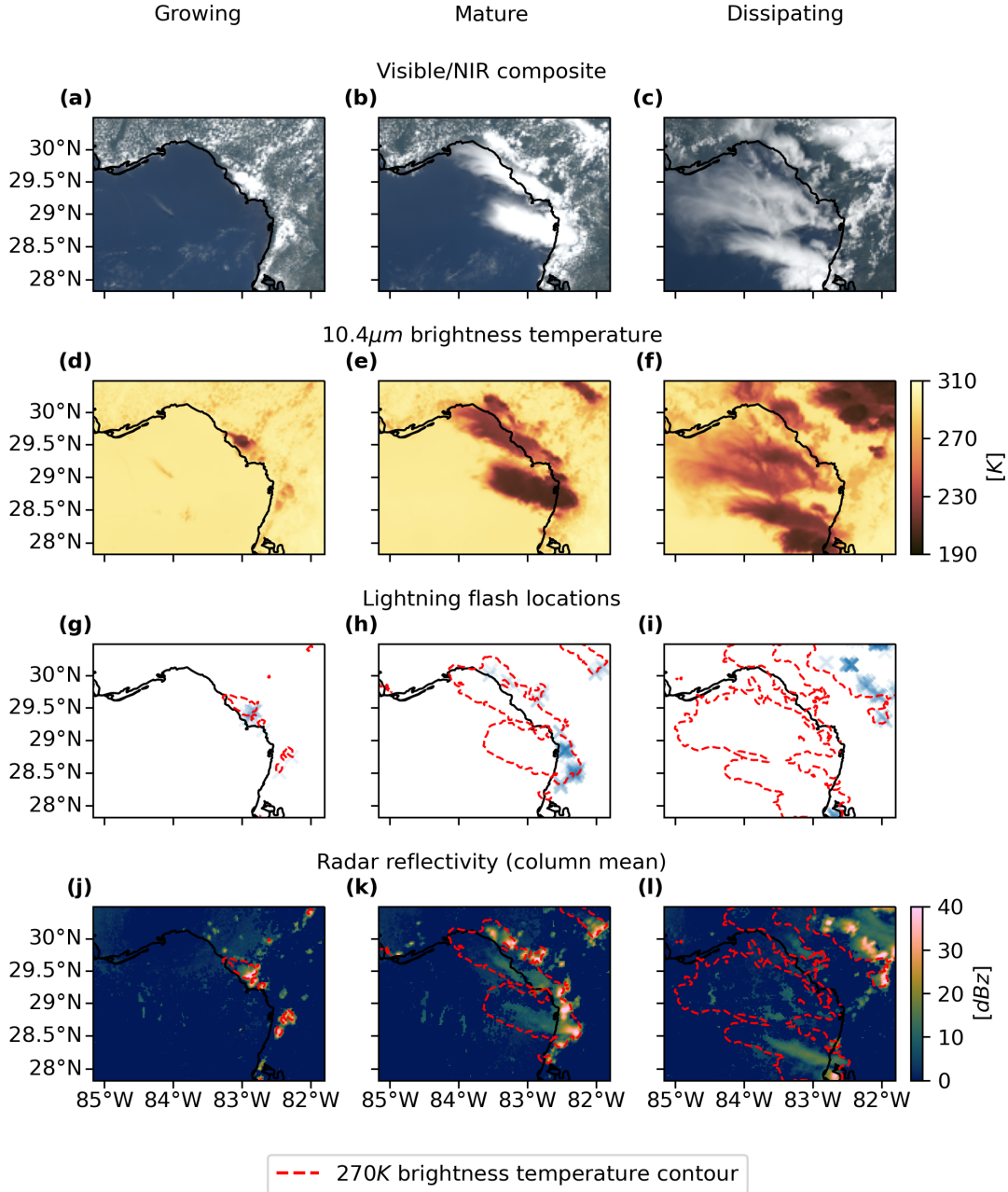


Figure 2.1: Observations of a cluster of DCCs over North-West Florida throughout three stages of their lifecycle. This cluster of DCCs occurred on the afternoon of 19<sup>th</sup> June 2018. The "growing" column was observed at 17:00 UTC, the "mature" column at 19:00 UTC, and the dissipating column at 21:00 UTC. The four rows show observations of ABI visible/NIR composites (a,b,c), and 10.4  $\mu\text{m}$  BT (d,e,f); lightning flash locations observed by GLM (g,h,i), and column mean radar reflectivity observed by NEXRAD (j,k,l). Note that, unless otherwise specified, this case study is used for all subsequent figures in this chapter.

due to the inability to directly observe the convection that drives DCCs using passive visible and IR observations. This is unlike radar and lightning observations, which can directly observe deep convection due to the strong correlations between core updraft intensity and radar reflectivity and polarisation [Austin, 1987; Rosenfeld et al., 1993; Zipser and Lutz, 1994], and lightning flash occurrence [Williams et al., 1989; Deierling and Petersen, 2008; Wang et al., 2017]. Instead, a proxy for convective activity must be used to detect deep convection in visible/IR satellite imagery. The approaches used for this can generally be separated into two separate methods. Firstly, the use of thresholds on BT (BT) or other observed fields, which are capable of detecting DCC anvil clouds [e.g. Schmetz et al., 1997; Hong et al., 2005; Schröder et al., 2009; Liang et al., 2017; Senf et al., 2018a]. Secondly, the detection of rapidly growing cloud tops by observing changes in the anvil cloud-top radiative cooling, or by other similar approximations of cloud growth [Zinner et al., 2008; Bedka et al., 2010; Müller et al., 2019].

Developing a detection method using either approach is made challenging by the dynamic nature of DCCs themselves. DCC cores typically have diameters of around 10 km, and updraft velocities on the order of  $10 \text{ ms}^{-1}$  [Weisman, 2015], and exist for 1-3 hours [Chen and Houze, 1997]. Large, mesoscale convective systems (consisting of multiple cores joined by a single large anvil [Roca et al., 2017]) may span areas several orders of magnitude larger than isolated DCCs [Houze, 2004], and typically exist to 10-20 hours or longer [Chen and Houze, 1997]. The life cycle of a DCC can be split into three phases: an initiation or growing phase, a mature phase and a dissipating phase after the cessation of convective activity [Wall et al., 2018]. There exists a significant difference between the diurnal cycles of deep convection over the land and over the ocean, with observed DCCs over land clustered towards the end of the day [Taylor et al., 2017].

The difficulties of detecting DCCs using various proxy approaches are demon-

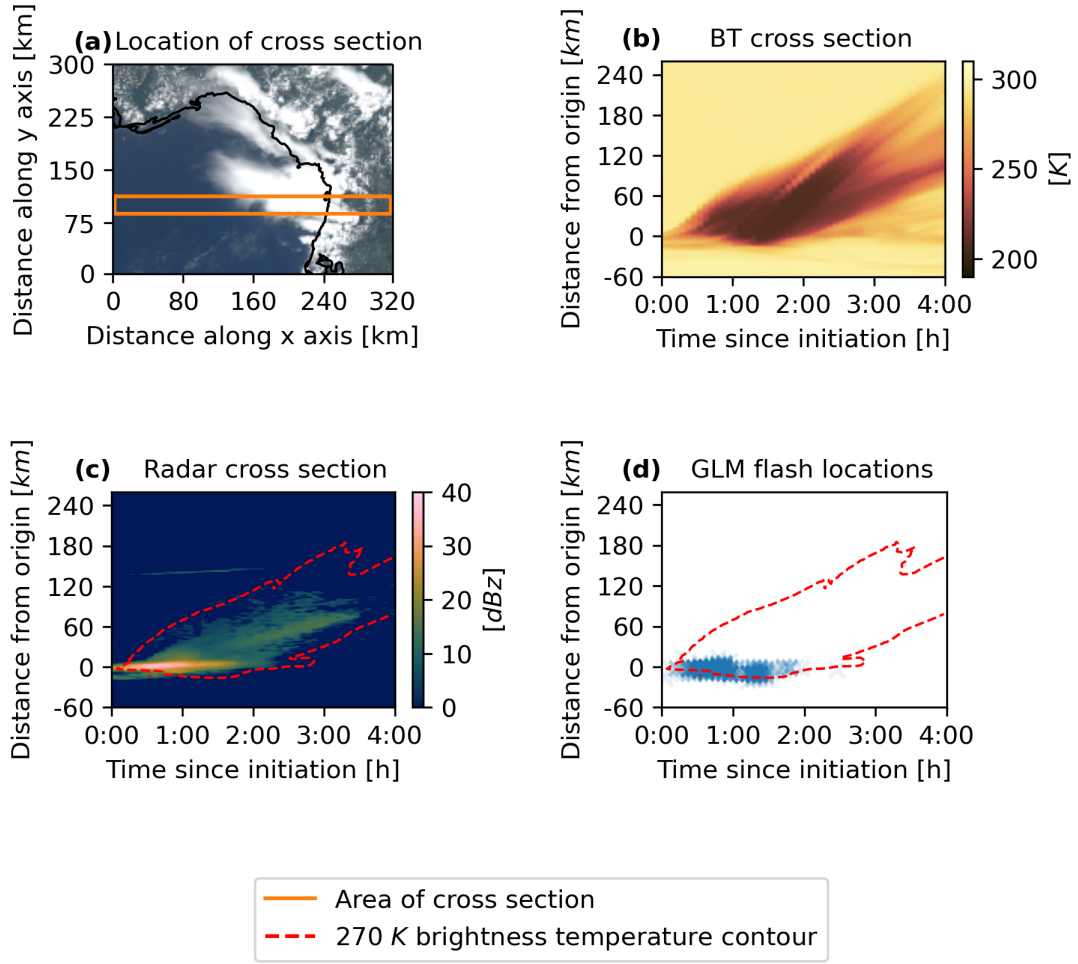


Figure 2.2: Cross sections of the DCC observed in figure 2.1 as they develop over time. a.: The location of the cross-section within the observed DCC. The mean of values is taken in the North-South axis. b.: ABI  $10.8\text{ }\mu\text{m}$  BT, showing rapid cooling for the first 30 minutes, followed by an expanding region of anvil cloud that begins to thin and warm after 2-3 hours. c.: Column mean radar reflectivity, showing the presence and location of the convective core. d.: Lightning flash locations observed by GLM, which closely match the core observed by NEXRAD. Initiation occurred at  $82.0^{\circ}\text{W}$   $28.5^{\circ}\text{N}$  at a time of 17:00 UTC.

strated by the cross-sections of an observed DCC over time in fig. 2.2. The observed  
920 BT of the DCC anvil cloud shows wide variation over time, with the anvil cloud thinning due to dissipation after the end of convective activity which results in a warmer BT due to greater signal from the surface. This variety of observed temperatures leads to large differences in the chosen threshold value between different algorithms [see discussion in Bennartz and Schroeder, 2012]. This choice of the threshold value  
925 is further complicated due to the overlap in observed BTs between DCC anvils and non-convective clouds [Konduru et al., 2013]. As a result, any detection method using a BT threshold must compromise between missed detection of DCCs, or false detections of non-DCC clouds.

The cooling of the cloud top is only visible for a short period during the initial  
930 phase of the DCC, before the anvil cloud top reaches the tropopause temperature after approximately 30 minutes. As a result, any method that solely relies on detecting the growth of the DCC will be unable to detect the anvil cloud after this initial growth phase has ended. While such algorithms provide accurate detection of these early phases of DCC growth [Zinner et al., 2013], they are unable to continue tracking the  
935 anvil cloud after convective activity is no longer observed.

Fiolleau and Roca [2013] identified this need to compromise on the accuracy of detecting DCCs as a problem caused by the commonly used two-step framework for detecting and tracking DCCs. In this framework, DCCs are first detected in individual images, and then linked together over time in sequences of images. As a result,  
940 the detection method chosen must be capable of detecting DCCs at each individual time step in order to track their entire lifecycle. Instead Fiolleau and Roca [2013] implemented a single-step framework for mesoscale convective systems that treats a sequence of images as a "3D" volume, and performs detection and tracking simultaneously by applying a watershed method over both spatial and temporal dimensions.  
945 Whereas this approach was successful for large, mesoscale systems, where the ad-

vection of the anvil is small compared to the overall anvil area, it is less capable of tracking small, rapidly moving convective cores. To improve the tracking of small DCCs, we have developed a semi-Lagrangian framework for single-step detection and tracking which accounts for the motion of DCCs using optical flow.

950 By utilising the semi-Lagrangian framework, we are able to combine the best elements of both growth-based and threshold-based detection methods. We show that it is possible to detect growing DCCs to a high degree of accuracy using methods similar to those of Zinner et al. [2008], and then extend the detected DCC over the entire anvil cloud using the "3D" watershed method of Fiolleau and Roca [2013].  
955 This framework reduces the compromise required between the rate of missed DCCs and falsely detected DCCs, improving the overall accuracy of our detection method compared to existing approaches. Furthermore, this method allows the anvil cloud to be detected and tracked even after the region of cloud top cooling is no longer detected. Finally, the "3D" method handles the merging and splitting of intersecting  
960 DCCs by detecting all DCCs that intersect at any point during their lifetime as a merged object.

## 2.2 Data

Three sources of data are used throughout this chapter. Primarily, visible and IR imagery from ABI aboard the GOES-16 weather satellite is used for the detection  
965 of DCCs. Secondarily, observations from the NEXRAD weather radar network and the GLM (also aboard GOES-16) are used to assess and validate the tracking and detection method presented here.

### 2.2.1 Advanced Baseline Imager

The ABI is a visible and IR radiometer aboard the GOES-16 series of weather satellites [Schmit et al., 2016]. GOES-16, also known as GOES-East, is situated in a

geostationary orbit at 75.2 °W above the equator, providing a field of view (or ‘Earth-disc’) covering most of the western hemisphere, including all of South America and most of North America. ABI has 16 channels operating in a range of spectral bands in the visible, NIR and thermal-IR. The majority of these channels have a resolution  
975 of 2 km at the sub-satellite point, although this reduces to approximately 3 km across most of the Continental United States (CONUS) due to the satellite viewing angle. ABI operates in a flexible scan mode, imaging the continental US (CONUS) once every 5 minutes, the full disc every 10 minutes (15 minutes prior to April 2019), and two mesoscale regions of approximately 2500 by 2500 km every minute. Additionally, it is  
980 capable of scanning the full disc every five minutes if no other scans are performed. This combination of high spatial and temporal resolution makes ABI suitable for detecting and tracking small and developing DCCs, as well as providing the spatial coverage to also track large mesoscale convective systems [Heikenfeld et al., 2019].

Compared to older geostationary instruments, ABI has higher spatial and tempo-  
985 ral resolution, more channels in both the LW IR window spectrum and the LW IR Water Vapour (WV) spectrum, and low noise (table 2.1) [Iacovazzi and Wu, 2020]. This, combined with many of the channels being derived from those aboard the Visible Infrared Imaging Radiometer Suite, make the data from ABI more suitable for research purposes than that from older instruments [Heidinger et al., 2020]. A number  
990 of artifacts are known to occur in ABI imagery [Gunshor et al., 2020]. Although the majority of these artifacts are removed using the data quality flag associated with the ABI data, we have found a number of cases in which bad detector stripes (described in section 3.2 of Gunshor et al., 2020) are not flagged in the data, and so detection and tracking of DCCs has not been performed during the time periods these artifacts  
995 occurred.

In this chapter, we have used the ABI level 2 Multi-channel Cloud and Moisture Imagery Product (MCMIP) which provides calibrated reflectances and BTs for all

Instrument	ABI	SEVIRI	Imager
Temporal resolution (minutes)	5	15	30
Nadir spatial resolution (km)	2	3	4 (8 for WV)
Number of IR LW window channels	3	2	2
Number of IR WV channels	3	2	1
Noise equivalent temperature (K @ 300 K)	0.1	0.25	0.09

Table 2.1: Comparison of data from ABI to that from older geostationary instruments SEVIRI aboard the second generation meteosat satellites, and the imager aboard the second generation GOES.

ABI channels on a common grid [Schmit and Gunshor, 2020], using the 5-minute frequency imagery provided over the CONUS region. The case study shown in the 1000 figures throughout this paper is for a subset of the CONUS scan region centred at 83.7 °W, 29.2 °N, over the time period of 17:00:00 to 21:00:00 UTC on the 19th June 2018. Validation was performed on the CONUS scan region over the entirety of 2018. All data has been sourced through the NOAA Big Data Program.

### 2.2.1.1 Selection of ABI Channels and Channel Combinations

1005 In order to have an equal performance during both day and nighttime, a selection of LW IR ABI channels are used for the detection and tracking of DCCs (see fig. 2.3). These channels consist of the 10.4  $\mu\text{m}$  and 12.4  $\mu\text{m}$  LW (also known as the clean and dirty window channels respectively due to the presence of WV in the latter), and the upper and lower troposphere WV channels at 6.2  $\mu\text{m}$  and 7.3  $\mu\text{m}$  respectively. 1010 Whereas the LW window IR BT is commonly used for the detection of anvil clouds using threshold-based methods, we have decided not to use it for this purpose in this method due to the wide range of BTs observed within anvil clouds, and the variance of anvil cloud temperature because of changes in tropopause temperature due to meteorology and latitude. However, the information contained within this field 1015 is used for the optical flow calculation of the cloud motion field.

Two additional combinations of channels are used to detect areas of DCC anvil.

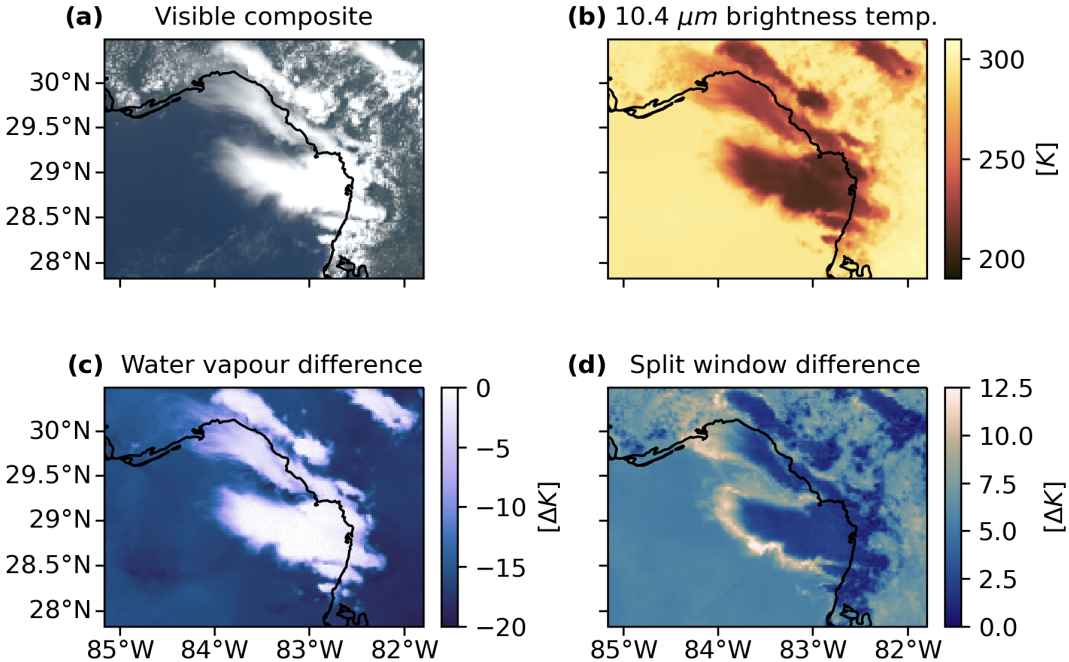


Figure 2.3: ABI channels and channel differences used with the detection and tracking algorithm. a.: A composite of visible and NIR channels. b.: The  $10.4\text{ }\mu\text{m}$  BT, or clean LW window channel, which can differentiate clouds at all altitudes by their BT. c.: the WVD combination, of the  $6.2\text{ }\mu\text{m}$  upper troposphere WV channel minus the  $7.3\text{ }\mu\text{m}$  lower troposphere WV channel, which is strongly negative for clear sky and low cloud, but approaches positive values for thick, high clouds. d.: the SWD combination of the  $10.4\text{ }\mu\text{m}$  clean LW window channel minus the  $12.4\text{ }\mu\text{m}$  dirty LW window channel, which is near zero for thick clouds, around K for clear skies and approximately 10 K for thin, ice clouds.

The Water Vapour Difference (WVD) combination (fig. 2.3 c) of the upper troposphere WV channel minus the lower troposphere WV channel has been shown to provide a high detection rate for DCCs [Müller et al., 2018, 2019]. In clear sky or  
 1020 low cloud conditions, WVD shows the temperature difference between the upper and lower troposphere of generally around -20 K. However, in the presence of high, thick clouds the  $6.2\text{ }\mu\text{m}$  has an additional contribution from stratospheric WV resulting in a warmer, and in extreme cases positive WVD value [Schmetz et al., 1997]. Because both the WV channels are strongly absorbed by WV in the lower troposphere, the  
 1025 WVD field is not affected by surface and low altitude features and so provides a

clear distinction between thick, high clouds and the background across a wide range of situations. Müller et al. [2019] found that a threshold of -5 K gave a high detection rate of anvil clouds. Furthermore, as the WVD values are relative to the lower stratosphere temperatures, this field is much less affected by location and meteorology  
1030 than the LW IR channels. However, the WVD is still prone to the false detections of non-convective clouds when using a thresholding method as it cannot directly distinguish between thick, high-altitude clouds that are associated with deep convection and those that are not.

The Split Window Difference (SWD), consisting of the clean IR window channel  
1035 minus the dirty IR window channel (fig. 2.3 d), aids in the detection and separation of optically thin anvil cloud (including cirrus outflow) from optically thick anvil due to the difference in ice particle emissivity between these two channels [Heidinger and Pavolonis, 2009]. As a result, this combination displays warm temperatures of around 10 K for thin, ice clouds, near 0 K for thick clouds, and approximately 5 K for clear  
1040 skies due to the contribution of boundary layer WV. The SWD is, however, also sensitive to low-level clouds and low-level WV concentrations, and so cannot be used alone to detect DCCs. It remains important to consider the SWD field due to the difficulty in separating anvil clouds from cirrus when using LW IR BT alone [Hong et al., 2005]. By subtracting the value of the SWD from the WVD, we can reduce the  
1045 sensitivity of our detection scheme to thin cirrus clouds, reducing the rate of erroneous detections. Additionally, adding the SWD field to the WVD field can enhance the appearance of cirrus, enabling the detection of thin ice clouds associated with cirrus outflow and dissipating anvils.

Figure 2.4 shows the clear sky vertical weighing functions for the 6.2, 7.3, 10.4  
1050 and 12.4  $\mu\text{m}$  ABI channels. The weighting functions are calculated using a radiative transfer model with temperature and humidity profiles observed by rawinsonde observations on 12:00:00 UTC 2020/08/10 at the Tampa RAOB station (KTBW -

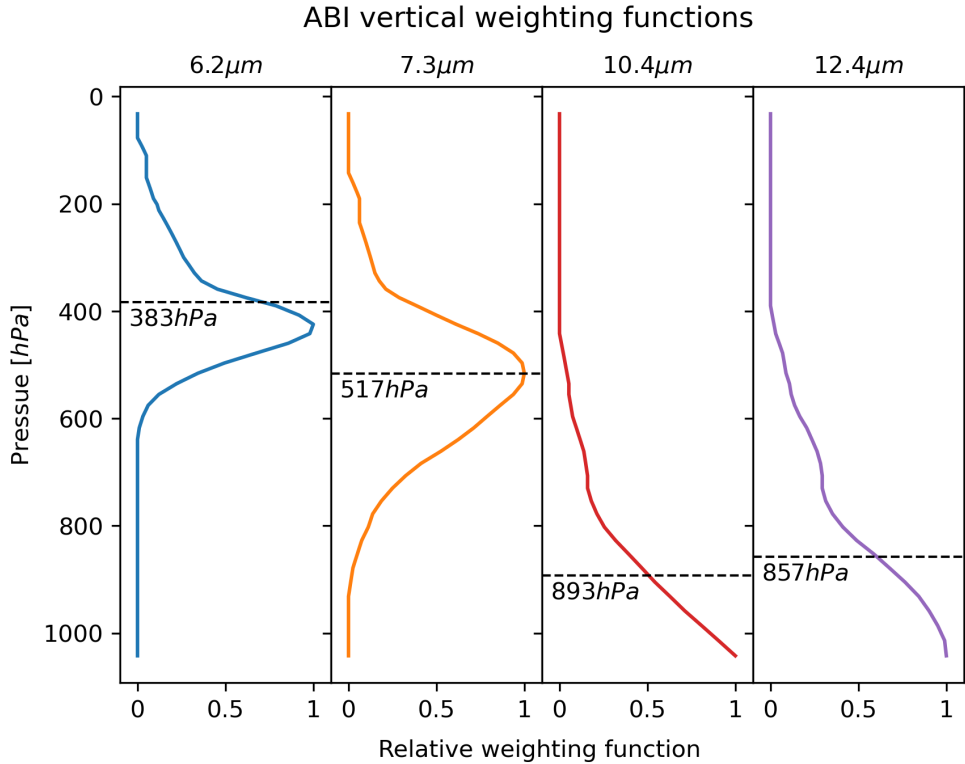


Figure 2.4: Clear sky vertical weighting functions for the 6.2, 7.3, 10.4 and  $12.4\mu\text{m}$  ABI channels calculated from rawinsonde profiles measured on 12:00:00 UTC 2020/08/10 at the Tampa RAOB station (KTBW - 72210). The dashed lines and associated pressure values show the weighted average emission height for each channel. Data from [https://cimss.ssec.wisc.edu/goes-wf/plot-viewer/#/plot-viewer/plot/raob/abi16/default/20200810\\_1200Z/72210](https://cimss.ssec.wisc.edu/goes-wf/plot-viewer/#/plot-viewer/plot/raob/abi16/default/20200810_1200Z/72210)

72210).

### 2.2.2 Geostationary Lightning Mapper

1055 The GLM is also mounted on GOES-16 and detects lightning flashes using an optical transient detector. The optical transient detector utilises a single, narrow-band NIR channel centred on 777 nm [Orville and Henderson, 1984] to detect momentary changes in brightness associated with lightning events at a frequency of 400  $\mu\text{s}$  [Christian et al., 2003], providing a 70 % minimum efficiency of detection [Goodman et al.,  
1060 2013]. GLM has the same field of view as the ABI instrument, albeit with a lower

spatial resolution of 8 km at the sub-satellite point.

As lightning observations are strongly correlated with DCCs, data from GLM is used to validate the detection of DCCs using ABI. The level 2 GLM Lightning Cluster-Filter Algorithm product provides a dataset of events, groups and flashes processed from the GLM data [Peterson, 2019], and filters artifacts from the level 1 GLM data [Peterson, 2020]. From this dataset, we extract detected flashes as evidence of DCC occurrence. These locations are then processed by mapping their frequency onto the ABI grid for validation of the algorithm.

### 2.2.3 Next Generation Radar

NEXRAD, also known by its technical name Weather Surveillance Radar, 1988, Doppler (WSR-88D), is a network of weather radars operated by the National Weather Service across the USA [Crum and Alberty, 1993]. WSR-88D operates in the S-band spectrum, between 2700 and 3000 MHz. NEXRAD stations scan at a range of elevations, typically between 0.5° and 19.5° above horizontal, with a typical scan cycle taking between 4 ½ and 6 minutes, comparable to the temporal sampling of ABI over the CONUS region.

Cloud radar reflectivity is proportional to the droplet number density and the droplet radius to the sixth power, making it particularly sensitive to convective rainfall [Yau and Rogers, 1989]. As a result, cloud radar observations are ideal for showing the locations of convective cores [Austin, 1987; Rosenfeld et al., 1993; Zipser and Lutz, 1994], and in this chapter it is used to qualitatively assess our ability to detect developing convective cores using ABI. Level 2 NEXRAD radar reflectivity observations from multiple sites are gridded to the same resolution as ABI, and column mean reflectivity is calculated between the altitudes of 2.5 and 15 km.

Option	Value	Description
rte_solver	disort	DISORT solver
source	thermal	thermal IR spectra
wavelength	3000–15000	3–15 $\mu\text{m}$
output_user	lambda edir eup uu	wavelength, direct, diffuse irradiance and all radiances
zout	0 TOA	surface and ToA
albedo	0.5	surface albedo
umu	-1.0, 1.0	downward & upward
sza	0	solar zenith angle
mol_abs_param	reptran fine	REPTRAN parameterisation
atmosphere_file	afgl.dat	tropical atmosphere profile

Table 2.2: Selected options for the libRadTran simulations.

## 1085 2.3 Theory

To better understand how DCCs appear in GOES ABI observations, a series of experiments were performed using a radiative transfer model. These experiments were performed using libRadTran v2.0.4 [Emde et al., 2016], utilising the DISORT radiative transfer solver [Buras et al., 2011] and the REPTRAN absorbtion parameterisation [Gasteiger et al., 2014]. A tropical atmospheric profile was used to represent the atmospheric conditions under which deep convection typically occurs. A complete list of the options used to set up the radiative transfer model across all simulations is provided in table 2.2.

In each of the simulations, a cloud layer is included in addition to these options to represent a DCC in different phases of the lifecycle. For liquid cloud droplets we use the Hu parameterisation [Hu and Stammes, 1993], and for ice particles we use the Fu scheme [Fu, 1996; Fu et al., 1998]. To show how the simulated clouds are observed by GOES-16, we calculate BT from the simulated radiances, and then integrate over the spectral response function of each of the ABI channels.

<sub>1100</sub> **2.3.1 Observing growing convective cores**

The first experiment aims to represent how a vertically developing DCC core would appear in ABI observations. To do so, we run a series of simulations with increasing cloud top heights between 1 and 15 km at 1 km intervals. These cloud layers are given a base height of 0 km, Liquid Water Content (LWC) of  $1,000 \text{ gm}^{-2}$ , and droplet Effective Radius ( $r_e$ ) of  $15 \mu\text{m}$ . These values were chosen to represent typical conditions seen in a convective core. Although we use liquid droplets at all altitudes, simulations with ice cloud droplets showed negligible differences for cloud layers of this thickness.

Figure 2.5 shows BT spectra for increasing cloud height, with the spectral response functions of the ten thermal IR ABI channels plotted in the background. With such a large LWC, the BT matches the CTT apart from the absorption regions of CO<sub>2</sub> (4.2–4.5  $\mu\text{m}$  and 13.2  $\mu\text{m}$ ) and ozone (9.4–10.2  $\mu\text{m}$ ), and the WV absorption for low-level clouds (5–8  $\mu\text{m}$ ).

The change in observed BT with height for the 6.2, 7.3, 10.4, and 12.4  $\mu\text{m}$  BT channels along with the WVD and SWD is plotted in Fig. 2.6. Above 3 km, the 10.4 and 12.4  $\mu\text{m}$  channels show a constant decrease observed BT at the moist pseudo-adiabatic lapse rate of 6 K. Due to the contribution of WV to the 6.2 and 7.3  $\mu\text{m}$  channels at lower Cloud Top Height (CTH), the WVD shows the most response to vertical development between 6 and 10 km. The SWD shows a response to clouds developing at a low altitude. It has been proposed that this can be used to detect the onset of convection in clear sky conditions before other observations, such as cloud radars [Lindsey et al., 2014, 2018].

Figure 2.7 shows the change in BT observed over a vertically developing core in units of  $\text{K}\text{min}^{-1}/\text{ms}^{-1}$  (i.e. the BT change per minute, per  $\text{ms}^{-1}$  of vertical CTH growth rate). Although this is an odd choice of unit, it is used to better compare the observed change in BT by a geostationary satellite (measured in K, with a typical sampling time on the order of minutes), to the vertical velocity of the cloud

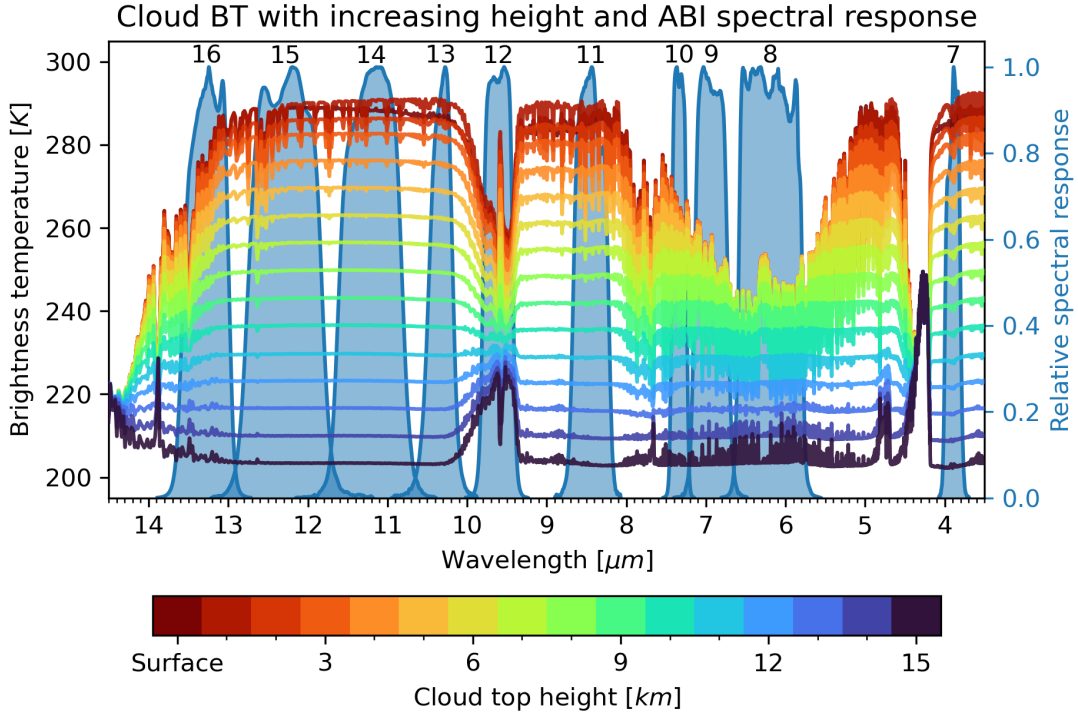


Figure 2.5: ToA BT spectra for a simulated cloud representing a DCC core at heights between 1 and 15 km, indicating that the largest difference in BT are seen in the LW window regions. The filled blue areas in the background show the relative spectral response functions for each of the LW ABI channels.

top (typically measured in  $\text{ms}^{-1}$ ). Above 3 km, the  $10.4 \mu\text{m}$  BT shows a consistent cooling rate of  $0.4 \text{ K minute}^{-1}$ . Roberts and Rutledge [2003] found a threshold for severe convection of 8 K cooling over 15 minutes, or approximately  $0.5 \text{ K minute}^{-1}$ , which would represent a cloud top vertical velocity of  $1.25 \text{ ms}^{-1}$  according to our simulation. The WVD shows a maximum rate of change between 7 and 8 km, with a warming rate of half the magnitude of the BT cooling rate.

Overall, we see from this experiment that the  $10.4 \mu\text{m}$  BT channel from ABI can be used to clearly identify a vertically developing core across a wide range of altitudes. On the other hand, the WVD is only sensitive to vertically developing clouds in a narrower range of altitudes, and shows a weaker rate of BT change. However, this sensitivity to vertical development at a mid to high altitude may be

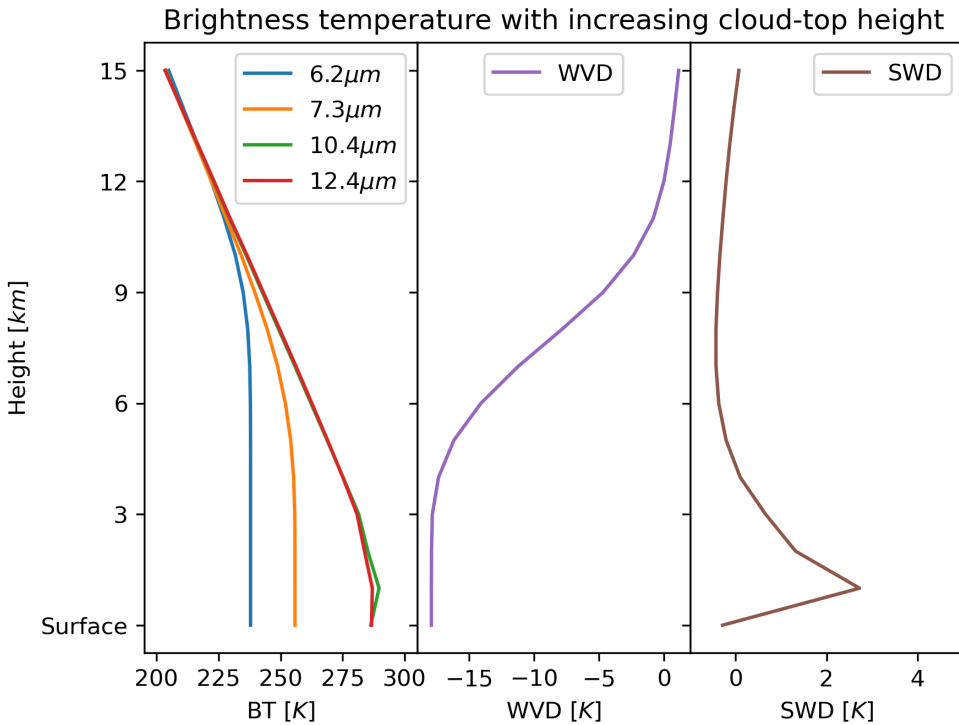


Figure 2.6: Simulated observations of the 6.2, 7.3, 10.4 and 12.4  $\mu\text{m}$  ABI channels, WVD and SWD for a DCC core of increasing height.

helpful in distinguishing between DCCs and other, vertically developed clouds at lower altitudes, such as cumulus congestus.

### <sup>1140</sup> 2.3.2 Observing anvil clouds

In the second experiment, we investigate how anvil clouds of different Optical Depth (OD) appear in ABI observations. The simulations were run with an ice cloud with CTH at 14 km, cloud base height at 12 km and cloud top  $r_e$  of 20  $\mu\text{m}$ , aiming to represent the typical properties of a dissipating anvil cloud [Sokol and Hartmann, <sup>1145</sup> 2020]. This simulation was then run for a range of OD between 0.125 and 10, with intervals of 0.125 between 0.125 and 1, 0.25 between 1 and 2, 0.5 between 2 and 5, and 1 between 5 and 10.

BT spectra for these simulations are shown in Fig. 2.8, along with the ABI spectral

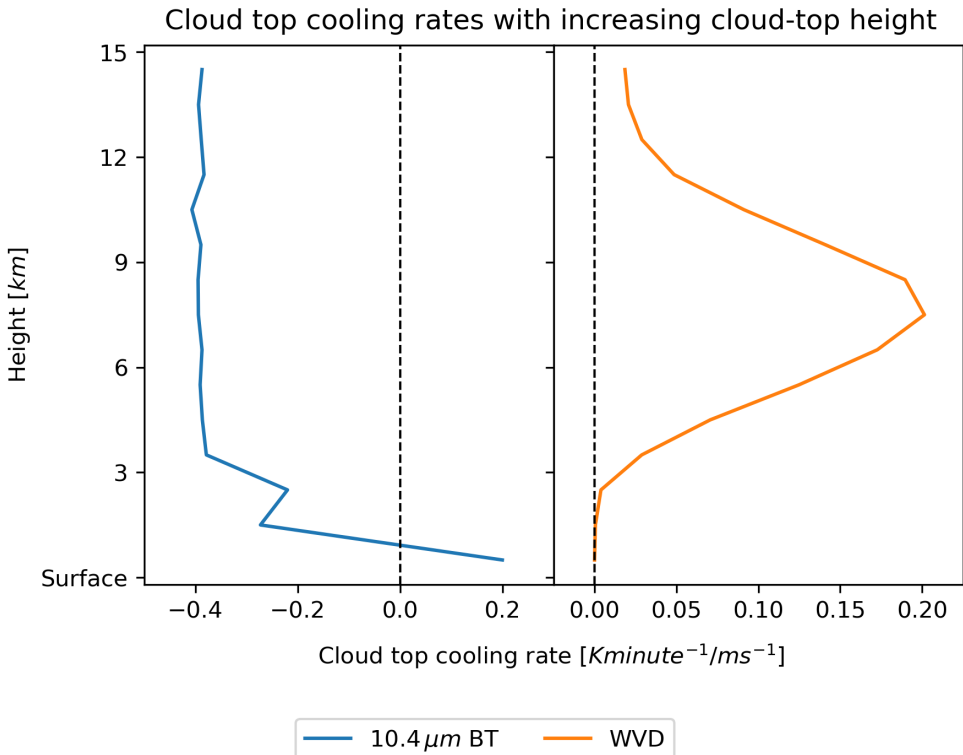


Figure 2.7: Simulated observed cooling rates of the  $10.4\text{ }\mu\text{m}$  ABI channels and the WVD combination for a convective core growing at a rate of  $1\text{ ms}^{-1}$ .

response functions as in Fig. 2.5. As before, we see absorption due to  $\text{CO}_2$ , ozone, and  
 1150 WV. Unlike the simulations in section 2.3.1 however, we see a difference in the BT spectra across the LW window ( $10\text{--}13\text{ }\mu\text{m}$ ) for clouds with OD between 0 and 2, with colder BT at longer wavelengths. This is due to the difference in ice emissivity across this range of wavelengths [Fu, 2015]. As the emissivity of ice particles reduces for wavelengths at  $10\text{ }\mu\text{m}$  and below there is a greater contribution from the atmosphere  
 1155 below the cloud layer and, as a result, warmer BTs are observed. It should be noted that this difference is dependent on the size of the ice particles, with smaller  $r_e$  resulting in a larger difference in emissivity [Dubuisson et al., 2008].

Figure 2.9 shows simulated ABI observations for the  $6.2$ ,  $7.3$ ,  $10.4$ , and  $12.4\text{ }\mu\text{m}$  BT channels, the WVD and the SWD for a range of OD between 0.1 and 10. At  
 1160 high OD, all channels show a cold BT close to that of the CTT, however, for OD

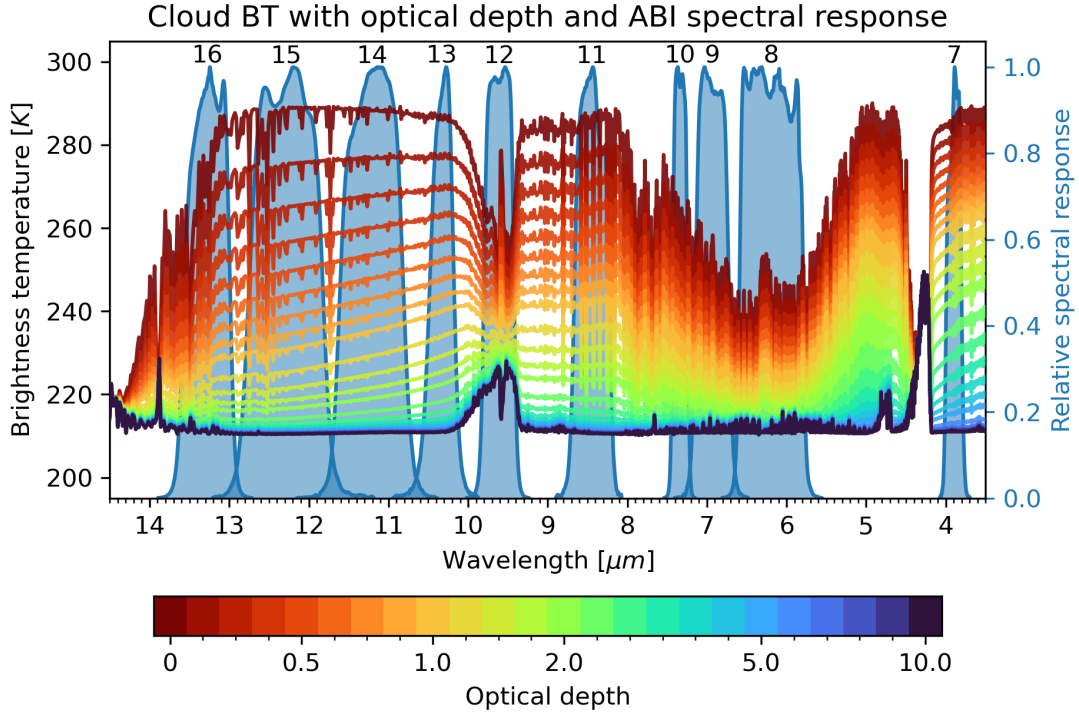


Figure 2.8: ToA BT spectra for a simulated anvil cloud with optical thickness between 0 and 10.

below 3, the increased contribution from the atmosphere below results in warmer BT. The WVD similarly shows a more negative BT difference at OD below 3, with a continual decrease for smaller OD. The SWD however shows an increasingly positive BT difference for OD below 5, peaking at 10 K around 1 OD. However, below this OD

1165 the SWD decreases towards smaller positive values. As a result, the SWD has the potential to detect thin anvil cirrus at much lower OD than BT channels or WVD, down to values around 0.25 Optical Depth (OD).

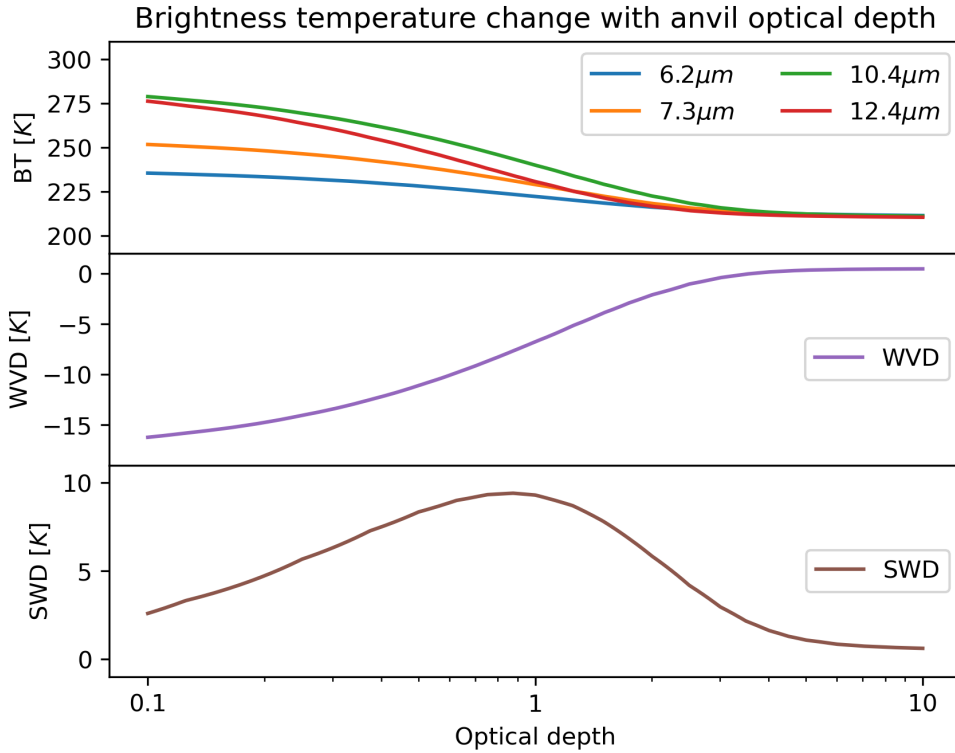


Figure 2.9: Simulated ABI BT observations for a DCC anvil of decreasing optical depth for the 6.2, 7.3, 10.4, and 12.4  $\mu\text{m}$  BT channels, the WVD and the SWD.

## 2.4 Method

We present here a novel method for detecting and tracking both the growing cores

1170 and anvils clouds of DCCs, consisting of the following steps:

1. Ingest of LW IR BT fields from geostationary satellite imagery, including calculation of WVD and SWD fields from IR WV and LW IR window channels.
2. Calculation of optical flow vectors to be used as an *a priori* estimate of cloud motion for use in the semi-lagrangian framework.
- 1175 3. Detection of growing DCC cores using cloud top cooling rate.
4. Detection of thick and thin anvil clouds associated with detected cores using a semi-lagrangian "3D" watershedding method.

5. Grouping of cores into multi-core systems, calculation of statistics and validation using lightning observations.

#### **1180 2.4.1 Estimation of cloud motion vectors using optical flow**

The retrieval of AMVs has been performed since the earliest geostationary satellite observations [Menzel, 2001]. AMVs provide information about the motion of clouds in the atmosphere, including DCCs [Bedka and Mecikalski, 2005], and are routinely generated for the majority of operational geostationary earth observation satellites, 1185 including GOES-16 [Daniels et al., 2016]. However, although AMVs may provide useful information about the motion of DCCs, the non-geostrophic nature of wind fields in these conditions may result in the AMVs being calculated inaccurately or rejected by quality control checks [Bedka and Mecikalski, 2005].

Optical flow algorithms are a family of algorithms used to estimate the apparent 1190 motion of objects observed in a series of images [Aggarwal and Nandhakumar, 1988]. A wide range of optical flow algorithms exist, and these have been successfully applied to many computer vision applications. It should be noted that optical flow does not necessarily represent the physical motion of an object, but is instead an estimation of the relative motion between an object and the observer and additionally any change 1195 in the apparent object (including growing, shrinking or other warping of the object).

Optical flow algorithms have been previously shown to be accurate for the prediction of AMVs using geostationary satellite images [Wu et al., 2016], as long as the observations are sufficiently frequent such that the motion of unique features between images is less than the length scale at which neighbouring features can be resolved 1200 [Bresky and Daniels, 2006]. Heikenfeld et al. [2019] found that at imaging frequencies of less than 5 minutes the motion of DCC cores was less than the spacing between neighbouring cores in the majority of cases, indicating that the frequency of the ABI CONUS scan region is suitable for calculating optical flow vectors of DCCs. The use

of optical flow has several advantages over traditional AMVs for the retrieval of DCC motion vectors: optical flow can be calculated quickly using only two subsequent images and no *a priori* information, aiding in near real-time applications; and also have no requirement for geostrophic balance. Optical flow algorithms are routinely used in the nowcasting of convective precipitation, and can be used to provide accurate predictions of DCC with an hour of lead time using either radar or satellite observations [e.g. Bowler et al., 2004; Bechini and Chandrasekar, 2017; Woo and Wong, 2017]. Optical flow, and similar motion vector techniques, have also been successfully applied to both the detection of developing deep convection [Zinner et al., 2008; Zhang et al., 2014] and tracking detected deep convective features [Senf et al., 2018a] separately.

It should be noted that we are using optical flow to estimate the apparent motion of the cloud field between subsequent images, with the aim of using these vectors to map the locations of DCCs from one step to the next, instead of calculating actual AMVs corresponding to winds. This approach avoids a number of challenges with the use of optical flow for calculating AMVs including the estimation of the height of estimated flow vectors and the detection of diverging or converging motion vector fields in situations of growing and dissipating clouds respectively. In the latter case, we in fact aim to include the divergence and convergence within the optical flow vector field to map both the location and shape of observed clouds between time steps.

#### 2.4.1.1 Evaluation of Optical Flow Methods

As different optical flow algorithms may provide better accuracy in different situations [Baker et al., 2011], we compare a number of different algorithms to assess their suitability for tracking the motions of DCCs. We consider six different optical flow algorithms implemented in the OpenCV library [Bradski, 2000], which are listed below:

- Farnebäck [Farnebäck, 2003]

- Deep Inverse Search (DIS) [Kroeger et al., 2016]
- DeepFlow [Weinzaepfel et al., 2013]
- Dual Total Variation Regularisation & Robust L<sup>1</sup> Norm (Dual TV-L<sup>1</sup>) [Zach et al., 2007; Pérez et al., 2013]
- Sparse to Dense [Bouguet, 1999]
- Principle Component Analysis (PCA)-Flow [Wulff and Black, 2015]

The first four of these algorithms are dense optical flow methods, which calculate motion vectors for every pixel in the image. The final two calculate sparse optical flow—motion vectors between detected objects in each image, rather than individual pixels—and then map these to all pixels based on a region segmentation approach.

The sparse to dense and PCA-flow algorithms use the Lucas-Kanade method [Lucas and Kanade, 1981] and the PCA method respectively to calculate the sparse motion vectors.

Each algorithm was applied to a sequence of images from the 10.4  $\mu\text{m}$  channel, with the algorithms estimating motion vectors between each consecutive pair of images.

As the methods require 8-bit images, a linear normalisation was applied to the BT images between each pair's minimum and maximum values. To improve the accuracy of the detected motion vectors, a variational refinement process [Brox et al., 2004] is applied to the calculated flow vectors. This process minimises the energy functional of the pixel value, pixel gradient, and local smoothness to reduce the angular error of the detected flow vectors. Finally, vectors are calculated both forwards and backward in time between each pair of images, and these two sets of vectors are interpolated to each others locations and averaged to ensure that they are equal and opposite.

Figure 2.10 shows the ABI BT at 19:00:00 UTC (fig. 2.10 a), along with the optical flow vectors calculated by each of the algorithms with the subsequent time step. For

1255 each set of optical flow vectors, the average vector over each  $5 \times 5$ -pixel area is plotted by the red arrows, and the vector velocity magnitude is plotted in the background. The two sparse methods (fig. 2.10 f,g) show a closer match of the areas where optical flow vectors to the edge of the anvil cloud than the dense methods (fig. 2.10 b–e), which have a tendency to smooth the detected vectors over a large area. Of all the  
1260 methods, the Farnebäck algorithm tends to produce larger magnitudes, but correctly detects zero flow in areas without clouds, unlike most of the algorithms.

Figure 2.11 shows the difference in BT between subsequent observations when taking into account the cloud motion predicted by the different optical flow algorithms. The plots are again shown for the time step at 19:00:00 UTC, with the  $10.4 \mu\text{m}$  BT  
1265 at this time step shown again for reference in fig. 2.11 a. Figure 2.11 b shows the Eulerian difference in BT; the difference in the BT observed at the same pixel locations on subsequent time steps. We see large cooling rates of the left (downwind) side of the anvil cloud, not because the CTT is cooling, but because of the expansion of the anvil cloud into previously cloud-free areas. Removing these erroneous observations  
1270 of cloud-top cooling caused by the motion and expansion of the anvil cloud is the main objective of the semi-Lagrangian approach.

The dense optical flow methods (fig. 2.11 c–f) show good performance in removing the anomalous cooling observations seen downwind of the anvil cloud. The Farnebäck,  
DIS and DeepFlow algorithms (fig. 2.11 c–e) all show a warming tendency towards  
1275 the edge of the anvil cloud. Although this may be explained by an overestimation of the cloud motion by these algorithms, this may also be a real observation of apparent warming due to thinning of the detraining anvil cloud. The Dual TV-L<sup>1</sup> algorithm (fig. 2.11 f) shows generally smaller differences than the other algorithms. This is likely due to the algorithm accounting for changes in brightness between observations,  
1280 whereas the other algorithms assume that the brightness of tracked objects remains constant between observations.

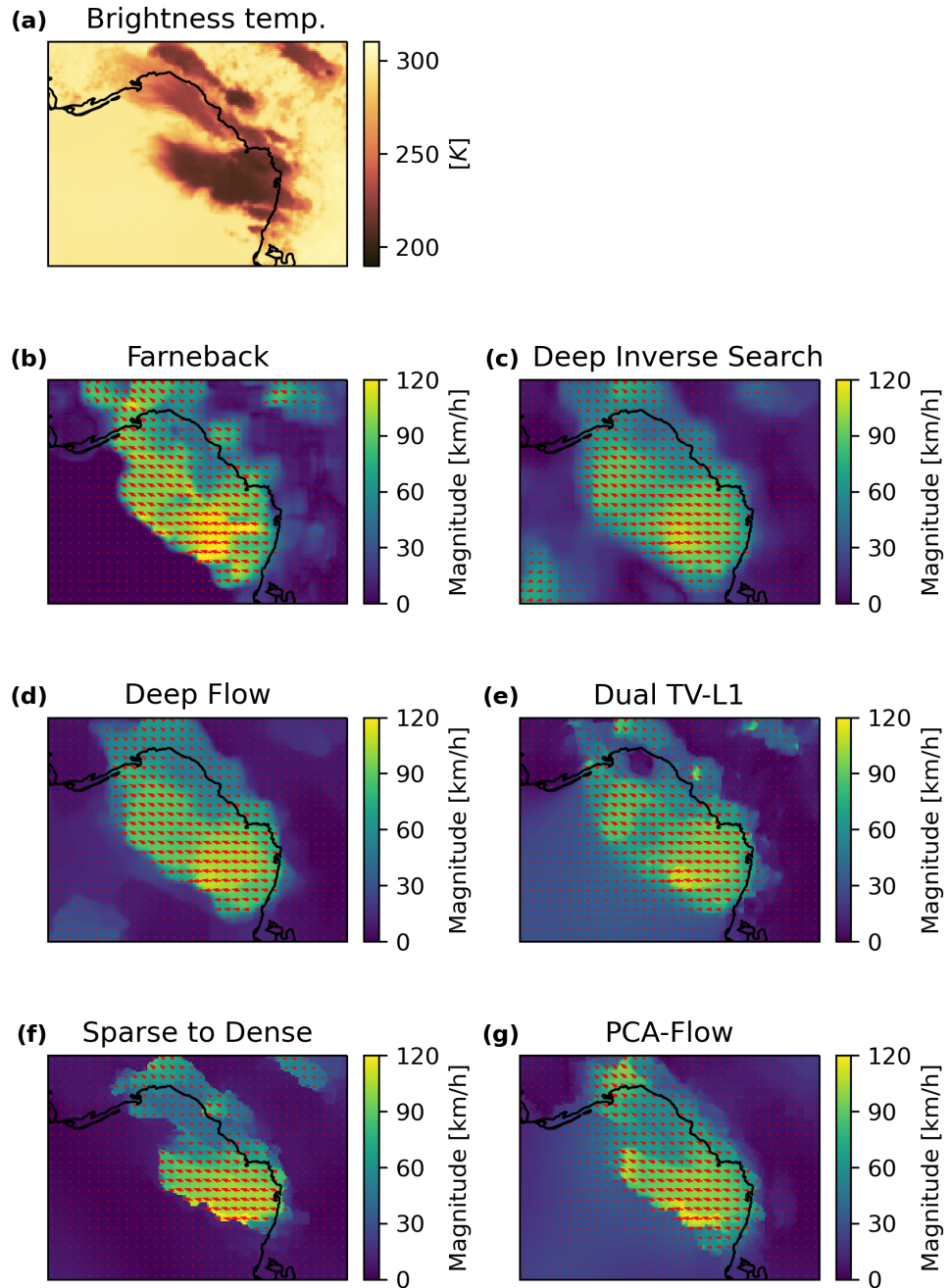


Figure 2.10: A comparison of the motion vector fields generated by the (b) Farnebäck, (c) DIS, (d) DeepFlow, (e) Dual TV-L<sup>1</sup>, (f) Sparse to Dense, and (g) PCA-Flow. Optical flow vectors shown are estimated between the 10.4  $\mu\text{m}$  channel at 19:00:00 UTC (a) and the subsequent image. Red arrows (b–g) show the motion vectors averaged over each 5  $\times$  5-pixel area is plotted by the red arrows, and the background shows the magnitude of the velocity vectors.

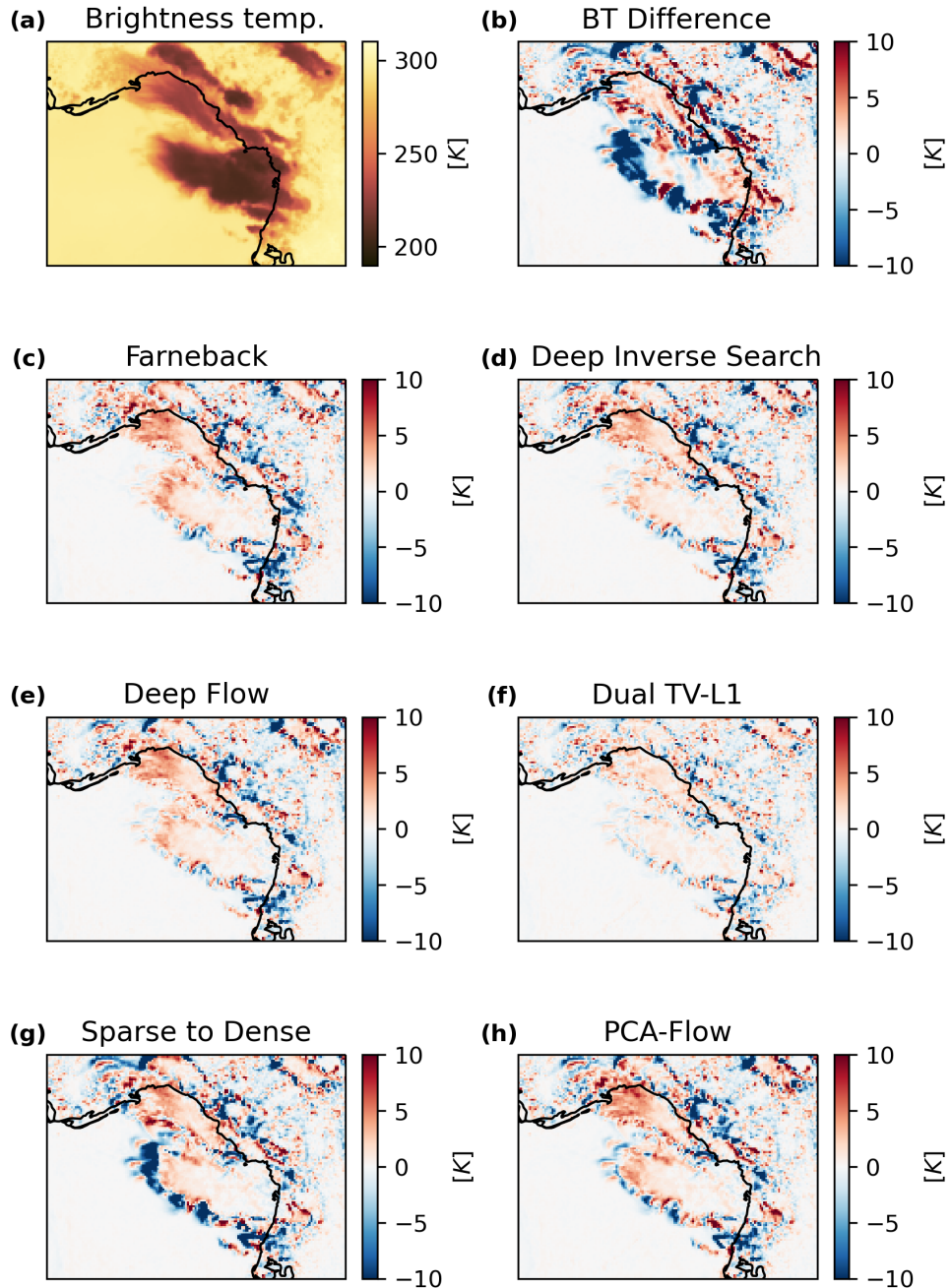


Figure 2.11: The difference in BT between subsequent ABI observations when taking into account the cloud motion predicted by the different optical flow algorithms. The plots are again shown for the time step at 19:00:00 UTC, with the 10.4  $\mu\text{m}$  BT at this time step shown for reference (a). b: the Eulerian difference in BT; c-h: the Lagrangian difference in BT using motion vectors predicted by each of the optical flow algorithms.

The two sparse optical flow algorithms (fig. 2.11 g,h) both show worse performance, with the sparse to dense method performing particularly poorly. Both algorithms show cooling downwind of the anvil, likely because the region-based methods used to map the sparse motion vectors to the whole image do not detect this region well.

Figure 2.12 a shows the Mean Square Error (MSE) of the BT differences shown in fig. 2.11 for each algorithm. As seen in fig. 2.11, the Dual TV-L<sup>1</sup> algorithm has the smallest differences, the other dense algorithms perform similarly, and the PCA-Flow and sparse to dense algorithms perform the worst. It should be noted that we should expect some differences in the BT due to actual changes in the CTT. Figure 2.12 b shows the MSE of the BT differences for pixels with BT less than 273 K, representing cold cloud observations.

To estimate the uncertainty in the calculated motion vectors, we calculate the residual motion vectors for each algorithm. The residual motion is calculated by first warping each image to the locations predicted by the optical flow vectors, in the same manner used to calculate the BT differences in fig. 2.11. Then the optical flow algorithms are used to calculate a second set of residual vectors between each image and the subsequent warped image. In theory, if the initial motion vectors were calculated perfectly, warping the image by the optical flow vectors should result in the subsequent cloud in the same position as the prior image, and so the second set of motion vectors should calculate as zero. The magnitude of the residual motion vectors is therefore considered as the uncertainty in the initial set of motion vectors.

Figure 2.12 c,d show the MSE of the residual vector magnitudes for all pixels and pixels less than 273 K respectively. The DeepFlow and Dual TV-L<sup>1</sup> algorithms again show the best accuracy, and sparse to dense the worst. The Farnebäck algorithm shows good accuracy across all pixels, as seen in the ability to correctly detect zero motion in cloudless skies in fig. 2.10. However, when considering only cold pixels the Farnebäck algorithm performs slightly worse than DIS.

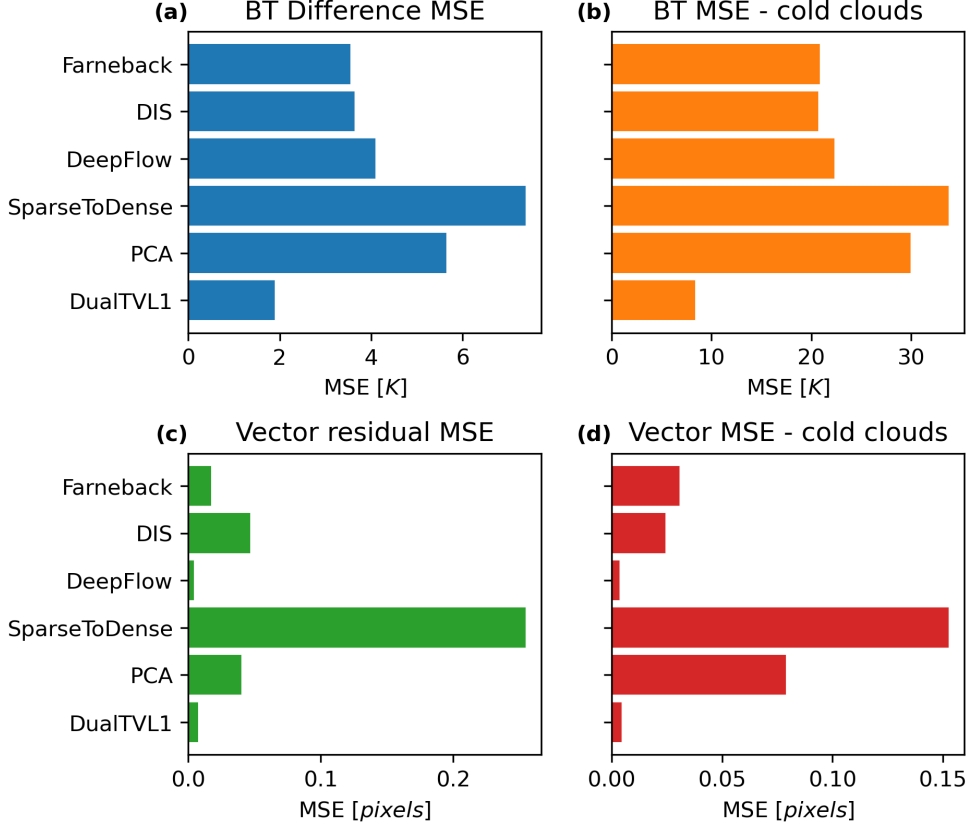


Figure 2.12: A comparison of the MSE for each of the optical flow algorithms. a: BT difference MSE for all pixels and (b) for pixels with BT < 273 K. c: MSE of the residual vector magnitude for all pixels and (d) for pixels with BT < 273 K.

The results shown in fig. 2.12 suggest that the Dual TV-L<sup>1</sup> algorithm is the best choice for estimating the motion vectors in satellite observations of DCC. However, due to the large size and long sequences of images produced by ABI, it is also important to consider the computational cost of each algorithm. Figure 2.13 shows the run time in seconds for each algorithm applied to a sequence of 48 300×300 pixel ABI BT images. Both the DeepFlow and Dual TV-L<sup>1</sup> algorithms show significantly longer run times than any of the other algorithms. As a result, we have selected the Farnebäck algorithm for our tracking method as it offers the best balance of accuracy and computational performance for running on large datasets.

An example of the motion vectors calculated by the Farnebäck algorithm when ap-

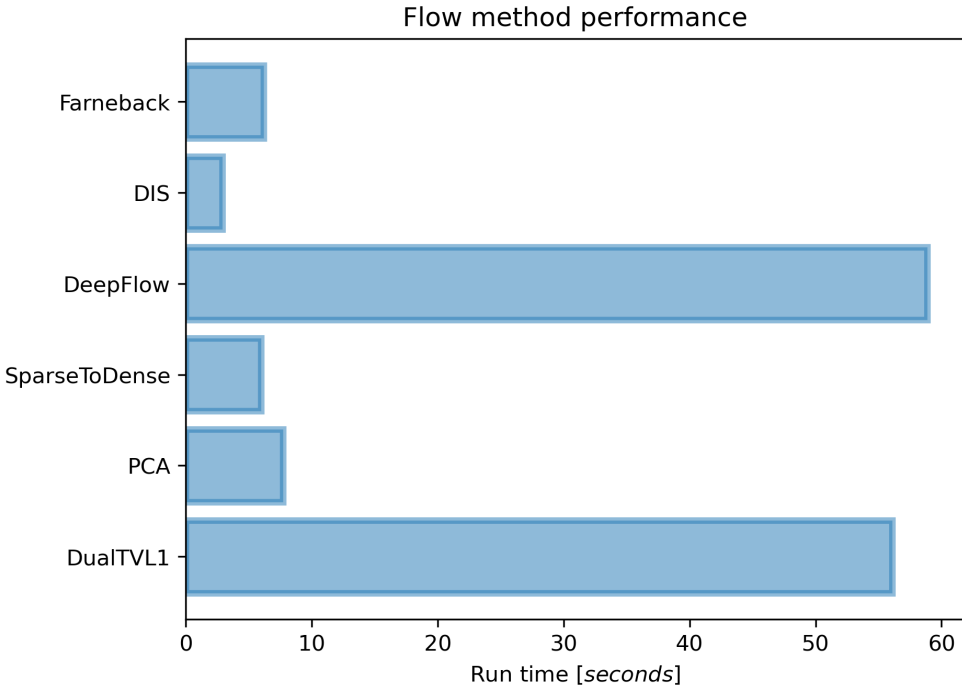


Figure 2.13: A comparison of the computational performance of each optical flow method. Run-time was measured for a sequence of 48  $300 \times 300$  pixel ABI 10.4  $\mu\text{m}$  BT images.

plied to the 10.4  $\mu\text{m}$  BT field is shown in fig. 2.14. Figure 2.14 c shows the residual flow  
 1320 vectors, which are small compared to the detected cloud motion vectors (fig. 2.14 b).  
 The main areas in which residual flow vectors can be seen are the regions around  
 the edge of anvil clouds and in the center of thick anvil clouds where there are no  
 clear features to track. Figure 2.14 d shows the distribution of residual vector errors  
 proportional to the detected cloud motion vectors. The majority of the residual er-  
 1325 rors are close to zero, and very few exceed 0.5. As in the majority of applications for  
 the semi-Lagrangian we are only interested in the motion to the nearest pixel, these  
 errors are acceptable.

Two potential sources of uncertainty are the assumptions made by the Farnebäck  
 algorithm that the feature being tracked remains the same size and intensity in sub-  
 1330 sequent images. For optical flow tracking using BT images of growing DCCs, neither

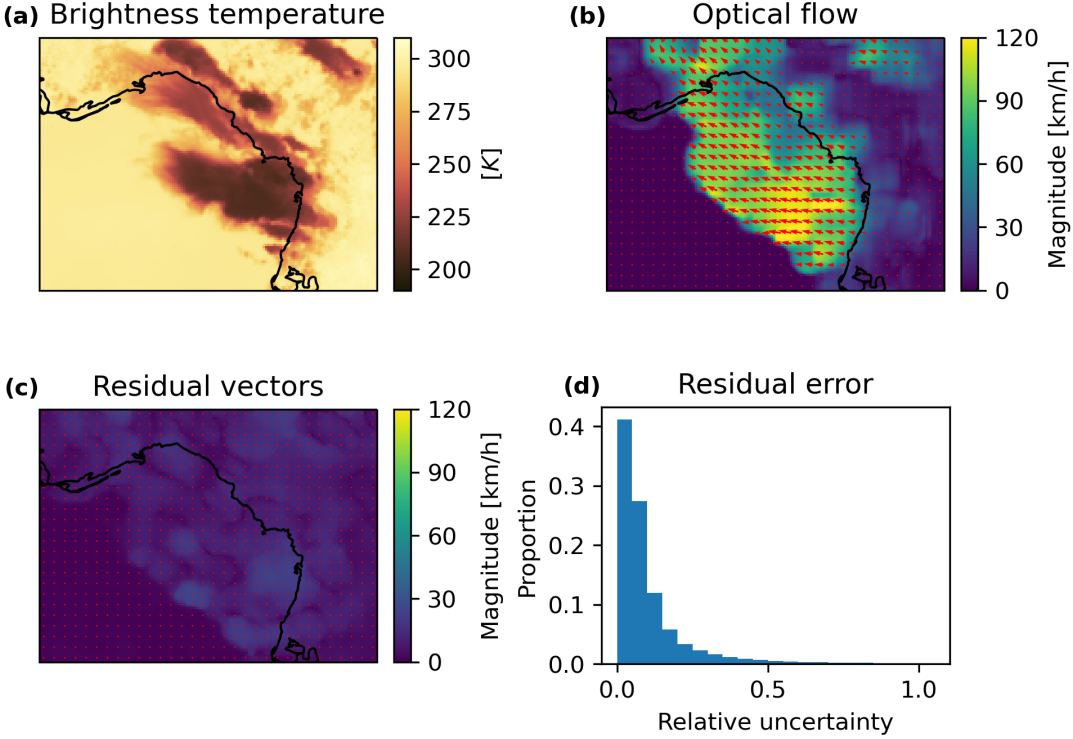


Figure 2.14: An example of the motion vectors and their residual errors calculated using the Farnebäck algorithm. a: the  $10.4\text{ }\mu\text{m}$  BT field at 19:00:00 UTC for which the motion vectors are shown. b: the calculated motion vectors. c: the residual motion vectors, indicating the uncertainty in the optical flow. d: the magnitude of the residual motion vectors as a proportion of the magnitude of the optical flow vectors for cold pixels (less than  $273\text{ K}$ )

of these assumptions are true. However, we have taken steps to reduce the impact of both these sources of uncertainty on the tracking algorithm. For the first of these assumptions, we find that in the case of small, fast-moving DCCs – where the accuracy of the optical flow vectors is most important – the changes in the size of the DCC is small compared to the overall motion, and so the uncertainty introduced is small. Comparably, for large DCCs where the changes in size may be large compared to the motion, the uncertainty introduced has less impact on the tracking algorithm. In the worst-case scenario, the estimated optical flow field will be zero, in which case the "3D" detection and tracking algorithm works in the same manner as that of Fiolleau

1335

1340 and Roca [2013], which is suitable for use on these larger DCCs.

## 2.4.2 A Semi-Lagrangian Framework for Morphological Image Processing

Morphological image operations analyse images using their geometrical and structural properties. Core to many morphological algorithms, from simple filters to complex 1345 neural networks [Kalchbrenner et al., 2014], is the kernel, or convolution method. A convolution method performs operations on the pixels of an image by applying a convolution stencil to the pixel and its neighbours. In a conventional convolution scheme, such as that used in the methods of Fiolleau and Roca [2013], the convolution stencil acts on adjacent pixels in both time and space (see fig. 2.15 a). In this Eulerian 1350 framework, different locations in time are considered in the same manner as those in the spatial dimensions. However, we know from previous analysis of DCCs that the motion of convective cores between images can be similar to the spacing of cores and their size [Heikenfeld et al., 2019]. As a result, it is important to include the effects of advection when comparing images across time steps.

1355 To perform morphological operations which take into account this advection, we have developed a novel Lagrangian convolution method. For spatial operations, the Lagrangian stencil operates identically to that of a classical convolution method. However, when sampling points at prior or subsequent time steps, the location of the 1360 stencil are offset by the relevant optical flow vectors (fig. 2.15 b). Values at the offset stencil locations are interpolated, providing a Lagrangian reference frame for changes in the observations over time. When applying the convolution stencil to every pixel in a sequence of images, this provides a semi-Lagrangian framework for morphological operations, combining the Lagrangian reference frame for evaluating changes over time while maintaining the regular grid of the images.

1365 We have developed new implementations of several existing image processing operations within the Lagrangian convolution framework, including:

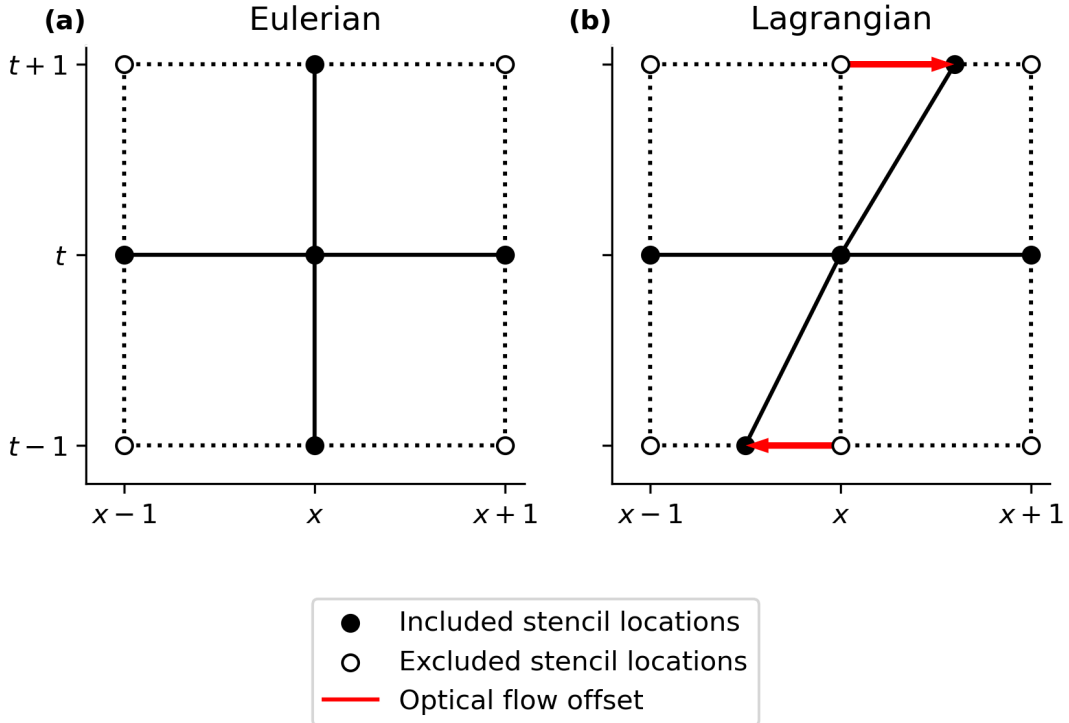


Figure 2.15: A comparison of convolution stencils with square connectivity in Eulerian (a) and Lagrangian (b) frameworks. In the Lagrangian framework, the points at prior and subsequent time steps are offset by the calculated optical flow field.

- Sobel edge detection [Sobel, 2014]
- Watershed segmentation using the connected-components method [Bieniek and Moga, 2000]
- Labelling of connected components [Hoshen and Kopelman, 1976]

These operations are used in this method to detect the full extent of the anvil cloud associated with the DCC, to perform detection continuously across multiple time periods while accounting for the motion of the DCC, and to identify individual DCCs and DCC clusters across multiple time periods respectively.

The Sobel method detects edges in an image using the magnitude of the local gradient at each pixel. Edge detection enables the segmentation of an image into separate regions without pre-defined thresholds (such as in BT) to separate them.

Watershed algorithms are a method of image segmentation that equate an image to a topographical map, with elevation according to the value of the pixel. Each pixel  
1380 is then descended towards its local minima until it reaches a predefined marker region. The method takes its name from the geographical feature of the same name, which refers to the separation between adjacent drainage basins. Although this physical interpretation of the algorithm applies to two-dimensional images, the method can be applied to arrays with any number of dimensions, such as the method used by  
1385 Fiolleau and Roca [2013] which applied watershedding to a three-dimensional field.

Labelling algorithms assign unique identifiers to each segmented region provided by either the edge detection or watershed algorithms.

### 2.4.3 Detection of Growing Deep Convection

Growing deep convective cores are detected in a similar manner to that used by Zinner  
1390 et al. [2008]. The growth rates are calculated using the finite difference of the 10.4  $\mu\text{m}$  BT and WVD fields in the Lagrangian perspective. We have found that combining both the 10.4  $\mu\text{m}$  BT and the WVD field provides the best observations for detecting growing deep convective cores. The BT field shows cooling cloud tops throughout the troposphere, while the WVD isolates growth in the mid- to upper-troposphere,  
1395 removing spurious observations of growth due to boundary layer convection and cloud formation.

We classify a region of growing deep convection as a region of either continuous cooling of greater than 0.5 K per minute in the 10.4  $\mu\text{m}$  BT field, or continuous warming of the WVD field of at least 0.25 K per minute. These growth rates must be  
1400 detected over a minimum 15-minute period, covering an area of at least 3 by 3 pixels (approximately 7.5 by 7.5 km) at each time step. Each region of detected growth is given a unique label, the average BT of the detected cloud at each time step is calculated, and any label which fail to meet the cooling rate thresholds of 8 K over

a 15-minute period (from [Roberts and Rutledge, 2003; Hartung et al., 2013]) are removed. Finally, each label is checked to ensure that the growth region ends with a WVD field with a value of greater than -5, indicating that the growing core reaches a high altitude [Müller et al., 2018].

Figure 2.16 shows a comparison between the detected core cooling rates in ABI imagery and the corresponding column radar reflectivity measured by NEXRAD for the case of newly developing convection (fig. 2.16 a,c,e) and mature DCC (fig. 2.16 b,d,f). Both 10.4  $\mu\text{m}$  BT and WVD growth rates show growth detected in the same locations as the high column radar reflectivity from NEXRAD. As predicted by the results in section 2.3.1, the observed growth rates in the WVD are about half of those in the 10.4  $\mu\text{m}$  BT.

Both 10.4  $\mu\text{m}$  and WVD growth rates in the growing phase (fig. 2.16 c,e) show good agreement with column radar reflectivity (fig. 2.16 a). However, during the mature stage of the DCC, discrepancies develop between the observed growth rates (fig. 2.16 d,f) and the radar reflectivity (fig. 2.16 b) due to the development of the anvil cloud blocking satellite observations of the core underneath.

#### 2.4.4 Detection of Anvil Clouds

The region of anvil cloud associated with the growing convective clouds detected in section 2.4.3 is detected and tracked using an edge-based watershed segmentation approach. The edge-based approach to cloud detection avoids the use of a fixed threshold for anvil temperature, and so can detect a more accurate extent of the anvil cloud [Dim and Takamura, 2013]. We define an upper threshold for the WVD field of -5 K, as used by Müller et al. [2018], and a lower threshold of -12.5 K, which we define as definite non-anvil cloud. Because the presence of thin cirrus outflow from the anvil clouds can make it difficult to determine the extent of the anvil cloud, we use the SWD field as described in section 2.1 to either remove or include the region

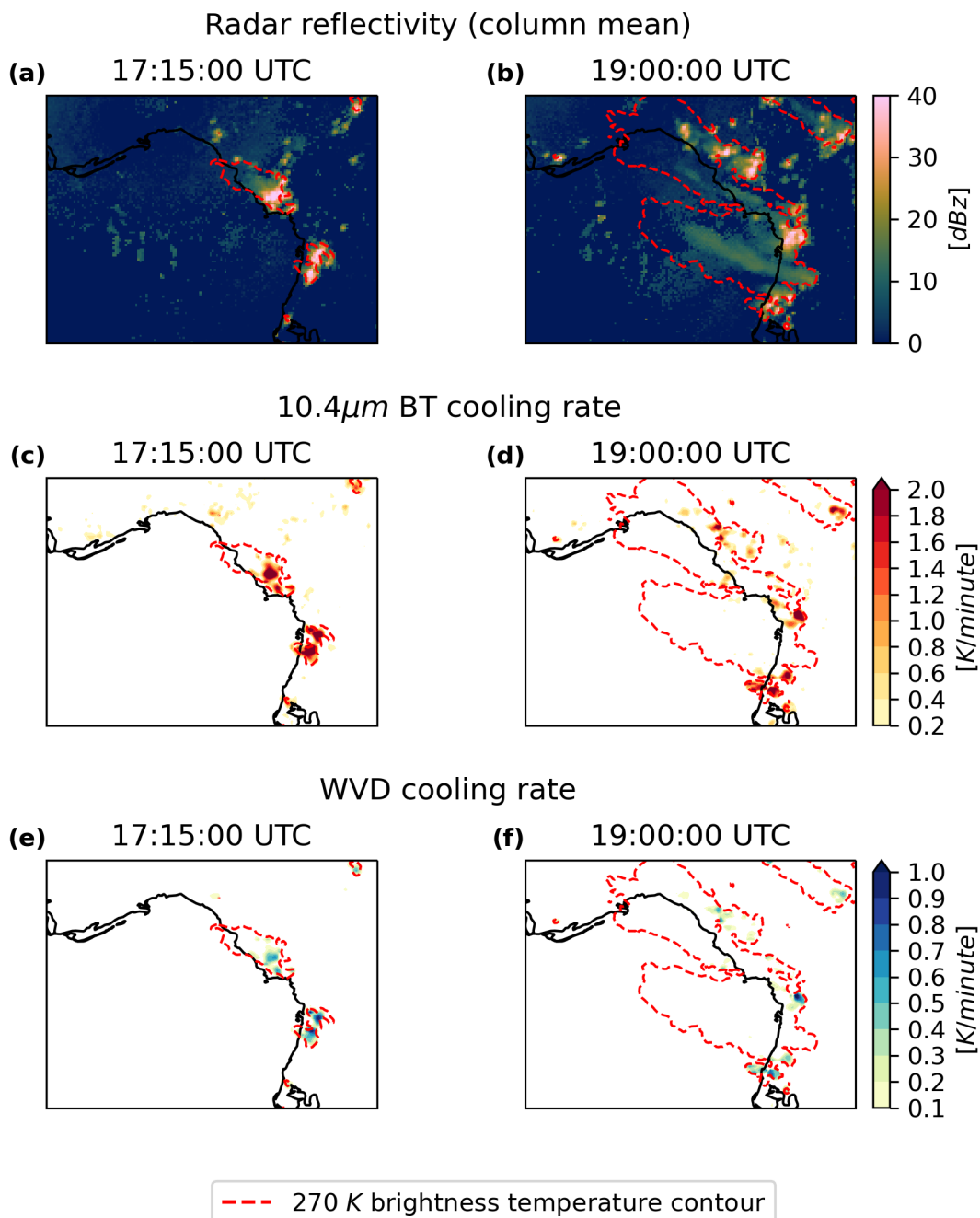


Figure 2.16: Detection of growing DCC regions for the DCC cluster in figure 2.1. a,b: NEXRAD column mean radar reflectivity remapped to the ABI grid. c,d: cooling rate of the  $10.4\mu\text{m}$  BT field. e,f: warming rate of the WVD field.

1430 of cirrus outflow in the detected anvil region. To detect the thick anvil cloud, we subtract the SWD field (fig. 2.17 a). In this case, the upper and lower thresholds remain the same as the SWD field is approximately 0 K for thick, high clouds, and so has no effect on the temperature of these features. For detecting the thin anvil region, we add the SWD field and increase the value of both thresholds by 5 K to 0 K  
1435 and -7.5 K respectively (fig. 2.17 c). This change is made to account for the effect of low-level WV on the SWD field which gives a background value of approximately 5 K. Between these two thresholds, we have a region in which we are uncertain of the extent of the anvil cloud. By applying a Sobel filter to detect the local gradient magnitude of the combined WVD/SWD field [Sobel, 2014], we detect the outer extent of the  
1440 anvil cloud within this region where we see the greatest magnitude in the detected edges (see fig. 2.17 b,d).

When applied to the detected edges of the anvil clouds using the Sobel filter, with the growth regions detected previously as markers, the watershed method allows us to detect those anvil regions associated with detected regions of growing DCCs, while  
1445 avoiding the detection of non-convective regions of high, cold clouds. Furthermore, due to the application of the watershed algorithm to both the spatial and temporal dimensions of the sequence of images through the semi-Lagrangian framework, we are able to detect the associated anvil clouds after the growth of the DCC is no longer observed.

1450 Figure 2.18 shows an example of the results of detecting and tracking DCC cores (outlined in red) and the associated anvils (outlined in orange and blue for the thick and thin anvil regions respectively). During the growing phase (fig. 2.18 a,b) we see a number of developing cores, as well as the initial growth of primarily thick anvil cloud. In fig. 2.18 c–e we see the mature phase of the DCC, where we see the thick  
1455 anvil expand and the thin anvil cirrus start to detrain towards the top-left side of the figure. Due to the anvil cloud reaching its maximum height, we no longer observed

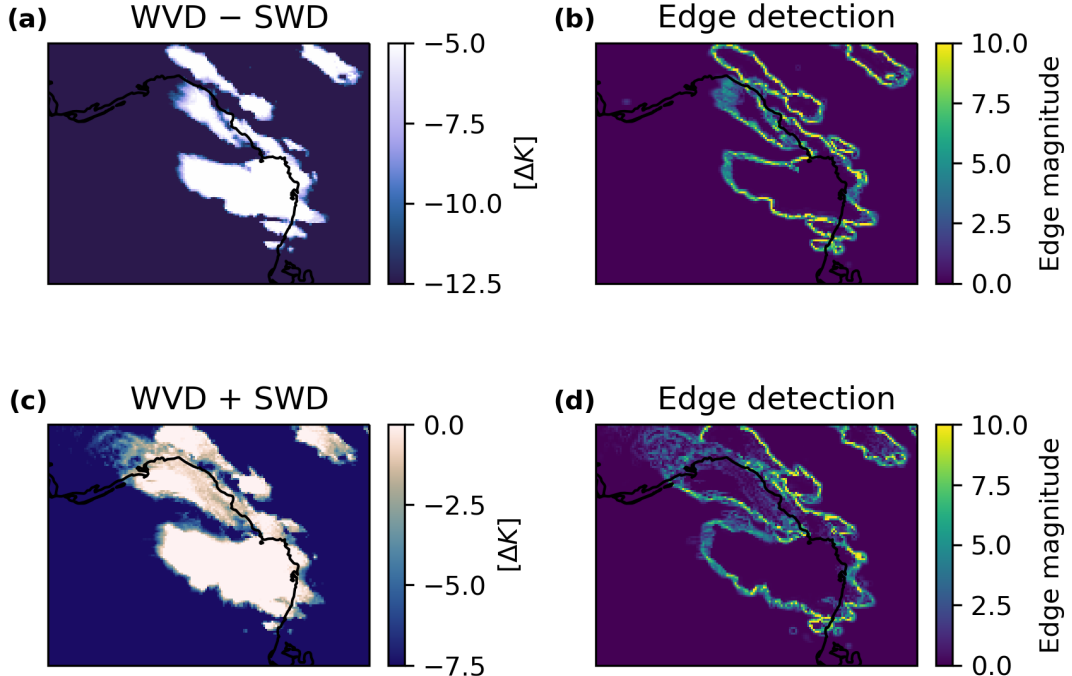


Figure 2.17: Detection of anvil cloud extent for the mature DCC cluster in 2.1 using the edge gradient method. a.: The combined field of the WVD minus the SWD, to isolate the thick anvil, between the upper and lower thresholds of -5 and -12.5 K respectively. b.: the detected edge gradient magnitude of the field between these thresholds, which is used to detect the outer extent of the thick anvil cloud. c.: the combined field of WVD plus the SWD, to enhance the thin anvil, and d.: the calculated edge magnitude of this field.

the initial developing cores seen in fig. 2.18 a,b as we can no longer observed the cloud-top cooling. Instead, we observe new cores developing on the edges of the anvil cloud. In fig. 2.18 f–h, we see the detected anvil cloud beginning to dissipate. The thick anvil area decreases, however the thin anvil area continues to increase as the anvil dissipates and detrains. At this point in the lifetime of the tracked DCC we stop observing new growing core, however the "3D" approach allows the continued tracking of the anvil cloud until it dissipates.  
 1460

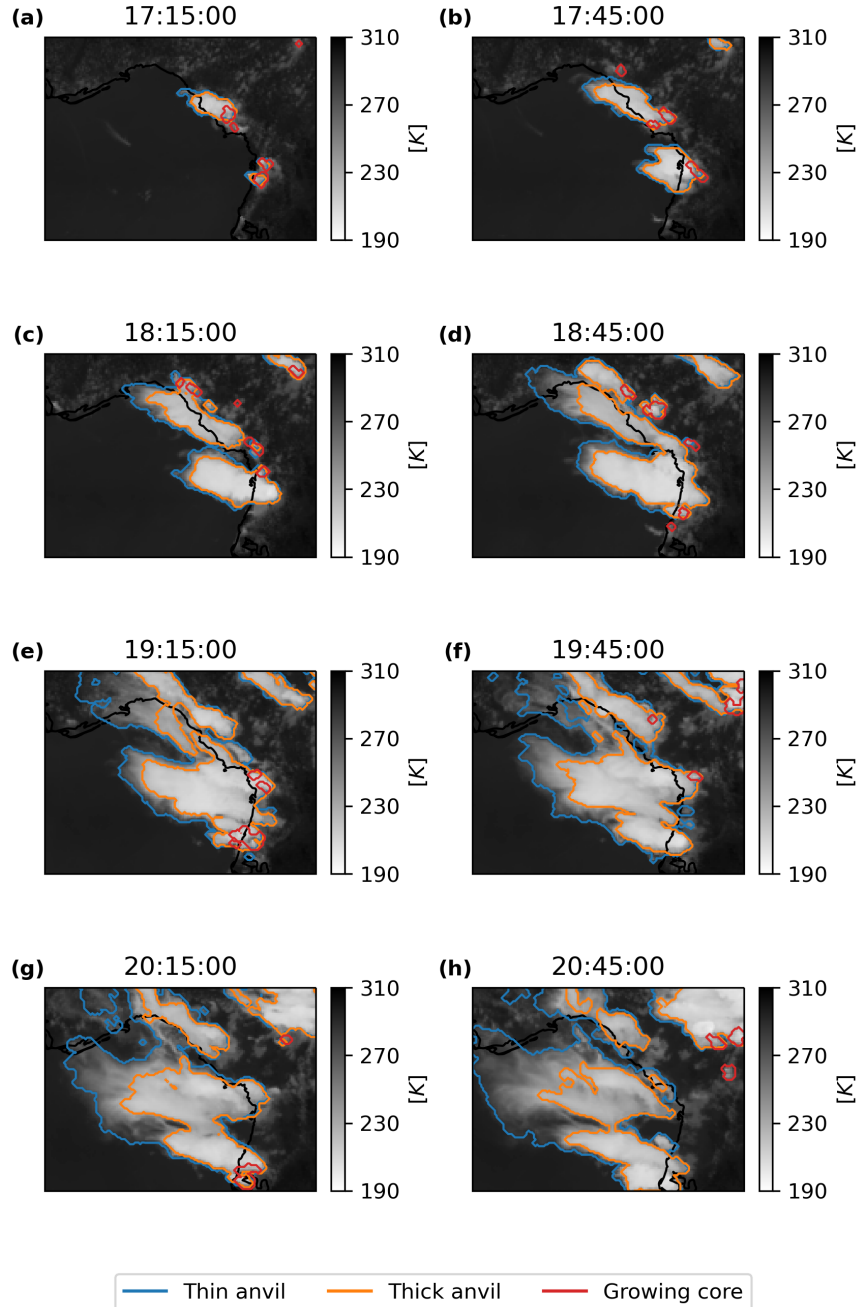


Figure 2.18: Detected regions of thin anvil cloud (blue), thick anvil cloud (orange), and developing cores (red) overlaid on the GOES-16 ABI 10.4  $\mu\text{m}$  BT field for the DCC cluster from figure 2.1. The three stages of the DCC lifecycle are shown; the growth phase (a,b), the mature phase (c–e), and the dissipating phase (f–g).

## 2.5 Evaluation

1465 The effectiveness of the semi-Lagrangian framework for the detection of DCCs is evaluated by analysing the proximity of detected anvil cloud regions to lightning flash detection from GLM. Lightning observations are frequently used to validate detection methods for deep convection [e.g. Zinner et al., 2013; Müller et al., 2019] due to the strong correlation between deep convective updraughts and lightning activity.

1470 Although GLM is not capable of detecting all lightning events (approximately 70% of lightning events are detected) [Peterson, 2020], the high frequency of lightning flashes per DCC mean that these observations provide a suitable ground truth for validation. It should be noted that lightning observations are only suitable for validating the detection of the thick anvil region, as lightning does not occur in the cirrus outflow.

1475 As a result, validation of the detection of the thin anvil region would require the use of other data such as cloud profiling radar or lidar observations, and is not considered further in this paper.

Here we apply the same validation method as used by Müller et al. [2019] to evaluate the semi-Lagrangian framework for the detection of DCCs. We classify 1480 detection events into three categories:

- Correct detection (CD), when the algorithm detects a DCC that is collocated with one or more lightning observations
- False detection (FD), when the algorithm detects a DCC but no lightning flash is observed
- Missed detection (ND), when the algorithm does not detect a DCC but a lightning flash is observed

Using these three categories of events we can define two measures of accuracy for the detection of DCCs. The Probability of Detection (POD) is defined as the number

of correct detections divided by the total number of correct and missed detections.  
1490 This provides a measure of how likely the algorithm is to detect a DCC that exists  
in the ground truth. The False Alarm Rate (FAR) is defined as the number of false  
detections divided by the total number of correct and false detections. This provides  
a measure of how likely a DCC detected by the algorithm is not present in the ground  
truth. The  $F_1$ -score is calculated as the harmonic mean of the POD and the recall  
1495 (where the recall in is  $1 - \text{FAR}$ ), and provides an overall measure of accuracy between  
0 and 1.

When evaluating whether detected DCC regions and lightning observations were  
collocated, Müller et al. [2019] considered events within 32 km and 15 minutes to  
be collocated. This margin of uncertainty was separated into two components, half  
1500 from the physical separation between observed lightning strikes, and the remaining  
half from uncertainty in the collocation and geolocation of the satellite and lightning  
observations. For a typical ABI pixel length over the CONUS of 2-2.5 km, this margin  
of error translates into 15 pixels in the ABI view. The distance between a GLM  
lightning flash and detected cloud region is defined as the distance between the flash  
1505 and the nearest ABI pixel within that region, with GLM flashes that fall within a  
detected DCC given a distance of 0. When considering that the resolution of GLM  
is a factor of four less than that of ABI, we consider that the same justification  
for the margin of error used by Müller et al. [2019] is also applicable to collocated  
observations from ABI and GLM.

1510 Validation was performed using GOES-16 ABI data from the CONUS scan region  
for the entirety of 2018, which was processed using the method described in this  
chapter. In total validation was performed for 319 days of ABI data, the remaining  
46 days being excluded due to missing observations from either the ABI (1 day) or  
GLM (45 days) instruments aboard GOES-16.. Detection and tracking of DCCs was  
1515 performed the CONUS scan region of ABI for each 24-hour period. By performing

Detection Method	n	POD	FAR	$F_1$ -score
Growth-based	598,038	0.4017	0.2136	0.5318
WVD threshold	678,854	0.9727	0.6457	0.5194
Semi-Lagrangian	145,969	0.9837	0.1611	0.9056

Table 2.3: POD, FAR and  $F_1$ -score for three different detection methods validated against observed GLM flashes ( $n=116,671,289$ ). Growth based refers to the detection of growing DCCs using the method described in section 2.4.3 WVD threshold uses the threshold method developed by Müller et al. [2018]. Semi-Lagrangian refers to the detection of anvils clouds connected to growing cores using the edge-based water-shedding method described in section 2.4.4.

validation over both a large region, including a range of both land and ocean domains, and a full year time period, we aim to avoid any bias in the validation associated with the variability of the accuracy of the method with location and season.

Results of the validation of the detected anvil region, as well as those for the 1520 detection of growing deep convection and the WVD filter, are shown in table 2.3. The regions of growing DCCs detected using the method described in section 2.4.3 shows low scores for both the FAR and POD metrics. While the detection of growing DCCs shows a low FAR of 0.21, the short time frame in which growth can be observed leads to a high rate of missed detections of lightning flashes, which results in a POD 1525 of 0.40. This is not necessarily because we are failing to detect cores, but because many lighting observations occur during the mature phase of convection (see fig. 2.1 h, 2.2 d) we fail to detect these lightning flashes as we can only observed the core during the growing phase.

For comparison, we also evaluate the accuracy of detecting anvils only by a fixed 1530 threshold of the WVD without detecting growing cores, as used by Müller et al. [2018]. Compared to the detection of growing DCC regions, the WVD threshold shows a much higher POD of 0.97, but also has a high FAR of 0.64, repeating the findings of Müller et al. [2019] which show that although the WVD threshold method is capable of detecting the majority of DCCs, it is incapable of distinguishing between

1535 anvil clouds and other thick, high altitude clouds. Furthermore, the WVD threshold  
detection detects a larger number of objects ( $n=678,854$ ) compared to either of the  
other detection methods, further indicating that a large number of non-convective  
clouds are detected using the threshold method on its own. Note that both the  
core detection and WVD threshold approach have similar  $F_1$ -scores (0.53 and 0.51  
1540 respectively) as both prioritise one measure of accuracy over the other.

Finally, the anvil regions detected using a combination of the detected growth  
regions and the WVD field using the semi-Lagrangian framework described in section  
2.4.4 are validated. The novel method has a high POD of 0.98 similar to that of  
the WVD threshold, while also maintaining much of the low FAR of the detection of  
1545 growing DCCs (FAR=0.16). As a result, the Semi-Lagrangian method displays a high  
overall  $F_1$ -score of 0.91. This result highlights the capability of the semi-Lagrangian  
detection framework to use growth-based detection methods to substantially reduce  
the compromise between POD and FAR error rates by combining multiple methods  
for the detection of DCCs.

## 1550 2.6 Summary

Algorithms for the detection and tracking of DCCs perform a vital role in both fore-  
casting and research applications. Sequences from geostationary satellites provide  
unique observations of DCC anvil clouds over their entire lifecycle. However, the tra-  
ditional framework used by such algorithms requires a compromise between the rates  
1555 of false and missed detections due to the overlap in signature from convective and non-  
convective clouds [Konduru et al., 2013]. Whereas novel methods have approached  
this problem for the detection of large, mesoscale convective systems [Fiolleau and  
Roca, 2013], such approaches do not take advantage of the capability of the latest  
generation of geostationary imaging satellites to detect individual deep convective  
1560 cores.

By developing and implementing a novel semi-Lagrangian framework for the detection and tracking of DCCs we are able to combine the detection of growing DCC cores [Zinner et al., 2008] and DCC anvils [Müller et al., 2018] to detect and track DCCs over their entire lifecycles. The novel methods developed here for the Semi-  
1565 Lagrangian computer vision framework, along with implementations of multiple image processing operations commonly used for object detection, allow the accurate detection and tracking of moving objects utilising both spatial and temporal information. These methods may have impacts on applications of computer vision beyond the detection and tracking of DCCs. Furthermore, the novel framework is able to achieve  
1570 higher levels of accuracy without compromising on the number of DCCs detected, as with previous algorithms [Müller et al., 2019].

By using this novel methodology, we are able to detect and track both small, isolated DCCs and large, mesoscale convective systems with a high degree of accuracy, high spatial and temporal resolution and across large domains such as the CONUS.  
1575 The data provided about the behaviour of DCCs over their entire lifetime will allow new research into vital topics such as the response of deep convection and climate change, and the interactions and feedbacks between DCCs and large-scale atmospheric thermodynamics [Varble, 2018].

# Chapter 3

## **1580 Linking the Properties of Deep Convective Cores and their Associated Anvil Clouds Observed over North America**

### 3.1 Introduction

1585 Understanding the relationships between the properties of deep convective cores and anvils is vital to understanding the behaviour of DCCs in both the present day and future climate. Our ability to study these relationships is limited, however, by a lack of datasets connecting convective processes to anvil properties over the entire DCC lifetime [Gasparini et al., 2023]. The capabilities of the newest generation of  
1590 geostationary satellite instruments provide opportunities to address this issue. Data from the GOES-16 ABI instrument's CONUS domain provide many advantages for investigating convective processes. The higher spatial and temporal resolutions and number of channels allow us to move beyond the traditional tracking of large, cold cloud shields to instead track DCCs from the initial development of the core to the  
1595 final dissipation of the anvil across scales spanning isolated DCCs to large MCSs. Furthermore, the CONUS domain contains a wide variety of regimes which we expect to impact the properties of DCCs, including land, ocean, tropics and mid-latitudes.

Deep convective storms play an important role in both the weather and climate

of North America. The continent experiences tropical, subtropical and extra-tropical  
1600 convection across a range of modes, including isolated DCCs, MCSs and supercell  
convection [Brooks et al., 2019]. The North American Monsoon, which transports  
warm, moist air from the south-east Pacific and the Gulf of Mexico into the conti-  
nent, strongly influences the seasonal cycle of these convective events [Adams and  
Comrie, 1997; Higgins and Shi, 2001]. DCCs are responsible for a wide range of ex-  
treme weather events, including heavy rainfall and flooding, hail, derechos, lightning  
1605 and tornadoes [Westra et al., 2014; Houze, 2014; Williams et al., 1992; Bruning and  
MacGorman, 2013; Punge and Kunz, 2016; Matsudo and Salio, 2011]. Additionally,  
DCCs—in particular MCSs—provide the majority of precipitation across many re-  
gions of North America [Feng et al., 2019; Li et al., 2021]. As a result, a wide array  
1610 of observational networks have been deployed to study deep convection over North  
America, including satellite observations and cloud radar [Brooks et al., 2019].

The United States of America (USA) East of the Rocky Mountains experiences  
a wide variety of convection. The Rocky Mountains block the Westerly zonal winds  
except at higher altitudes. At lower altitudes, instead, there is a Southerly low-level  
jet transporting warm, moist air from the Gulf of Mexico. The combination of these  
1615 two air masses provides both a high shear environment and a high atmospheric lapse  
rate and hence high instability which provides the conditions for intense convection—  
including both MCSs and supercells—to initiate over the Great Plains and Midwest  
regions of the USA [Coniglio et al., 2010; Song et al., 2019]. These MCSs propagate  
1620 eastward and provide the majority of precipitation across these regions [Feng et al.,  
2019]. In the southeastern USA the lapse rates, and hence instability, tend to be lower,  
but the water vapour mixing ratio is higher which produces a tendency towards more  
frequent but less intense convection [Brooks et al., 2007].

Mexico also experiences frequent MCSs, which produce heavy rainfall and risks  
1625 from flooding [Douglas et al., 1993]. Topographic interactions play an important role

in the development of these systems. Warm, moist air from the Eastern Pacific and Gulf of Mexico is lifted and converges as it meets the mountainous terrain of Mexico, driving the development of MCSs [Farfán and Zehnder, 1994]. Unlike in the USA, there is typically less shear in this environment, and so there is a lower tendency for  
1630 the production of supercell convection (and the associated risks) except in the North of Mexico [Weiss and Zeitler, 2008].

The impacts of extreme weather across North America drive interest in the research of convective systems and their behaviour. Furthermore, global warming is expected to drive an increase in a number of factors affecting convection, including  
1635 CAPE [Seeley and Romps, 2015b], with a corresponding increase in the intensity of deep convective storms [Trapp et al., 2007; Seeley and Romps, 2015a]. However, many models generally do a poor job of representing convective storms, particularly MCSs, over much of North America [Pinto et al., 2015]. Although convective resolving models have improved this [Stevens et al., 2020], there are still shortcomings in  
1640 their representation of convective cloud processes which limit their capabilities [Jeevanjee, 2017; Prein et al., 2021]. As a result, studying the distribution of convective systems and their properties remains an important task both more understanding these processes, improving models and forecasting the weather [Brooks et al., 2019].

Geostationary satellite observations have provided a key tool for studying the  
1645 behaviour of DCCs over North America due to the large spatial coverage of their observations. Early studies focused on the behaviour of mesoscale convective complexes; large, elliptical MCSs which propagate eastward from the Rocky Mountains [Maddox, 1980b; Augustine and Howard, 1988, 1991]. Tsakraklides and Evans [2003] found that linear organised convective systems (such as squall lines) showed different lifecycles  
1650 to those of mesoscale convective complexes over North America, indicating that the structure of convection plays an important role in their behaviour. More recently, Feng et al. [2019] and Li et al. [2021] used a combination of satellite and radar data

to track both isolated and mesoscale convection, and provide better characterisation of their spatial properties. However, the low temporal resolution of 1 hour limits the ability to the properties of individual cores, and the reliance on ground-based radar restricts the study to DCCs which occur over land over the USA.

By leveraging the full temporal and spatial resolution of GOES ABI observations over the CONUS, we have created a 5-year dataset of observed DCCs, tracking both cores and anvils. By analysing this dataset, we are able to show new discoveries about the lifecycle of DCCs, and how their properties correspond to those of their cores.

## 3.2 Data

To detect and track DCCs across North America, we use ABI MCMIP data from the 6.2, 7.3, 10.4 and 12.4  $\mu\text{m}$  channels observed in the CONUS region, as described in section 2.2.1. We use the full extent of the ABI CONUS domain of 2,500 pixels E–W by 1,500 pixels N–S. This domain covers a region of around 60–120 °W in longitude and 15–50 °N in latitude, covering an area of approximately 5,700 by 3,900 km. Figure 3.1 shows the satellite zenith angle of ABI observations across the CONUS domain. As the viewing angle increases the accurate detection and tracking of DCCs becomes more difficult. This is due to the confounding between vertical and horizontal motion, and also due to the area of each pixel increasing with the zenith angle. The large sensor zenith angles in the North-West of the domain may introduce large errors in the detection and tracking algorithm, so for the rest of this chapter we will only consider DCCs detected east of 110 °W and south of 45 °N.

Five full years of data—from the start of 2018 to the end of 2022—are used to produce a dataset of detected DCCs and their properties. This period spans all complete years of operational data from GOES-16 ABI. To improve to continuity of observations, we then perform a gap-filling procedure. If time gaps between observations of greater than 15 minutes are present we use observations from the full-disc ABI

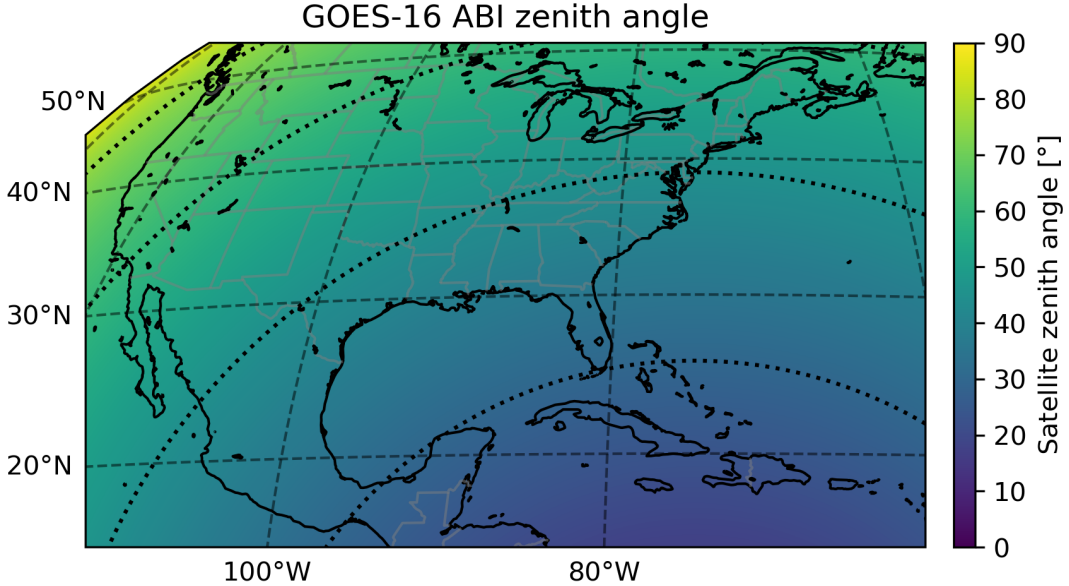


Figure 3.1: The sensor zenith angle of GOES-16 ABI observations across the CONUS domain. Dotted arcs are shown for each 15 °interval of zenith angle.

scan to fill these gaps. Full disc imagery is typically available every 10 or 15 minutes  
 1680 depending on the operating mode. This gap filling is particularly important during the periods in which ABI uses its mode 4 scan pattern, in which no CONUS domain scans are made, but the full-disc is scanned every 5 minutes. Using the full-disc observations allows us to maintain temporal sampling throughout these periods.

### 3.3 Method

1685 Detection and tracking of convective cores and anvil cloud is performed using the *tobac-flow* method [Jones et al., 2023a] described in section 2.4. Initial detection of DCCs is performed separately over 24-hour periods spanning from 12:00:00 UTC (approximately 6am local time over North America) to the same time the next day. This 24-hour period was dictated due to performance constraints, as the large domain  
 1690 combined with the high spatial and temporal resolution of ABI data results in a large memory requirement. The start time corresponds with the minima of convective

activity over land, and so was chosen in order to minimise the number of DCCs missed at the start and end of the detection period. Each period is extended by six ABI observations at each end to ensure at least one hour of overlap between successive days.

To track long-lived DCCs that last beyond one day, we apply a linking algorithm which combines DCCs observed across multiple days. The linking algorithm combines DCCs detected at the same locations within the overlap period of two daily detection files. Splitting and merging of objects is taken into account, so a single object which splits into two, or two objects which merge into one in the subsequent file are all considered a single, tracked object. The linking algorithm is applied separately to each month of data for performance reasons.

After linking, a processing step is applied to calculate the properties of detected cores and anvils at each step of their lifecycles. Finally, core and anvil step properties are aggregated over each month of observation, and overall core and anvil properties are calculated. During this final step quality flagging is performed to isolate detected features that fail one or more quality checks. The quality criteria are split into two groups. The first set of criteria—for core or anvil removal—removes features that we cannot verify are correctly tracked DCCs. This may happen because there are large time gaps in the dataset, or missing data due to artifacts in the ABI observations. Detected features which flag any of these criteria are removed from the aggregated

Core removed if:	Core invalid if:
Initial BT – final BT < 8 K	Intersects edge of domain
Lifetime < 15 minutes	Intersects start of domain
Time gaps > 15 minutes	Intersects end of domain
Maximum area > 10,000 km <sup>2</sup>	Adjacent to bad ABI data
Any NaN values in core properties	

Table 3.1: Validity criteria for detected cores. Cores which flag any of the removal criteria are removed in their entirety from the dataset. Those which flag any of the invalid criteria are retained, but removed from subsequent analysis.

Anvil removed if:	Anvil invalid if:
No associated cores	Intersects edge of domain
Lifetime < 15 minutes	Intersects start of domain
Time gaps > 15 minutes	Intersects end of domain
Maximum area < maximum core area	Adjacent to bad ABI data
Anvil detected before initial core	Associated with invalid cores
Anvil dissipated before final core ends	Maximum area reached before end
Any NaN values in anvil properties	of initial core

Table 3.2: Validity criteria for detected anvil. Anvils which flag any of the removal criteria are removed in their entirety from the dataset. Those which flag any of the invalid criteria are retained, but removed from subsequent analysis. The majority of anvils removed are due to have no associated cores, or because the anvil was observed before any developing cores.

dataset in their entirety. This step in particular removes anvils which have no cores associated with them, or are not detected as initiating with a developing core.

The second set of criteria is used to identify detected cores or anvils for which we do not observe their entire extent or lifecycle. Cores and anvils which flag are of these criteria are still included within the aggregated properties dataset, but are removed from the analysis DCC properties throughout this chapter. Quality criteria for cores are listed in table 3.1, and those for anvils in table 3.2.

The complete processing pathway is outlined by the following steps:

- 1720 1. Detection of cores and anvils in ABI observations over each 24-hour period.
- 2. Linking of overlapping objects detected in subsequent 24-hour periods over each month.
- 3. Calculation of core and anvil step properties.
- 4. Quality criteria applied to core and anvils, properties aggregated over each month

1725 Two datasets are produced. The first consists of daily core and anvil spatial

maps, with step properties, produced by processing step 3. The second, consisting of aggregated monthly core and anvil properties, is produced by step 4.

Figure 3.2 shows an example of detected cores and anvils over the CONUS region, against backgrounds of composite visible imagery (fig. 3.2 a) and 10.4  $\mu\text{m}$  BT (fig. 3.2 b). Cores and anvils which are removed from the aggregated dataset are outlined with dotted lines, and those which are marker invalid are shown with dashed outlines. The large, organised convective system centred at 95°W, 27°N has been removed as it is intersected by a scan-line artifact later in its lifetime. The DCCs observed along the eastern edge of the domain have been marked invalid as, while they are considered true detections of DCCs, they intersect the edge of the domain.

Over the five-year observing period we detect a total of 3,877,130 cores, of which 3,615,533 are valid, and 1,643,030 are linked with an anvil cloud. We detect a total of 648,345 anvils, of which 391,050 are valid, and these valid anvils contain 792,522 cores. The disparity in the number of valid cores and the number of cores contained with valid anvils is due to additional filtering applied to the anvils. As the larger and longer-lived anvils are more likely to intersect the edges of the domain, they are more likely to be marked invalid than the cores. In these cases, we may consider the cores themselves to be valid for analysis, as we observe their evolution and connect them with an anvil cloud, but exclude the anvil itself from analysis as we do not capture its entire extent and lifetime. The exclusion of anvils that intersect the edges of the domain introduces a bias towards removing larger, long-lived systems near the edge of the domain, which should be considered when assessing the properties of the observed DCCs.

Detected cores and anvils 2018-06-19-18:03:43 UTC

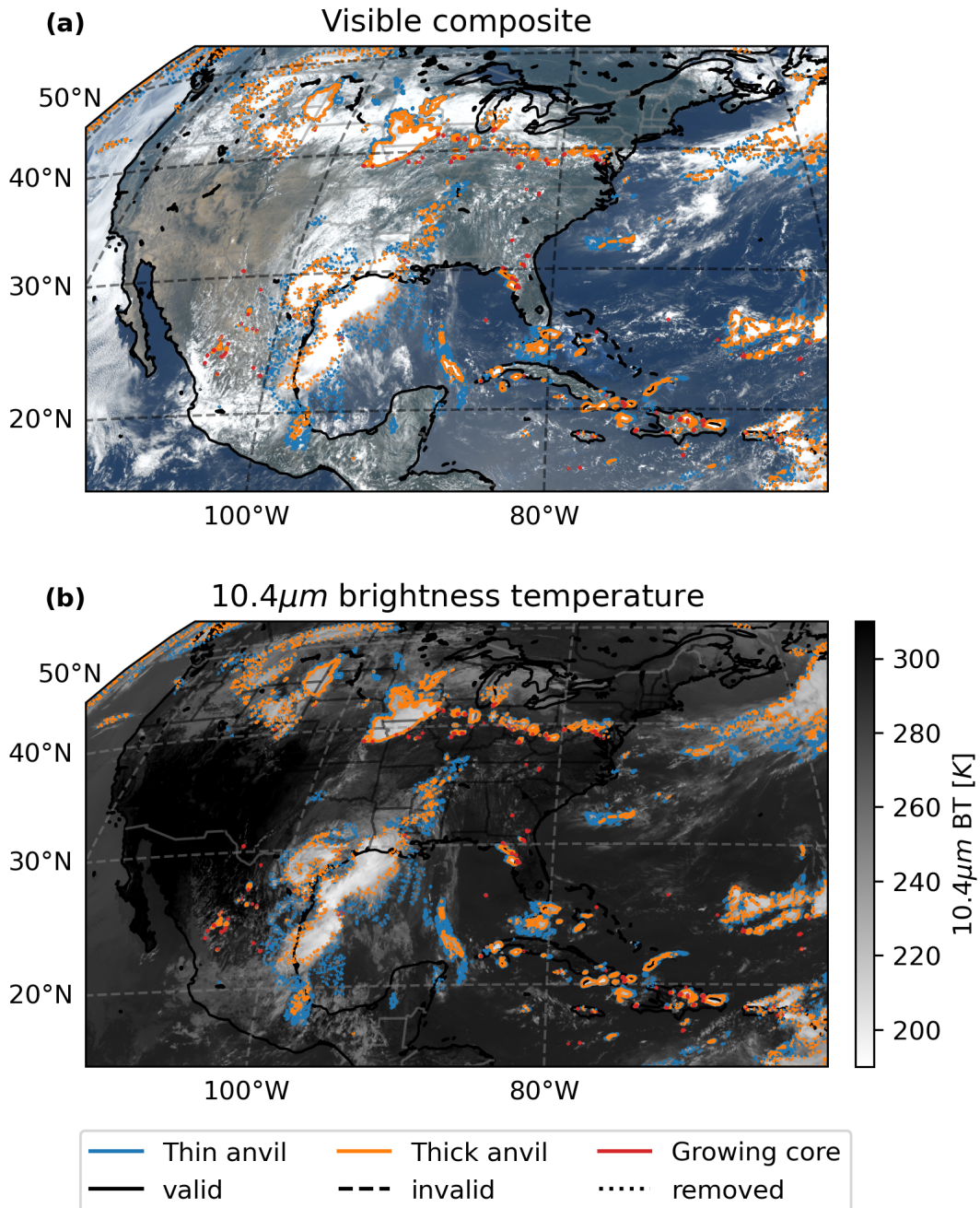


Figure 3.2: Detected cores and anvils from a snapshot of GOES-16 CONUS domain observations. Cores and anvils removed from the aggregated dataset are shown with dotted outlines. Those which are flagged as invalid are shown with dashed outlines. Detected features are shown against (a) visible composite imagery and (b) 10.4  $\mu$ m BT

1750 **3.4 Results**

**3.4.1 Distributions and properties of developing convective cores**

To begin, we investigate the distribution of detected DCC cores throughout the dataset. In fig. 3.3 we plot the distribution of observed cores over North America separated by season. Large variations in the spatial distribution of cores can be observed across the different seasons. Overall, in winter and spring (fig. 3.3 a,b) we see lower rates of the observed DCCs than in the summer and autumn (fig. 3.3 c,d).

In winter (fig. 3.3 a) the majority of convection observed occurs over the ocean, particularly in the areas of the Gulf of Mexico and West Atlantic associated with warm currents. In spring (fig. 3.3 b) we see a similar pattern over the ocean, however there is also an increase in convection detected over land in the Caribbean, Mexico and the central and southern USA. In summer (fig. 3.3 c) we see a large increase in convection over land and ocean, with the highest rates of convection of any season. In particular, we see high rates of convection over Mexico, the Caribbean, the southern USA (Florida in particular) and adjacent ocean regions. In Autumn (fig. 3.3 d), we see a large reduction in the number of convective cores detected over land regions. The number of detections over the ocean remains high, however, indicating a possible lag in the seasonal cycle of convection over oceans compared to that over land.

Figure 3.4 shows the proportion of cores detected in each month over the annual cycle for land and sea regions. Both land and sea regions show a peak of convective activity in the summer, and a low in the winter months. However, as suggested by fig. 3.3, there is a time lag of about 1 month between the annual cycle of convection over land and that over the ocean, likely due to the time lag in ocean heating. Comparing between the tropics and mid-latitudes, we see that the monthly distribution of convection is much more sharply focused on July–August in the mid-latitudes compared to the broader distribution seen in the tropics.

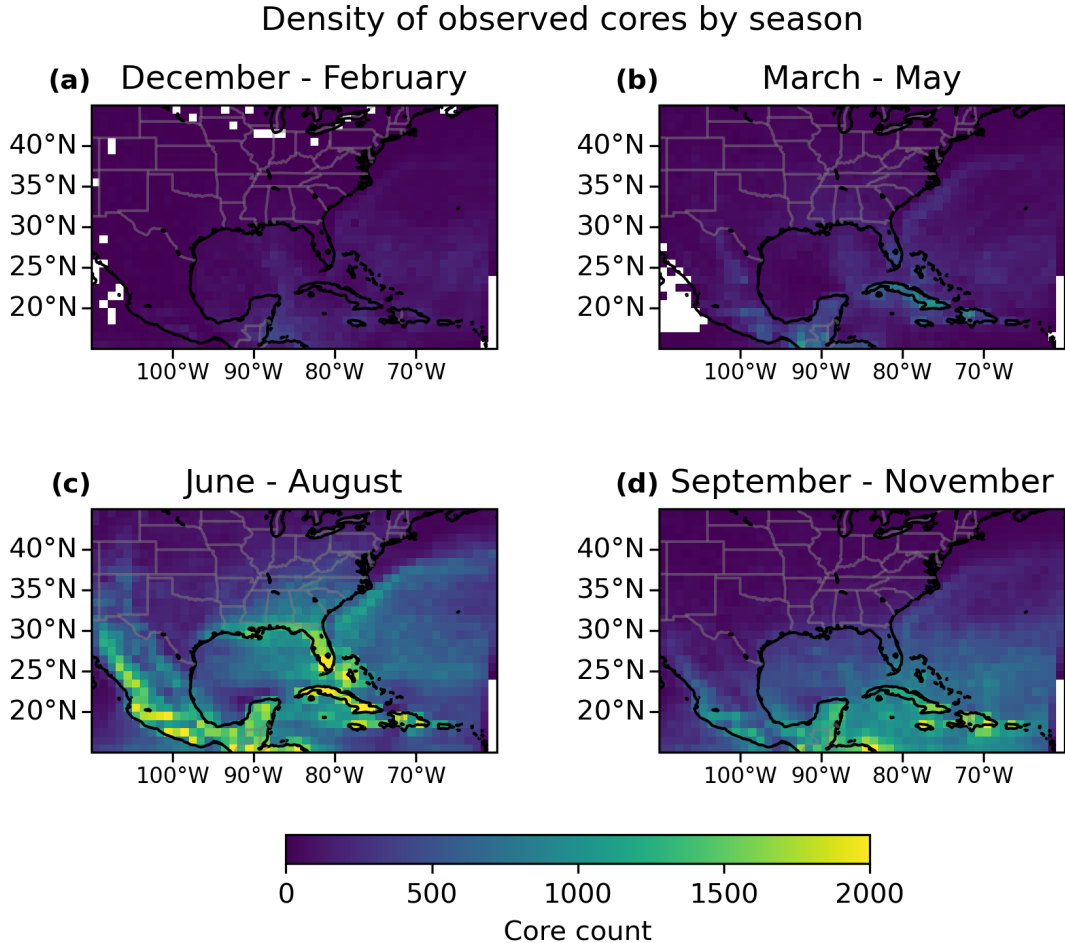


Figure 3.3: The spatial distribution of observed cores, broken down by season and accumulated into  $1 \times 1^\circ$  grid boxes of latitude and longitude. The density of observed cores is greatest during summer (c) and smallest during winter (a).

Figure 3.5 shows the average speed of propagation for cores observed in each 1-degree grid box, with the average direction of propagation shown by arrows for each 2-degree grid box. We see a clear change in the direction of propagation from 1780 an easterly motion in the tropics (below  $25^\circ\text{N}$ ) to a south-westerly motion in the mid-latitudes.

Figure 3.6 displays the mean lifetime of observed cores over each 1-degree box of latitude and longitude. We define the lifetime as the period of time over which we detect each core, which represents the time in which the core is developing vertically.

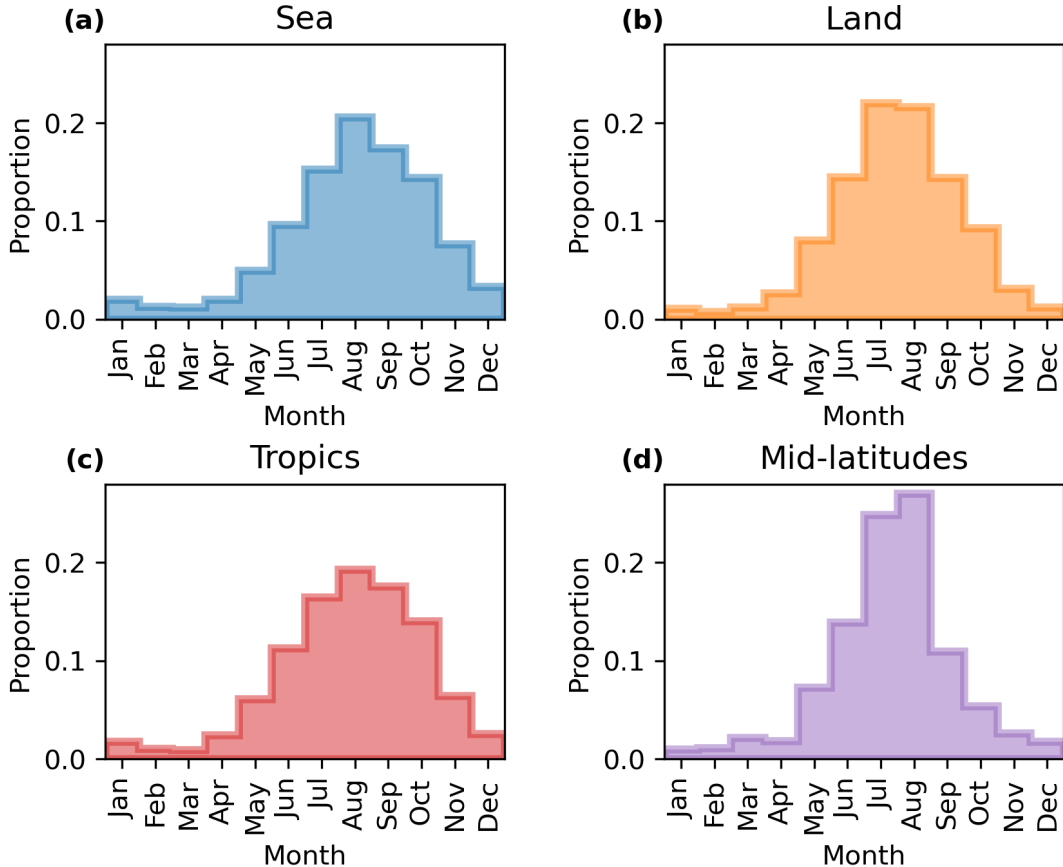


Figure 3.4: Monthly distributions of the proportion of cores detected each month over (a) sea, (b) land, (c) tropics ( $<30^{\circ}\text{N}$ ) and (d) mid-latitudes ( $>30^{\circ}\text{N}$ ).

1785 Convection will continue in the core after this point, but the motion of the cloud top will instead be a horizontal divergence of the anvil. The average lifetimes appear mostly uniform across the domain, with a small reduction with increasing latitude. This reduction in the lifetime of the developing core at higher latitudes is likely due to the lower tropopause height restricting the vertical development of the cores.  
 1790 Similarly, we see a slight reduction in average lifetime over the more mountainous, inland regions of Mexico compared to the adjacent coastal regions. This again may be linked to the reduction in the depth of the convective cores, although in this case due to an increased surface height rather than a lower tropopause.

Figure 3.7 shows the average cooling rate of observed cores. The contrasts here

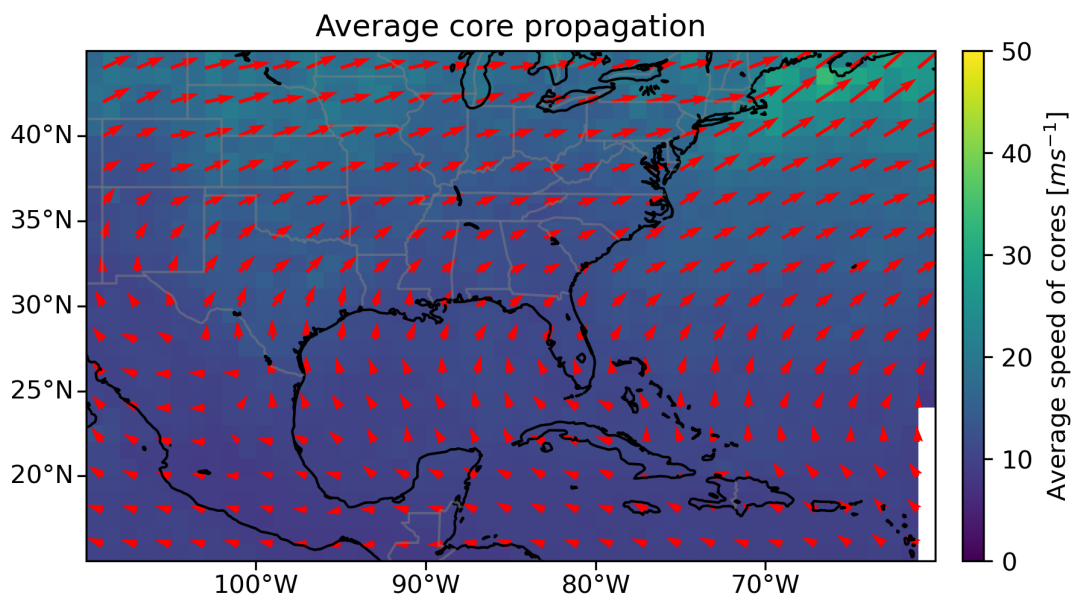


Figure 3.5: The average speed and direction of propagation of cores observed within each  $1 \times 1^\circ$  grid box. The colouring shows the average speed of propagation, and the red arrows show the average direction for each  $2 \times 2^\circ$  grid box

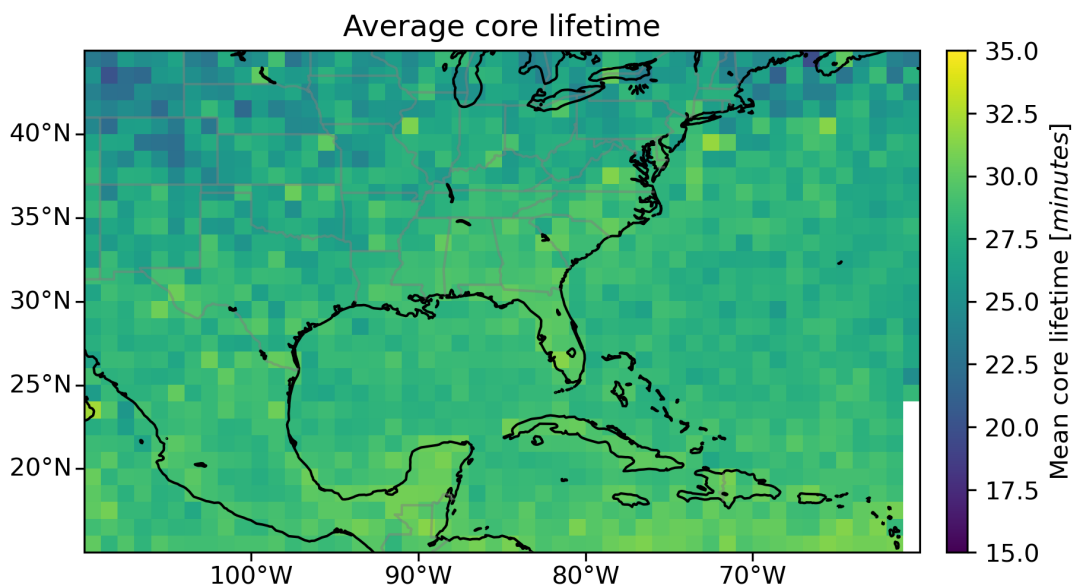


Figure 3.6: A map showing the mean lifetime in minutes of cores within each  $1 \times 1^\circ$  grid box.

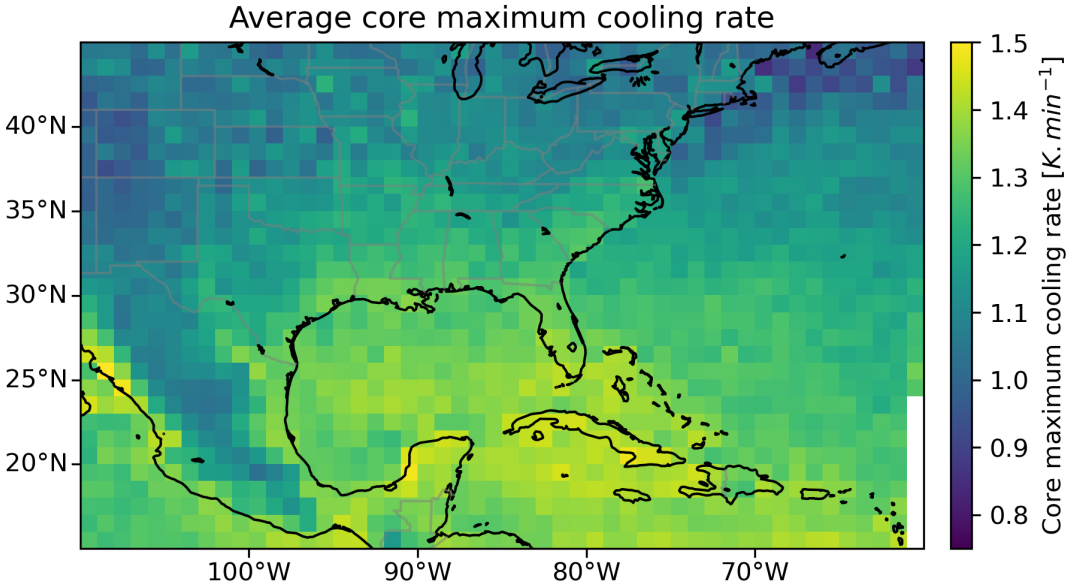


Figure 3.7: A map of the average maximum core cooling rate for each  $1 \times 1^\circ$  grid box.

1795 are more pronounced than those shown in fig. 3.6. We see a reduction in the average cooling rate with latitude, likely due to the reduction in solar heating and hence lower CAPE. Orography also has a factor, with lower cooling rates observed over the mountains of Mexico and the North American Rockies. We see the largest average core cooling rates in coastal regions, indicating potential land–sea interactions.

1800 Figure 3.8 shows the distributions of lifetime (fig. 3.8 a), maximum area (fig. 3.8 b), cooling rate (fig. 3.8 c), and minimum BT (fig. 3.8 d). We see a peak in the observed lifetime of cores between 15 and 20 minutes, with a large tail extending beyond 60 minutes in some cases. Note that due to the requirement of a minimum of three consecutive observations, cores lasting less than 10 minutes will not be detected, truncating the distribution. In fig. 3.8 b we see a peak in the maximum core area of around 1805 150–200 km<sup>2</sup>, representing cores approximately 12–14 km in diameter. Figure 3.8 c shows that the core cooling rate peaks at values of 1–1.25 K minute<sup>-1</sup>, representing vertical cloud top velocities of approximately 2.5–3 ms<sup>-1</sup>. The distribution is slightly truncated by the requirement for detected cores to have a cooling rate of atleast

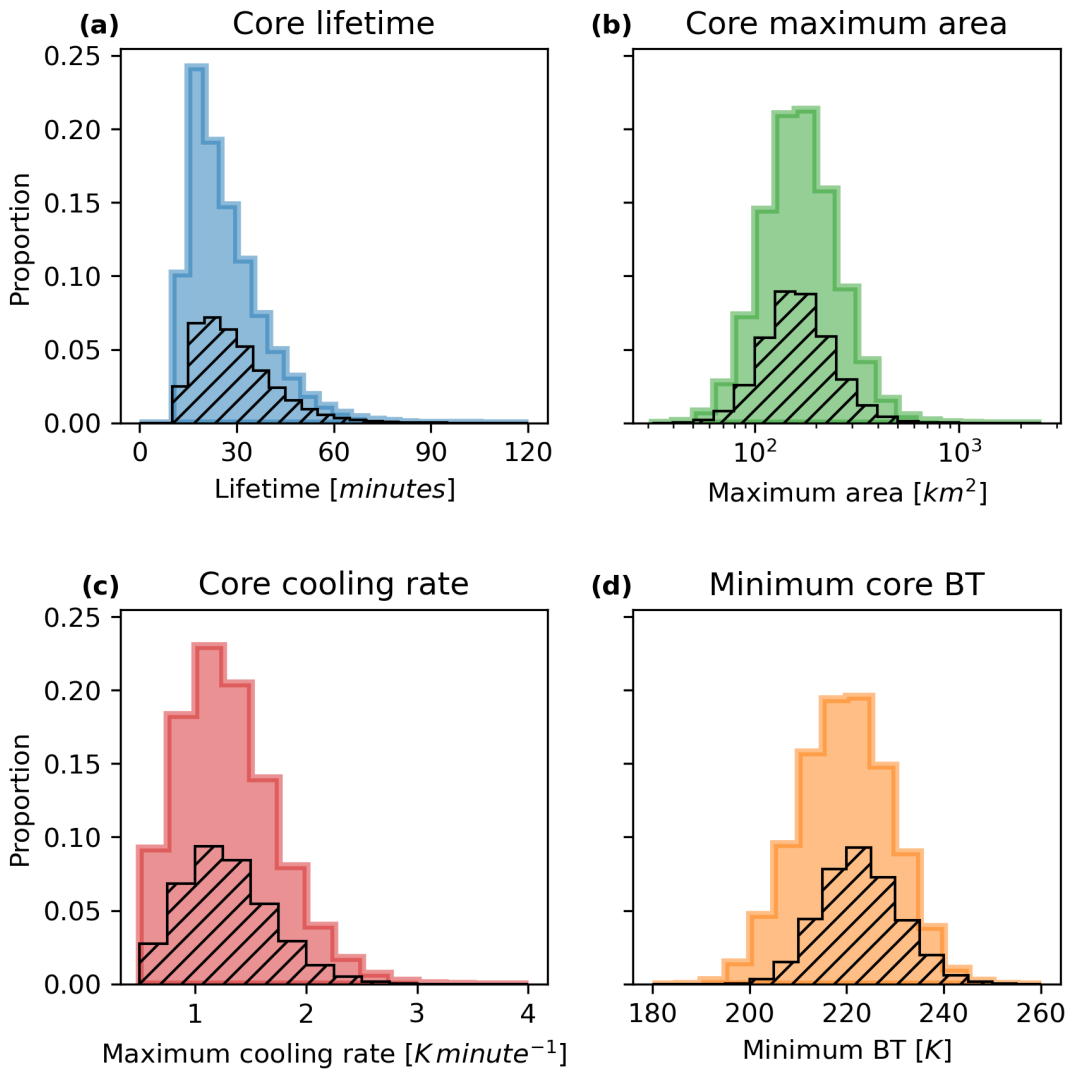


Figure 3.8: Histograms showing the distributions of observed (a) core lifetime, (b) maximum area, (c) maximum cooling rate, (d) and minimum BT. The hatched areas show the proportion of each distribution consisting of the initial detected cores within each tracked DCC.

<sub>1810</sub>  $0.5 \text{ K minute}^{-1}$ . Finally, the minimum core BT (fig. 3.8 d) peaks around 220 K, the temperature of the radiative tropopause [Jeevanjee and Fueglistaler, 2020]

The hatched areas in fig. 3.8 show the proportion of each distribution consisting of the initiating cores of tracked DCCs. For these initiating cores the possibility of the observations being masked by an overlaying anvil cloud, and so we expect these <sub>1815</sub> to provide the most complete measurements of the properties of the developing core. For the lifetime, maximum area and cooling rate these show close similarities to the shape of the distribution for all cores, indicating that masking due to anvils does not significantly effect our ability to observe the core properties. For the minimum core BT, we see that the initial cores tend to have warmer BT than later cores, indicating <sub>1820</sub> an increased presence of cold cores and overshooting tops in organised convection.

In fig. 3.9 we show how the mean core lifetime, maximum area, cooling rate and BT vary between different regions. There is little difference in the mean core lifetime between regions, echoing the results seen in fig. 3.6. Maximum core area is larger over land than sea, and larger in the mid-latitudes than in the tropics. We see little <sub>1825</sub> difference in the cooling rate between sea and land, but on average cores in the tropics cool  $\sim 0.2 \text{ K minute}^{-1}$  faster than those in the mid-latitudes. There is a small difference in the minimum BT of cores observed over land and ocean, with the former  $\sim 1.5 \text{ K}$  colder than the latter. A more noticeable difference is seen with latitude, with cores in the tropics having, on average, minimum BT  $\sim 5 \text{ K}$  colder than those in the <sub>1830</sub> mid-latitudes.

Overall, fig. 3.9 show differences in core intensity between land and ocean, and between the tropics and mid-laitudes, with these differences most prominent in the minimum BT. However, these differences may result from changes in different properties of the cores as the difference in cooling rate between tropics and mid-latitudes <sub>1835</sub> is not seen when comparing sea and land.

Figure 3.10 a compares how the average lifetime of detected cores changes with

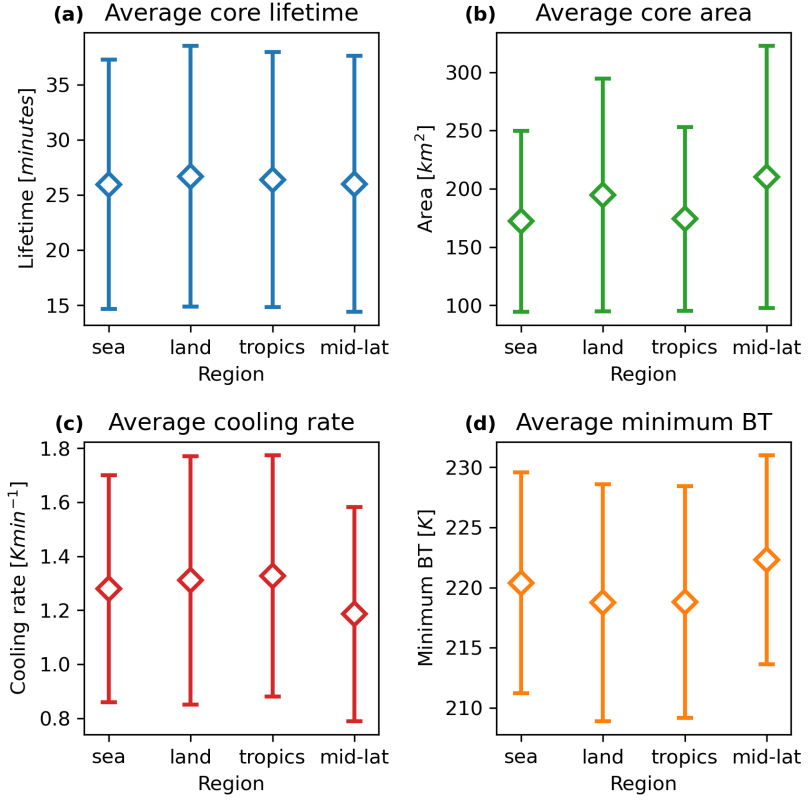


Figure 3.9: The mean observed (a) lifetime, (b) maximum area, (c) maximum cooling rate, (d) and minimum BT for cores detected over land, sea, tropics and mid-latitudes. Error bars show standard deviation of each point.

their maximum observed cooling rate. For low values of core cooling rate, we see a similar, positive linear relationship between cooling rate and lifetime between all regions, indicating that more intense convection leads to longer periods of cores being observed. However, beyond cooling rates of around  $1.5 \text{ Kmin}^{-1}$  we see an inflection in the relationship, with larger cooling rates leading to shorter lifetimes. This may be explained by the cores with faster cooling rates reaching their level of neutral buoyancy faster, and therefore showing cooling cloud tops for a shorter period of time. The inflection in the core lifetime may also explain why we do not see differences in average lifetime between different regions, despite changes to other convective properties.

Figure 3.10 b shows how the minimum BT changes with the maximum cooling rate of the core. Unlike fig. 3.10 a, we see a continuous decrease in BT with core

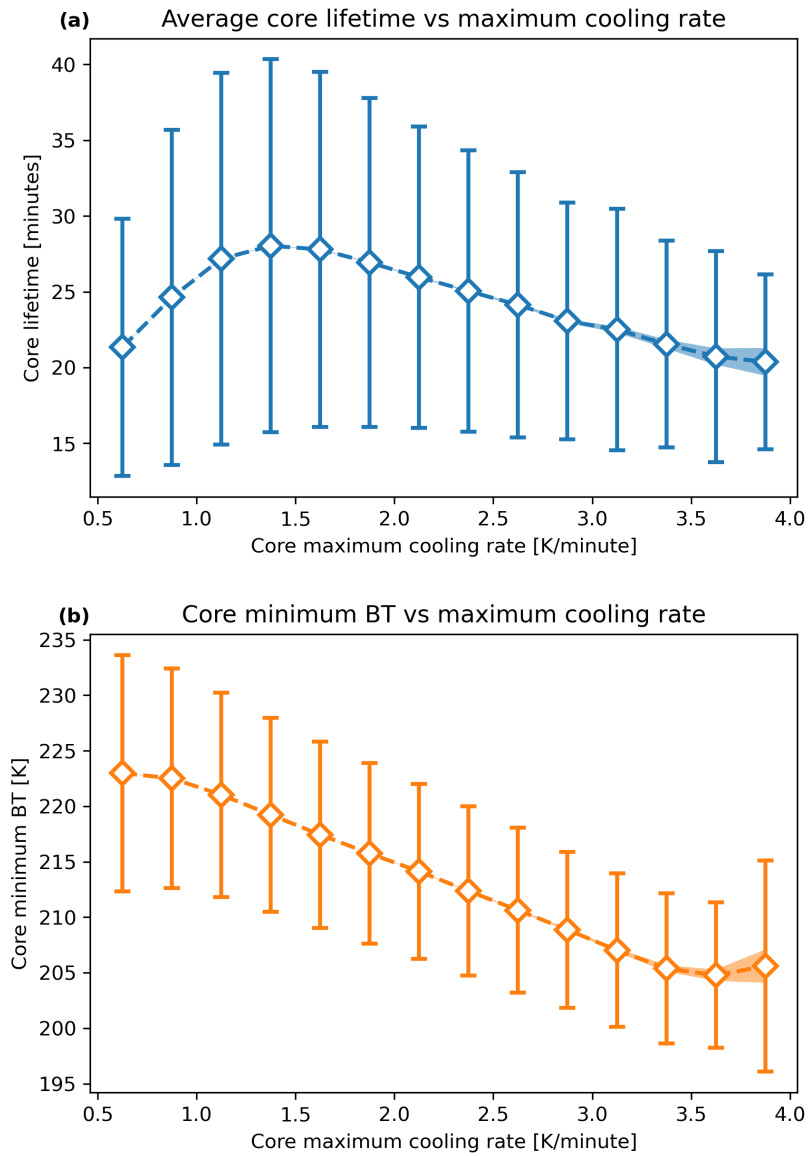


Figure 3.10: Average core lifetime (a) and minimum BT (b) with increasing core cooling rate. Error bars show the variance of the data, while the shaded area shows the standard error of the mean.

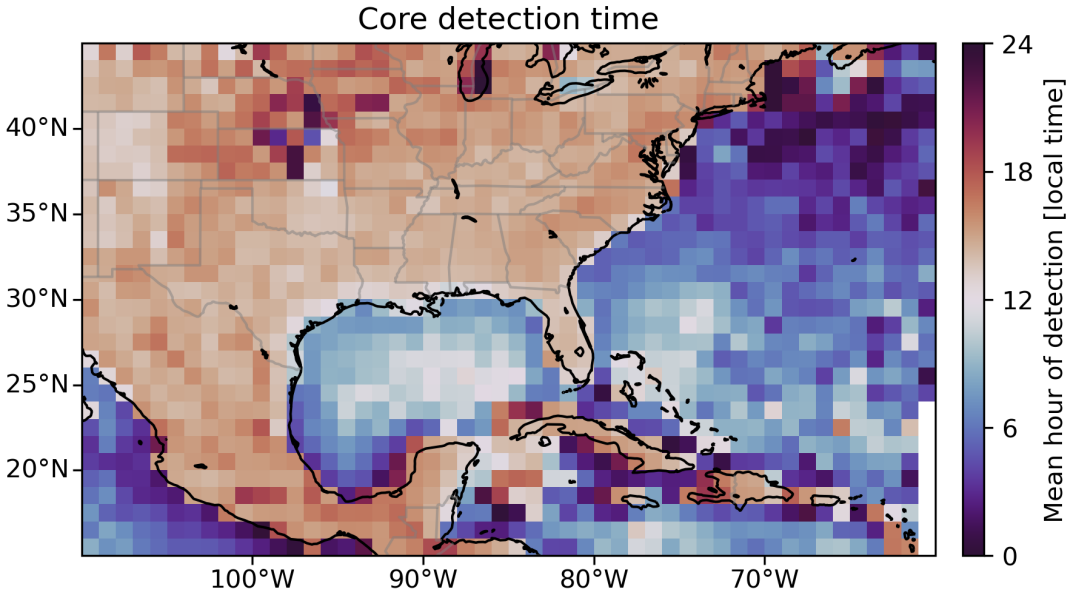


Figure 3.11: The average time of day of initiation of cores observed within each  $1 \times 1^\circ$  grid box. The time of initiation is calculated as the local solar time based on longitude, and the mean is calculated as the circular mean over a 24-hour period to account for the cyclical aspect of the hour of day.

cooling rate, indicating that faster cooling rates tend to result in cores with colder CTT and hence higher CTH. Figure 3.10 b also provides context for the results seen  
 1850 in fig. 3.10 a. If we assume that cores are detected around the freezing level (273 K), then we see that the overall temperature change over the core lifetime ranges from ~45 K for the least intense cores to ~65 K for the most intense cores. Although this continues to increase with cooling rate, the proportional change is less than that of the core cooling rate itself. As we can approximate the core lifetime as the core BT  
 1855 change divided by the cooling rate, the larger proportional change in cooling rate will result in a shorter lifetime for more rapidly cooling cores.

### 3.4.2 Diurnal cycle of convective cores

In fig. 3.11, we show the mean time of detection for cores detected within each 1-degree grid square. The most notable feature in fig. 3.11 is the strong land-sea contrast,

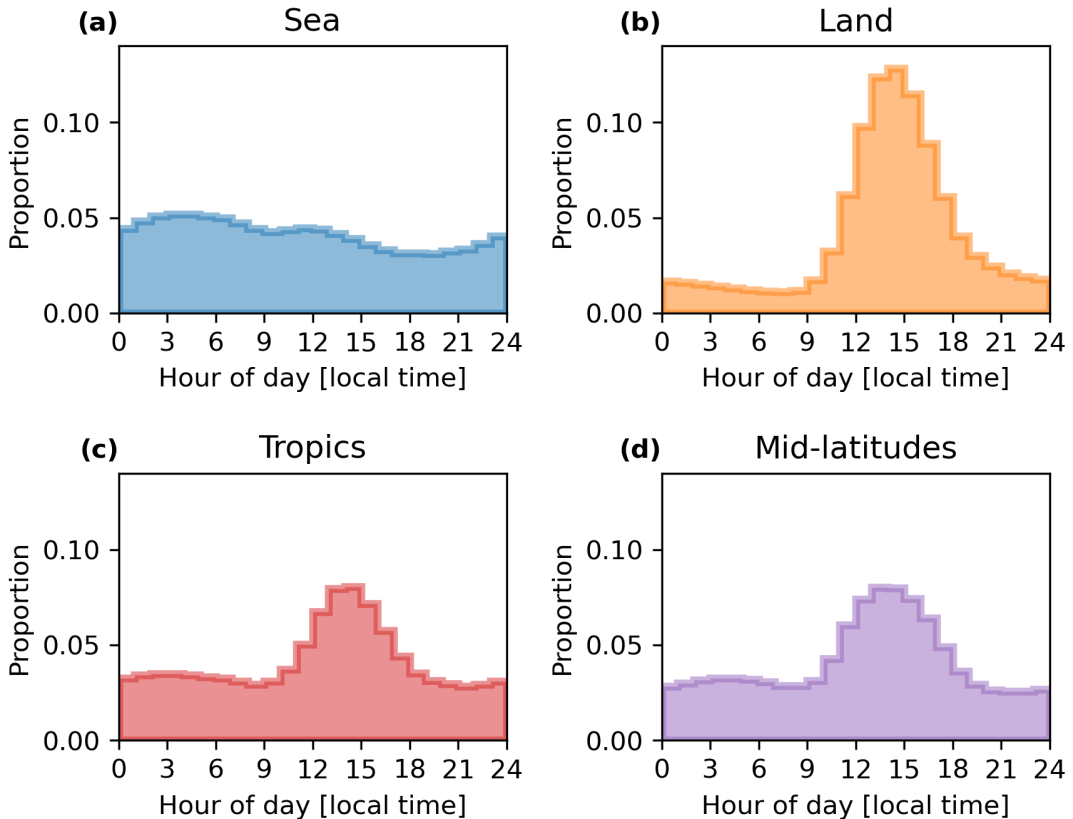


Figure 3.12: The diurnal distributions of the local time of detection for cores, binned by hour detected over (a) sea, (b) land, (c) tropics ( $<30^{\circ}\text{N}$ ) and (d) mid-latitudes ( $>30^{\circ}\text{N}$ ).

with the majority of land regions showing convective activity occurring during the afternoon, and the majority of ocean regions showing activity before midday. In addition, we see a few major features of the detected time of initiation across both land and sea regions. In coastal regions in the Gulf of Mexico and the Caribbean Sea, we see earlier initiation times closer to coastlines, while regions further from land have average times of detection closer to midday. Over the land, we also see a later time of initiation over the Northern Great Plains ( $90\text{--}100^{\circ}\text{W}$ ,  $37\text{--}47^{\circ}\text{N}$ ).

Figure 3.12 shows the distribution of core detections across the diurnal cycle for land, sea, tropics and mid-latitude regions. Over land, we see a sharp peak in convective activity initiating in the mid-afternoon between 2 and 3 pm, with a tail ex-

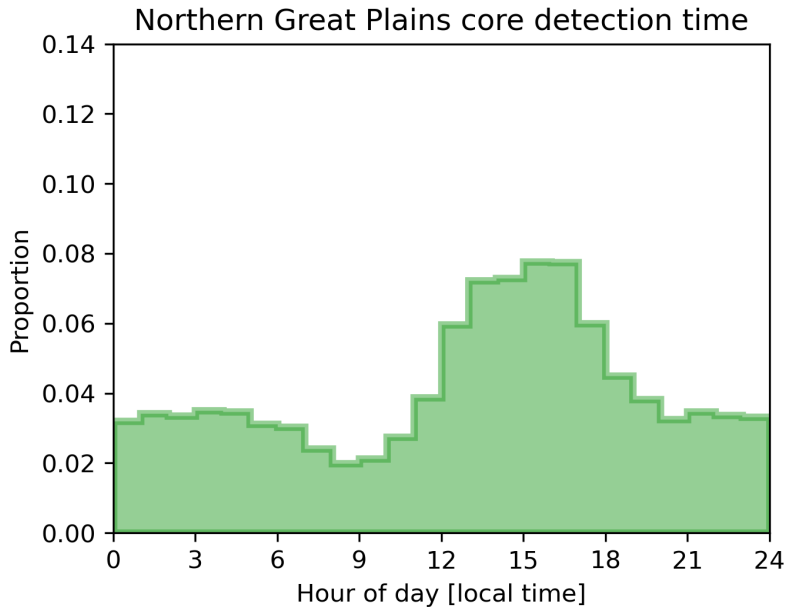


Figure 3.13: The diurnal distribution of cores detected in the NGP region ( $37\text{--}45^\circ\text{N}$ ,  $90\text{--}100^\circ\text{W}$ ).

tending into the night-time. Over the sea, the distribution of core detections is much more uniform across the diurnal cycle. There is still a peak observed in the early hours of the morning (3–6 am), and a low in the evening (6 pm), but the difference between these is much less pronounced than that over land. Both the tropics and mid-latitudes have peaks in convection at the same time as that seen for all land regions in fig. 3.12 b. The peak for mid-latitudes is slightly broader however, with more convection occurring later in the day.

In fig. 3.11 we saw a noticeably later average time of detection over the Northern Great Plains (NGP) region. Figure 3.13 shows how the diurnal distribution of core detection time varies within this area, which we define as  $37\text{--}45^\circ\text{N}$ ,  $90\text{--}100^\circ\text{W}$ . In contrast to the distribution seen over all land regions in fig. 3.12 b, the NGP region shows a later peak of convective activity between 3 and 4 pm, as well as much higher rates of convection observed during the nighttime and into the early morning until around 7 am. Previous studies have found a similar bimodal distribution in convective

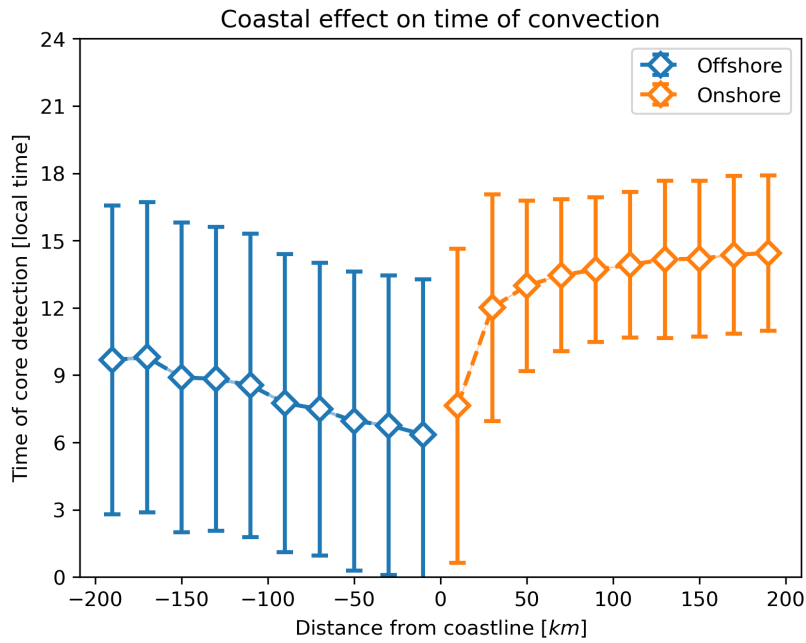


Figure 3.14: The change in average time of core detection with distance from the coastline. Negative distances along the x axis show cores detected further to sea, and positive distances show cores detected further inland. Error bars show the circular standard deviation of the local solar hour of detection.

precipitation over the NGP Li et al. [2021].

In fig. 3.14 we examine the effect of the distance to the coast on core detection time over the Gulf Coast region ( $22.5\text{--}32.5^\circ\text{N}$ ,  $82.5\text{--}100^\circ\text{W}$ ). Negative distances indicate locations further offshore, and positive distances those locations further inland. In fig. 3.11 we saw a change in the average time of detection of cores in locations closer to the coast, and that effect is shown again here. For cores detected over the sea, we see a linear decrease in the average time of detection as the distance to the coast increases. For cores detected over land, we see a sharp decrease in the time of detection very close to the coast, however further than 50 km from the coast this becomes a shallower linear gradient. The linear change of core detection time with distance from the coastline may be linked to offshore and onshore breezes triggering convection. For cores over land, we see a reduction in the variance of the time of detection between

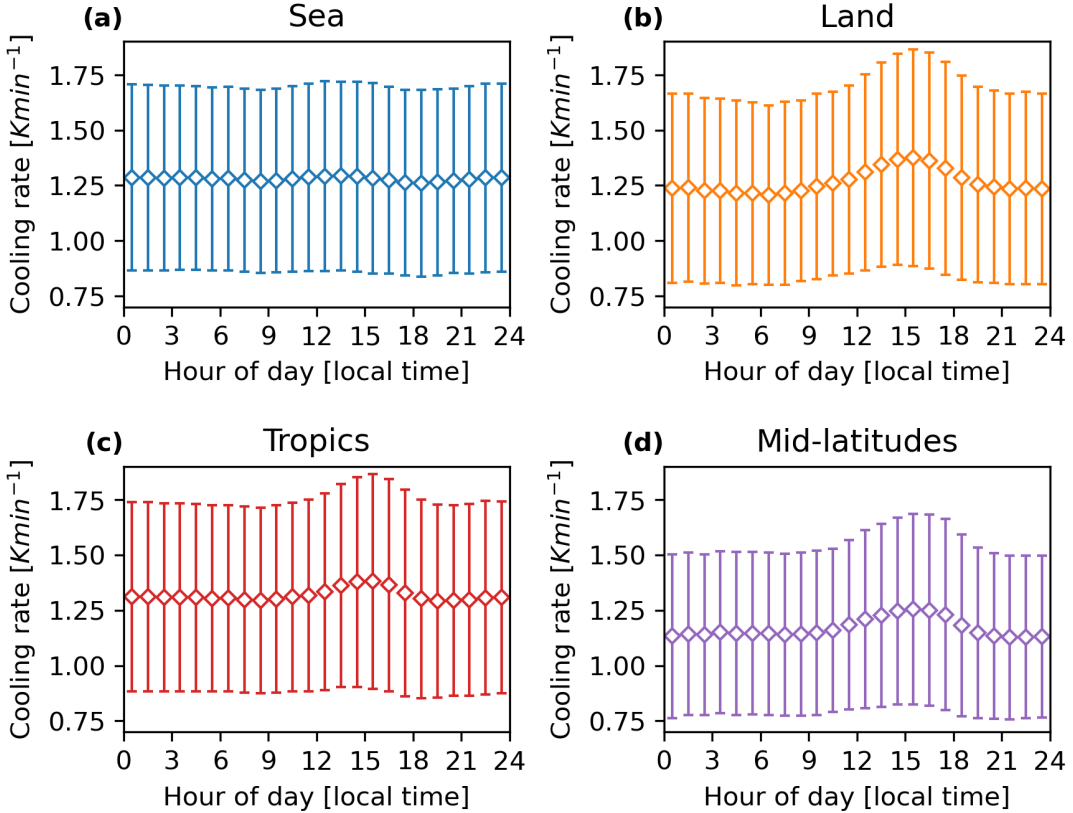


Figure 3.15: The diurnal cycle of the maximum cooling rate of cores detected over (a) sea, (b) land, (c) tropics ( $<30^{\circ}\text{N}$ ) and (d) mid-latitudes ( $>30^{\circ}\text{N}$ ). Each point shows the mean of the maximum cooling rate of cores detected during that hour. Error bars show the standard deviation of maximum cooling rate.

50 and 150 km from the coast, which may also indicate that an external forcing from sea breeze is triggering convection in these areas, and hence constraining the time of initiation of convection.

Figure 3.12 shows how the mean maximum cooling rate of cores changes across the 1900 diurnal cycle. While over sea there is little change in cooling rate, over land there is a noticeable increase in the cooling rate throughout the daylight hours. This leads to a peak at around 4 pm, before cooling rate falls back to its nighttime levels which are lower than that seen over ocean. Both tropics and mid-latitudes show similar diurnal cycles to land, albeit with a difference of  $0.2\text{ Kmin}^{-1}$  across the entire diurnal cycle.

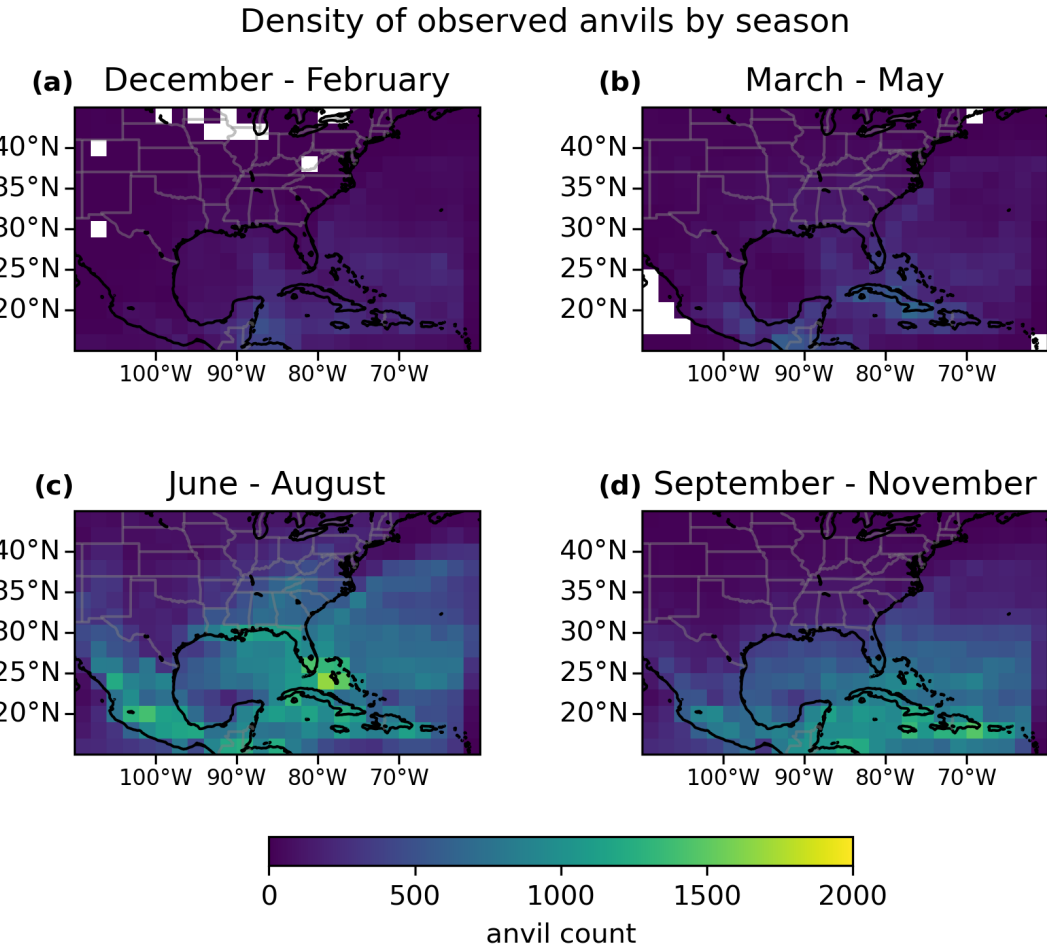


Figure 3.16: Maps showing the spatial distribution of observed anvils for (a) winter, (b) spring, (c) summer and (d) autumn, each binned to a  $2 \times 2^\circ$  grid.

### <sup>1905</sup> 3.4.3 Distributions and properties of observed anvil clouds

In this section, we examine the properties of anvil clouds detected in our dataset.

Anvils are detected and tracked independently from cores. Although they must be associated with observed cores at the start of their lifetime, we continue tracking the anvils beyond the extent of the observed core lifetime. This also allows us to detect

<sup>1910</sup> anvils that are associated with multiple cores, providing insight into the effects of convective organisation.

Figure 3.16 shows the counts of anvils for each  $2 \times 2^\circ$  grid box, separated by season.

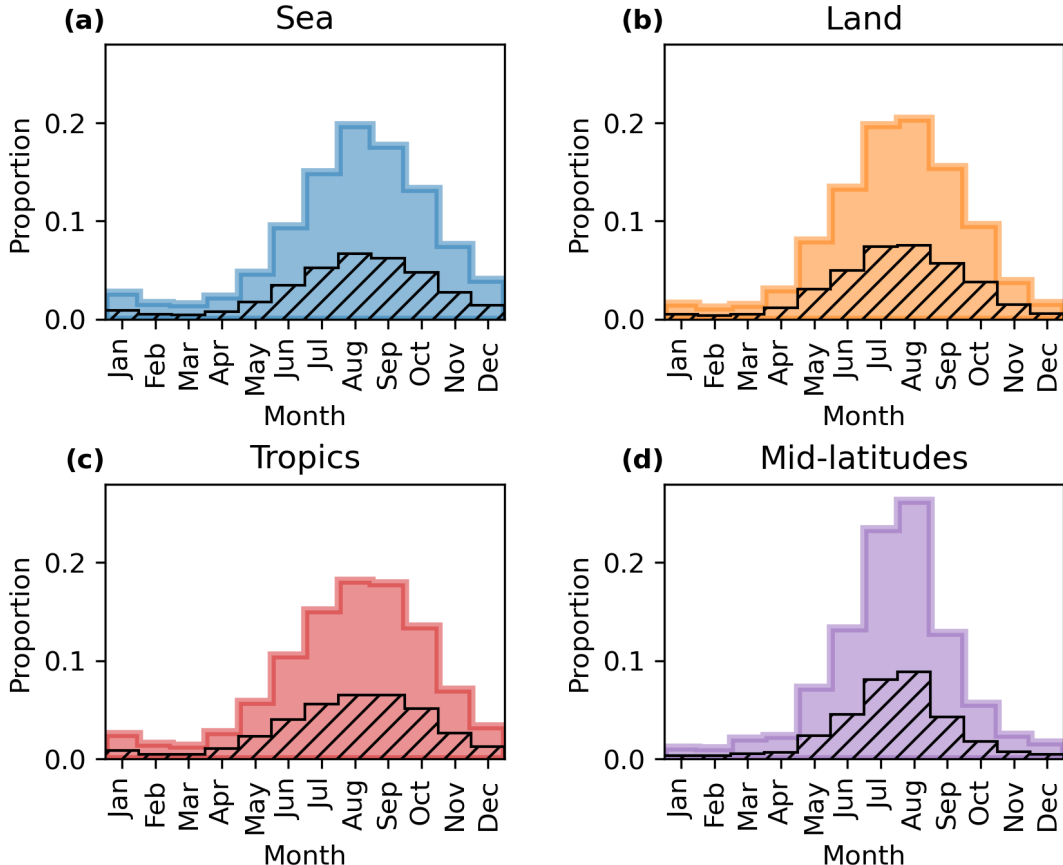


Figure 3.17: Monthly distributions of the proportion of cores detected each month over (a) sea, (b) land, (c) tropics ( $<30^{\circ}\text{N}$ ) and (d) mid-latitudes ( $>30^{\circ}\text{N}$ ). The hatched area shows the proportion of the distribution consisting of anvils with multiple cores.

We see a similar seasonal cycle and distribution to fig. 3.3. In winter (fig. 3.16 a) and spring (fig. 3.16 b) we see low rates of convection, with the majority of convection observed over warm ocean regions. In summer (fig. 3.16 c), we see the highest rates of anvil detections, with a large increase in the observations of anvils over land. In spring (fig. 3.16 d), the number of anvils observed over the ocean remains high, but that over land reduces.

Figure 3.17 shows how the annual distribution of anvil detections changes by month across different regions. Similarly to the annual distribution of cores shown

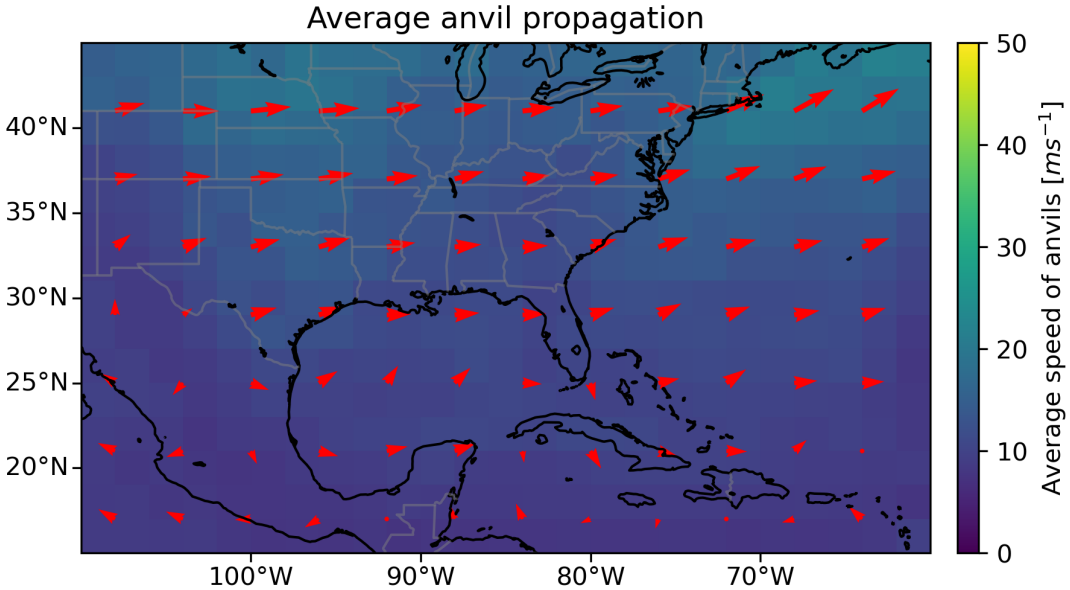


Figure 3.18: The average speed and direction of propagation of cores observed within each  $2 \times 2^\circ$  grid box. The colouring shows the average speed of propagation, and the red arrows show the average direction of propagation for each  $4 \times 4^\circ$  grid box

in fig. 3.4, we see a later peak over oceans of August–September compared to July–August over land. The mid-latitudes have a sharper peak around these two months, while the tropics show a broader distribution of anvil detections throughout the year.

Figure 3.18 shows the average propagation speed and direction for anvils in the same manner as shown for cores in fig. 3.5. In the extra-tropics ( $>30^\circ\text{N}$ ), there is generally an westerly motion, without the southerly motion seen in the cores. This westerly motion corresponds to the prevailing high level winds. The change in direction and differences in the speed of propagation between anvils and cores indicates a typical shear between the two. Over the tropics ( $<30^\circ\text{N}$ ), we see no clear overall motion.

Figure 3.19 a shows the average maximum area of anvils for each  $2 \times 2^\circ$  grid box. We again see a land–sea contrast in the Caribbean and Gulf of Mexico. The most notable change is the increase in anvil area as we move towards the North–West of

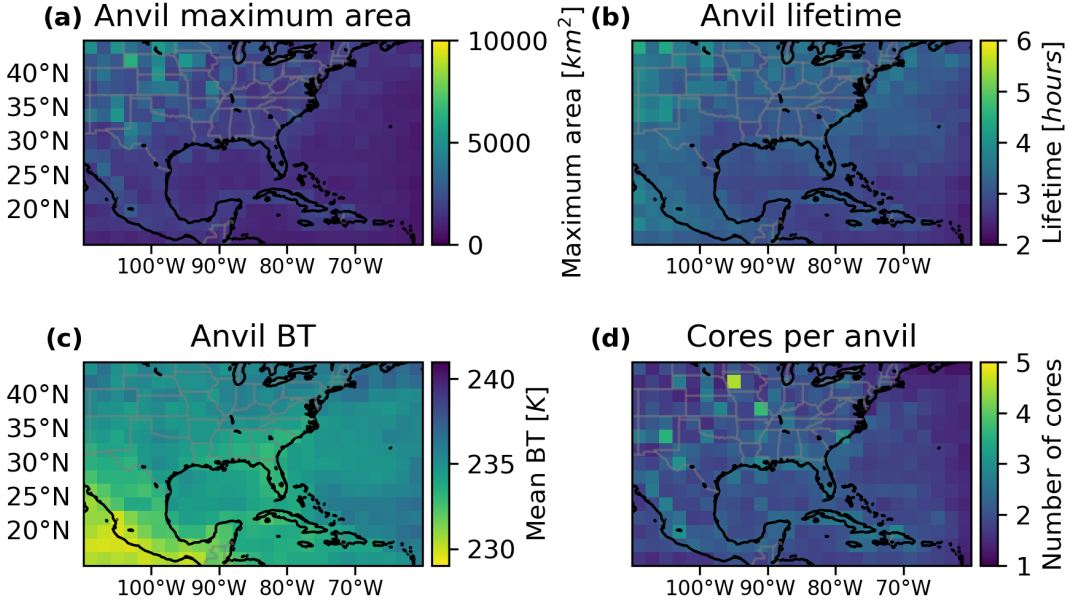


Figure 3.19: Maps showing the spatial changes in the averages of (a) anvil maximum area, (b) lifetime, (c) BT and (d) number of cores, binned to a  $2 \times 2$   $^\circ\text{grid}$ .

the domain. This correlates with the change in sensor zenith angle—and hence the  
 1935 area of each pixel—shown in fig. 3.1. It is possible that we are seeing a bias towards observing larger anvils due to the larger pixel area at larger zenith angles. However, previous studies have shown that this region is where most MCSs in North America originate from [Feng et al., 2019] which may also explain the large areas.

Figure 3.19 b shows the average anvil lifetime (in hours) for each  $2 \times 2$   $^\circ\text{grid}$  box.  
 1940 We see a similar, but smaller, trend towards longer lived anvils in the North-West of the domain as that seen for area in fig. 3.19 a. In addition, we see a tendency for average lifetimes over ocean to be shorter than adjacent land regions.

Figure 3.19 c shows the average BT of anvils in each grid box. We see an increase (warming) of BT with latitude over land. In addition, there is a land-sea contrast,  
 1945 with warmer BT over sea than land. The coldest average BT are observed over the Western coast of Mexico.

Figure 3.19 d shows the average number of cores associated with each anvil in each

grid box. Over the Caribbean, we see a noticeable land–sea contrast with an increase in the average number of cores over land, indicating that there is greater organisation of convection occurring there compared to over the sea. For the majority of land regions the average is reasonably noisy. This is primarily due to the presence of a small number of very large systems (including MCSs), which have a very large number of cores and hence introduce noise to the spatial average. In addition, we see a reduction in the average number of cores towards the edge of the map which is likely due to larger anvils being more likely to be removed from the dataset by the criteria in table 3.2.

In fig. 3.20, we show the distributions of anvil properties, with the proportion consisting of multiple-core anvils shown by the hatched area. The anvil maximum area distribution has a similar shape for both thick anvils (fig. 3.20 a) and thin anvils (fig. 3.20 b), with the mean shifted to large values for the thin anvil. It should be noted that the thin anvil area includes that of both thick and thin anvil regions, so will always be larger than that of the thick anvil alone. The anvil lifetime distributions for the thick (fig. 3.20 c) and thin (fig. 3.20 d) anvils show a similar relationship, with a shift of the distribution to longer lifetimes for the thin anvil. In both cases, despite the log scaling on the x-axis, we see a longer tail towards larger area values and longer lifetimes. Furthermore, this large tail consists primarily of multiple-core systems, as shown by the hatched area, indicating the impact of organisation on the area and lifetime of DCCs.

Figure 3.20 e and fig. 3.20 f show the average and minimum anvil BT over each detected anvil. The minimum anvil BT has a broader distribution than that of the average anvil BT. Multiple core anvils generally have colder anvil BT, particularly so for the minimum BT. The cold tail of the minimum BT, with values less than 200 K, indicates the presence of overshooting tops within these organised systems.

Figure 3.21 a, b, c and d the average of the thick anvil maximum area, thin anvil

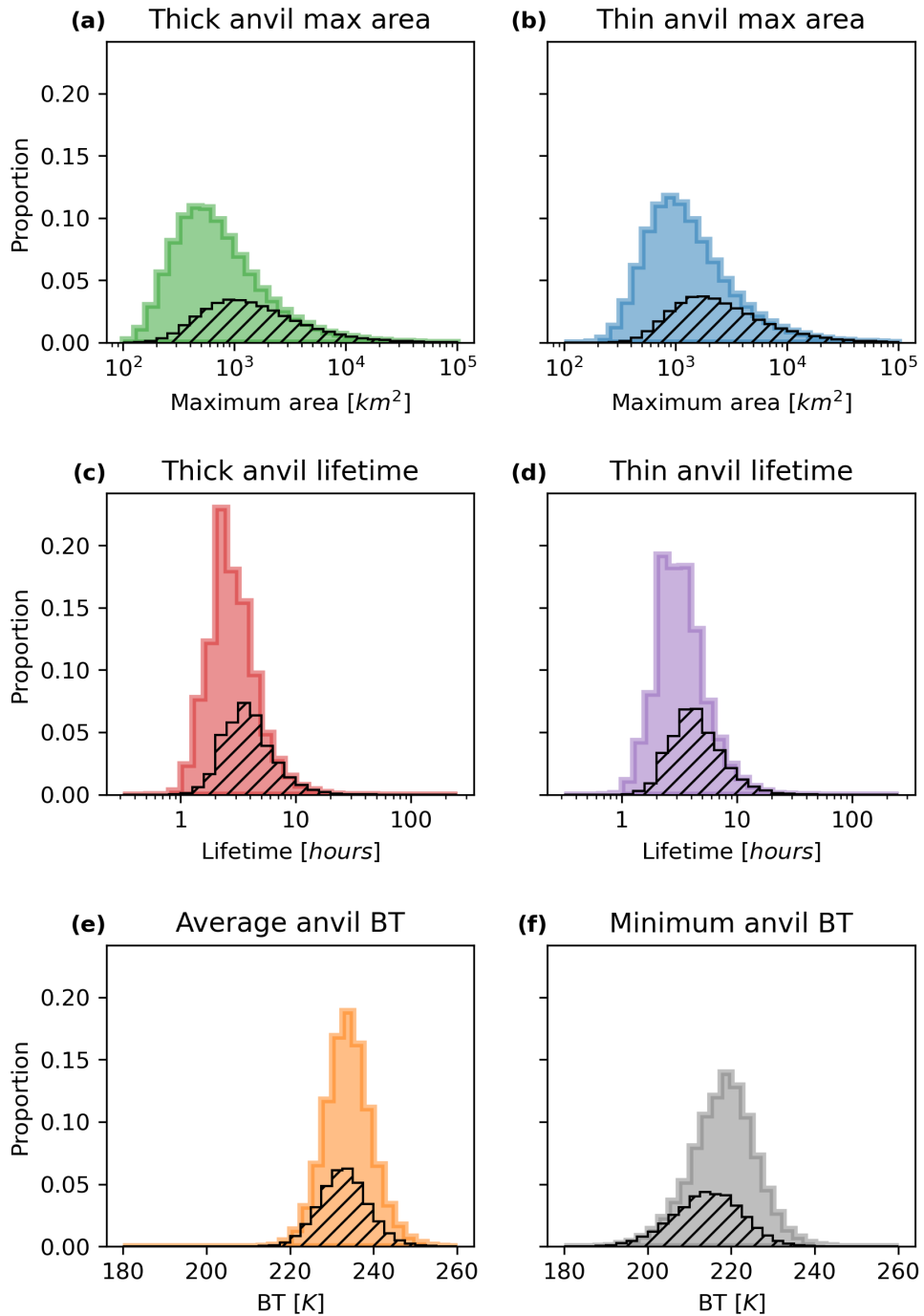


Figure 3.20: Histograms showing the distribution of observed anvil properties, with the hatched area showing the proportion associated with multiple core anvils. (a) The maximum area of the thick anvil cloud; (b) the maximum area of the thin anvil cloud (which includes both the thick and thin anvil regions); (c) the lifetime of the thick anvil and (d) the thin anvil; and (e) the average and (f) minimum observed BT within each anvil.

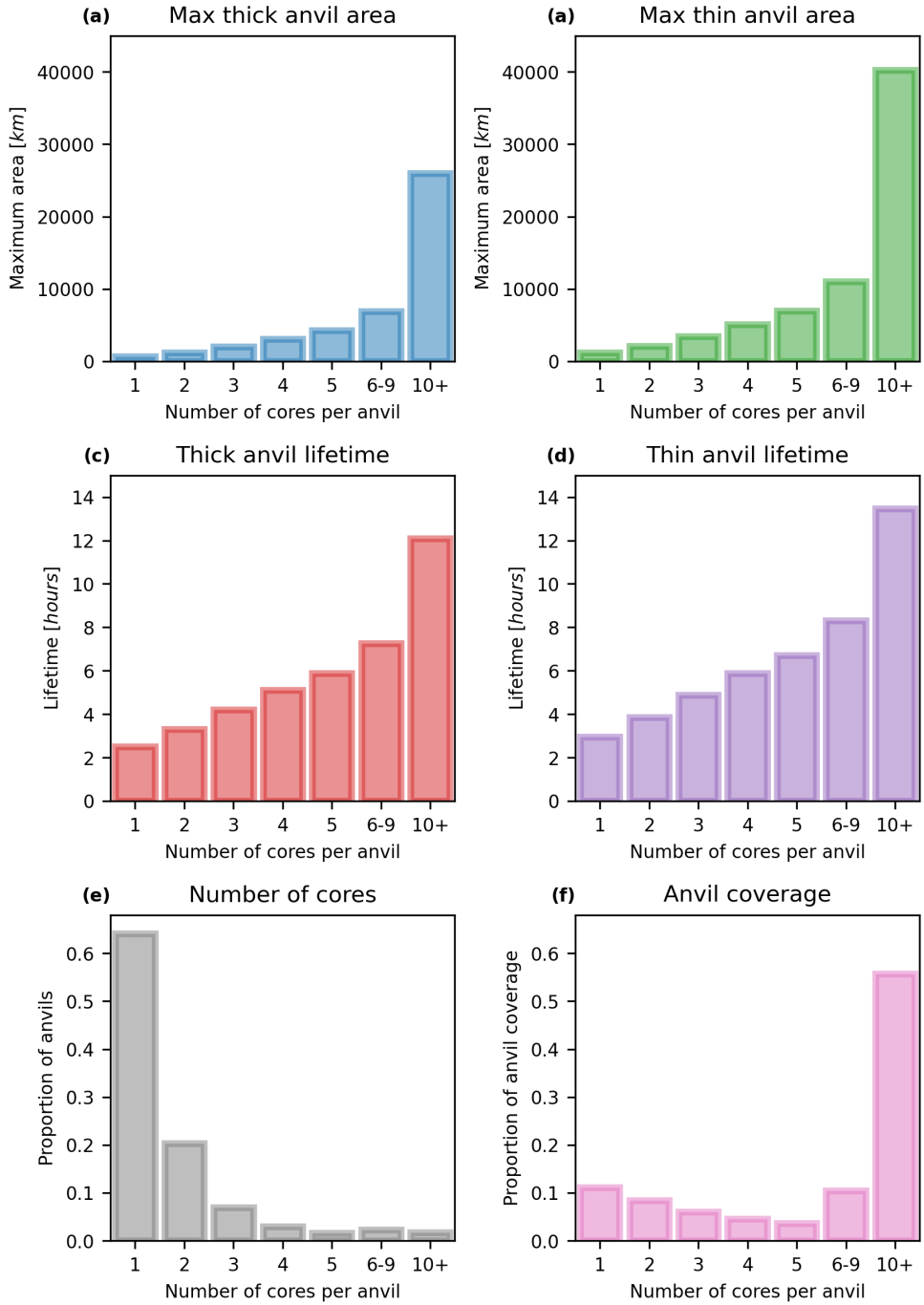


Figure 3.21: The change in the average area and lifetime of anvils with different number of cores. Mean values of (a) maximum thick anvil area, (b) maximum thin anvil area, (c) thick anvil lifetime and (d) thin anvil lifetime all increase with increasing number of cores. (e) The proportion of all anvils with different numbers of cores and (f) the fraction of total anvil coverage attributed to those anvils.

1975 maximum area, thick anvil lifetime and thin anvil lifetime for anvils with different numbers of cores. We see that in all cases these areas and lifetimes increase with increasing number of cores. In particular, the increase in number of cores has a large impact on the maximum area of anvils, The most organised systems, which contain 10 or more cores, have areas that are more than two orders of magnitude greater on  
1980 average than the anvils of isolated DCCs.

Figure 3.21 e and f show the distribution of the number of cores associated with each detected anvil, and the proportion of total anvil coverage attributed to anvils with different core counts respectively. Overall, the vast majority of anvils detected are isolated DCCs with only a single core. For anvils with greater than five cores,  
1985 the number of systems observed drops so low that we have decided to group these into bins of 6–9 cores and 10 or more to ensure that we have a representative sample size. Despite making up the majority of observed DCCs, single core systems only make up 12% of the total anvil coverage. Instead, despite being few in number, it is the most organised DCCs—those with ten or more cores—which are responsible  
1990 for the majority of anvil coverage due to their large area and lifetime. The large area and lifetime of these systems—seen in the long tails of those distributions in fig. 3.20—compound to result in this large coverage.

In fig. 3.22 we show how the averages of the maximum areas, lifetimes, BT and number of cores vary between different regions. We see that for both isolated and  
1995 multi-core convection, the average areas and lifetimes shown in fig. 3.22 a and b respectively are larger over land than sea, and in the mid-latitudes than in the tropics. For the anvil BT shown in fig. 3.22 c, we see that both the mean and minimum BT of anvils is colder over land than sea, and also colder in the tropics than in the mid-latitudes. DCCs over land tend to have more cores than those over sea, however is  
2000 is clear that as this differences also apply to isolated DCCs that they are connected to changes in the convective processes and anvil evolution in the different regions,

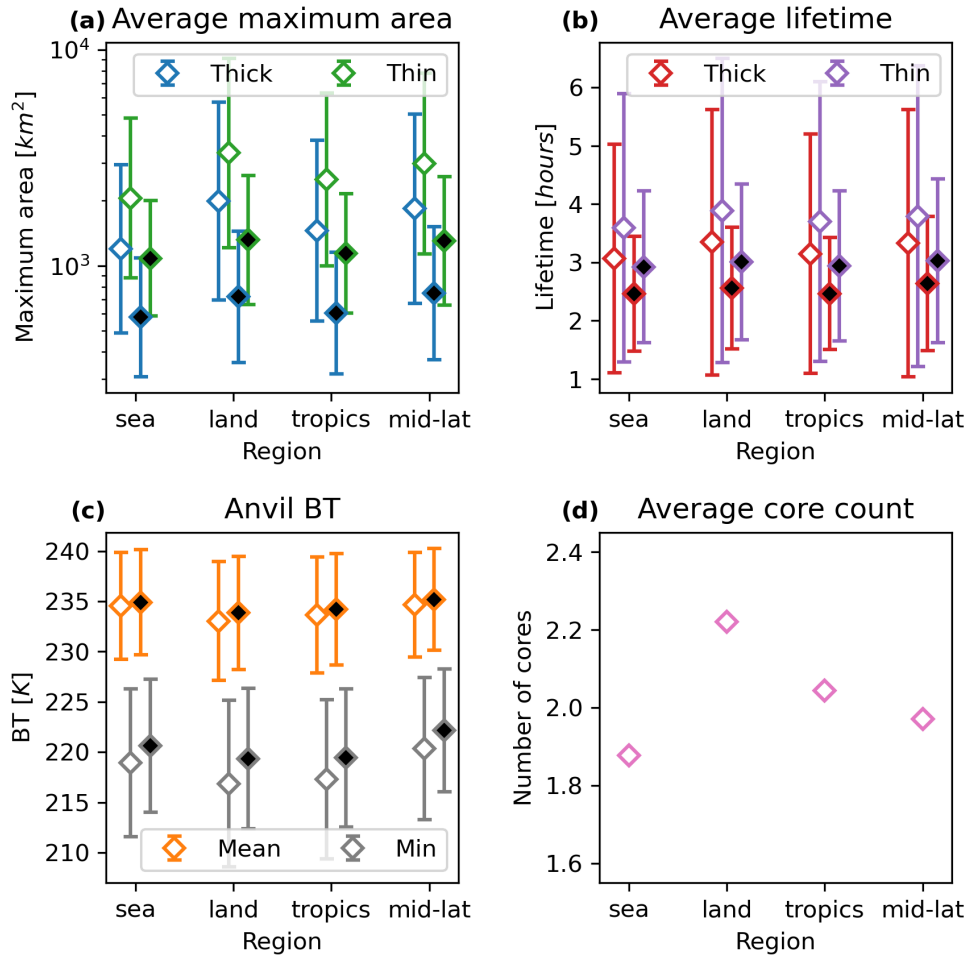


Figure 3.22: The change in the average (a) areas, (b) lifetimes, (c) BT and (d) number of cores of anvils observed over sea, land, tropics and mid-latitudes. The points with no fill show the average across all DCCs, whereas the points with the black fill show the average for isolated DCCs (with one core) only. Error bars show the standard deviation on the mean.

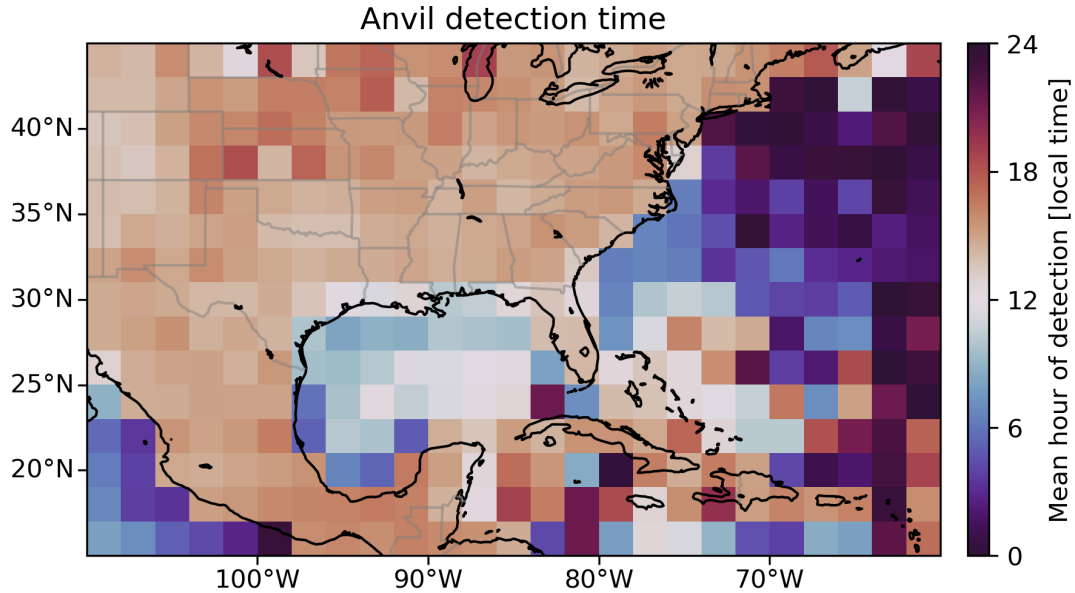


Figure 3.23: The average time of day of detection of anvils observed within each  $2 \times 2^\circ$  grid box, calculated as the circular mean of the local solar time.

rather than simply a sampling effect.

#### 3.4.4 Diurnal cycle of anvils

Figure 3.23 shows the average local time of day of anvil detection. Similar to fig. 3.11  
 2005 we see a strong land-sea contrast. However, over parts of the Caribbean sea we see  
 that the average time of anvil detection is in the afternoon rather than in the morning,  
 which may be linked to anvils that initiate over land but are advected away. We also  
 see a later average time of detection of anvils over the NGP region, however there is  
 less of a contrast seen than that for detected cores. This indicates that the second  
 2010 peak of core convective activity during the nighttime and early morning in fig. 3.13  
 is linked to long-lived, multiple core systems including MCSs, similar to what was  
 found by Feng et al. [2019].

In fig. 3.24 we plot the distributions of the diurnal cycle of anvil detections by region. The distributions generally match those seen of the core detection times

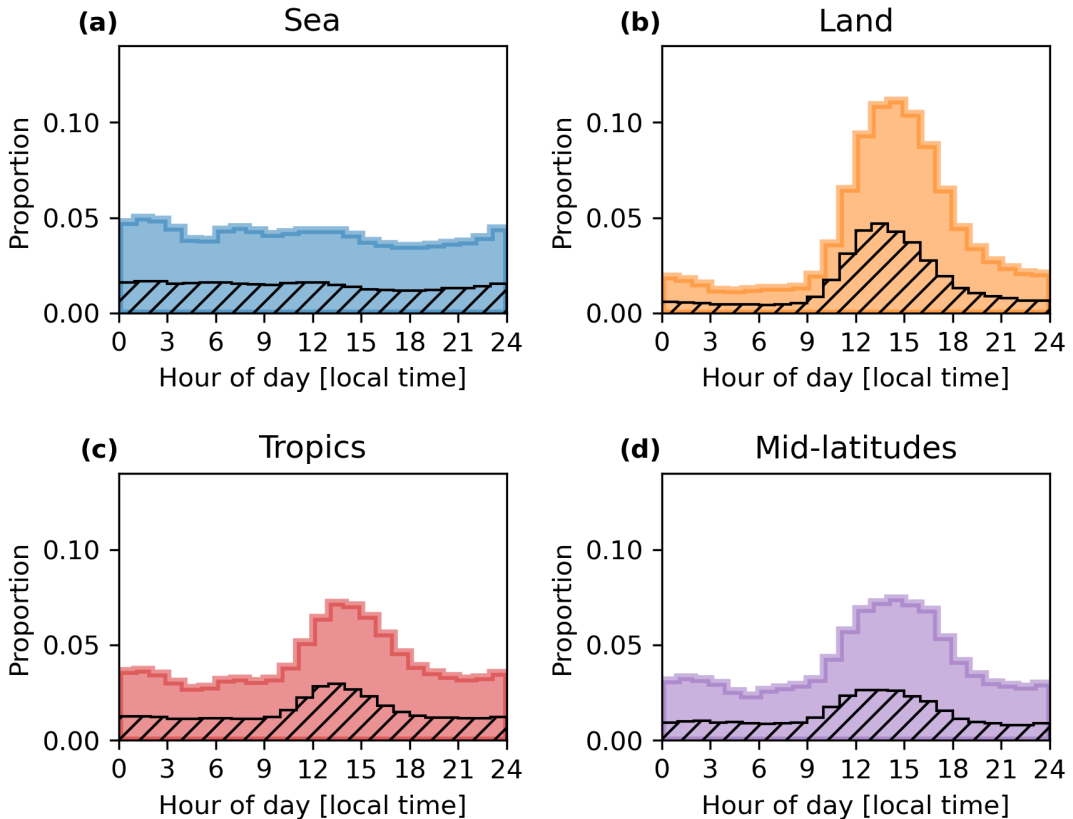


Figure 3.24: The diurnal distributions of the local time of detection for anvils, binned by hour detected over (a) sea, (b) land, (c) tropics ( $<30^{\circ}\text{N}$ ) and (d) mid-latitudes ( $>30^{\circ}\text{N}$ ). The hatched area shows the proportion of each distribution associated with multi-core anvils.

2015 shown in fig. 3.12, as the majority of the observed anvils are isolated systems. The  
diurnal cycle of anvil detections over sea is much less pronounced however, which  
may lead to the increased variability seen in fig. 3.23. When we look at the hatched  
areas, indicating the proportion of the distribution consisting of multi-core anvils, we  
see that over land, tropics and mid-latitudes that the initiation of these organised  
systems occurs earlier in the day compared to isolated DCCs.  
2020

Figure 3.25 shows the average time of observation for anvils. Unlike the previous  
map of detection time shown in fig. 3.23, in this figure we show the average of all  
the time steps at which an anvil is detected. Over the land, the effect is to shift the

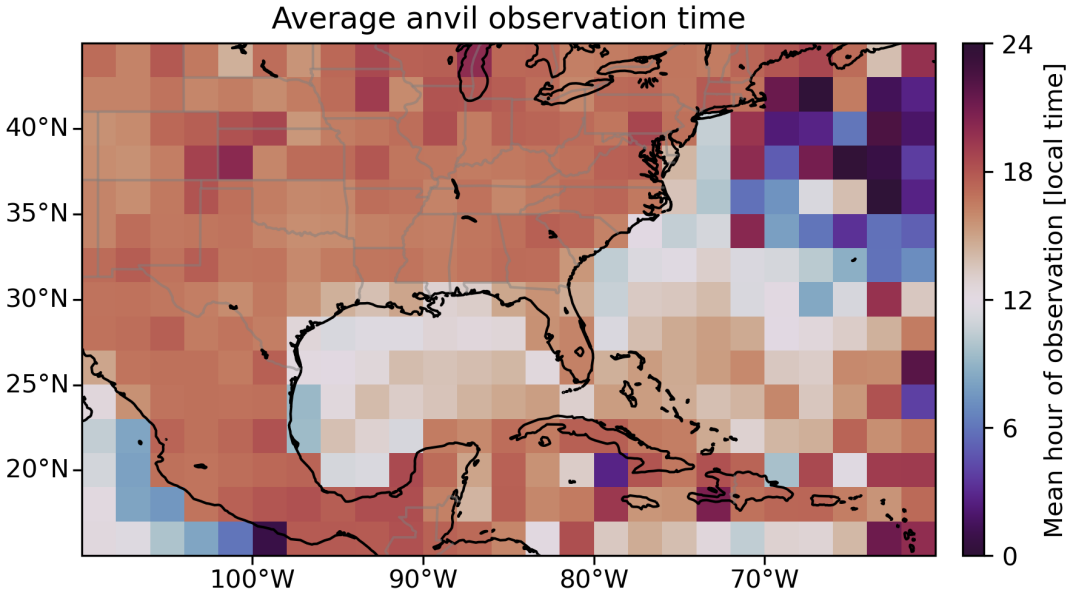


Figure 3.25: The average time of day of observation of anvils observed within each  $2 \times 2^\circ$  grid box, calculated as the circular mean of the local solar time. Unlike fig. 3.23, this is the average of the time of observation at every time step along the anvil lifetime.

timing of the maximum to a later point in the diurnal cycle, which we expect is a  
 2025 shift of approximately half the average lifetime. Over sea however, we see a much larger shift with much of the Caribbean showing a similar time of day to adjacent land regions.

In fig. 3.26 we show the diurnal cycle of anvil observations for each of the four regions. For the land, tropics and mid-latitudes regions, we see a shift in the peak  
 2030 of the distribution to 4–5 pm, along with a lengthening of the right tail of the distribution. The distribution of multi-core anvils appears to match that for all DCCs. While we saw in fig. 3.24 that the initiation time of these organised anvils tends to be earlier in the day, their longer lifetime means that they tend to exist at the same times. However, this longer lifetime also mean that organised DCCs make up a larger  
 2035 proportion of anvil observations during the nighttime and morning, and fewer during the afternoon during the peak in isolated DCCs. In fig. 3.26 a, we see that the

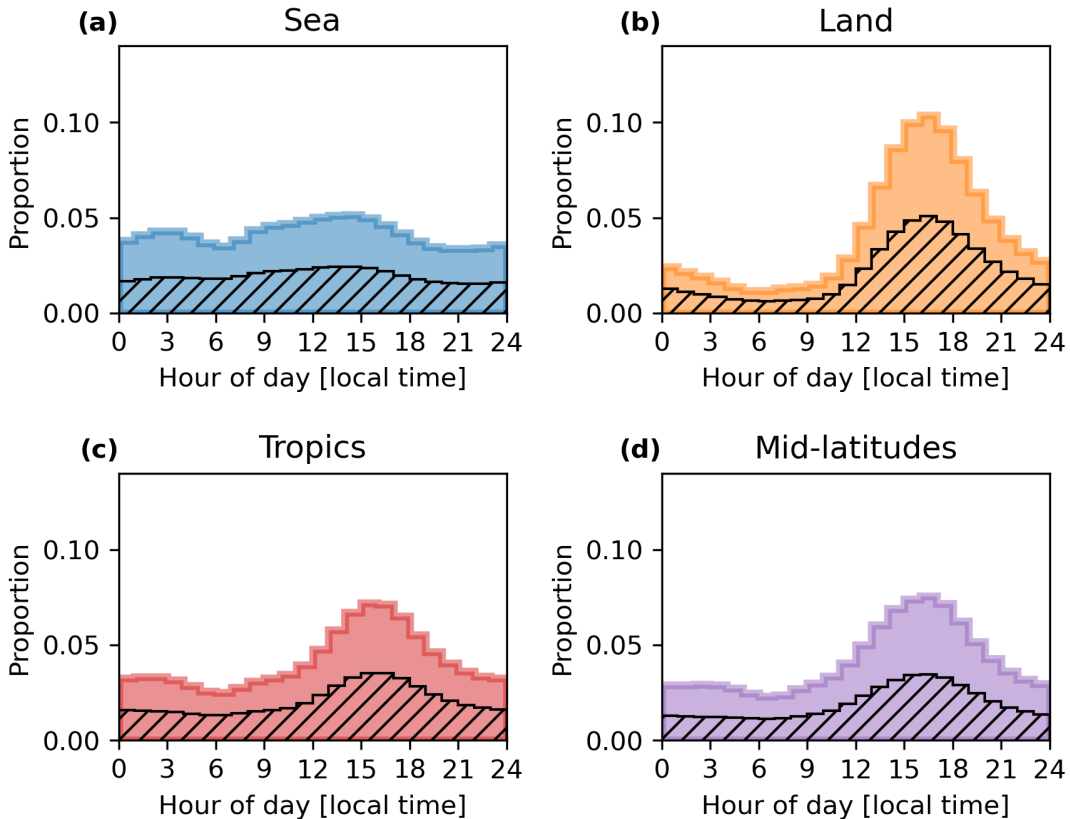


Figure 3.26: The diurnal distributions of the local time of observation for anvils, binned by hour detected over (a) sea, (b) land, (c) tropics ( $<30^{\circ}\text{N}$ ) and (d) mid-latitudes ( $>30^{\circ}\text{N}$ ). The hatched area shows the proportion of each distribution associated with multi-core anvils.

peak of the diurnal distribution over sea is in the afternoon, with a gradual increase of observations throughout the day. Previous research has shown that solar heating during the daytime increases the area and lifetime of anvils [Gasparini et al., 2022], which may explain why we see more anvils during the day, despite more initiations occurring at night.

The difference in the distributions of anvil initiation times and anvil observation times indicates that the lifetime and age of observed anvils changes across the diurnal cycle. Figure 3.27 shows the average age of anvil observed during each hour of the diurnal cycle. The increase in the age of anvils observed over sea throughout the

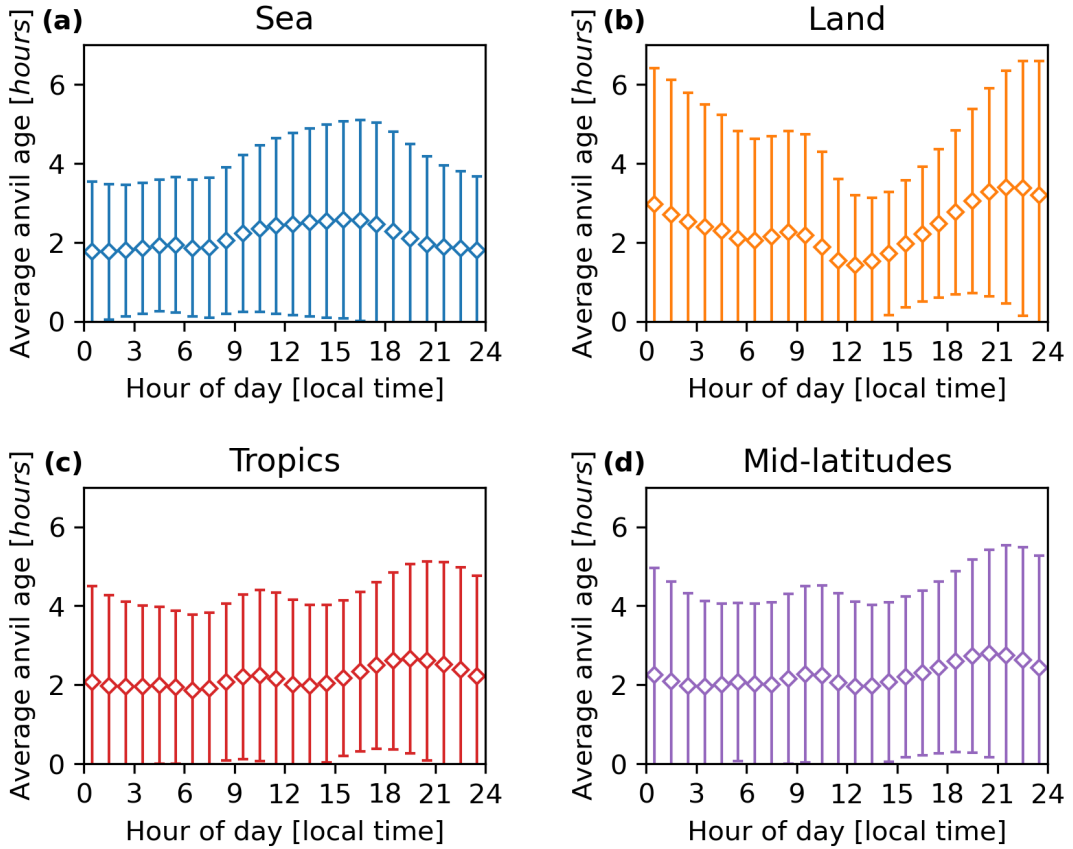


Figure 3.27: The average age of anvils observed over (a) sea, (b) land, (c) tropics ( $<30^{\circ}\text{N}$ ) and (d) mid-latitudes ( $>30^{\circ}\text{N}$ ) throughout the diurnal cycle. Error bars show the standard deviation of the mean.

daytime provides further evidence for the enhancement of anvil lifetime by SW radiation. For anvil observations over land, we see a stronger interaction with the diurnal cycle of convection. In fig. 3.27 b we see a minima of the anvil age between midday and 1 pm, coinciding with the onset of the afternoon peak of anvil initiations seen in fig. 3.24 b. The age increases to a maxima around 20 pm, before decreasing again until midday. The variation in the average age of observed anvils is larger over land than over the ocean. Over the tropics and mid-latitudes however, the combination of opposite signals from sea and land means that there is much less variation of anvil age across either region.

## 2055 3.5 Summary

By applying the *tobac-flow* algorithm to five years of multi-channel BT observations from the GOES-16 ABI CONUS scan region, we produce an extensive dataset of DCC cores and anvils and their properties over time. Containing approximately 1.6 million cores and 400 thousand anvils which considered valid for analysis over their 2060 entire lifecycle, this dataset provides valuable information about their properties, distributions and lifecycle in a Lagrangian framework. With five minute temporal resolution, we find that we are able to accurately measure to properties of developing convective cores, and then link these to the entire evolution of the anvil cloud.

We see a number of key differences in the seasonal, diurnal and regional patterns 2065 of DCCs across North America. The spatial distribution of DCC cores depends strongly on the seasonal cycle. We see a large land/sea contrast in time of initiation, which also displays a sea breeze effect which extends for approximately 200 km inland. The properties of cores themselves, including the lifetime, cooling rate, and time of initiation, have regional dependencies, with more intense convection occurring over 2070 land during the daytime and in the tropics.

These differences extend to the anvils produced by these convective cores. The seasonal and diurnal cycles of anvils are closely related to those of the convective cores. Furthermore, we see differences in the properties of anvil between different regions where we saw differences in convective properties. In particular, we see that 2075 DCCs over land have larger areas, longer lifetimes and colder BT than those over the ocean.

While the majority of observed anvil clouds are associated with a single growing core, there remain a large number of multi-core anvils detected in our dataset. The frequency of multi-core anvils as a proportion of all observed anvils increases with 2080 latitude. Finally, while the properties of the individual growing cores observed in

single- and multi-core anvils show no significant difference, the lifetime and area of anvils shows a large increase with the number of cores.

Some of these findings, such as the larger area of DCCs over land, contrast with studies made using polar-orbiting satellites [Ge et al., 2024]. However, our investigation of the age of anvils observed throughout the diurnal cycle provides a mechanism for this discrepancy. The area of DCC anvils evolves as they age [Futyan and Del Genio, 2007]. Impacts of radiative heating and the diurnal cycle act to modify this however [Gasparini et al., 2022]. As a result, we see that the average age of anvils varies throughout the day. At the time of the Cloudsat overpass (1:30 pm), the average age of anvils over land is at its minima, while those over the ocean are near their maxima. As a result, we would expect that the average area of anvils observed at this time over land would be smaller than those over the ocean, not because of a difference in their processes but because they are being observed earlier in their lifetime before they have reached their maximum area. While at the nighttime overpass time (1:30 am) the average age of anvils over land is older, the reduced number of land DCCs at this time means that any set of snapshot observations will be biased towards younger anvils over land.

By using temporally resolved observations, and placing these in a Lagrangian framework using cloud tracking, we can account for these changes in convective cloud behaviour across the diurnal cycle. Furthermore, linking the properties of the developing cores to the resulting anvil clouds over their entire lifetime provides the potential to investigate how the processes of the former affect the latter. Connecting these properties allows investigation of previously uncertain DCC processes, and, in particular, may help shed light on how anvil optical properties, structure and diurnal cycle respond to climate change.

# Chapter 4

## Contrasting effects of convective intensity and organisation on the structure and lifecycle of DCCs

### <sup>2110</sup> 4.1 Introduction

Understanding how the structure of anvil clouds changes in response to changes in convective behaviour is vital to understanding the radiative impacts and climate feedbacks of DCCs. Around 50% of cirrus clouds in the tropics originate from deep convection [Massie et al., 2002; Luo and Rossow, 2004]. Overall, anvil clouds have a <sup>2115</sup> near-neutral radiative impact on the tropics, despite their large SW reflectance and LW absorption [Hartmann et al., 1992; Hartmann, 2016]. Their radiative effect is not homogeneous however; while the optically thick portion of anvil clouds generally have a cooling effect on the ToA radiative balance, the thin, detrained cirrus has a strong warming effect [Berry and Mace, 2014]. As a result, changes in convective <sup>2120</sup> activity that result in a change in the size and structure of anvil clouds may have large impacts on the climate.

The change of anvil cloud area in response to warming—the iris effect [Lindzen et al., 2001; Bony et al., 2016]—is generally considered to have a cooling feedback in response to climate change. However, it is the largest source of uncertainty in cloud–<sup>2125</sup> climate feedbacks, with around a third of models predicting a warming response

[Sherwood et al., 2020]. To address this uncertainty, a better understanding of the links between convective processes and anvil properties, changes in anvil structure and the properties of ice clouds are required [Gasparini et al., 2023].

Assessing the extent of thin anvil cirrus is challenging due to the difficulties in observing these clouds using IR radiometers. The low emissivity of thin cirrus clouds means that observed BT is dominated by radiances from the lower atmosphere and surface below. Protopapadaki et al. [2017] used cloud emissivity and cloud top pressure, rather than BT, to detect convective cores, thick and thin anvil cirrus clouds. Data from the AIRS instrument was used to retrieve these emissivity values, as the hyperspectral sounder is more sensitive to thin cirrus than IR radiometers. They then compared the proportion of each anvil cloud consisting of thin anvil to the minimum observed cloud top temperature within the convective core, a proxy for the convective depth which is, in turn, a proxy for convective intensity. It was found that the thin cirrus anvil proportion increased with colder cloud top temperatures, indicating that stronger convection increases the detrainment of thin cirrus.

Takahashi et al. [2017b] built upon this study using collocated measurements from the Cloud Profiling Radar (CPR) aboard CloudSat. The CPR measurements provide the echo top height, measuring the convective depth directly, and also provide another proxy for convective intensity, the echo top distance, which is independent of convective depth [Takahashi and Luo, 2014]. It was again found that the proportion of thin cirrus increased with the echo top height, and also increased with decreasing echo top distance (indicating stronger convection).

It should be noted that both of these studies were performed using observations from polar-orbiting satellites in the A-train, and so do not fully sample the diurnal cycle. While both studies consider the maturity of the DCCs observed, the thin anvil proportion is measured at a single point in time, and so differences in the lifetime of the thick and thin anvil cirrus are not considered. Furthermore, we should expect

that the structure of the anvil changes over its lifetime, with the thin anvil fraction increasing as the anvil dissipates. However, the observed BT of the anvil also changes over its lifetime [Futyan and Del Genio, 2007], and so the use of BT as a proxy for convective intensity may introduce confounding factors. While the use of echo top height avoids this confounding issue, these collocated measurements can only be made when the Deep Convective Cloud (DCC) is convectively active and so cannot be used to assess the structure of dissipating anvils.

In chapter 3 we developed a large dataset of tracked DCCs, including cores, and thick and thin anvils, and showed that it captures differences in convective and anvil properties. By using geostationary satellite observations changes in the structure of DCC anvils can be investigated throughout their lifecycles, along with changes in the lifetime of both thick and thin anvils. Furthermore, the impacts of convective organisation on anvil structure can be investigated by taking into account the number of cores associated with each anvil.

## 4.2 Data

The dataset of tracked DCCs first presented in chapter 3 is utilised here to investigate how the structure of observed DCCs depends on the properties of their convective cores. Produced using the method detailed in chapter 2, convective cores are tracked during their vertically growing period, and thick and thin anvils are subsequently tracked using two different channel combinations. Changes in the proportion of thick and thin anvil coverage, considering both spatial extent and the lifecycle of the anvil cloud, can be investigated.

Data filtering is applied to detected anvils according to the criteria shown previously in table 3.2. This results in a total of 391,050 anvils considered for analysis, which between them are connected to a total of 792,522 cores. The filtering requires that every anvil in the analysis dataset begins with a valid observed core, ensuring

that the subsequent development of the anvil can be linked to the properties of the  
2180 core. In addition, it ensures that each anvil is observed for its entire lifetime, and the entire extent of both thick and thin anvil are observed over this period. While this does mean that fewer large anvils are considered valid as their greater extent means that they are more likely to intersect the edges of the domain, it ensures that changes in both thick and thin anvil area can be considered robust over the entire lifecycle of  
2185 the analyses anvils.

The dataset contains a range of properties relating to the observed DCCs. In this chapter, we will focus our investigations on how the area of the detected cores, thick and thin anvils change with each time step. We also analyse two related properties, which are the maximum area of the thick and thin anvil, i.e. the area at the time step  
2190 when the anvil reaches its maximum observed extent, and the total area which is the sum of the areas observed at each time step over each anvil's lifetime. The thin anvil proportion refers to the area of the detected thin anvil divided by the total area of both anvil and core. In general, this is calculated as the total over the entire DCC lifetime, however in section 4.4.4 we will investigate how this changes over the DCC  
2195 lifecycle.

In addition, we consider how the BT of each core and anvil change over time. The area-weighted average of the 10.4  $\mu\text{m}$  BT is taken at each time step for each core, thick and thin anvil. The 10.4  $\mu\text{m}$  LW window BT has a minimal contribution from water in the atmosphere, and so can provide temperature measurements of clouds from near  
2200 the surface to the top of the atmosphere. It should be noted that the BT is affected by the emissivity of the cloud, and so for thin cirrus it will be warmer than the actual CTT due to the contribution from the atmosphere below. As a result of this we use the mean BT of the thick anvil as a proxy for convective cloud height as this avoids a bias from the warmer thin anvil. The (negative) cooling rate of each core is calculated  
2205 as the largest change in the mean core BT measured over any 15 minute period. This

relates to the vertical growth of the DCC core as discussed in section 2.3.1.

## 4.3 Method

### 4.3.1 Detection of thick and thin anvils

Observing thin cirrus anvils using satellite BT is difficult due to their low emissivity.

Furthermore, BT is affected both by the height of the observed cloud and its optical thickness. As shown in fig. 2.9, the observed BT increases as optical depth decreases. For detection using a fixed threshold, as used in many anvil detection algorithms, this means that the limit of optical depth at which the anvil is detected increases as the height of the cloud decreases. This results in the detected anvil area varying with height, with an anvil at a lower altitude being detected as smaller than one at a higher altitude even if there size and structure are otherwise identical. This problem with detected anvil area using BT thresholds was identified as early as Augustine and Howard [1988], but remains a feature of many detection algorithms to this day (see e.g. section 1.4).

While observing the thin cirrus anvil is challenging, we have shown in section 2.4.4 that by using a combination of BT differences we are capable of detecting thin cirrus. Furthermore, the use of channel differences reduces the height dependence of the detection of anvils compared to the use of a single BT. Figure 4.1 shows simulated BT observations using the libRadTran model [Emde et al., 2016], as described in section 2.3. The top panel shows simulation BT observations by ABI at 10.4  $\mu\text{m}$  at heights of 10, 12 and 14 km (shown by the solid, dashed and dotted lines respectively). Also shown by the grey, dashed line is an example of the 241 K BT threshold. At this threshold there is substantial variance in the limit of OD at which anvil clouds are detected, which ranges from 1 at 14 km to 3 at 10 km. This provides clear support for the argument made by Augustine and Howard [1988] that the anvil area detected using this threshold is “subjective”.

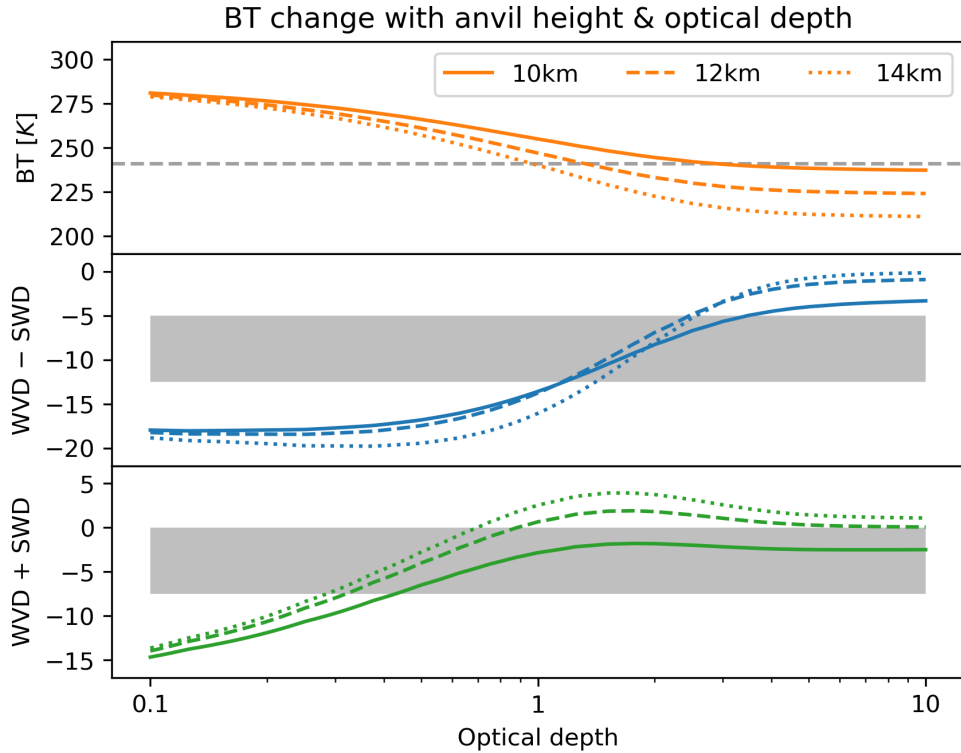


Figure 4.1: Simulated ABI BT observations for DCC anvils at 10 km (solid lines), 12 km (dashed lines) and 14 km (dotted lines) at optical depths between 0.1 and 10. Panels show (top) 10.4  $\mu\text{m}$  BT; (middle) WVD minus SWD, used in thick anvil detection; and (bottom) WVD plus SWD, used in thin anvil detection. The grey dashed line shows the 241 [K] threshold, and the grey shaded regions show the range in which cloud edge detection is performed for thick and thin anvils.

The middle and bottom panels in fig. 4.1 show the simulated OD for the combinations of WVD minus SWD and WVD plus SWD respectively. Section 2.4.4 describes how these two channel combinations are used for the detection of thick and thin anvils. In both panels, the grey shaded region shows the BT range in which edge detection is used to find the anvil area. Compared to 10.4  $\mu\text{m}$  BT, the WVD minus SWD combination shows very little variance in the optical depths at which the anvil cloud is detected within the threshold range. Throughout the threshold range of  $-5$  to  $-12.5$  K the OD corresponding to the same observed BT difference varies by approximately 0.1–0.2 between differing heights, compared to 1–2 for 10.4  $\mu\text{m}$  BT.

The WVD plus SWD combination is shown in the bottom panel of fig. 4.1. Greater variance between different heights is seen, particularly for the 10 km anvil simulation. However, the OD corresponding to the observed BT differences are very similar throughout the detection range of 0 to  $-7.5\text{ K}$  for heights of 12 and 14 km. Lidar observations of thin cirrus anvil have shown that the heights of these clouds typically exceed 12 km [Wall et al., 2020; Horner and Gryspeerdt, 2023], and so we expect there to be little difference in the sensitivity to most observed anvils.

It should be noted that the simulations shown in fig. 4.1 were calculated using a standard tropical atmospheric profile to best represent the moist environment in which deep convection occurs. While anvils occurring in the extra-tropical parts of the CONUS domain are expected to have lower cloud top heights, there is also expected to be a colder temperature profile. As a result, we expect that the observed BT for extra-tropical DCCs behave more like that of the 12 and 14 km simulations shown in fig. 4.1, rather than that at 10 km.

### 4.3.2 Estimation of convective intensity and organisation

As we cannot observe the vertical velocity or convective mass flux of DCC updrafts directly using geostationary satellite observations, a proxy is needed to estimate their intensity instead. The minimum BT of an observed DCC is commonly used as a proxy for convective intensity, and is used by Protopapadaki et al. [2017] for this purpose. This property is more closely related to the height of the DCC, however. While the height of a DCC is related to the intensity of convection, it is also related to the tropopause height and level of neutral buoyancy which may vary with location and meteorology independent of convective processes. While we use the minimum BT of observed anvils in this chapter to compare to previous studies, a more direct proxy for convective intensity is desired.

The primary proxy for convective intensity in this chapter is the maximum cooling

rate of the initial observed core for each DCC. As described in section 2.3.1, the core cooling rate is linked to the vertical development of the core over time. A cooling rate of  $1 \text{ K minute}^{-1}$  approximately represents a cloud top vertical velocity of  $2.5 \text{ ms}^{-1}$ .

2270 While this should not be confused with the updraft velocity of the core itself, and is expected to be less due to the effects of entrainment and overturning circulation at the top of the updraft, it is linked to the updraft velocity directly. In section 3.4.1 it was shown that the core cooling rate and minimum core BT are correlated. The initial detected core is selected for the maximum cooling rate to ensure that we have suitable observations of the core throughout its growth that are not masked by an anvil above. While the updraft may strengthen later in the development of the DCC, or subsequent cores in a multi-core system have stronger updrafts, we consider this the most direct proxy we have available for the updraft intensities of observed DCCs.

2280 The number of cores associated with each DCC is used as a measure of its organisation, again providing the most direct proxy available. While it may not be possible to observe all the cores associated with larger MCSs due to the anvil blocking observations of cores below, it is still expected that many separate cores associated with such systems are detected. As shown in chapter 3, tracked DCCs with many cores show the properties expected of MCSs.

### 2285 4.3.3 Lifecycle analysis

To analyse changes in the lifecycle of DCCs, we categorise their lifetime based on the method developed by Futyana and Del Genio [2007]. This method separates the anvil cloud into growing, maturing and dissipating stages based on observations of BT and anvil area. Futyana and Del Genio's method defines the end of the growing phase as the time at which the anvil reaches its minimum observed BT, and the end of the mature phase as the time at which the anvil reaches the maximum observed area. While simple, this approach applies to a wide range of observed DCCs including both

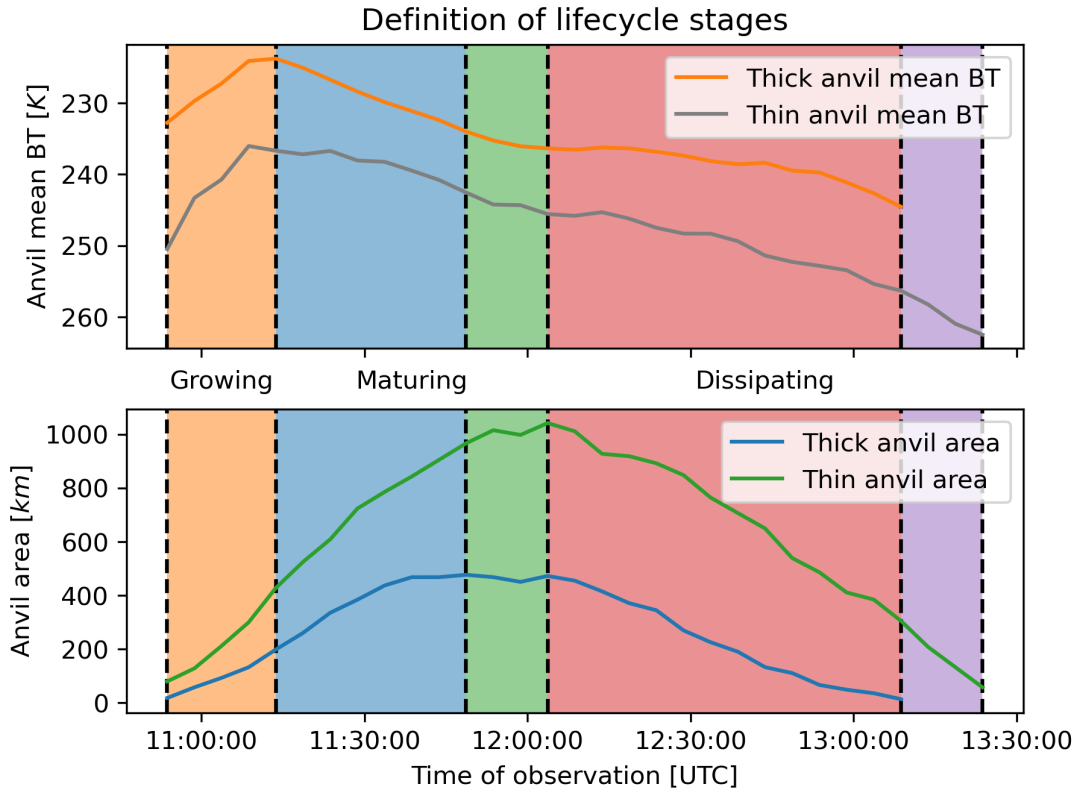


Figure 4.2: Definition of anvil lifecycle stages based on the method of Futyana and Del Genio [2007]. The top panel shows the evolution of the mean BT of the thick and thin anvil regions over the DCC lifecycle, and the bottom panel shows the evolution of the anvil area. The growing phase (orange) is defined as the time between initial detection and the minimum observed BT. The mature phase for the thick (blue) and thin (green) anvil is defined as the time between the minimum BT and maximum thick and thin anvil area respectively. The dissipating phase for the thick (red) and thin (purple) anvils is defined as the time between the anvil maximum area and the final time of detection of the thick and thin anvil respectively.

isolated and organised convection. Furthermore, by determining the anvil lifecycle only in terms of the observed anvil properties, we can treat the properties of the detected cores as independent variables allowing straightforward analysis of their impacts on lifecycle.

We extend Futyau and Del Genio's method in this chapter through consideration of the development of both thick and thin anvil, which results in the lifecycle stages shown in fig. 4.2. The growing stage (orange) is defined as the time from the initial detection of the DCC to the time at which the thick anvil has its coldest average BT. The thick anvil maturing stage (blue) occurs between this time and the time at which the thick anvil reaches its maximum area, and the thin anvil maturing stage (green) occurs until the thin anvil reaches its maximum area. In this stage, the thin anvil continues to expand while the thick anvil begins to shrink. The thick anvil dissipating stage (red) ends at the final detection time of the thick anvil, while the thin anvil dissipating stage (purple) ends at the final detection time of the thin anvil, which is also the final detection time of the tracked DCC. By increasing the granularity of the lifecycle definition in this manner we can investigate how the impact of convective processes on DCC lifecycle might also impact their structure.

#### 4.3.4 Composite analysis

To compare how the structure of tracked DCC evolve over their lifecycle, we interpolate the area of their cores, thick and thin anvils over a normalised lifetime. In this normalised lifetime, 0 is defined as the time of initial core detection, and 1 is the time of the final anvil detection. By normalising their lifetimes in this manner, the change over time of DCCs with different lifetimes can be composited and compared.

An example composite of the average properties of all analysed anvils in this chapter is shown in fig. 4.3. Figure 4.3 a shows the average change in area of the core (red), thick anvil (orange) and thin anvil (blue) over the normalised lifetime of the

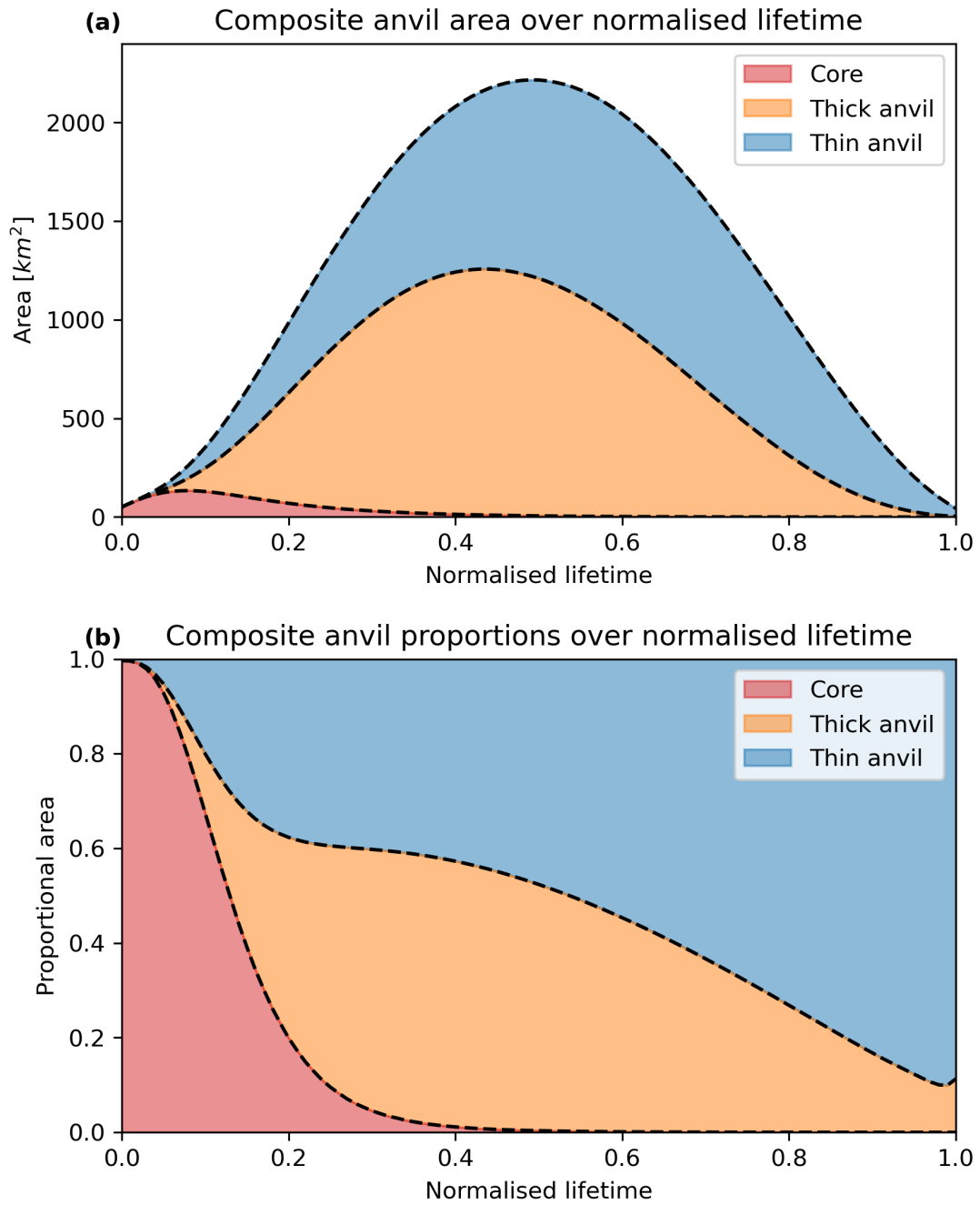


Figure 4.3: The average evolution of composites of cores (red), thick anvils (orange) and thin anvils (blue) over their normalised lifetimes, where 0 is the initial core detection time and 1 is the final anvil detection time. Panel (a) shows the average area of anvils, and (b) shows the proportion of the total area corresponding to each part of the anvil structure.

DCCs. Figure 4.3 b shows how these areas change as a proportion of the net DCC area. From fig. 4.3 b we can see how, on average, the structure of DCCs evolves over their lifetime. Initially, the DCC consists entirely of a growing core, with the initial anvil formation occurring between 10% and 20% of the DCC lifetime. The initial expansion of the anvil is mostly thin, likely because the majority of the mass flux is still travelling upwards, and the area of thick anvil is covered by the developing core. Between 20% and 40% of the normalised lifetime, while the anvil is maturing, the thick and thin anvil expand at similar rates and so the proportion of thin anvil remains consistent. Beyond this point, the thick anvil reaches its maximum area before the thin anvil and dissipates faster, and the fraction of thin anvil increases until the end of the DCC lifecycle. Note that the average thin anvil fraction does not reach 100% at the end of the normalised lifetime due to the presence of some DCCs where we detect the dissipation of the thick and thin anvil to occur at the same time.

Through the use of composite analysis, we can investigate how the anvil structure changes throughout the DCC lifecycle in response to convective processes, rather than limiting our analysis to bulk properties or snapshots.

## 4.4 Results

### 4.4.1 Change in thin anvil fraction with intensity and organisation

To begin, we compare how the net thin anvil fraction of observed anvils changes with the mean anvil BT, initial core maximum cooling rate and number of cores. In fig. 4.4 a we show how the thin anvil proportion changes with the average thick anvil BT. Note that we only consider the thick anvil BT to avoid a dependence between the anvil BT and the thin anvil area. We see an increase of thin anvil proportion with the average anvil BT, agreeing with the results of Protopapadaki et al. [2017]. Figure 4.4 b compares how the thin anvil fraction changes with the maximum cooling

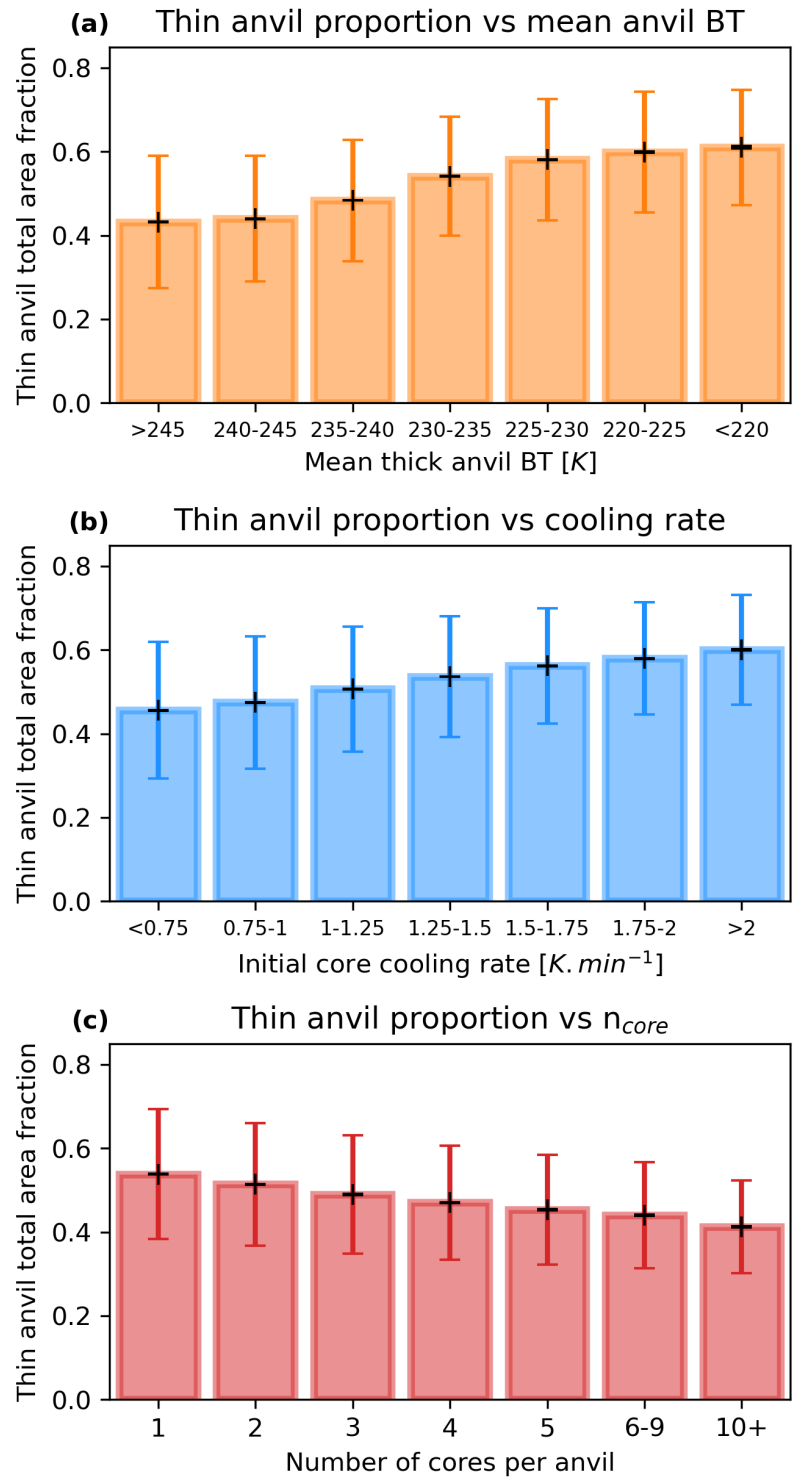


Figure 4.4: Thin anvil proportion of anvils categorised by (a) mean anvil BT, (b) initial core cooling rate, and (c) number of cores. Black error bars show the standard error of the mean, and coloured error bars show the standard deviation.

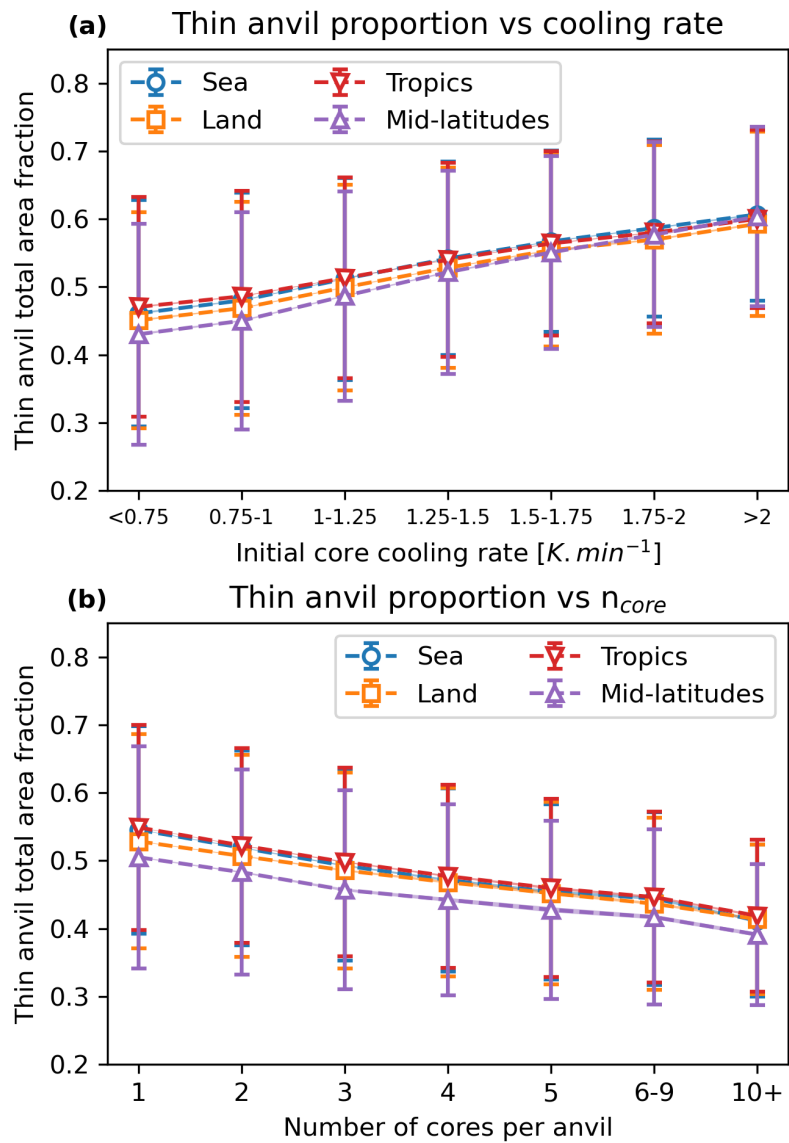


Figure 4.5: A comparison of the change in thin anvil proportion with (a) maximum core cooling rate and (b) number of cores for four different regions: sea (blue diamond markers), land (orange square markers), tropics ( $<30^{\circ}\text{N}$ ; red downward triangle markers) and mid-latitudes ( $>30^{\circ}\text{N}$ ; purple upward triangle markers). Error bars show the standard deviation of thin anvil fraction.

2345 rate of the initial core associated with the anvil, and again shows a positive relation between the strength of convection and the thin anvil fraction. While the measured proportion of thin anvil differs from that observed in previous studies, this is expected as we are both using different methods to define thick and thin, and the proportion is measured over the entire DCC lifetime rather than at a single point in time.

2350 In fig. 4.4 c, we compare the thin anvil fraction to the number of cores associated with each anvil. In contrast to fig. 4.4 b and c, we see a decrease in the thin anvil fraction with an increase in the number of cores. As this occurs despite the tendency for multiple-core anvils to have colder average BT, this indicates that further factors are involved in the thin anvil fraction than the temperature and height of the anvil.

2355 To ensure that these relationships are not caused by differences in the properties and distributions of DCCs across different regions, we further break down the relationship between cooling rate and number of cores and the thin anvil fraction with four different regions, shown in fig. 4.5. As with previous studies we find that the fraction of thin anvil is very similar for DCCs observed over land and ocean. While 2360 we do see a difference in the thin anvil fraction of approximately 0.05 between DCCs located in the tropics and mid-latitudes (defined as  $<30^{\circ}\text{N}$  and  $>30^{\circ}\text{N}$  respectively), this difference decreases with increasing convective intensity. Overall, the near identical relationship of thin anvil fraction to intensity and organisation across multiple regions indicates that this is linked to the convective processes themselves, rather 2365 than a co-variance with local conditions.

#### **4.4.2 Impact of intensity and organisation on DCC properties**

Both the intensity and organisation of DCC cores have impacts on the properties of their anvil clouds. In this section we will investigate how these processes affect the 2370 bulk properties of these anvils; the anvil maximum area and the anvil lifetime for both thick and thin anvils, and the anvil BT. Comparing the bulk properties of these

anvils provides an indication of how their structure changes, however, as we will see, they do not fully explain the differences shown in figs. 4.4 and 4.5.

In fig. 4.6 we show how the area, lifetime and BT of DCCs changes with the core cooling rate. Figure 4.6 a shows that the average thick and thin anvil maximum areas vary very little with cooling rate, except for at the highest observed values of cooling rate. There is however a slight widening in the gap between thick and thin anvil maximum area with increasing core cooling rate, as the thin anvil increases in maximum area while the thick anvil remains consistent. Figure 4.6 b shows that while the average thick anvil lifetime remains constant with increasing core cooling rate, the thin anvil lifetime increases. We also see a consistent decrease in both average and minimum thick anvil BT with cooling rate, shown in fig. 4.6 c. This change in anvil BT with the core intensity agrees with the results shown previously in fig. 3.10 b which showed that more intense cores have colder minimum BT.

In fig. 4.7 we examine how the anvil properties change with the number of cores associated with each anvil cloud. Figure 4.7 a shows that both the thick and thin anvil maximum area increase substantially with an increasing number of cores (note that it is plotted against a log scale). However, the thin anvil area increases at a slower rate proportional to the thick anvil. Similarly, there is an increase in both the thick and thin anvil lifetime with increasing number of cores shown in fig. 4.7 b. We see a similar rate of the decrease of average anvil BT with the number of cores in fig. 4.7 c as we did in relation to core cooling rate in fig. 4.6 c. The minimum anvil BT decreases at a notably faster rate with the increasing number of cores, however. Although this is indicative of an increased likelihood of overshooting cores in more organised DCCs, we must also note that the larger area of these systems also makes it more likely to observe colder pixels. The changes in anvil properties with intensity and convection are intriguing due to both their differences and similarities. Both processes result in anvils with colder BT, which is commonly used as a proxy for convective intensity.

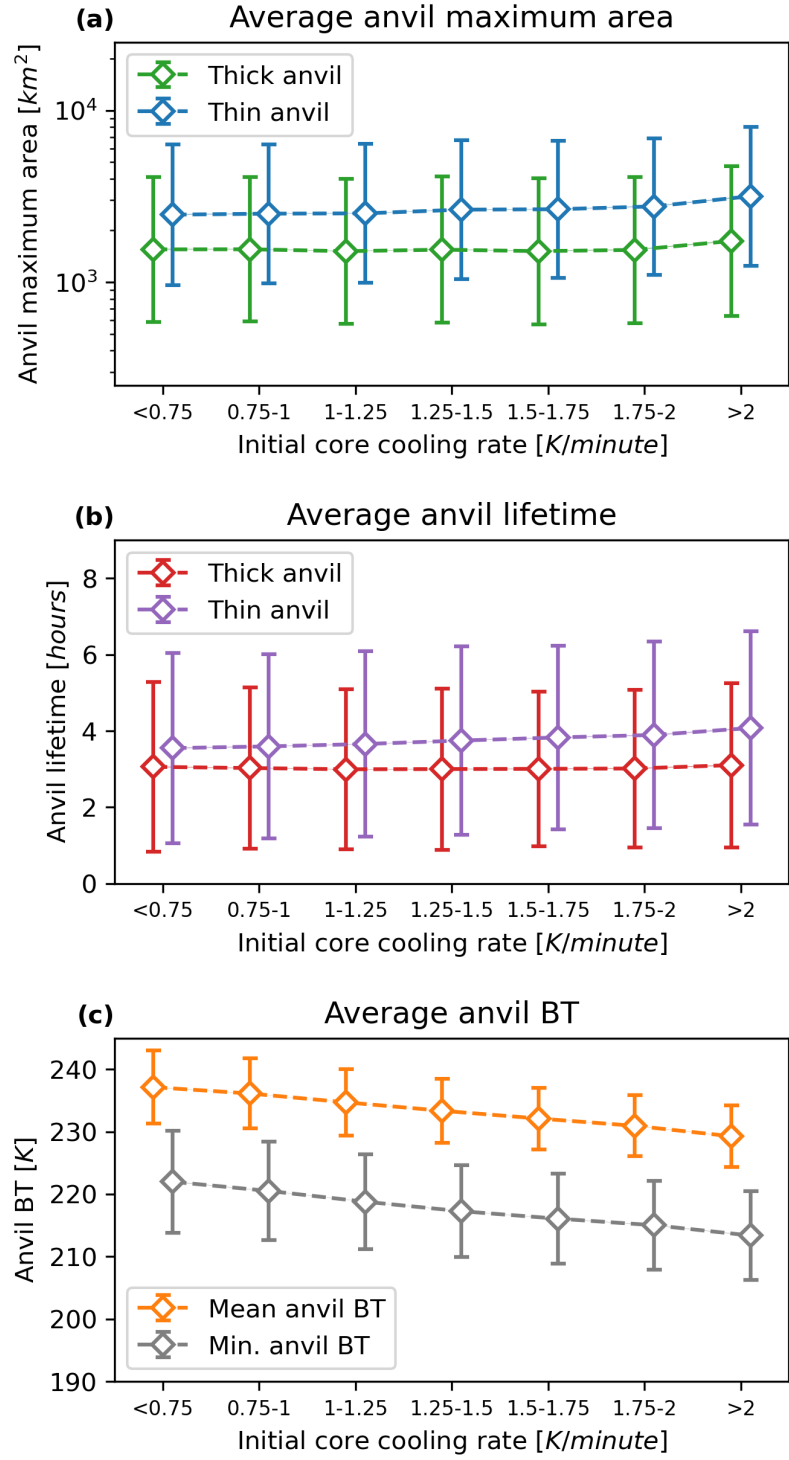


Figure 4.6: The effect of initial core cooling rate on (a) maximum anvil area, (b) anvil lifetime, and (c) mean and minimum BT. Error bars show the standard deviation. Points have been staggered to show the thick and thin anvil properties more clearly, but correspond to the same tick marks on the x axis.

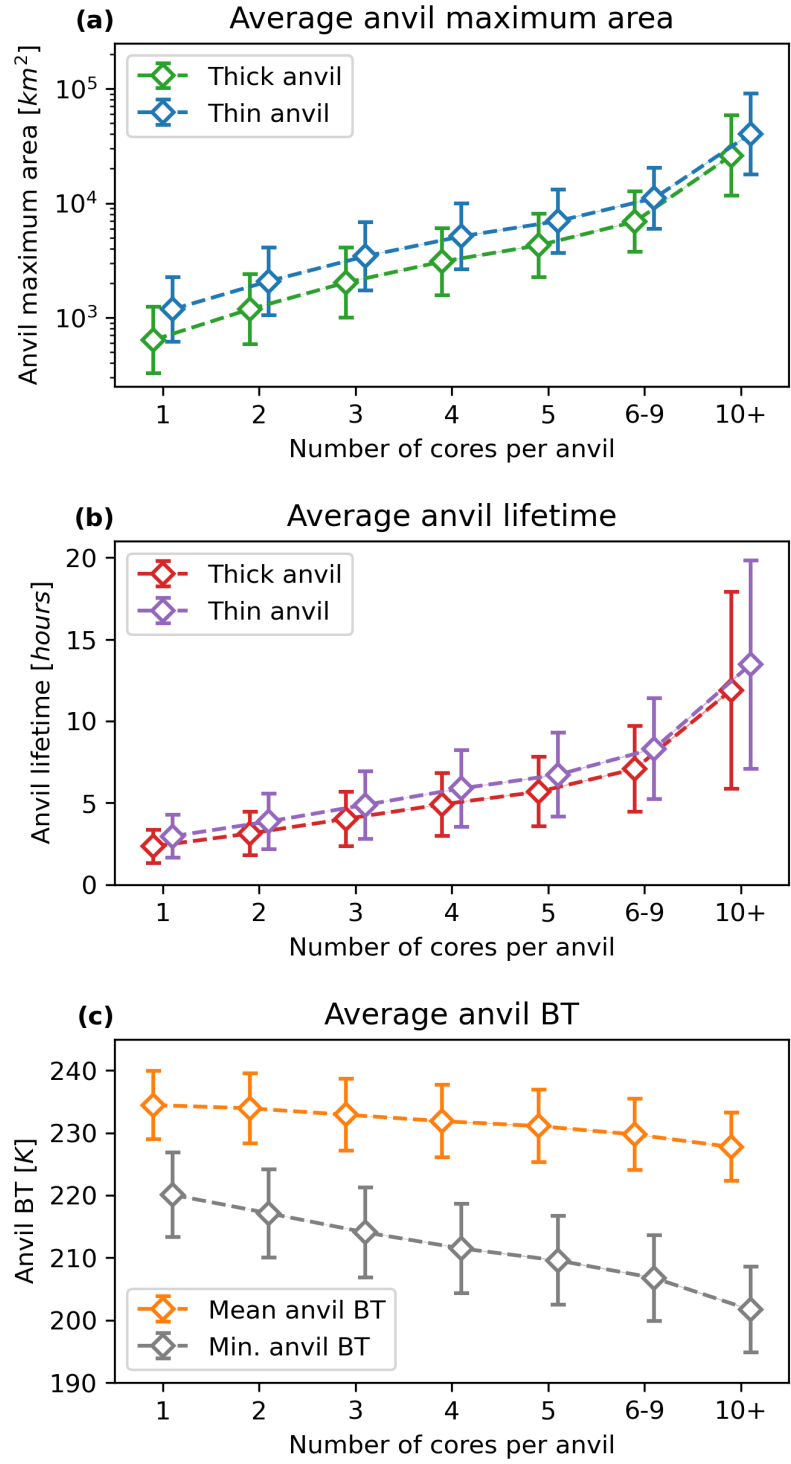


Figure 4.7: The effect of the number of cores on (a) maximum anvil area, (b) anvil lifetime, and (c) mean and minimum BT. Error bars show the standard deviation. Points have been staggered to show the thick and thin anvil properties more clearly, but correspond to the same tick marks on the x axis.

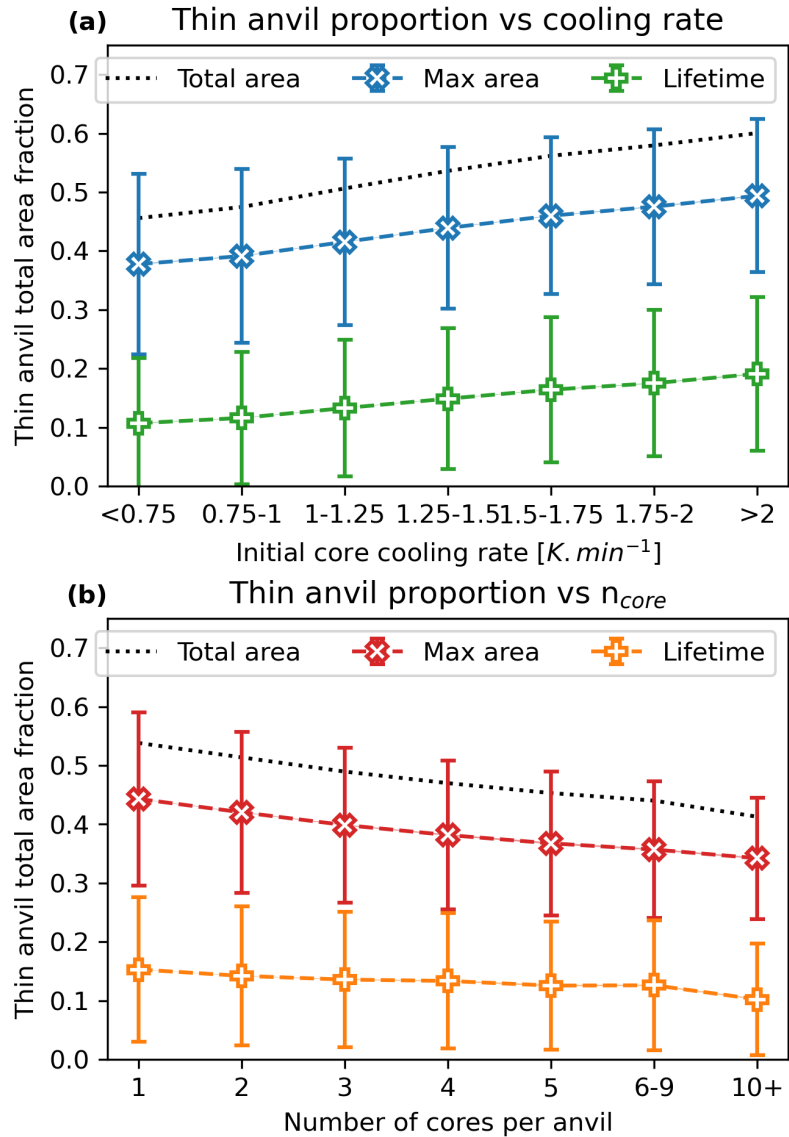


Figure 4.8: A comparison of the proportion of thin anvil measured at the time of maximum anvil area, and the proportional difference in lifetime, compared to the overall thin anvil proportion. Panel (a) shows the change in thin anvil proportion with core cooling rate, and (b) shows the changes with the number of cores. In both panels, the black dotted line shows the total thin anvil proportion over the entire DCC lifecycle. Error bars show the standard deviation of the thin anvil fraction, and while some extend below zero all measured thin anvil fractions are positive.

However, the differences in the changes in anvil areas and lifetimes show that these  
2400 processes cannot be lumped together so simply. In particular, the impact of intensity  
on the thin anvil properties without changing the bulk properties of the thick anvil  
show a clear impact of this process on anvil structure.

In fig. 4.8 we investigate how much of the thin anvil fraction can be attributed to  
the bulk changes in anvil maximum area and lifetime. We see that the proportional  
2405 difference in the maximum area of the thick and thin anvils represents approximately  
80% of the change in thin anvil fraction across both convective intensity and organisa-  
tion. This shows that while the trend in thin anvil fraction can be captured by  
snapshot observations from polar-orbiting satellites, they will underestimate the total  
thin anvil fraction over the entire DCC lifetime. The proportional difference in the  
2410 thick and thin anvil lifetimes shows a smaller contribution to the net thin anvil frac-  
tion. Furthermore, there is a stronger (positive) trend of the lifetime proportion with  
intensity and a weaker (negative) trend with organisation. Note that while some of  
the errorbars (showing the standard deviation) extend below zero, all values for the  
thin anvil fraction are positive. In the next section, we will investigate the differences  
2415 in how intensity and organisation affect DCC lifecycle in more detail.

#### 4.4.3 Changes in DCC lifecycle with intensity and organisa- tion

It is clear from the impact on anvil lifetime that both the intensity and organisation of  
convection affect DCC lifecycle. Furthermore, from fig. 4.8, we see that these different  
2420 processes have different impacts on the lifecycle that warrant further investigation.  
In this section, we show how both convective processes affect the different lifecycle  
stages of DCCs. We use the modified Futyan and Del Genio method explained in sec-  
tion 4.3.3 throughout to break the anvil lifecycle into growing, mature and dissipating  
stages.

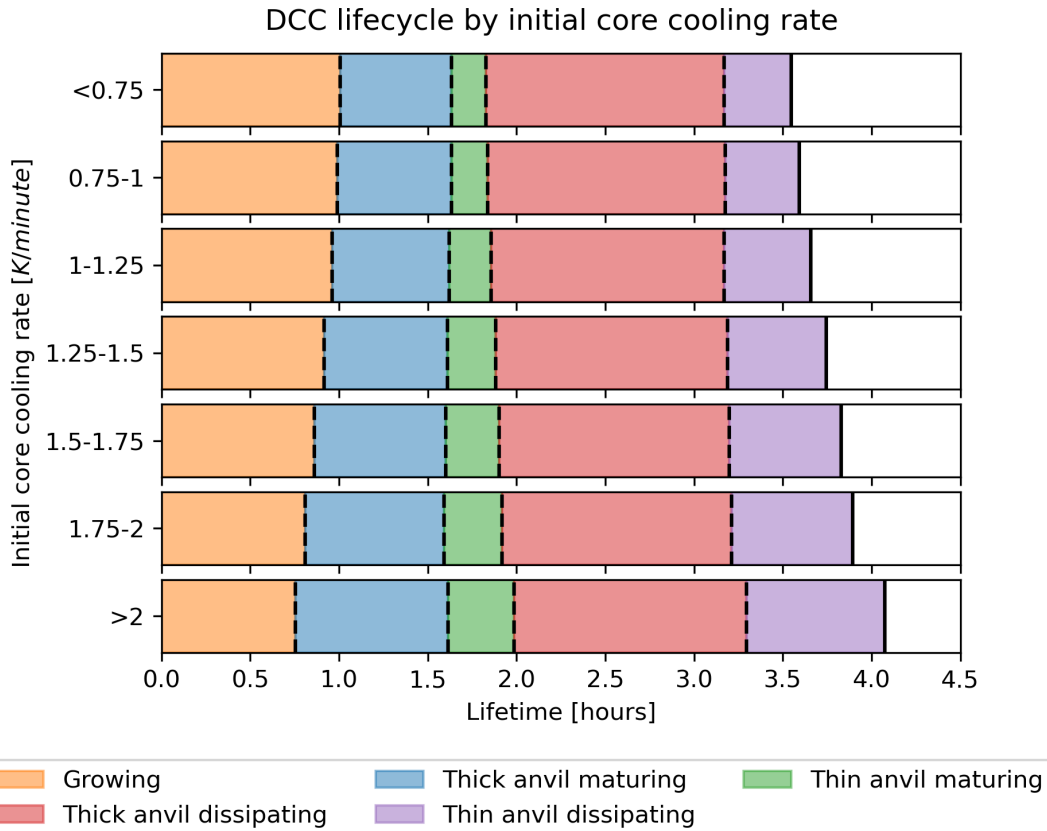


Figure 4.9: The lifetime of each of the lifecycle stages defined in section 4.3.3 for anvils categorised by initial core cooling rate.

2425     Figure 4.9 shows the lifetime of the different lifecycle stages for DCCs with increasing core cooling rates. The lifetime of the growing stage decreases from 1 hour to 45 minutes for the most intense convection. While these growing lifetimes are longer than those of the detected cores shown in fig. 3.10, the trend agrees with the shorter lifetime for more intense cores. Despite the colder BT and hence higher cloud top heights exhibited by these DCCs, the stronger vertical growth rates result in an anvil which reaches its minimum BT in a shorter time frame.

2430

The timing of the maximum extent of the thick anvil remains consistent at just over 1.5 hours for all cooling rates, while the time of the maximum thin anvil area increases from 1 hour 45 minutes to 2 hours for the most intense DCCs. Similarly, the timing of the dissipation of the thick remains consistent at just over 3 hours for most

2435

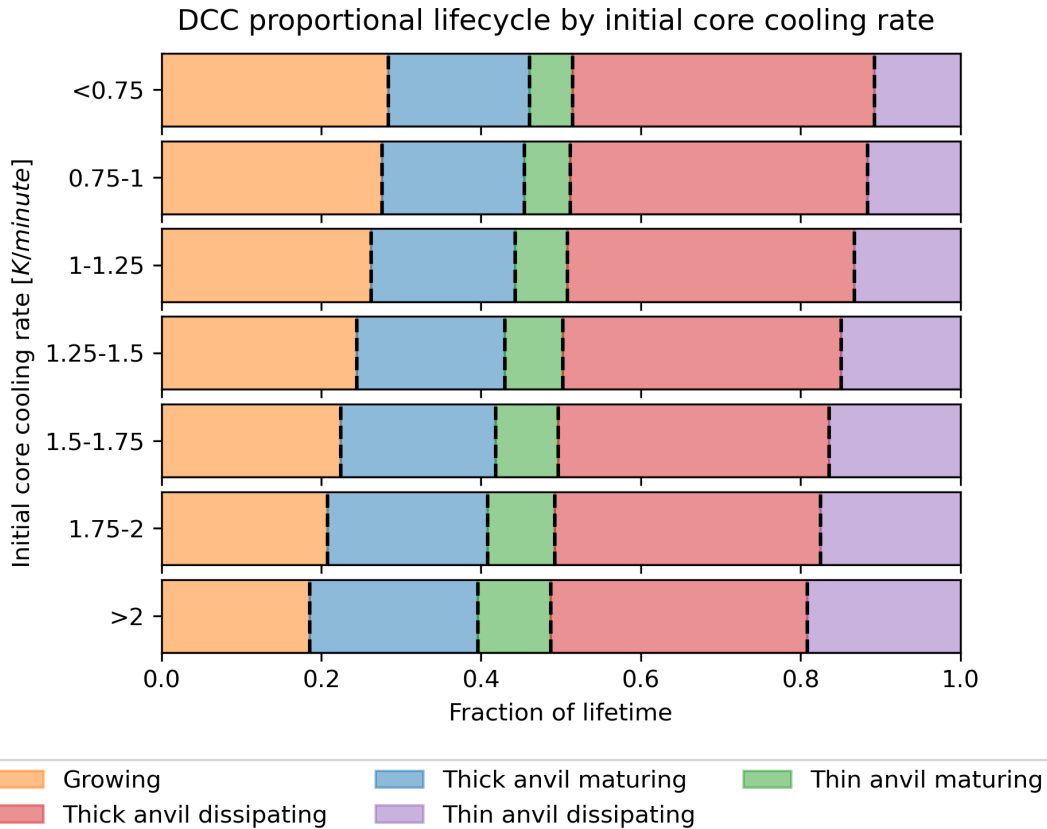


Figure 4.10: The average fraction of anvil lifetime of each of the lifecycle stages defined in section 4.3.3 for anvils categorised by initial core cooling rate. Each bar is normalised such that the total length of the row is equal to the mean thin anvil lifetime of its cooling rate bin.

cooling rates, however the thin anvil dissipation time increases from 3.5 hours to 4 hours for more intense DCCs. These findings reinforce what was shown in fig. 4.6, that the core cooling rate affects the lifetime of the thin anvil but not the thick anvil.

Figure 4.10 displays the average proportion of anvil lifetime spent in each of the stages shown in fig. 4.9. We normalise the anvil lifetime using the method described in section 4.3.4, where 0 is the time of the initial detection of the DCC and 1 is the time of the final detection of the dissipating thin anvil. By analysing these lifecycle stages as a proportion of the total lifetime, we can gain better insight into how changes in lifecycle impact the structure and bulk properties of observed DCCs.

The reduction in the lifetime of the growing phase and increase for thin anvil

<sup>2445</sup>

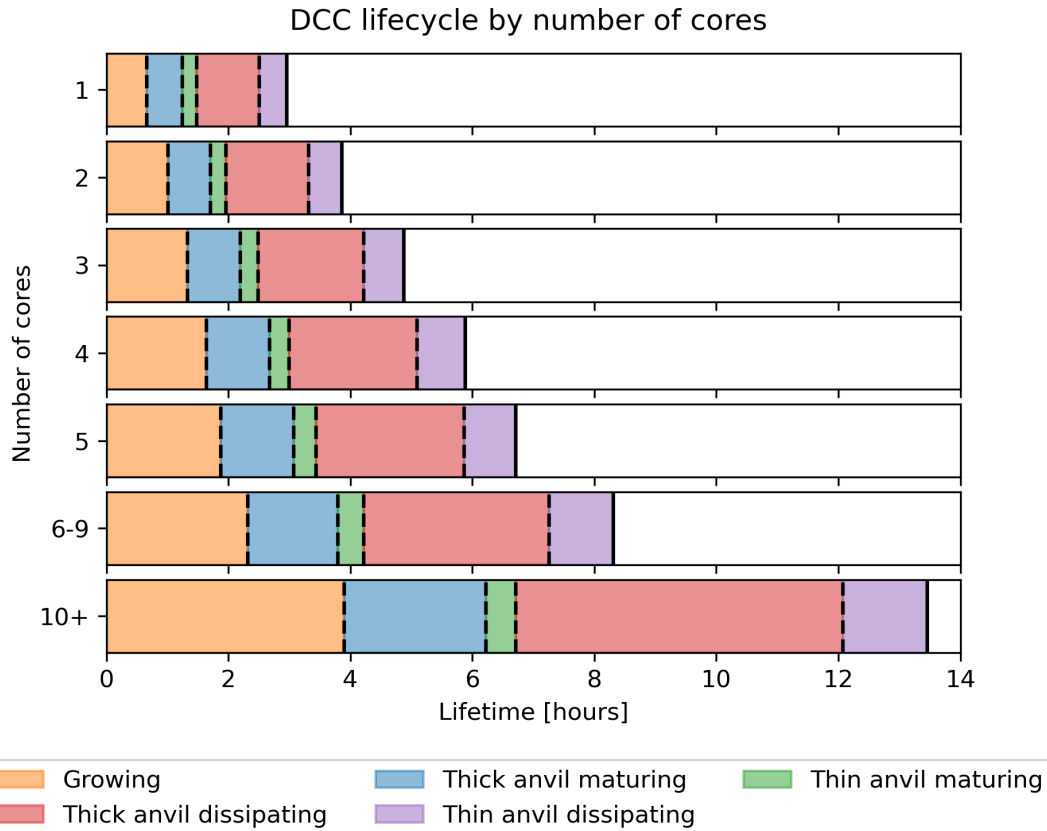


Figure 4.11: The average lifetime of each of the lifecycle stages defined in section 4.3.3 for anvils categorised by number of cores.

dissipation for more intense DCCs is again apparent. The time between these two stages, representing the period in which the thick anvil matures and then dissipates, lasts for around 60% of the total anvil lifecycle for all core cooling rates. The shorter growing period and longer thin anvil dissipating period act together to shift the evolution of the thick anvil earlier in the DCC lifecycle for more intense DCCs. For DCCs over land, where there is a pronounced peak in occurrence in the afternoon, we expect this to shift the time in which the anvil is at its thickest and has the largest extent earlier in the day, with potential impacts on its SW CRE.

Figure 4.11 shows how the timing of the different anvil stages changes with increasing number of cores. It is immediately apparent that the large increase in overall lifetime with number of core shown in fig. 4.7 also applies to each of the lifecycle stages.

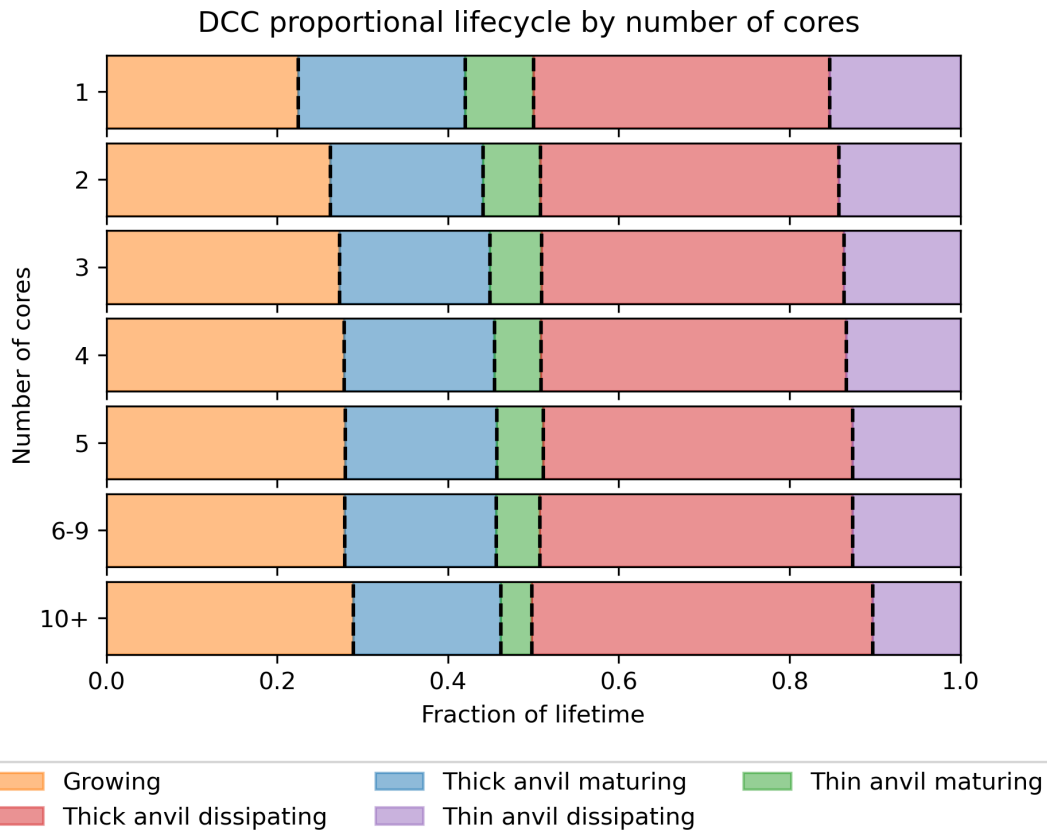


Figure 4.12: The average fraction of anvil lifetime of each of the lifecycle stages defined in section 4.3.3 for anvils categorised by number of cores. Each bar is normalised such that the total length of the row is equal to the mean thin anvil lifetime of its number of cores bin.

This increase in lifetime occurs to such an extent that the average growing period for DCCs with 10 or more cores lasts longer than the average of the entire lifetime of isolated DCCs. The large spread in lifetimes makes it difficult to compare how the 2460 lifecycle changes with organisation, and so we move immediately to the normalised lifetime view.

Figure 4.12 shows the lifetime of each lifecycle stage as a proportion of the total lifetime for DCCs with different numbers of cores, in the same manner as used for fig. 4.10. In contrast to the effect of increasing intensity, we see that with increasing 2465 organisation the length of the growing phase increases and the length of the thin anvil dissipating phase decreases as a proportion of the overall lifetime. We see a

similar behaviour of the period from the start of the mature phase to the thick anvil dissipation, which remains a consistent length for all core counts. With increasing organisation this period shifts later in the lifetime of the DCC.

<sup>2470</sup> It should be clarified, however, that these differences are only in relation to the proportion of total lifetime. While more organised systems spend a smaller proportion of their lifetime in the thin anvil dissipating phase, the much greater overall lifetime means that this stage still lasts substantially longer than for Deep Convective Cloud (DCC)s with fewer cores.

#### <sup>2475</sup> 4.4.4 Changes in thin anvil fraction over DCC lifecycle

While the contrasting changes in DCC lifecycle with increasing intensity and organisation (in particular the change in the thin anvil dissipating stage) go some way to explaining the difference in the thin anvil fraction, we have already seen in fig. 4.8 that the change in lifetime cannot account for the change in thin anvil fraction alone.

<sup>2480</sup> The contrasting changes in lifecycle do, however, indicate that the two convective processes influence how DCCs evolve over their entire lifetimes. To further investigate how convective processes impact structure and lifecycle, we use the composite area approach described in section 4.3.4 to show how the thin anvil fraction evolves over the anvil lifecycle for DCCs with differing core cooling rates and number of cores.

<sup>2485</sup> Figure 4.13 shows composites of the thin anvil fraction for DCCs group by core cooling rate, with larger cooling rates shown in darker shades of blue. Each of the composites has a similar shape to the evolution of thin anvil fraction shown in fig. 4.3 b; an initial rapid increase as the anvil develops, a plateau during the maturing stage and a continual increase as the anvil dissipates. Two sections of the lifecycle show <sup>2490</sup> divergence in the thin anvil fraction with core cooling rate. Firstly, more intense cores produce a higher thin anvil fraction during the developing phase. This difference in thin anvil fraction is then maintained throughout the mature phase. Secondly, the

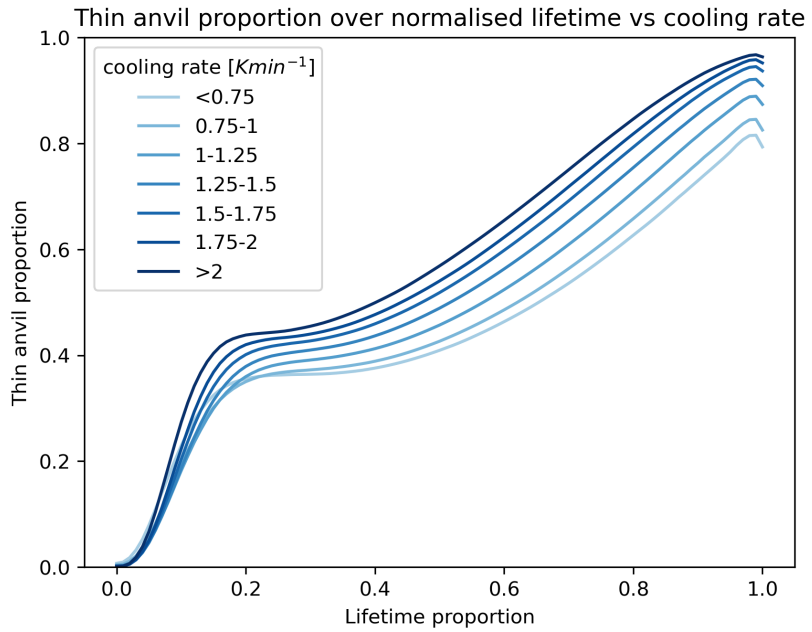


Figure 4.13: Mean thin anvil proportion for composites of anvil area of normalised lifetime categorised by the cooling rate of their initial cores. More intense core cooling rates are shown by the darker blue lines.

thin anvil fraction further diverges during the dissipating phase, with the anvils originating from more intense cores having a larger increase in thin anvil fraction. This  
 2495 difference during the dissipating stage may be related to the difference in the thin anvil lifetime seen previously.

In fig. 4.14 we compare how the mean thin anvil fraction changes for composites grouped by the number of cores. The composites with a greater number of cores are shown by the darker shades of red. In contrast to fig. 4.13, we see a difference from  
 2500 the typical shape of the thin anvil fraction established in fig. 4.3 for more organised DCCs. At the end of the initial development phase of the anvil we see a similar thin anvil fraction of  $\tilde{0.4}$  across all cases. While the more organised DCCs reach this point faster, this is simply due to the initial anvil time making up a smaller proportion of the total lifetime due to the latter's increase with organisation.

2505 After the initial development of the anvil, we see a divergence in the thin anvil

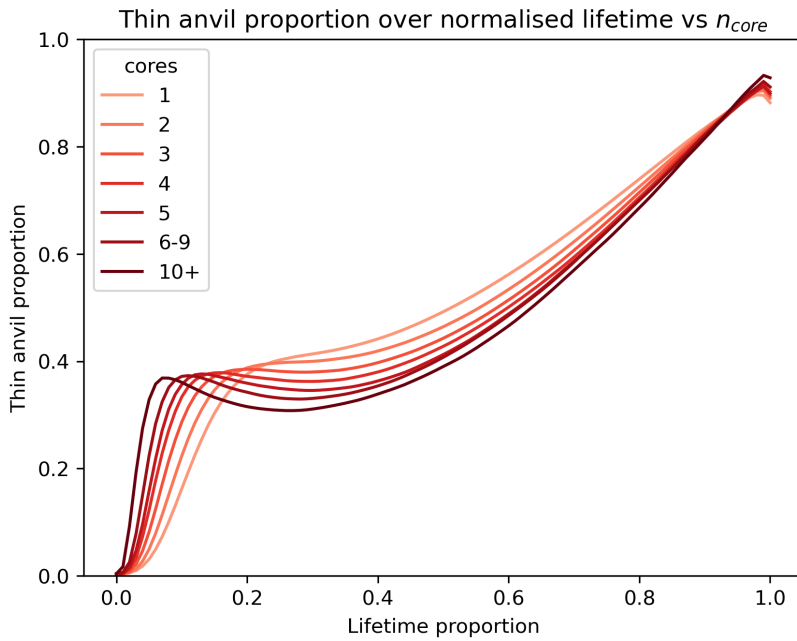


Figure 4.14: Mean thin anvil proportion for composites of anvil area of normalised lifetime categorised by the number of cores. Anvils with a larger number of cores are shown by the darker red lines.

fraction during the later growing stage and the mature stage. For the most organised DCCs, we observe a reduction in the thin anvil fraction during this period, indicating that the continuous, organised convection from multiple convective cores leads to a thickening of the anvil. This difference in thin anvil remains into the dissipating 2510 stage, however the composites all converge to a similar fraction by the end of their lifecycles.

The investigation of changes in thin anvil fraction over DCC lifecycle using composites reveals further complexity to the response of thin anvil structure to convective processes. Not only do changes in intensity and organisation have contrasting effects 2515 on the net thin anvil fraction and the lifecycle, they also impact the anvil structure at different stages throughout the DCC lifetime. The timing of when then differences in structure are seen may help in investigating the processes through which they occur.

## 4.5 Summary

Deep convective anvil clouds have a characteristic ToA CRE that is near neutral  
2520 [Hartmann, 2016]. Anvils are, however, not homogeneous objects, and exhibit structures that transition from thick near the convective cores to thin, detrained cirrus further away. The tendency of reflectivity to reduce faster than emissivity with reducing cloud optical thickness, combined with the large SW and LW CRE of anvils, means that the CRE varies widely with changing thickness [Berry and Mace, 2014].  
2525 Despite this, the response of anvil optical properties to climate change remains largely uncertain, in part due to the lack of data connecting the behaviour of convective cores and anvils Gasparini et al. [2023].

Previous studies have found that the fraction of thin anvil increases with increasing convective intensity [Protopapadaki et al., 2017; Takahashi et al., 2017b]. These  
2530 studies were performed using sun-synchronous polar-orbiting satellite data, and so could not resolve changes across the lifecycle of DCCs. With the dataset of tracked DCC cores and anvils we can relate changes in the convective properties to changes in structure observed over the entire anvil lifecycle.

Using the initial core cooling rate and number of cores as proxies for the intensity  
2535 and organisation of convection respectively, we find a similar increase in thin anvil fraction with increasing intensity, but a decrease with increasing organisation. The relationships are found to be robust across a wide range of convective environments. We also find contrasting impacts on DCC lifecycle as a result of both processes. In more intense DCCs, we see a reduction in the growing phase and an increase in  
2540 the thin anvil lifetime, whereas we see the opposite in more organised cases. These corresponding changes in lifecycle indicate that the thin anvil fraction cannot be determined from single snapshots alone.

By analysing composites of the change in thin anvil fraction over the DCC lifecycle, we see that the impacts of intensity and organisation also occur at different periods

2545 during the DCC lifetime. The timing of these changes also indicates which processes may be impacting the anvil structure in each case. For the more intense convection, we see an increase in the thin anvil fraction during the initial formation of the anvil, which is then maintained as the anvil matures. Studies of anvil evolution in high-resolution convective resolving models have shown that, during the initial growth of  
2550 the anvil, before the development of compensating downdrafts within the core, the divergence of the anvil is directly linked to the updraft velocities within the core [Senf et al., 2018b]. After the formation of compensating downdrafts after around 15–20 minutes, this connection is broken which may explain why this difference only occurs during the very early formation of the anvil.

2555 We also see a second period of increasing difference in thin anvil fraction during the dissipating stage of the DCCs. As this occurs after the end of the convective updrafts, it cannot be related directly to the convective processes but instead to their impact on the anvil properties. Over the lifetime of anvils, radiative heating of the cloud base and cooling of the cloud top result in circulations within the anvil cloud  
2560 which have a thinning effect [Gasparini et al., 2019]. Once the anvil is sufficiently thin however (with optical depths around 1), these radiatively driven circulations cease and instead the remainder of the dissipation occurs due to the sedimentation and sublimation of the remaining thin cirrus [Sokol and Hartmann, 2020]. At the higher altitudes and colder temperatures of the anvils produced by more intense convection  
2565 these processes are substantially slower [Seeley et al., 2019a], potentially resulting in larger extents and lifetimes for the thin, but not thick, anvil.

For more organised DCCs we observe a reduction in the thin anvil fraction not during the initial anvil formation but during the subsequent growing and maturing period of the anvil. Unlike isolated systems, we expect the continuous development of  
2570 new convective cores throughout most of the lifecycle of the more organised DCCs. It is possible that the thickening is a result of the mesoscale circulations associated with

large, organised MCSs, which transports additional moisture directly into the anvil where it increases the cloud water content at high levels. Alternatively, convective aggregation may result in moister environments surrounding the cores of these organised DCCs, slowing the dissipation of the thick anvil, and also drying the surrounding regions resulting in faster decay of the thin anvil further from the core. The convergence of the thin anvil fraction during the dissipating phase of DCCs is indicative of the characteristic decay patterns seen in convective anvils across scales [Roca et al., 2017; Elsaesser et al., 2022].

Further investigation of how these processes impact anvil structure and lifecycle may be difficult due to the lack of time-resolved observational data that can measure these processes. The use of modelling, including both convective resolving models and more idealised experiments, may provide a route to isolate the impacts of each process on DCC evolution [Gasparini et al., 2022].

The final element to consider is how these observed changes in anvil structure may impact the anvil CRE. Considering the thin anvil fraction alone, we could expect that more intense DCCs are more warming due to their thinner structure, and vice versa for more organised convection. However, this neglects other factors relevant to anvil CRE that are also impacted by convective processes. Both convective intensity and organisation affect the temperature of anvil clouds, resulting in a warming effect for increases in both. Furthermore, the observed changes in the lifecycle and the timing of the maximum extent of the thick anvil within the DCC lifetime may impact the SW CRE, particularly over land due to the pronounced diurnal cycle of convection. Observational studies have, shown a link between increasing convective organisation and domain mean ToA cooling [Bony et al., 2020]. While this has traditionally been explained as a result of greater clear sky LW emissions to space [Bony et al., 2016], this could also result from the response of anvil CRE to changes in structure.

# Chapter 5

## **The Lifecycle and Cloud Radiative Effect of Deep Convective Clouds Over Africa**

### **5.1 Introduction**

DCC play a key role in the tropical atmosphere. Forming the ascending branch of the Hadley cells near the equator, DCCs are critical to the circulation and heat transfer of the tropics [Riehl and Malkus, 1958; Weisman, 2015]. DCCs are also a cause of extreme weather events including floods, lightning and hail [Westra et al., 2014]. MCS—large, long-lived convective systems in which the anvils of multiple convective cores combine into a single, large ‘cloud shield’ [Chen and Houze, 1997; Houze, 2004; Roca et al., 2017]—are responsible for the majority of precipitation in the tropics [Feng et al., 2021]. Changes in the behaviour of DCCs with climate change have the potential for major impacts on the atmosphere, weather and society.

DCCs also exert a key influence on the temperature of the tropics through their CRE. Due to their size, height and depth, DCC anvils have large radiative effects in both the SW and LW, with both having average magnitudes in excess of  $100 \text{ W m}^{-2}$  [Hartmann, 2016; Wall and Hartmann, 2018]. However, due to the opposite signs of these two components, the average anvil CRE in the tropics is approximately zero [Ramanathan et al., 1989; Hartmann et al., 1992; Stephens et al., 2018]. Radiation

is also key to the lifecycle of DCCs. Over land, convection is typically initiated by the heating of the surface and lower troposphere by solar SW radiation, resulting in a peak of convective activity in the late afternoon. Over the ocean, however, convection is often triggered by LW cooling of the upper troposphere, and so convective activity occurs more frequently in the morning. However, the occurrence of convection is more uniform throughout the diurnal cycle compared to that over land [Taylor et al., 2017]. Radiation also has an impact on DCC lifecycle through the differential heating of the anvil cloud, which destabilises the anvil cloud leading to dissipation due to entrainment and evaporation. However, SW heating of the anvil cloud top during daytime acts to stabilise and delay this process, leading to differences in anvil lifetime depending on the diurnal cycle [Harrop and Hartmann, 2016; Sokol and Hartmann, 2020; Wall et al., 2020].

Much of the focus on the anvil CRE feedback to global warming has been placed on the LW response, either to a change in anvil cloud area [Lindzen et al., 2001; Bony et al., 2016] or anvil cloud height [Hartmann and Larson, 2002; Seeley et al., 2019b]. While these mechanisms have competing effects, and so may act to maintain the neutral anvil CRE, there are large uncertainties associated with these feedbacks [Sherwood et al., 2020] and other feedbacks may be underestimated [Hill et al., 2023]. In addition, these mechanisms ignore changes in the SW CRE of anvil clouds, which may be affected by changes in cloud microphysics [Ramanathan et al., 1989; Gasparini et al., 2023]. Furthermore, changes in the diurnal cycle of convection over Africa may lead to changes in CRE of  $\pm 10 \text{ Wm}^{-2}$  [Nowicki and Merchant, 2004]. Further investigation into the response of anvil CRE to changes in the diurnal cycle highlighted the need for cloud tracking approaches to study CRE over the anvil lifetime [Bouniol et al., 2016, 2021].

In this chapter, we use a novel cloud tracking methodology in conjunction with derived all-sky and clear-sky radiative fluxes to characterise the CRE over the life-

cycles of individual anvil clouds. This methodology is applied to 4 months of data produced for the ESA Cloud-Climate Change Initiative (CCI)+ project over sub-Saharan Africa. This dataset allows us to investigate both the CRE of individual CREs, as well as the net anvil CRE over the entire region. We find that the overall distribution of anvil CRE is determined by the relationship between DCC lifecycle and the diurnal cycle of the SW CRE, and discuss the implications of this for the response of DCCs to a changing climate.

## 5.2 Data

For this case study, we used data from SEVIRI [Aminou, 2002] aboard the Meteosat Second Generation (MSG) Meteosat-11 satellite, which is in a geostationary orbit above the equator at 0°W. We use data from 4 months (May–August 2016) over sub-Saharan Africa (approximately 18 °W–46 °E, 31 °S–15 °N) at the full resolution of SEVIRI (3 km at nadir) as well as retrieved cloud properties and derived broadband fluxes produced by the ESA Cloud-CCI+ project. BT from SEVIRI is used by the tracking algorithm, and reflectances and BT are used by the cloud retrieval.

Channel	Wavelength ( $\mu\text{m}$ )	Description	Tracking	Retrieval
1	0.64	Visible		✓
2	0.81	NIR		✓
3	1.64	NIR		✓
4	3.92	NIR Window		✓
5	6.25	Upper troposphere WV	✓	✓
6	7.35	Lower troposphere WV	✓	✓
7	8.70	Mid-IR window		
8	9.66	Ozone		
9	10.8	Clean LW window	✓	✓
10	12.0	Dirty LW window	✓	✓
11	13.4	$\text{CO}_2$		✓
12	0.6–0.9	High-resolution visible		

Table 5.1: SEVIRI channels and their use in the DCC tracking algorithm and cloud properties retrieval.

2660 SEVIRI is a visible and IR radiometer with a nadir spatial resolution of 3 km and a  
temporal sampling time of 15 minutes for the full earth disc. SEVIRI has 12 channels  
across the visible, NIR and thermal-IR spectrum, with one being a high-resolution  
visible channel with a nadir resolution of 1 km. A brief overview of these channels,  
along with which are used for tracking DCCs and the cloud properties retrieval, is  
2665 provided in table 5.1.

An example of observations from SEVIRI is shown in fig. 5.1 for 15:00:00 UTC on  
1<sup>st</sup> June 2016. A visible composite (fig. 5.1 a) is constructed using the 1.64  $\mu\text{m}$  and  
0.81  $\mu\text{m}$  near-infrared and 0.64  $\mu\text{m}$  visible channels for the RGB channels respectively.  
In this composite, ice clouds (which appear cyan) can be seen over central Africa and  
2670 the southern Atlantic. fig. 5.1 b shows the 10.8  $\mu\text{m}$  brightness temperature for the  
same scene, showing the coldest temperatures for the high ice clouds over central  
Africa. Two combinations of channels are used for the detection of anvil clouds. The  
WVD, shown in fig. 5.1 c, consists of the 6.3  $\mu\text{m}$  BT minus the 7.4  $\mu\text{m}$  BT. In clear  
skies the WVD is negative, with values around  $-20$  to  $-15$  K, due to the higher, and  
2675 thus colder, emission height of the 6.3  $\mu\text{m}$  channel. In high, thick clouds, however,  
the temperatures of the 6.3 and 7.4  $\mu\text{m}$  channels converge and so the WVD becomes  
closer to 0. In the cases of the highest clouds, the WVD can become positive due to  
emission from stratospheric WV in the 6.3  $\mu\text{m}$  channel. The SWD, shown in fig. 5.1 d,  
consists of the 10.8  $\mu\text{m}$  BT channel minus the 12.0  $\mu\text{m}$  channel. While the SWD is  
2680 sensitive to near-surface WV due to absorption in the 12.0  $\mu\text{m}$  channel, it is also  
sensitive to thin ice clouds due to the difference in emissivity of ice particles between  
the two channels. While for thick clouds the SWD will be 0 K, for thin ice clouds the  
lower emission height of the 10.8  $\mu\text{m}$  BT channel results in a positive value of 5 K.  
The 10.8  $\mu\text{m}$  and 12.0  $\mu\text{m}$  channels of SEVIRI have relatively wide wavebands and as  
2685 such are less sensitive to the presence of thin ice clouds. As a result, we found that  
the detection of thin anvil is unreliable using this technique with SEVIRI, and so is

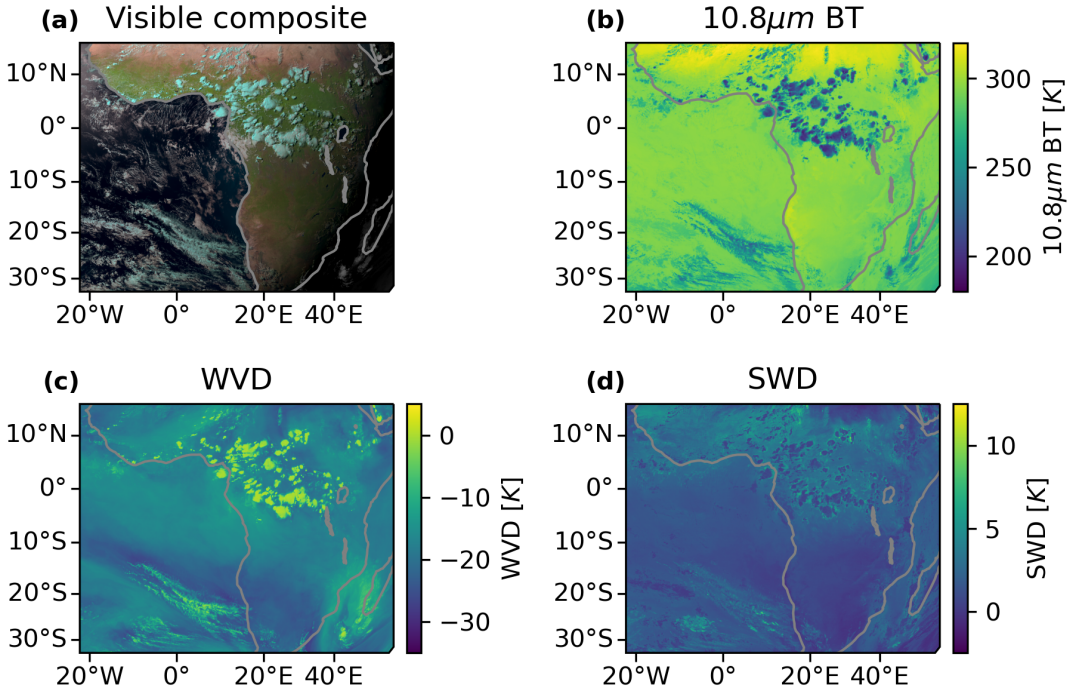


Figure 5.1: Example observations from the Meteosat SEVIRI instrument at 15:00:00 UTC on 2016/6/01. a: A visible composite formed using the 1.6, 0.81 and 0.64  $\mu\text{m}$  channels as the RGB channels respectively, with 10.8  $\mu\text{m}$  BT during the night-time. The scene shows a cluster of cold cloud tops (cyan) over central Africa and over the Southern Atlantic. b: 10.8  $\mu\text{m}$  BT. c: WVD formed by the 6.3  $\mu\text{m}$  channel minus the 7.4  $\mu\text{m}$  channel. d: SWD formed by the 10.8  $\mu\text{m}$  channel minus the 12.0  $\mu\text{m}$  channel.

not considered within this chapter.

Retrieved cloud properties, including optical thickness, effective radius, liquid/ice water path, CTT and height, are provided by the Community Cloud Retrieval for Climate (CC4CL) algorithm [Sus et al., 2018; McGarragh et al., 2018]. These properties are all retrieved at the same resolution as the input SEVIRI data. Broadband fluxes are derived using the BUGSRad radiative transfer model [Stephens et al., 2001] using input cloud properties from the CC4CL retrieval and vertical temperature, moisture and trace gas profiles from ERA-5 [Hersbach et al., 2020]. The BUGSRad model provides ToA and Bottom-of-Atmosphere LW and SW radiative fluxes for both all-sky and clear-sky conditions. An example of these derived fluxes is shown in fig. 5.2.

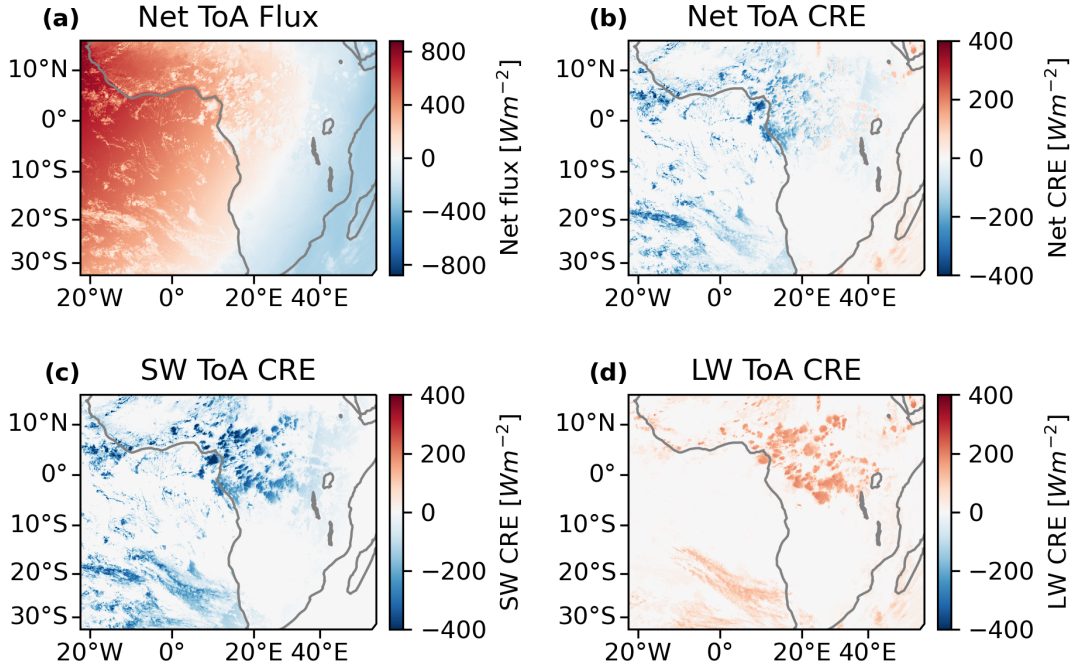


Figure 5.2: An example of the ToA CRE derived using the radiative flux model, for the same time as shown in fig. 5.1 (15:00:00 UTC on 2016/6/01). a: net ToA radiative flux. b: net ToA CRE. c: SW downwards CRE. d: LW downwards CRE.

Figure 5.2 a shows net ToA fluxes, with a net warming during the daytime on the Western side of the image, and a net cooling at night-time on the Eastern side. Figure 5.2 b shows the net ToA CRE, with a net cooling effect during the daytime and warming during the night-time for observed high clouds over central Africa. The SW (fig. 5.2 c) and LW (fig. 5.2 d) components of the CRE show that while the LW, warming component has a smaller magnitude than the day-time, cooling SW CRE, it remains constant during both day- and night-time.

Validation of the SEVIRI broadband fluxes was performed against monthly-mean observations of ToA broadband CRE from the Clouds and the Earth's Radiant Energy System (CERES) [Loeb et al., 2018] Energy Balanced and Filled (EBAF) climate data record. The results of this validation are shown in fig. 5.3. Monthly mean fluxes were calculated for SEVIRI by first calculating the mean daily fluxes over each  $1 \times 1^\circ$  grid

square for days in which we have over 23 hours of observations, and then averaging  
2710 these daily means over each month. Comparison of the net ToA CRE to CERES revealed a bias of  $-3.67 \text{ Wm}^{-2}$  (fig. 5.3 a,b), consisting of a SW bias of  $-3.04 \text{ Wm}^{-2}$  (fig. 5.3 c,d) and a LW bias of  $-0.63 \text{ Wm}^{-2}$  (Fig 5.3 e,f). Correction for these biases have been applied uniformly to all further CRE values given in this chapter.

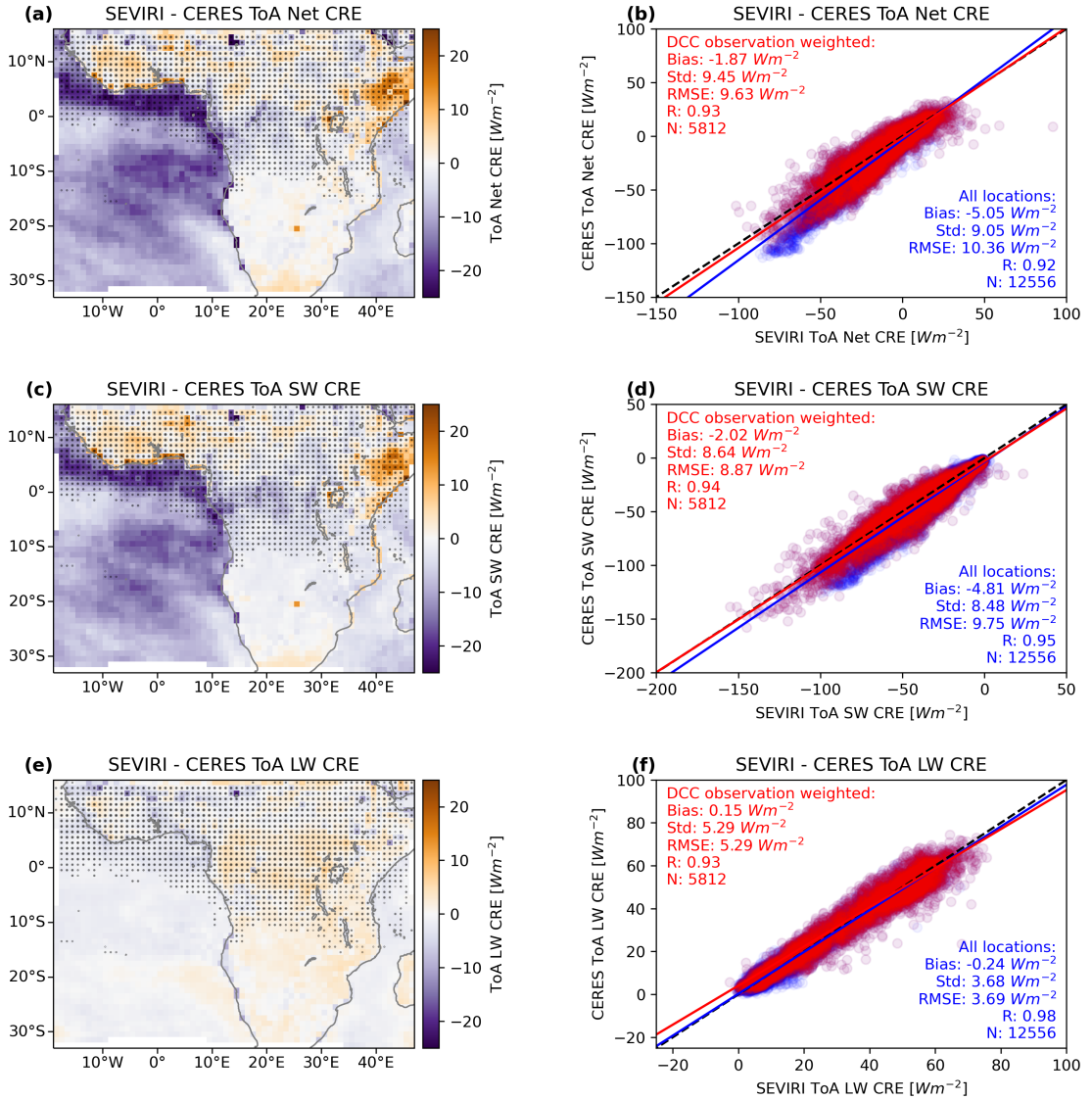


Figure 5.3: Validation of derived broadband fluxes against monthly CERES-EBAF CRE. a.: The mean difference in net ToA CRE by  $1 \times 1^\circ$  grid square. b.: A comparison of observed ToA net CRE for SEVIRI against CERES, with all locations in blue, and those where we observe DCC anvils in red. c.: the mean difference in SW ToA CRE. d.: comparison of SW ToA CRE for SEVIRI and CERES. e.: the mean difference in LW CRE. f.: comparison of LW ToA CRE. The stippling in a, c and e represents the locations in which we observe DCC anvils, with the size of the dots corresponding to the number of observations. The solid lines in b, d and f show the linear regression for all locations (blue) and the locations where we observe DCC anvils (red) weighted by the number of observations.

### 5.3 Method

2715 The detection and tracking of DCCs was performed using the tobac-flow algorithm [Jones et al., 2023a], which has been designed specifically to track both isolated and clustered DCCs in geostationary satellite imagery over their entire lifecycle. While geostationary satellite imagery provides high-resolution observations over large domains and long time periods, which is ideal for studying deep convection, the inability  
2720 of passive remote sensing to observe convective updrafts directly makes the detection and tracking of DCCs difficult.

Algorithms for the detection and tracking of DCCs in satellite imagery have generally been developed for one of two applications: tracking convective cores and isolated convection, or tracking large MCS anvils. Those designed for tracking deep convective cores, or isolated DCCs, include Cb-TRAM [Zinner et al., 2008, 2013] or tobac [Heikenfeld et al., 2019]. These algorithms work by detecting regions of convective updraft or a proxy (such as cloud top cooling rate), and then treating these regions as point-like objects that are advected over time. The second group, designed for tracking MCSs, include algorithms such as PyFLEXTRKR [Feng et al., 2022], TAMS [Núñez Ocasio et al., 2020] or TOOCAN [Fiolleau and Roca, 2013]. These algorithms detect large regions of cold cloud tops which indicate anvil clouds, and then link them over time by overlapping regions at subsequent time steps. There is no ‘best’ method for tracking all types of convection however [Lakshmanan and Smith, 2010]. The algorithms for tracking isolated convective cells perform worse for clustered convection  
2735 when the motion and shape of the DCC cannot be adequately represented as a single vector. On the other hand, the MCS tracking algorithms perform worse for smaller, isolated DCCs as the motion of the anvil between time steps may mean it does not overlap with the previous step.

To approach the challenge of tracking both isolated DCCs and large, clustered systems, we address the role of cloud motion in the scaling problem. tobac-flow first

estimates the motion of DCCs at each pixel using an optical-flow algorithm. Then, using these estimated motion vectors, we construct a semi-Lagrangian framework in which to perform the detection and tracking. This approach addresses two issues found in traditional cloud tracking approaches. First, estimating a motion vector  
2745 for each pixel allows complex motions (including divergence, rotation, splitting and merging) to be compensated for, rather than just the bulk motion found using the centroid tracking methods. Second, by estimating the cloud motion *a priori*, we are able to use this information within the detection step of the algorithm, and can separate changes in cloud properties such as BT from those observed due to cloud motion.  
2750 This framework removes the problem of DCC motion, allowing us to track both isolated and large DCCs at the same time.

Three channels and channel combinations from SEVIRI are used for the detection algorithm: the 10.8  $\mu\text{m}$  BT channel; the WVD (the difference between the 6.2  $\mu\text{m}$  and 7.3  $\mu\text{m}$  channels), and the SWD (the difference between the 10.8  $\mu\text{m}$  and 12.0  $\mu\text{m}$  channels). Estimation of cloud motion vectors using optical flow is performed using  
2755 the 10.8  $\mu\text{m}$  BT channel. Detection of cores utilises the 10.8  $\mu\text{m}$  BT channel and the WVD, and detection of anvils uses WVD and SWD.

We detect growing convective cores where we observe regions of rapid cooling in the 10.8  $\mu\text{m}$  BT channel of greater than  $0.5 \text{ K s}^{-1}$  and the WVD of greater than  
2760  $0.25 \text{ K s}^{-1}$ . In both cases DCCs close to the surface and continue tracking them into the upper troposphere. We classify a core as a region of cooling temperature that has existed for at least 15 minutes and has cooled by at least 8 K in a 15-minute period. This threshold provides a strong indicator of intense convective activity [Roberts and Rutledge, 2003], and so provides an accurate detection of growing DCCs.

2765 Starting from these convective cores, we then detect the surrounding anvil cloud using the WVD field [Müller et al., 2018, 2019] and continue to detect the anvil until its dissipation, even after the core is no longer visible. A core and anvil are

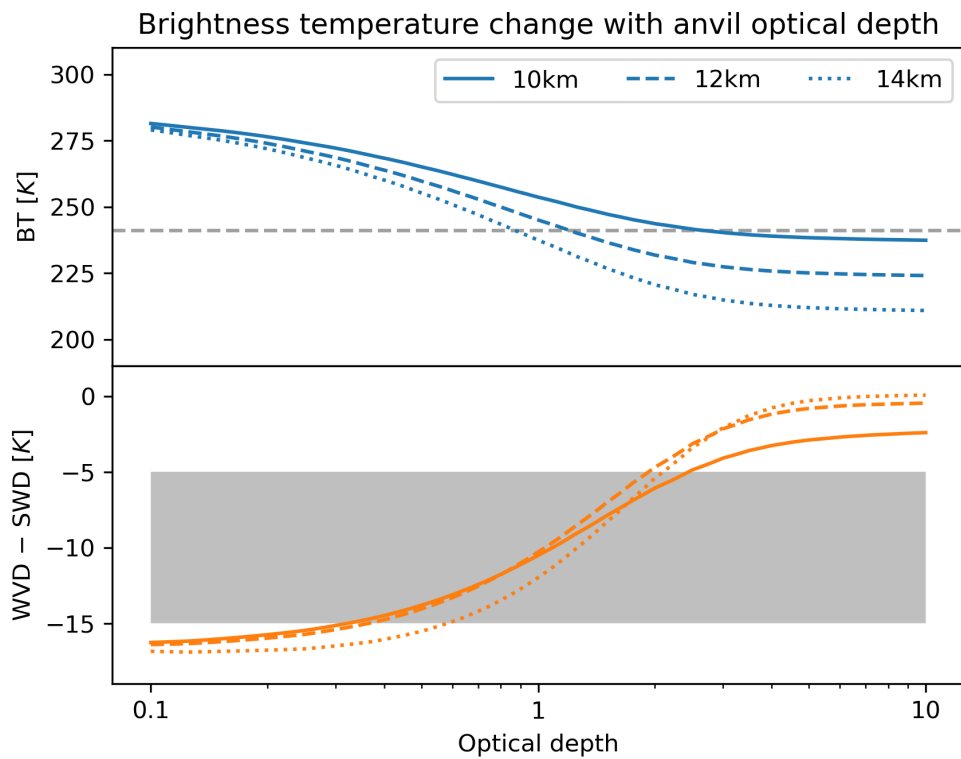


Figure 5.4: Simulated sensitivity of the SEVIRI 10.8  $\mu\text{m}$  BT (top) and WVD minus SWD (bottom) to anvil clouds of varying optical thickness at heights of 10, 12 and 14 km. The LibRadTran model was used to estimate the observed radiances, and all simulations used ice clouds with cloud top particle effective radius of 20  $\mu\text{m}$ . The grey dashed line shows the 241 K BT, which, although commonly used as a threshold for anvil detection in satellite imagery, shows large sensitivity of the minimum optical thickness detected with the height of the anvil cloud. The grey region in the lower plot shows the range of temperatures in which the edge of the anvil is detected, as described in chapter 2. Similar sensitivity is found for all three cloud heights, with the optical depths of around 1–1.5 seen in the middle of the hysteresis region. The median minimum retrieved optical depth of all tracked anvils in our dataset is found to be 1.45, although this value is biased high by the inability to retrieve optical depth accurately at night time.

linked with each other if the two overlap at a time when the core has mean WVD of  
2770 >5 K, indicating that it has reached the upper troposphere. Each anvil cloud can be  
associated with multiple cores, allowing us to identify cases of clustered convection. As  
we detect the cores based on cloud-top cooling, however, we can only detect the cores  
themselves during the growing phase, and cannot detect cores that occur underneath  
cold, high, anvil clouds. When determining the number of cores associated with an  
anvil, we count the total number of cores observed over the entire lifetime, even if  
2775 they do not occur at the same time, and including all merges and splits of the anvil  
cloud. This flexibility allows for a wide range of different organised systems to be  
analysed.

Due to the lack of sensitivity of the SEVIRI SWD to thin ice clouds, we only  
detect and track the thick portion of the anvil in this chapter. The WVD channel of  
2780 SEVIRI is capable of detecting anvils with optical thicknesses of approximately 1–1.5  
(see fig. 5.4). However, the closer spacing and narrower bandwidth of the SEVIRI  
LW window channels (see fig. 5.5), along with the higher noise means that the SWD  
is less sensitive to thin cirrus compared to instruments such as the GOES-16 ABI (see  
fig. 5.6). The anvils tracked in this paper have a median retrieved minimum optical  
2785 depth of 1.45, although this value is likely biased high as many anvils dissipate at  
night when accurate satellite retrievals of optical depth are not available. While this  
sensitivity captures much of the CRE of DCC anvils [Berry and Mace, 2014] the long  
lifetimes of dissipating thin anvils may have a significant warming contribution to net  
anvil CRE [Horner and Gryspeerdt, 2023]. As a result, it is expected that the anvil  
2790 CRE measured in this study is biased low.

An example of the cores and anvils detected by the tobac-flow algorithm is shown  
in fig. 5.7, at 3-hour intervals. In fig. 5.7 a, we see a large number of developing cores  
over central Africa. In fig. 5.7 b, we see more developing cores over Western Africa as  
the pattern of initiation has shifted with the diurnal cycle. In fig. 5.7 c,d we observe

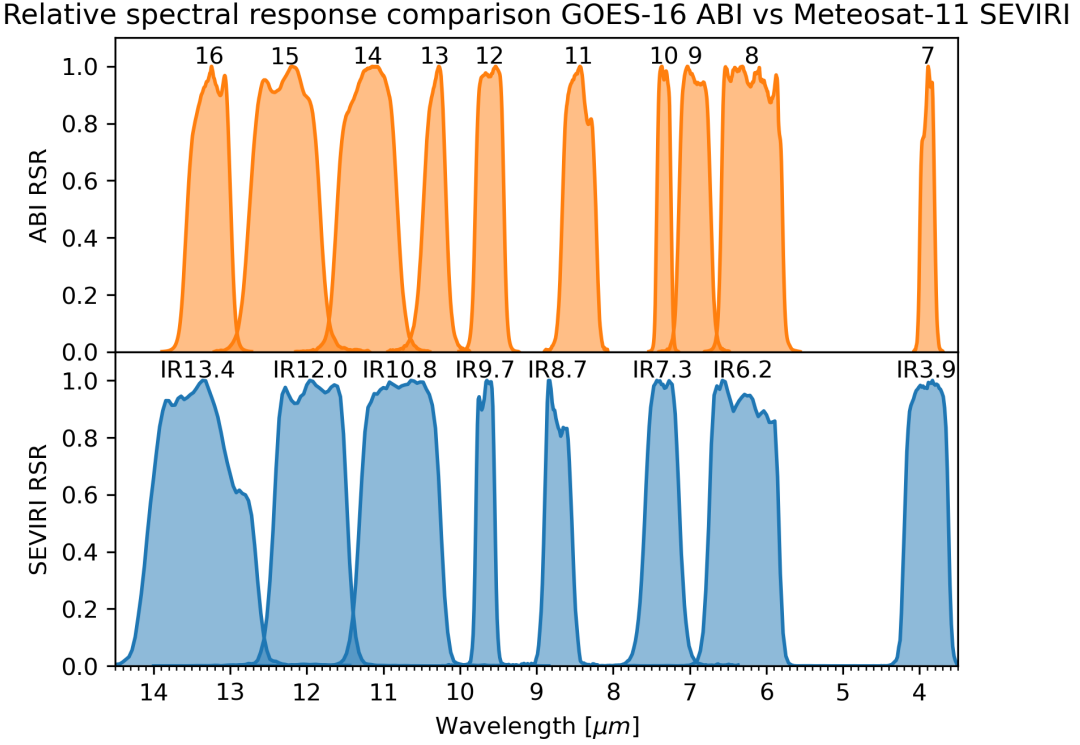


Figure 5.5: Comparison of the relative spectral response (RSR) functions for the GOES-16 ABI and Meteosat-11 SEVIRI thermal IR channels. The LW window channels on ABI (channels 13 and 15) have a wider spacing than those of SEVIRI (channels IR10.8 and IR12.0). This wider spacing allows ABI to be more sensitive to the emissivity difference of ice clouds at wavelengths between 10 and 12  $\mu\text{m}$ , and so it is better able to detect thin cirrus clouds.

<sup>2795</sup> fewer new developing cores later in the day, but the larger anvil clouds persist into the night-time.

Over the 4-month period of the case study we track a total of 145,463 cores (of which 79,592 are associated with anvil clouds) and 35,941 anvils. Using the detected regions of both core and anvil components of tracked DCCs, the cloud properties and <sup>2800</sup> CRE are calculated for each DCC at each time step from the retrieval and broadband fluxes data. The resulting dataset allows us to analyse the properties of each DCC over their lifetimes from a Lagrangian perspective. While the studied domain contains both land and sea regions, only a small proportion of tracked DCCs occurred over

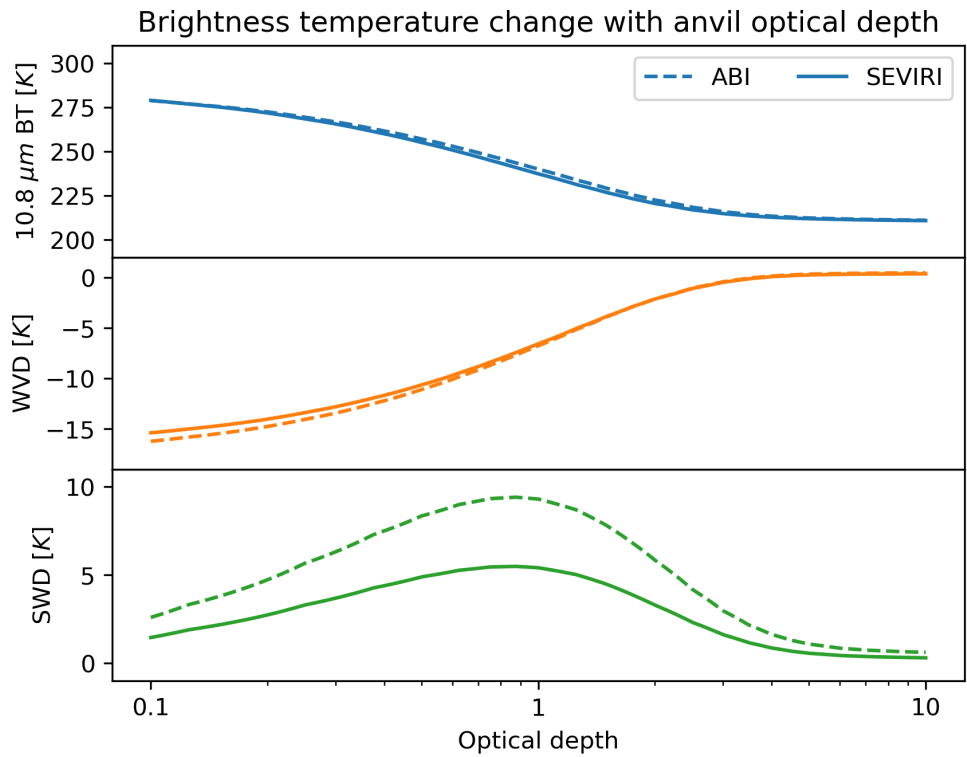


Figure 5.6: Comparison of the sensitivities of ABI (dashed lines) and SEVIRI (solid lines) to anvil clouds of different optical thickness, using the LibRadTran simulation of an anvil at 14 km as used in fig. 5.4. The  $10.8 \mu\text{m}$  BT (top panel) and WVD (middle panel) show very similar values for both instruments. The simulations of the SWD (bottom panel) show that SEVIRI is only about half as sensitive as ABI to thin ice clouds.

sea (11%), and so we have not separated the analysis of land and oceanic DCCs in

2805 this chapter.

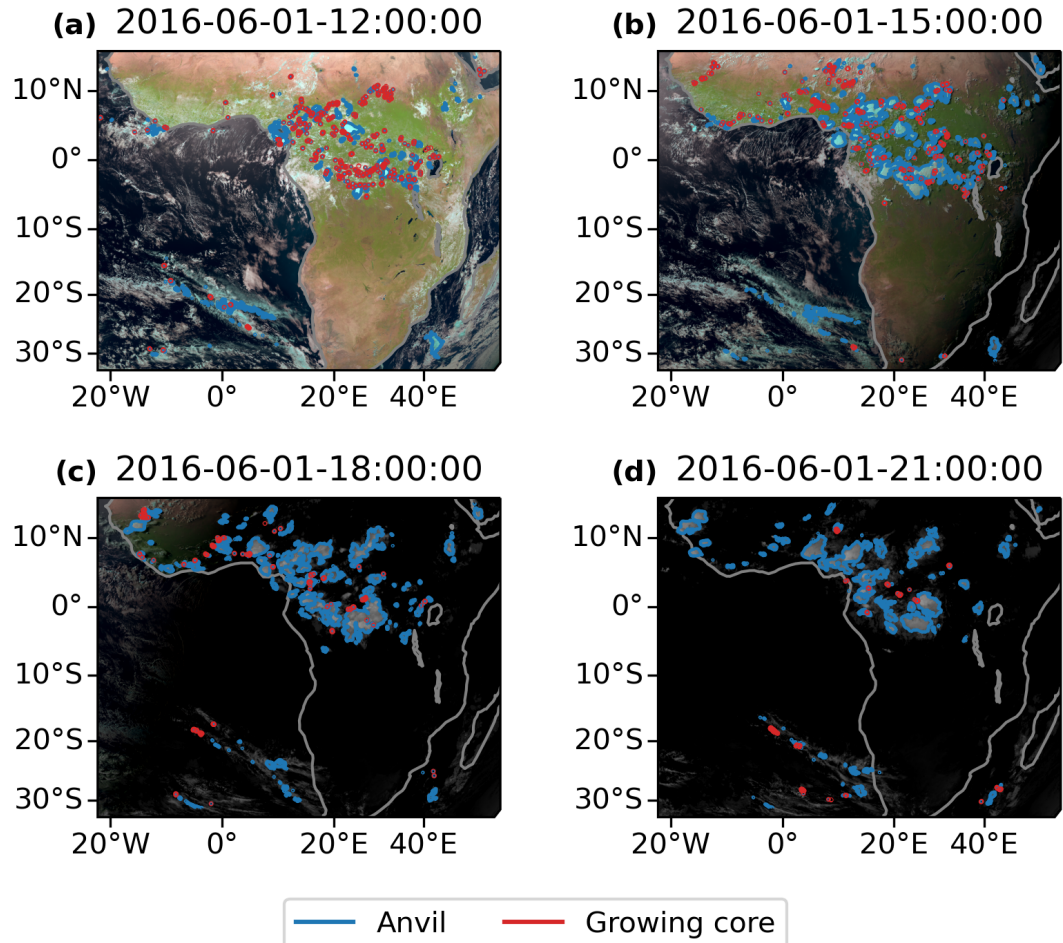


Figure 5.7: An example of the cores (red outline) and anvils (blue outline) detected by tobac-flow plotted over visible composite imagery from SEVIRI, shown at 3-hour time intervals. All times are given in UTC.

## 5.4 Results

### 5.4.1 Spatial and temporal distributions

Figure 5.8 a shows the frequency of core detections for each  $1 \times 1^\circ$  grid square over the period of the case study. The majority of observed convection occurs over the tropical rainforest regions. During the months of May-August, the Inter-Tropical Convergence Zone (ITCZ) is at its northernmost extent over Africa [Nicholson, 2018]. The West African monsoon occurs during these months, with the primary band of convection located between 5-15°N [Nicholson, 2009], which our observations agree with. We

observed the maximum frequency of convection at around 6°N, 12°E over the Western  
2815 High Plateau of Cameroon, with high frequencies of convection also observed over the Nigerian coastal plains to the West and the Jos Plateau in Northern Nigeria. High rates of convection are also observed over the coastal plains and inland highlands of Guinea, Sierra Leone and Liberia (5–12 °N, 5–15 °W)

Figure 5.8 b shows the average time of detection for convection in each  $1 \times 1$ °grid square. The average is calculated as the circular mean of the local solar times of core detection in the grid square. Grid squares with a standard deviation greater than 6 hours (indicating a broad spread of initiation times) are given single hatching, and those with standard deviations greater than 12 hours have cross-hatching. The most notable feature of the time of detection is the clear contrast between land and sea.  
2820 Convection over the land tends to occur in the afternoon (15:00–18:00), whereas over the ocean it occurs between midnight and early morning (00:00–09:00). Furthermore, convection over land tends to occur in a fairly narrow range of times whereas over the ocean convection occurs throughout the diurnal cycle, resulting in the hatching applied to much of the ocean region. There is also a noticeable lake effect on the time  
2825 of convection occurring over Lake Victoria (2°S, 34°E) and Lake Tanganyika (7°S, 31°E), with convection typically observed in the early morning.

When we compare the regions of Cameroon and Nigeria (4–10°N, 6–14°E), where we detect the most cores in fig. 5.8 a, with the average time of detection in fig. 5.8 b, we see that the grid squares with more cores also tend to have an earlier average  
2835 time of detection than the surrounding grid squares. Precipitation over the Nigerian plains and the Jos Plateau is linked to South-westerly winds bringing moist, warm air from the Gulf of Guinea [Vondou et al., 2010]. This warm air may then trigger convection both through the sea breeze effect and orographic lifting when it reaches the highlands, explaining both the higher frequency and earlier timing of convection  
2840 compared to surrounding regions. A similar relationship between the high frequency

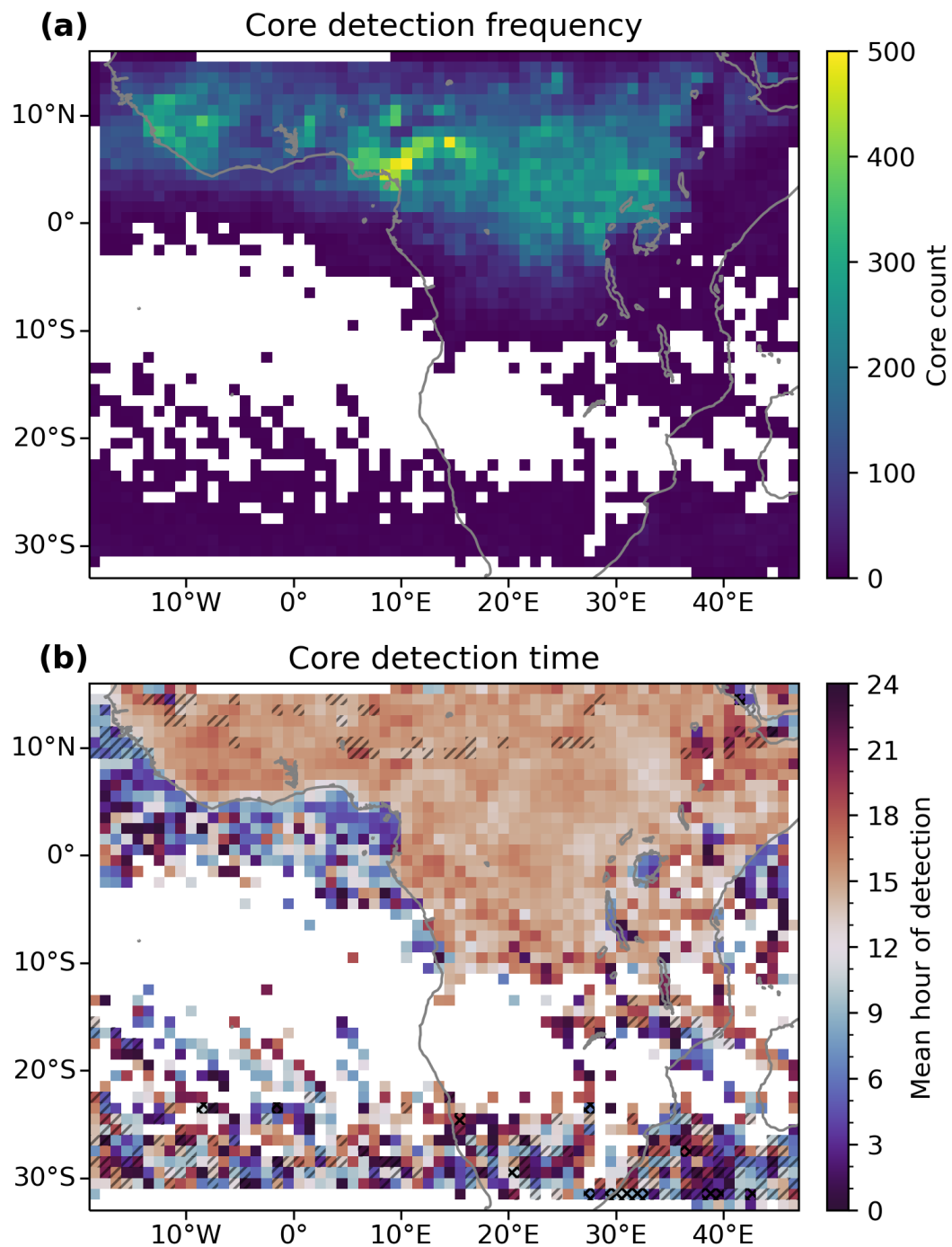


Figure 5.8: a.: The total number of DCC cores detected over the case study for each  $1 \times 1^\circ$  grid box. b.: The average hour of detection for the cores detected in each  $1 \times 1^\circ$  grid box. Grid boxes with a standard deviation greater than 6 hours are single-hatched, and greater than 12 hours cross-hatched.

of convection and earlier time of detection is also seen over the coastal region and adjacent highlands of Guinea, Sierra Leone and Liberia ( $5\text{--}12^\circ\text{N}$ ,  $5\text{--}15^\circ\text{W}$ ) which may be due to the same mechanism.

It should be noted that due to the method of detection, cores that develop under existing anvils are less likely to be detected than those in clear sky regions. As a result, we may underestimate the occurrence of later occurring cores, particularly in regions such as the Northern Sahel where a second, night-time peak of precipitation has been observed.

For all further analysis, we consider only cores and anvils that are detected north of  $15^\circ\text{S}$  in order to constrain our analysis to tropical DCCs.

#### 5.4.2 Anvil Cloud Properties

To investigate how the behaviour of DCC anvils is affected by their organisation, we group observed anvils based on how many cores are associated with them, from isolated DCCs with one core to highly-clustered DCCs (such as tropical cloud clusters and MCSs) with 10 or more cores. Anvils with 6–9 cores, and with 10 or more cores, are grouped together to ensure that these groups have a comparable number of members for analysis.

Figure 5.9 shows properties related to the anvil area and lifetime linked to the number of cores. In fig. 5.9 a we show the average anvil maximum area for each group. We find that the maximum area increases approximately linearly with the number of cores, with increasingly clustered anvils having increasingly larger maximum areas, and highly clustered anvils having substantially larger anvils. Figure 5.9 b shows the average anvil lifetime compared to the number of cores. While the lifetime also increases with the number of cores, the difference between isolated and highly clustered anvils is proportionately smaller.

Figure 5.9 c shows the number of anvils observed with differing numbers of cores.

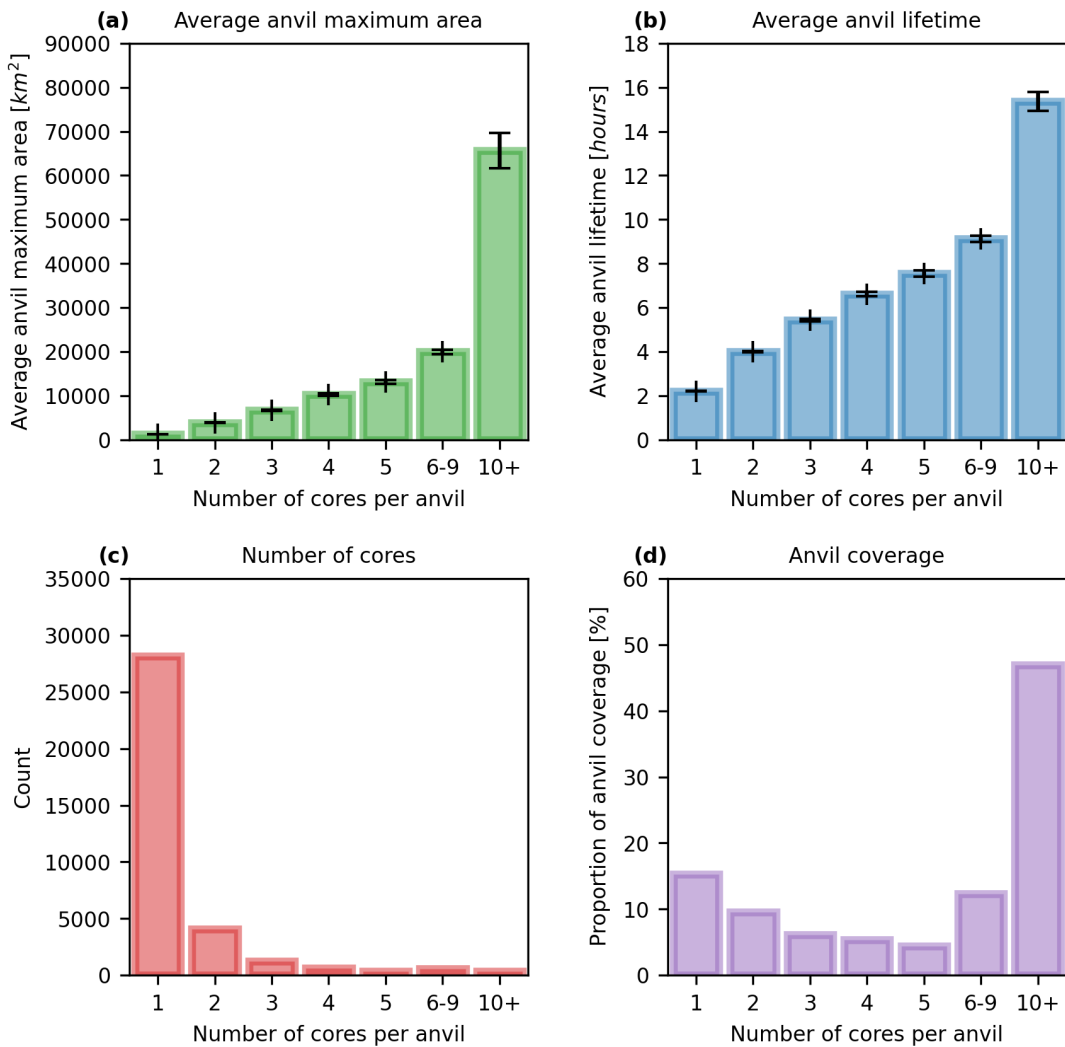


Figure 5.9: Anvil statistics by number of associated cores for a.: average maximum area; b.: average lifetime; c.: the number of observed anvils by number of cores; and d.: percentage of total anvil coverage. Error bars in a and b show the standard error of the mean.

We see that the vast majority of all anvils observed are isolated DCCs, with over 80% having a single detected core. As the number of cores increases, the number of anvils detected decreases rapidly. However, when considering the large increase in  
2870 both anvil area and lifetime with the number of cores, the total anvil coverage for highly clustered anvils is much larger (see fig. 5.9 d). Despite their high frequency, isolated DCCs only account for 12% of total anvil coverage, whereas highly clustered (10+ cores) account for over 50%. Previous studies have found that despite being few in number, MCSs account for the majority of precipitation in Western Africa [Vizy  
2875 and Cook, 2019].

Figure 5.10 a shows the average mean CTT, and fig. 5.10 b the average minimum CTT for anvils with different numbers of cores. While the more clustered anvils have colder average anvil CTT, this decrease plateaus below 220K indicating that the reduction in clear-sky cooling below this temperature may cap the anvil CTT for larger  
2880 DCCs. The minimum observed CTT within each anvil, however, are colder and show a greater difference with an increasing number of cores. The most clustered anvils tend to have a minimum CTT of around 180 K, indicating the presence of overshooting tops and the most intense convection. Care should be taken when interpreting such low retrieved CTT values due to the large uncertainty associated with sensor  
2885 noise at these cold temperatures.

Futyan and Del Genio [2007] divide the DCC lifecycle into growing, mature and dissipating phases based on the time of observation of the coldest anvil CTT, maximum anvil area and dissipation of the anvil. In fig. 5.11 we show the distribution of the time taken to reach each of these lifecycle milestones for anvils separated by the  
2890 number of associated cores. For all cases, the average time of minimum anvil CTT occurs before the maximum area, indicating that the anvils continue to grow beyond the maximum of convective activity. As the number of cores associated with each anvil increases, the time of the coldest CTT and largest area occur proportionately

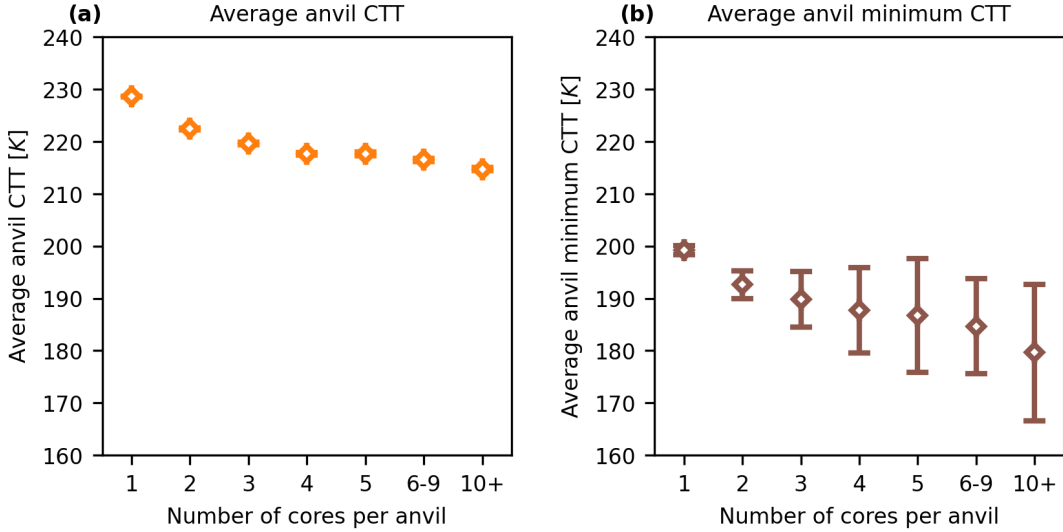


Figure 5.10: Anvil statistics by number of cores for a.: average anvil CTT; and b.: average minimum anvil temperature. Error bars show the standard error of the mean.

earlier during the lifetime of the anvil. As a result, these more clustered anvils spend  
2895 more of their lifetime existing with warming, shrinking anvils than the isolated DCCs.

In fig. 5.12, we compare the proportion of the overall anvil lifetime spent in each of the lifecycle phases defined by Futyan and Del Genio [2007] to the number of cores associated with the anvil. There is a clear trend that, as the number of cores increases, the proportion of the lifecycle spent in the growing phase decreases, and  
2900 the proportion spent in the mature and dissipating phases increases. Although this approach to classifying the lifecycle of anvil clouds is simplistic and does not capture the complexities of large, long-lived DCCs which may go through multiple cycles of growth, dissipation and re-invigoration, it can provide a useful perspective when considering the LW CRE of DCCs. The time of the coldest average CTT will be  
2905 when the LW CRE of the anvil cloud is at its greatest, and so can help understand the evolution of the anvil CRE over its lifetime.

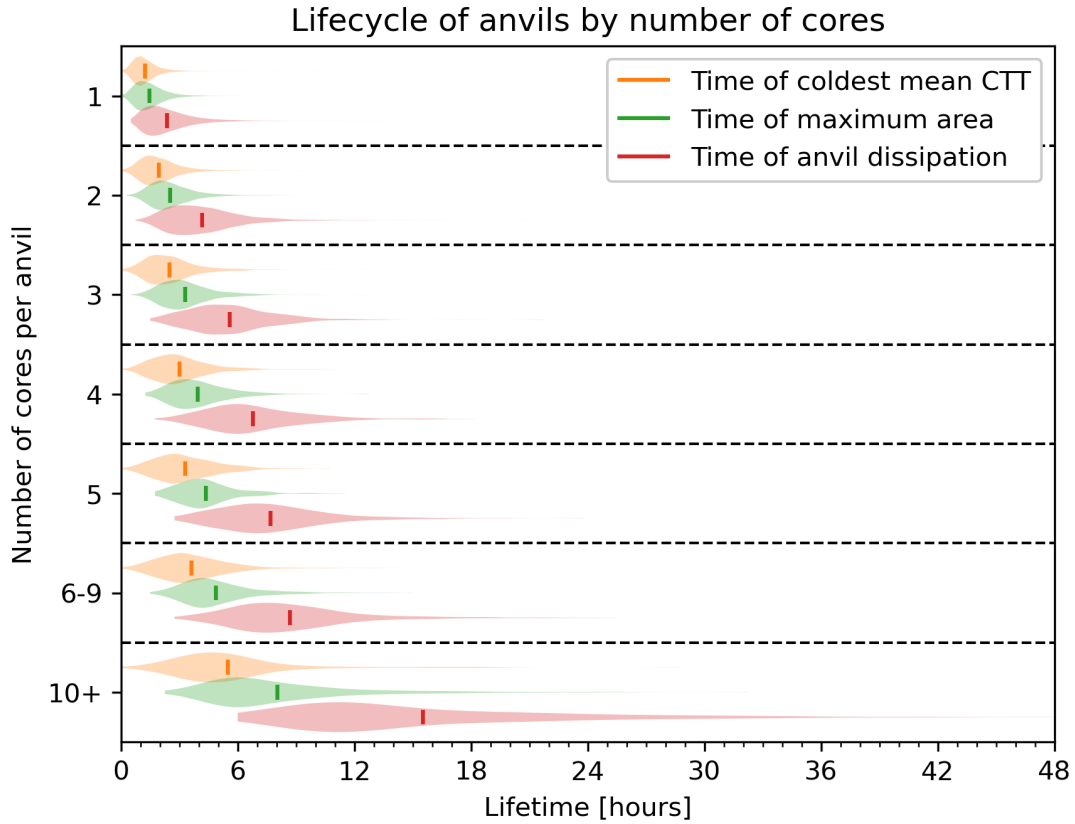


Figure 5.11: The distribution of time to coldest mean anvil CTT (orange), largest anvil area (green) and time of anvil dissipation (red) for anvils grouped by number of cores. The vertical lines show the mean time for each distribution.

### 5.4.3 Anvil CRE

Using the broadband fluxes data in conjunction with the tracked DCC dataset, we are able to track how the SW, LW and net CRE evolve over the lifetime of each tracked anvil. Figure 5.13 shows the time series of SW, LW and net CRE as well as the cumulative average CRE (the average of net CRE over anvil area and lifetime up until that point in time) for several different anvil lifecycles. Note that all fluxes are ToA and measured in the downward direction, so a positive value represents warming and a negative value represents cooling.

Figure 5.13 a shows the case of an isolated, short-lived DCC. The DCC initiates

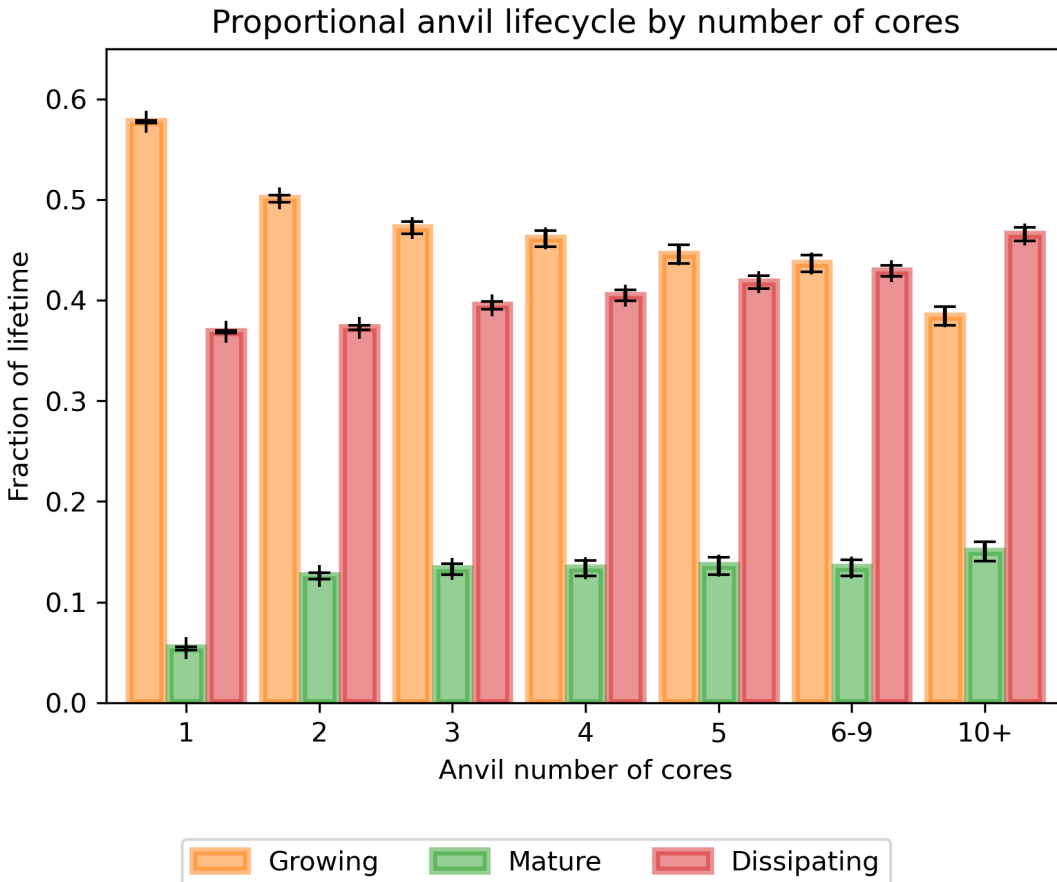


Figure 5.12: The proportion of anvil lifetime spent in the growing (orange), mature (green) and dissipating (red) phase, according to the criteria used by Futyana and Del Genio [2007]

during the daytime, during which the SW CRE dominates and the net CRE is negative (cooling). However, towards the end of the four-hour lifecycle of the DCC, it transitions to night-time and so while the SW CRE reduces and eventually becomes zero, the LW CRE dominates and the net CRE is positive (warming). While this period of warming moves the cumulative average CRE towards zero, it remains overall negative for the overall lifetime of the DCC both due to the longer period spent during the daytime, and the larger area of the anvil cloud during this period.

Figure 5.13 b shows the case of a longer-lived (22 hours), clustered DCC. It initiates in the morning, and so the SW cooling dominates for the first half of the anvil lifetime.

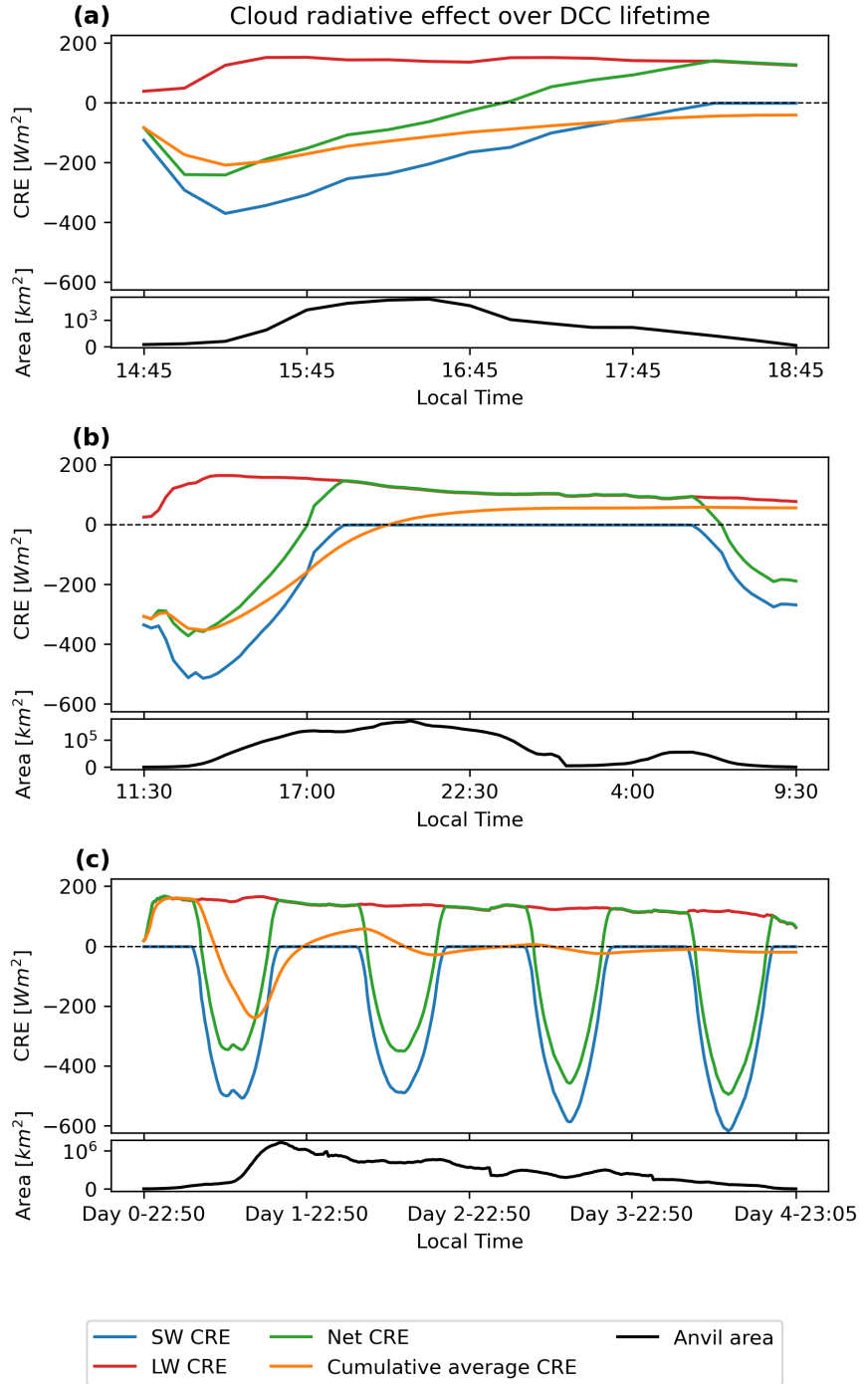


Figure 5.13: Anvil net, LW, and SW CRE, cumulative mean CRE over anvil lifetime and anvil area for a.: an isolated, short-lived (4-hour) DCC; b.: a moderately clustered, 1-day long DCC; and c.: a large, clustered, 4-day long DCC. All times are the local solar time, to the nearest 5-minute interval. The black lines show the change in area of each DCC over their lifecycle.

<sup>2925</sup> Compared to the isolated DCC, it exists for much longer during the night time, and so the cumulative average becomes positive over the full lifetime of the anvil cloud.

Figure 5.13 c shows the case of a four-day, highly clustered convective event. In this case, we see the net CRE alternates between warming and cooling throughout the diurnal cycle. The cumulative CRE also alternates between overall warming and <sup>2930</sup> cooling throughout the lifetime of the anvil and results in a small net cooling effect.

We see in both the longer-lived cases (fig. 5.13 b, c) that the LW CRE reduces towards the end of the anvil cloud lifetime. This may be reflective of the findings from fig. 5.11 that the minimum average CTT occurs before the mid-point of the cloud lifecycle for longer-lived systems. This reduction in LW CRE may be due to <sup>2935</sup> a thinning of the anvil cloud (allowing increased LW emission from the surface), or due to heating and stabilisation of the upper troposphere by the DCC. In addition, the cumulative radiative cooling of the anvil top may drive subsidence and reduce the cloud-top height of the anvil over time [Sokol and Hartmann, 2020]

Figure 5.14 shows the distribution of net lifetime CRE for all tracked anvils. The <sup>2940</sup> overall negative average value of  $-0.94 \pm 0.91 \text{ Wm}^{-2}$  is very close to zero considering the large spread in CRE. However, the distribution shows a bimodal structure, with two peaks at around  $+100 \text{ Wm}^{-2}$  (warming) and  $-180 \text{ Wm}^{-2}$  (cooling). The distribution is coloured according to the mean number of cores associated with the anvils in each bin of the distribution. Both the peaks of the distribution are mainly <sup>2945</sup> composed of isolated DCCs which occur during the daytime (negative peak) or night-time (positive peak). The centre of the distribution—with average CREs close to zero—shows a greater number of the clustered DCCs with multiple cores which, due to their longer lifetime, tend to exist during both the day- and night time.

In fig. 5.15 we break down the CRE distribution into that of the SW (fig. 5.15 a) <sup>2950</sup> and LW (fig. 5.15 b) components. The SW CRE shows a similar bimodal distribution to that of the net CRE, whereas the LW distribution shows a normal distribution.

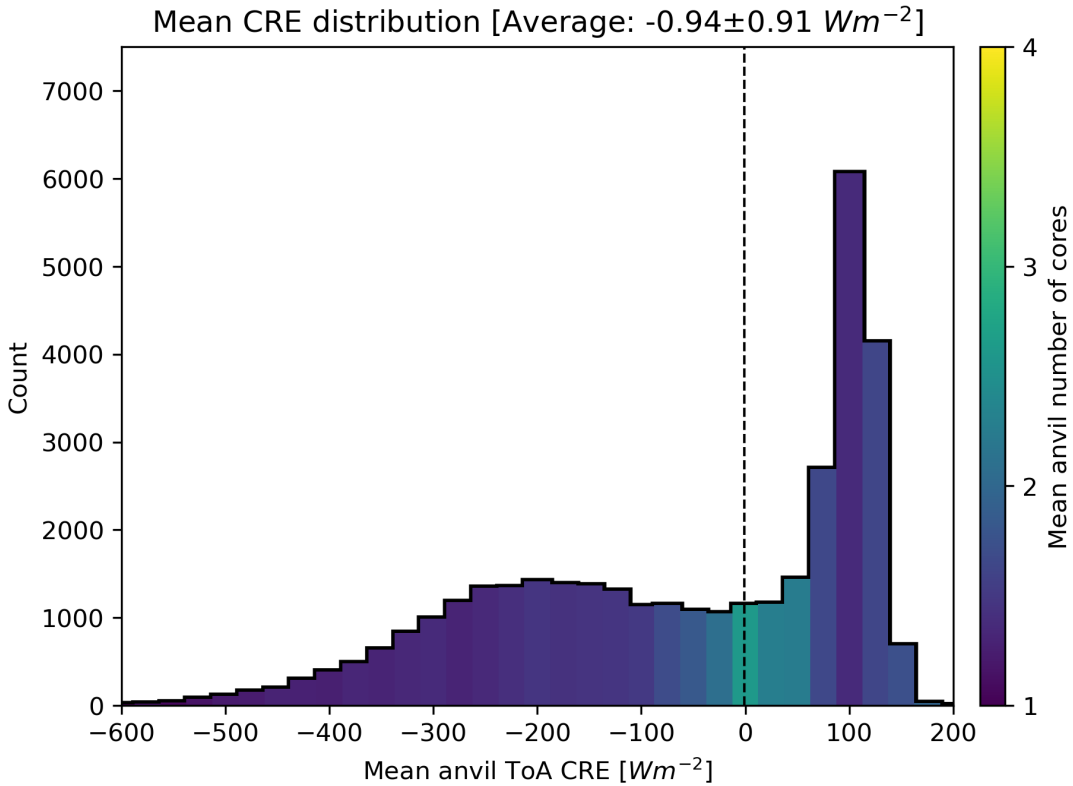


Figure 5.14: The distribution of lifetime anvil CRE for all observed anvils. The mean number of cores per anvil in each bin is indicated by the colour scale. The vertical dashed line shows the integrated mean CRE (over area and lifetime) over all anvils, weighted by the anvil areas ( $-0.94 \pm 0.91 \text{ Wm}^{-2}$ ).

The SW CRE has a large peak at  $0 \text{ Wm}^{-2}$  for DCCs that occur during the night-time, and a broad peak centred around  $-300 \text{ Wm}^{-2}$  consisting of daytime DCCs, with the average falling between the two. Note that the average for the LW falls to the right of the peak of the distribution because the average is integrated over the anvil area and lifetime, and the largest and longest-lived anvils tend to have colder CTT and hence larger LW CRE.  
2955

Figure 5.16 shows (a) the average instantaneous anvil CRE binned by the time of observation (local solar time) and mean anvil CTT, and (b) the average lifetime anvil CRE binned by time of initial detection (local solar time) and mean anvil CTT.  
2960  
 We see that, as expected, mean anvil CRE becomes more positive with decreasing

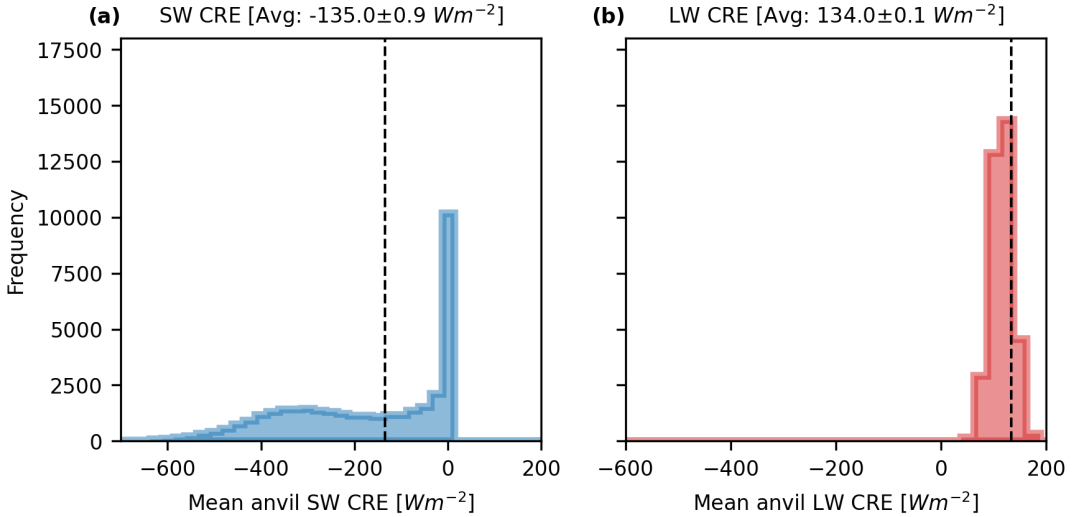


Figure 5.15: The distributions of mean anvil SW CRE (a) and LW CRE (b). The vertical dashed line shows the integrated mean CRE over all anvils (SW:  $-135.0 \pm 0.9 \text{ Wm}^{-2}$ , LW:  $134.0 \pm 0.1 \text{ Wm}^{-2}$ )

CTT due to increased LW warming. However, the diurnal cycle of detection shows a much stronger contrast, with anvils detected during the daytime having a net cooling effect compared to those at night which have a net warming CRE. This diurnal cycle effect is stronger for those anvils with warmer average CTT, generally representing isolated, shorter-lived DCCs, and is weaker for colder anvil CTT. Note also that in fig. 5.10 b that the phase of the diurnal cycle shifts to earlier times of detection as average anvil CTT become colder, as these DCCs tend to have longer lifetimes.

It is apparent from figs. 5.14 and 5.15 that the observed neutral net anvil CRE is not only due to a balance between the SW and LW, but also from a balance of the cooling effect of daytime DCCs and the warming effect of those occurring at night. If the number of DCCs occurring during the daytime were to reduce we would expect a net warming effect without any change to the CRE of individual DCCs. As the diurnal cycle of convection over the ocean is nearly uniform, we should expect little impact on anvil CRE from changes in the time of convective initiation. However, over land, where convective activity is much more common in the afternoon, changes in

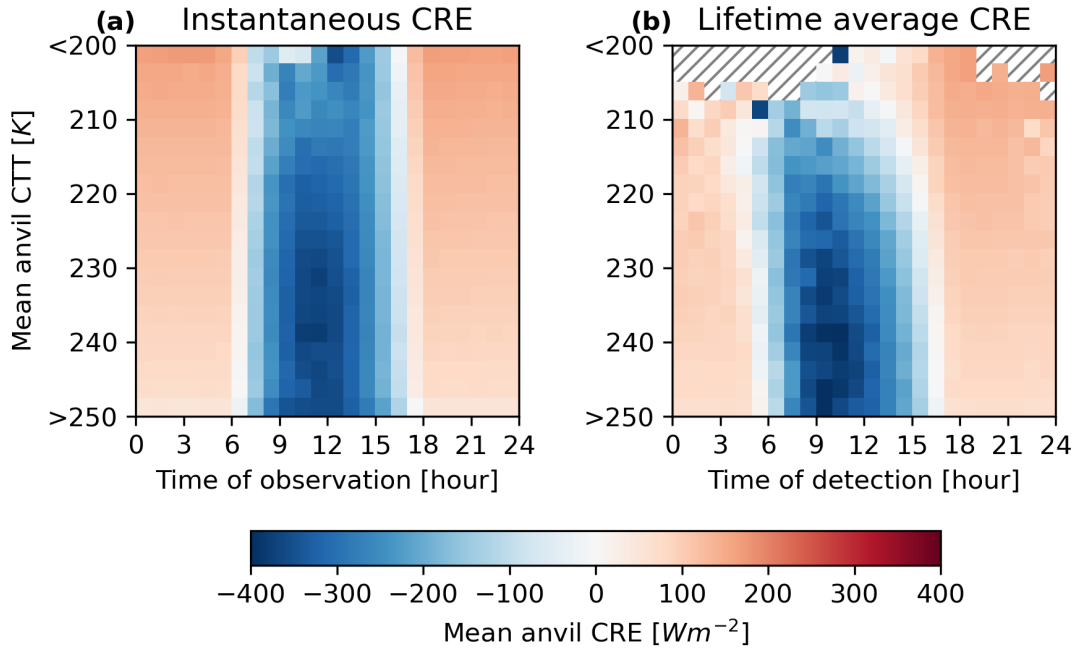


Figure 5.16: (a) Average instantaneous anvil CRE binned by the time of observation (local solar time) and mean anvil CTT. (b) Average lifetime anvil CRE binned by time of initial detection (local solar time) and mean anvil CTT. Hashed regions in (b) show bins in which no anvils were detected.

the diurnal cycle may have a much larger effect on anvil CRE.

Furthermore, fig. 5.16 b highlights that differences in anvil temperature are linked to the diurnal cycle of anvil CRE as colder anvils tend to have longer lifetimes.

As a result, if warming surface temperatures lead to the invigoration of DCCs, the warming effect we would see would be larger than the LW effect from the change in anvil temperature alone. Surface warming may also result in an earlier time of convective initiation, resulting in a cooling feedback.

## 5.5 Summary

By combining a novel cloud tracking algorithm with a new dataset of derived all-sky and clear-sky fluxes from geostationary satellite observations, we were able to detect and track DCC anvils and their associated cores for both isolated and clustered DCCs

and investigate their properties, lifecycle and CRE. As this study was performed using data from May-August (Northern hemisphere summer), we observed the majority of convective activity over the Guinea-Congo rainforest and Savanna regions, as the ITCZ is at its northernmost extent.

We evaluate the degree of convective clustering of each anvil by measuring the number of cores it is associated with. We find that, as expected, anvils with the greatest number of cores—including MCSs—have larger anvil areas, longer lifetimes and the coldest cloud tops. As a result, despite the majority of observed DCCs being isolated, the highly clustered anvils make up most of the anvil coverage, and so cause most of the anvil impact over this region. We also find that the proportion of the lifecycle spent in the mature and dissipating phases increases with the number of cores, and the proportion spent in the growing phase decreases.

When looking into the net CRE of anvils, we find that, although the average CRE across all observed anvils is close to zero, few anvils have near zero CRE themselves. We find a bimodal distribution of anvil CRE, with isolated DCCs that exist during the daytime causing the negative (cooling) peak, and those that exist during the night-time causing the positive (warming) peak. The systems with near zero CRE tend to live longer with more cores, and exist during both the day- and night-time. As a result, when considering the magnitude of the anvil CRE, isolated DCCs have an outsized contribution to the overall average anvil CRE of 21.4% compared to their proportion of all anvil coverage (15.3%) (see fig. 5.17).

The interaction between the diurnal cycle of convection and DCC lifetime plays a key role in the shape of the SW anvil CRE distribution and is important to consider in regard to anvil CRE feedback. As the LW CRE is normally distributed, a response to changing cloud top height or temperature may occur as a shift in the distribution. However, the bimodal distribution of the SW CRE must result in more complex adjustments to shift the overall mean. As the position of the peak at  $0 \text{ Wm}^{-2}$

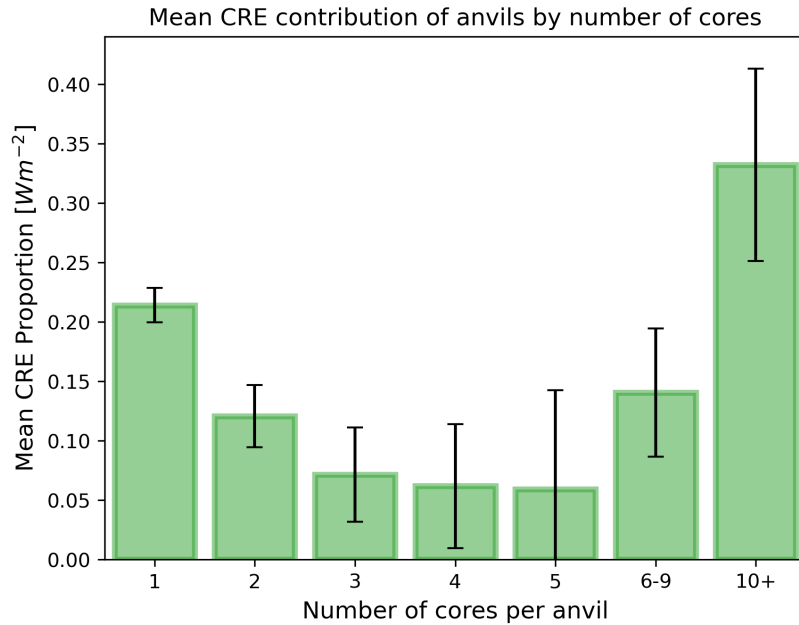


Figure 5.17: The contribution to the net CRE for anvils with differing numbers of cores, which is defined as the sum of the absolute CRE multiplied by anvil area for all anvils with that number of cores, divided by the total for all anvils. Due to the large variance and magnitude of the CRE of isolated DCCs, they have a large impact on the net CRE balance despite their small area.

3015 relating to night-time DCCs is fixed, to change the overall average SW CRE either the width of the distribution has to increase or decrease, or the number of DCCs occurring during the day- or night-time has to increase. The former has important implications for the diurnal cycle of temperature in the tropics, and the latter for the diurnal cycle of convection, which, in turn, affects the anvil lifecycle.

3020 Changes in the diurnal cycle of convection may not have a large impact on net anvil CRE over the ocean due to the mostly uniform occurrence of convection throughout the day. Over land, however, the afternoon peak of convection at around 3 pm solar time (see fig. 5.8) coincides with a time at which anvil CRE is very sensitive to shifts in the diurnal cycle (fig. 5.16 b). Furthermore, a reduction or increase in the number 3025 of DCCs occurring at a specific time of day may change the net CRE of anvils without any change in the CRE of individual DCCs.

Diagnosing a diurnal-cycle-related anvil cloud feedback in climate models may however be difficult. Beydoun et al. [2021] found that changes in anvil lifetime contributed little to CRE feedbacks in a cloud-resolving radiative-convective-equilibrium model. It is unclear how well the diurnal cycle of convection and convective lifecycle are represented in such a model, although convective-resolving models have been found to model these better than parameterised climate models [Prein et al., 2015; Feng et al., 2023b]. Disentangling the impacts of convective processes and anvil cirrus processes on anvil lifecycle and CRE is also a key challenge. Here, the use of model experiments such as Gasparini et al. [2022] may help understand the impacts of each process on anvil Cloud Radiative Effect (CRE) and the potential climate feedbacks.

There are, however, a number of limitations in this study which present opportunities for future research. Firstly, as this study only involved 4 months of data during the Northern Hemisphere summer, we were not able to investigate the impact of the seasonal cycle on the behaviour of DCCs and their CRE. Furthermore, extending to a larger domain would allow investigation of regional differences, in particular the important land–sea contrast of deep convection [Takahashi et al., 2023]. A major limitation of the SEVIRI data is its poor sensitivity to thin anvil cirrus, which has an important impact on net anvil CRE [Protopapadaki et al., 2017; Horner and Gryspeerdt, 2023]. The flexible combined imager [Martin et al., 2021] aboard the third-generation Meteosat may allow better detection and study of thin anvil cirrus over tropical Africa in the near future.

Cloud tracking provides a key capability for the study of deep convective anvil clouds [Gasparini et al., 2023]. The ability to observe changes over the lifetime of an anvil cloud independently of changes in the microphysical or macrophysical properties of DCCs. Further application of cloud tracking approaches may better our understanding of DCC lifecycle, its relation to the diurnal cycle of radiation, and its response to a changing climate.

# Chapter 6

## Conclusion

3055

### 6.1 Summary

DCCs—characterised by their great height, intense updraft velocities and large areas—are responsible for a wide range of extreme weather and subsequent natural disasters including extreme rainfall, flooding, hail, lightning and tornadoes. Furthermore, deep convection plays a key role in many parts of the climate, including the atmospheric general circulation, the radiative balance of the top-of-atmosphere, the energetic balance of the troposphere and the hydrological cycle. Global warming is expected to increase the intensity and frequency of deep convection. Understanding the behaviour of these systems is therefore vital to forecasting both weather in the present day and 3060 the future climate.

3065 Studying the behaviour of DCCs is made difficult by both their extreme dynamics, and also the range of scales over which their effects occur. DCCs involve typical vertical velocities on the order of  $10\text{ ms}^{-1}$ , substantially larger than seen elsewhere in the atmosphere. Their properties span a range of scales from the order of 100 m for thermals within updrafts, 10 km for convective cores, 100s–1000s km for their associated anvil clouds and even further for their coupling with the wider circulation of the atmosphere. Climate models have traditionally struggled to represent many of the behaviours of DCCs, and while km-scale convective resolving models have improved in this regard, there are still large remaining uncertainties.

3075 Geostationary satellite observations offer a unique capability to observe the entire extent and lifecycle of DCCs. Modern geostationary satellite instruments can observe processes occurring at single km and minute scales across domains spanning many thousands of km over multiple years. Algorithms to detect and track DCCs in geostationary satellite imagery have been used to capture the dynamical behaviour of  
3080 DCCs and represent them in a Lagrangian framework since the 1970s [Menzel, 2001]. Despite several decades of development, however, challenges remain in tracking DCCs across the wide range of scales at which they occur in nature. With the growing interest in Lagrangian studies of DCCs [Sokol and Hartmann, 2020; Gasparini et al., 2019; Bouniol et al., 2021], the development and application of cloud trackers focused  
3085 on the needs of the wider community is vital for investigating complex convective behaviours [Gasparini et al., 2023]

### 6.1.1 Chapter 2: harnessing new geostationary satellite measurements to track DCCs across all scales

Algorithms to track DCCs in geostationary satellite images have been in development  
3090 for over 50 years [Menzel, 2001]. Many methods remain in use despite their known drawbacks [Augustine and Howard, 1988] that limit their application to developing research areas. Historically, the large advances in cloud tracking methods have come from both taking advantage of new data sources and addressing the key scientific questions of the wider community. With the new generation of advanced geostationary instruments and a keen focus on Lagrangian studies of cloud evolution, now is  
3095 such a time when cloud tracking tools have the potential to become a vital tool in studying key climate questions.

In chapter 2, we develop a novel method to detect and track both the cores and anvils of DCCs across scales from isolated storms to MCSs. Through theory  
3100 developed using simple, 1D models [Emde et al., 2016], the ability to better detect the entire extent of thick and thin anvils and developing cores using a combination of

channel differences and temporal changes. We found that while changes in the clean LW window BT over time provide the best indication of growing DCCs, use of the WVD and SWD channel combinations provide greater insight into the detection of both thick and thin anvil clouds. The use of a semi-Lagrangian framework to remove the motion of observed DCCs was successfully applied to overcome the scaling issue encountered by existing algorithms [Lakshmanan and Smith, 2009], with optical flow successfully applied to estimate the cloud motion vectors. Combining a selection of novel approaches to cloud detection and tracking [Müller et al., 2019; Fiolleau and Roca, 2013; Zinner et al., 2008] within this framework allows the detection and tracking of DCCs from the initial detection of the growing core to the dissipation of the thin anvil cirrus, allowing tracking of the full extent of the DCC lifetime (fig. 2.18). In addition, the combined core and anvil tracking improves both the sensitivity and robustness of the algorithm, with an  $F_1$ -score of 0.91, providing a high degree of trust in the DCCs detected by the algorithm.

### 6.1.2 Chapter 3: relating the spatial distribution, properties and diurnal cycle of convective cores and anvils

Research into the interactions between convective processes and anvil clouds in the present-day climate has long been limited due to a lack of large, observational datasets linking their behaviours [Gasparini et al., 2023]. With the deployment of geostationary imagers such as ABI, we now have sources of observations that can capture both the changes in DCCs on short spatial and temporal scales while simultaneously observing large, varied regions of the planet. North America experiences a wide array of convective storms in both tropical and extra-tropical environments, over the ocean and over land.

In chapter 3, we apply the *tobac-flow* algorithm to five years of observations to study the behaviour of DCC cores and anvils in this region. Using this dataset, we investigate the spatial, diurnal and seasonal distributions of both cores and anvils,

and show the relation between them and their contrasting behaviour between land  
3130 and ocean. We find that sufficient observations can be made of developing cores to evaluate their properties, and link these properties to the subsequent development of the DCC. We find that DCCs tend to be larger, longer lived and colder over land than the ocean , and their cores more intense during the daytime. In addition, we show the extent to which both convective cores and anvils are impacted by the diurnal cycle.  
3135 Over the ocean, the enhancement of anvil cloud lifetime by SW heating [Gasparini et al., 2022] increases the occurrence of anvil clouds during the daytime, despite the contrasting nighttime peak in convective core development. In contrast, over land the diurnal cycle leads to a strong peak of convection in the afternoon, as well as increasing convective intensity throughout the day. These diurnal cycles are further  
3140 perturbed by coastal breeze effect both offshore and onshore.

In comparing the properties of DCCs over land and ocean, we find results that appear to conflict with recent studies that used sun-synchronous observations [Ge et al., 2024]. However, we show that without a Lagrangian perspective of DCCs that the measured properties of anvils over land can be biased due to the relationship between  
3145 anvil age, the diurnal cycle of convection, and the time of observation. Studies combining cloud tracking with polar orbiting satellite overpasses, such as [Bouniol et al., 2021], provide an excellent example for how the Lagrangian information provided by geostationary satellites can be combined with the active sensor measurements only available from polar-orbiting platforms.

### 3150 **6.1.3 Chapter 4: the effect of convective processes on the structure and lifecycle of anvil clouds**

Recent research has highlighted the importance of changes in anvil structure to future anvil cloud feedbacks [McKim et al., 2024; Sokol et al., 2024]. Previous studies have found that the proportion of thin anvil increases with increasing convective intensity  
3155 [Protopapadaki et al., 2017; Takahashi et al., 2017b]. In chapter 4, we use measures

of convective intensity and organisation from our observed cores to investigate their impact on anvil structure. While we found the same trends with increasing intensity, we found that, to the contrary, increasing convective organisation leads to a decrease in thin anvil fraction, despite organised DCCs sharing many of the properties of  
3160 intense isolated convection. Both cases also showed contrasting changes in the lifecycle of the observed DCCs. For isolated convection, increasing intensity leads to a shorter growing phase, but a longer mature and dissipating phase for the thin anvil. It is this increase in the lifetime of these phases, not the instantaneous area of the anvil, that primarily leads to the overall increase in thin anvil fraction. For organised convection,  
3165 we found the opposite effect, with an increase in the number of cores resulting in a longer growing phase and shorter mature and dissipating thin anvil phases.

However, neither the difference in maximum thick and thin anvil area nor the difference in lifetime alone could account for the net change in thin anvil fraction.

The novel approach used in this chapter has allowed new results to be found  
3170 that were not identified in the previous studies. Explicitly tracking the full lifetime of the anvil cloud results in attributing a larger proportion of thin anvil area than that seen by snapshot observations, and reveals changes caused by an increase in the anvil lifetime. Furthermore, the explicit tracking of convective cores associated with anvils showed the response of thin anvil area to organisation, whereas without this  
3175 the trends of organised convection would be hidden due to the majority of observed DCCs being isolated systems.

In addition, we show that the intensity and organisation of convection have opposing effects on both the lifecycle and structure of DCCs. The thin cirrus produced by DCCs may have a warming effect on the climate, and so understanding how the area  
3180 and lifetime of these clouds change with the properties of convection is important to understanding DCC feedbacks. As both the intensity of DCCs and the frequency of organised convective systems are expected to increase with global warming, so further

study of the response of thin cirrus to convective activity is vital.

#### 6.1.4 Chapter 5: the influence of the diurnal cycle on the 3185 CRE of tropical anvil clouds

Despite their large reflectance of Shortwave (SW) radiation, and absorption of Long-wave (LW) radiation, tropical anvil clouds have historically been found to have a net Cloud Radiative Effect (CRE) close to zero [Ramanathan et al., 1989; Hartmann et al., 1992; Hartmann and Larson, 2002]. Interactions involving the diurnal cycle of  
3190 deep convection may have large and important impacts on anvil CRE [Nowicki and Merchant, 2004], and lagrangian tracking of DCCs is required to better understand this [Bouniol et al., 2016]. In chapter 5, we combine the cloud tracking method developed in chapter 2 with retrieved cloud properties and radiative fluxes from SEVIRI observations over Africa. Together, this allows us to explicitly measure the CRE of  
3195 DCCs over their lifecycle, and analyse how they change with DCC properties.

The distributions of observed DCCs showed both similarities and differences from those seen in chapter 3. A similar land–sea contrast was shown in the timing of convective initiation. This contrast was also seen in the time of initiation over the African Great Lakes (particularly Lake Victoria), which may indicate similar mechanisms in action. The small number of DCCs due to the limited extent of the case  
3200 study prevented further investigation into this behaviour.

The observed DCC lifecycle, shown in fig. 5.12, shows notable difference to those found in chapter 3, which have several reasons. Firstly, there may be a difference in the lifecycle of DCCs between the tropics and extra-tropics. However, this difference  
3205 may have been due to the lower sensitivity of SEVIRI for observing thin anvils. This lower sensitivity reduces the length of time over which the anvil is observed, increasing the proportion of the lifecycle observed in the growing phase. Furthermore, this effect is expected to be greater for isolated DCCs as the thick anvil dissipates faster than for larger MCSs. Finally, the use of retrieved CTT, rather than observed BT, may

<sup>3210</sup> cause a difference. An increase in stratospheric WV, along with the thinning of the anvil cloud, will cause the observed BT of the anvil to increase over time. However, the retrieved CTT will remove these effects. As a result, the method of Futyau and Del Genio [2007] for measuring anvil lifecycle may produce a longer growing phase if CTT is used instead of BT.

<sup>3215</sup> The main aim of this chapter was the investigation of how the diurnal cycle affects the CRE of individual DCCs. Historically, studies into the CRE of tropical anvils have averaged over all areas of anvil cloud without tracking individual DCCs [Ramanathan et al., 1989; Hartmann et al., 1992; Stephens et al., 2018]. While the overall average CRE of our observed DCCs confirmed the neutral CRE of tropical anvil clouds, <sup>3220</sup> through the use of tracking we could study how the properties of individual DCCs contribute to this mean state.

The CRE of DCCs changes over their lifetime both due to the changing properties of the anvil cloud and the timing within the diurnal cycle. While both the LW and SW CRE reduce over the lifetime of the DCC, the SW CRE is also largely dependent on <sup>3225</sup> the time within the diurnal cycle. These two effects lead to the bimodal distribution for the CRE of individual DCCs, as shown in fig. 5.14.

We can identify three categories of DCCs that contribute to this distribution. The largest group is that of isolated DCCs, which form the two peaks of the distribution. Typically, these either initiate in the early afternoon and have a negative CRE due to <sup>3230</sup> the large SW effect during the daytime, or initiate in the early evening and instead have a positive CRE as they exist at night. The second group consists of moderately clustered DCCs which tend to exist for longer than isolated DCCs but less than a day. As these systems tend to initiate in the evening, they mostly exist at night and therefore predominantly have a LW warming effect. Finally, MCSs which exist for <sup>3235</sup> multiple days tend to have a neutral CRE as their SW and LW effects average out across the diurnal cycle.

The behaviour of these different DCCs may influence how they respond to climate change. Organised DCCs, including MCSs, may primarily respond through changes in their LW CRE including FAT and anvil area as SW changes tend to average out over their lifecycle. On the other hand, isolated DCCs tend to have CTT warmer than the top of the convectively active layer (220 K), and so FAT may not apply to them. The large magnitude of the CRE (both positive and negative) of individual isolated DCCs means that they have a substantially larger influence on the net anvil CRE balance than their area suggests. As a result, the response of these systems to global warming may have a larger effect on the overall anvil feedback than has been previously considered.

## 6.2 Discussion & Future work

In recent years there has been an increased focus on the study of anvil lifecycle [Wall et al., 2018; Sokol and Hartmann, 2020] and radiative effects [Bouniol et al., 2021]. The response of DCCs to climate change is both important and uncertain [Sherwood et al., 2020; Hill et al., 2023]. Improving our understanding of cirrus cloud properties and lifecycles is vital to improving this situation [Sullivan and Voigt, 2021; Gasparini et al., 2023].

The key results of this thesis are in the new observational insights into the lifecycle, structure and CRE of DCCs and their anvils. The development of a novel tracking algorithm allows both isolated and organised DCCs to be tracked across their entire lifetime across a wide range of scales. Furthermore, by tracking both cores and anvil clouds, we are able to link the behaviours of the convective cores to the evolution of the anvil clouds, and provide observational evidence for how these properties affect each other.

Chapters 3, and 5 showed significant differences in the lifecycles of DCCs over the land and the ocean. In particular, these differences may influence DCC cores and

anvils to different extents. Several processes, occurring over a range of scales, may influence the properties of observed DCCs. Lake effects, such as those seen over the 3265 African Great Lakes in chapter 5, may provide a useful case study for understanding these differences, as while their local and surface properties may be similar to that of oceans, the larger environmental conditions may be more affected by the adjacent land regions.

In chapter 4 we found contrasting impacts of convective intensity and organisation 3270 on the structure and lifecycle of anvil clouds. Analysing how the structure of these DCCs evolved over their lifetime provided key insights into which convective and anvil processes lead to the observed changes in thick thin anvils. These contrasts may help further understand the uncertainties in anvil radiative feedbacks, particularly that of the anvil area feedback. In addition, it highlights the importance of isolated DCCs 3275 to the total anvil CRE, motivating further study into how their behaviour differs from organised convection. Further investigating the contrast between the effects of intensification and organisation on the structure of DCCs anvils may provide insight into the net changes of anvil structure with climate change. However, while with these structural changes alone we would expect more intense DCCs to be warming, 3280 and more organised DCCs to be cooling, the changes in BT and the diurnal cycle observed for both of these processes may dominate any changes in CRE. The bimodal CRE distribution of tropical anvil clouds highlights that the contribution of isolated DCCs is more important to the anvil CRE balance than previously thought, and that these systems may be more sensitive to climate change. Combining research on both 3285 these effects may help understand whether the net impact of the response of DCCs to global warming will be a warming or cooling feedback.

Existing studies, including those of chapters 3 and 5 in this thesis, have observed how the microphysical, dynamical and radiative properties change in isolation. Investigating how these factors combine to produce the net behaviour and response

of anvils, including the contrasts between isolated and organised convection, could greatly help our understanding of these processes. Combining the use of modern geostationary satellite sensors including ABI, Advanced Himawari Imager and the upcoming Flexible Combined Imager aboard the third generation Meteosat [Durand et al., 2015], along with retrievals of anvil CRE and radiative heating, may help close the loop on these processes. A larger cloud tracking study, combining these elements, investigating how the microphysical, macrophysical properties and structure of DCCs change over their lifecycle and throughout the diurnal cycle, and then demonstrating the effect of these changes on the CRE of the anvil across both thick and thin parts and along its entire lifetime, could greatly reduce uncertainties in anvil cloud feedbacks. A new framework for decomposing anvil cloud feedbacks that includes structure, optical and lifecycle changes may prove key to their would greatly help understanding their behaviours.

While geostationary satellite observations provide unique insights into the behaviour of DCCs, they cannot observe processes occurring within the cloud. Active satellite instruments, including the CPR aboard Cloudsat and the Cloud-Aerosol Lidar with Orthogonal Polarization lidar as part of the Afternoon train (A-train), have substantially improved our understanding of processes occurring within DCCs [Stephens et al., 2018]. A number of new satellite missions across the coming decade look to build upon these discoveries and further improve our knowledge of DCC processes. The ESA Earth Cloud Aerosol and Radiation Explorer (EarthCARE) satellite, planned to launch in 2024, looks set to build upon the successes of the A-train by combining multiple active instruments aboard a single platform [Wehr et al., 2023]. The NASA Investigation into Convective Updrafts (INCUS) mission presents an innovative approach to studying the properties of deep convective updrafts [van den Heever et al., 2023]. By flying three satellites, each equipped with Ka-band rainfall radars, in close formation, INCUS observations can be used to calculate the convec-

tive mass flux. In turn, this property can be used to understand how the growth and lifecycle of anvils relate to the cores which feed them. NASA’s upcoming Atmosphere Observing System (AOS) mission will similarly focus on the use of active sensors to observe aerosol, cloud and convective and precipitation processes [Braun et al., 2023]. AOS will consist of a constellation of multiple satellites operating in different orbit configurations.

As the success of the A-train has shown [Stephens et al., 2018], the use of multiple satellite observations can provide much greater insight into cloud processes than those from a single source. Both the AOS and INCUS missions are planning on using cloud tracking from geostationary satellites in an operational role to locate their observations of DCCs within the lifecycle of the cloud. Upcoming observational missions, along with the development of global convective resolving models, and idealised simulation, look to enable a great number of advances in our understanding of DCCs. The opportunities opening up have led to the present being called “the decade of convection” [van den Heever et al., 2023], and cloud tracking algorithms and their applications will provide a key part of it.

### 6.3 Concluding remarks

DCCs play a key role in many atmospheric processes, and their response to global warming is both uncertain [Sherwood et al., 2020] and underestimated by current climate models [Hill et al., 2023]. While the new generation of convective resolving models may help to address this problem [Stevens et al., 2020], these models still do not fully resolve the issues in simulating the dynamics of deep convection [Jeevanjee, 2017] and the behaviour of anvil cirrus [Sullivan and Voigt, 2021]. Observational studies of DCCs using cloud tracking approaches have been highlighted as a key method to addressing some of these issues [Gasparini et al., 2023].

In this thesis, we have developed and utilised a novel cloud tracking algorithm to better investigate the properties of DCC cores and anvils as seen by the latest generation of geostationary weather satellites. Key results from chapters 3, 4 and  
3345 5 have shown new findings on the properties, structure and CRE of DCC anvils across their lifecycle, which provide insight into how DCCs may respond to changes in convective processes. The ability to track the properties of DCCs over their entire lifetimes has been key to these findings. Understanding the lifecycle of DCCs from a Lagrangian perspective has been highlighted as a key need for future satellite missions  
3350 [van den Heever et al., 2023], convective resolving model development [Prein et al., 2024], and upcoming observation campaigns, and so cloud tracking has a key role to play in future studies of deep convection.

# Bibliography

- Abercromby, R. (1887). On the identity of cloud forms all over the world; and on the  
3355 general principles by which their indications must be read. *Quarterly Journal of the Royal Meteorological Society*, 13(62):140–146.
- Adams, D. K. and Comrie, A. C. (1997). The North American Monsoon. *Bulletin of the American Meteorological Society*, 78(10):2197–2214.
- Agard, V. and Emanuel, K. (2017). Clausius–Clapeyron Scaling of Peak CAPE in Continental Convective Storm Environments. *Journal of the Atmospheric Sciences*, 74(9):3043–3054.  
3360
- Aggarwal, J. and Nandhakumar, N. (1988). On the computation of motion from sequences of images-A review. *Proceedings of the IEEE*, 76(8):917–935.
- Alduchov, O. A. and Eskridge, R. E. (1997). Improved Magnus' form approximation of saturation vapor pressure. Technical Report DOE/ER/61011-T6, Department of Commerce, Asheville, NC (United States).  
3365
- Allen, M. R. and Ingram, W. J. (2002). Constraints on future changes in climate and the hydrologic cycle. *Nature*, 419(6903):228–232.
- Aminou, D. M. A. (2002). MSG's SEVIRI Instrument. *ESA bulletin*, 111.
- Arnaud, Y., Desbois, M., and Maizi, J. (1992). Automatic Tracking and Characterization of African Convective Systems on Meteosat Pictures. *Journal of Applied Meteorology and Climatology*, 31(5):443–453.  
3370
- Augustine, J. A. and Howard, K. W. (1988). Mesoscale Convective Complexes over the United States during 1985. *Monthly Weather Review*, 116(3):685–701.
- Augustine, J. A. and Howard, K. W. (1991). Mesoscale Convective Complexes over the United States during 1986 and 1987. *Monthly Weather Review*, 119(7):1575–1589.  
3375
- Austin, P. M. (1987). Relation between Measured Radar Reflectivity and Surface Rainfall. *Monthly Weather Review*, 115(5):1053–1070.
- Baker, S., Scharstein, D., Lewis, J. P., Roth, S., Black, M. J., and Szeliski, R. (2011). A Database and Evaluation Methodology for Optical Flow. *Int J Comput Vis*, 92(1):1–31.  
3380
- Bechini, R. and Chandrasekar, V. (2017). An Enhanced Optical Flow Technique for Radar Nowcasting of Precipitation and Winds. *J. Atmos. Oceanic Technol.*, 34(12):2637–2658.

- 3385 Bedka, K., Brunner, J., Dworak, R., Feltz, W., Otkin, J., and Greenwald, T. (2010). Objective Satellite-Based Detection of Overshooting Tops Using Infrared Window Channel Brightness Temperature Gradients. *Journal of Applied Meteorology and Climatology*, 49(2):181–202.
- Bedka, K. M. and Mecikalski, J. R. (2005). Application of Satellite-Derived Atmospheric Motion Vectors for Estimating Mesoscale Flows. *J. Appl. Meteor.*, 44(11):1761–1772.
- Bennartz, R. and Schroeder, M. (2012). Convective Activity over Africa and the Tropical Atlantic Inferred from 20 Years of Geostationary Meteosat Infrared Observations. *Journal of Climate*, 25(1):156–169.
- Berry, E. and Mace, G. G. (2014). Cloud properties and radiative effects of the Asian summer monsoon derived from A-Train data. *Journal of Geophysical Research: Atmospheres*, 119(15):9492–9508.
- 3395 Beucler, T. and Cronin, T. (2019). A budget for the size of convective self-aggregation. *Quarterly Journal of the Royal Meteorological Society*, 145(720):947–966.
- Beydoun, H., Caldwell, P. M., Hannah, W. M., and Donahue, A. S. (2021). Dissecting Anvil Cloud Response to Sea Surface Warming. *Geophysical Research Letters*, 48(15):e2021GL094049.
- 3400 Bieniek, A. and Moga, A. (2000). An efficient watershed algorithm based on connected components. *Pattern Recognition*, 33(6):907–916.
- Boer, E. R. and Ramanathan, V. (1997). Lagrangian approach for deriving cloud characteristics from satellite observations and its implications to cloud parameterization. *Journal of Geophysical Research: Atmospheres*, 102(D17):21383–21399.
- 3405 Bony, S., Semie, A., Kramer, R. J., Soden, B., Tompkins, A. M., and Emanuel, K. A. (2020). Observed Modulation of the Tropical Radiation Budget by Deep Convective Organization and Lower-Tropospheric Stability. *AGU Advances*, 1(3):e2019AV000155.
- Bony, S., Stevens, B., Coppin, D., Becker, T., Reed, K. A., Voigt, A., and Medeiros, B. (2016). Thermodynamic control of anvil cloud amount. *Proceedings of the National Academy of Sciences*, 113(32):8927–8932.
- 3410 Bony, S., Stevens, B., Frierson, D. M. W., Jakob, C., Kageyama, M., Pincus, R., Shepherd, T. G., Sherwood, S. C., Siebesma, A. P., Sobel, A. H., Watanabe, M., and Webb, M. J. (2015). Clouds, circulation and climate sensitivity. *Nature Geoscience*, 8(4):261–268.
- Bouguet, J. (1999). Pyramidal implementation of the lucas kanade feature tracker.
- 3415 Bouniol, D., Roca, R., Fiolleau, T., and Poan, D. E. (2016). Macrophysical, Microphysical, and Radiative Properties of Tropical Mesoscale Convective Systems over Their Life Cycle. *Journal of Climate*, 29(9):3353–3371. Publisher: American Meteorological Society Section: Journal of Climate.

- Bouniol, D., Roca, R., Fiolleau, T., and Raberanto, P. (2021). Life Cycle–Resolved Observation of Radiative Properties of Mesoscale Convective Systems. *Journal of Applied Meteorology and Climatology*, 60(8):1091–1104. Publisher: American Meteorological Society Section: Journal of Applied Meteorology and Climatology.
- Bowler, N. E. H., Pierce, C. E., and Seed, A. (2004). Development of a precipitation nowcasting algorithm based upon optical flow techniques. *Journal of Hydrology*, 288(1):74–91.
- Bradski, G. (2000). The OpenCV Library. *Dr. Dobb's Journal of Software Tools*.
- Braun, S., Yorks, J., Thorsen, T., and Cecil, D. (2023). The NASA Atmosphere Observing System (AOS): Future Space-Based and Suborbital Observations for the Study of Coupled Aerosol-Cloud-Precipitation Interactions. Vienna, Austria.
- Bresky, W. and Daniels, J. (2006). The feasibility of an optical flow algorithm for estimating atmospheric motion. In *Proceedings of the Eight International Winds Workshop*, Beijing, China. EUMETSAT.
- Bretherton, C. S., Blossey, P. N., and Khairoutdinov, M. (2005). An Energy-Balance Analysis of Deep Convective Self-Aggregation above Uniform SST. *Journal of the Atmospheric Sciences*, 62(12):4273–4292.
- Brooks, H. E., Anderson, A. R., Riemann, K., Ebbers, I., and Flachs, H. (2007). Climatological aspects of convective parameters from the NCAR/NCEP reanalysis. *Atmospheric Research*, 83(2):294–305.
- Brooks, H. E., Iii, C. A. D., Zhang, X., Chernokulsky, A. M. A., Tochimoto, E., Hanstrum, B., Nascimento, E. d. L., Sills, D. M. L., Antonescu, B., and Barrett, B. (2019). A Century of Progress in Severe Convective Storm Research and Forecasting. *Meteorological Monographs*, 59(1):18.1–18.41.
- Brox, T., Bruhn, A., Papenberg, N., and Weickert, J. (2004). High Accuracy Optical Flow Estimation Based on a Theory for Warping. volume 3024, pages 25–36, Berlin, Heidelberg. Springer Berlin Heidelberg.
- Bruning, E. C. and MacGorman, D. R. (2013). Theory and Observations of Controls on Lightning Flash Size Spectra. *J. Atmos. Sci.*, 70(12):4012–4029.
- Bukowski, J. and van den Heever, S. C. (2021). Direct Radiative Effects in Haboobs. *Journal of Geophysical Research: Atmospheres*, 126(21):e2021JD034814.
- Buras, R., Dowling, T., and Emde, C. (2011). New secondary-scattering correction in DISORT with increased efficiency for forward scattering. *Journal of Quantitative Spectroscopy and Radiative Transfer*, 112(12):2028–2034.
- Burrows, S. M., McCluskey, C. S., Cornwell, G., Steinke, I., Zhang, K., Zhao, B., Zawadzowicz, M., Raman, A., Kulkarni, G., China, S., Zelenyuk, A., and DeMott, P. J. (2022). Ice-Nucleating Particles That Impact Clouds and Climate: Observational and Modeling Research Needs. *Reviews of Geophysics*, 60(2):e2021RG000745.

- Carvalho, L. M. V. and Jones, C. (2001). A Satellite Method to Identify Structural Properties of Mesoscale Convective Systems Based on the Maximum Spatial Correlation Tracking Technique (MASCOTTE). *Journal of Applied Meteorology and Climatology*, 40(10):1683–1701.
- 3460 Ceppi, P., Brient, F., Zelinka, M. D., and Hartmann, D. L. (2017). Cloud feedback mechanisms and their representation in global climate models. *WIREs Climate Change*, 8(4):e465.
- Chang, Y. M., Fujita, T. T., and Tecson, J. J. (1973). METRACOM System of Cloud Velocity Determination from Geostationary Satellite Pictures. *SMRP Research Paper*, 3465 (110).
- Chen, S. S. and Houze, R. A. (1997). Diurnal variation and life-cycle of deep convective systems over the tropical pacific warm pool. *Quarterly Journal of the Royal Meteorological Society*, 123(538):357–388.
- Christensen, M. W., Jones, W. K., and Stier, P. (2020). Aerosols enhance cloud lifetime and 3470 brightness along the stratus-to-cumulus transition. *Proceedings of the National Academy of Sciences*, 117(30):17591–17598.
- Christian, H. J., Blakeslee, R. J., Boccippio, D. J., Boeck, W. L., Buechler, D. E., Driscoll, K. T., Goodman, S. J., Hall, J. M., Koshak, W. J., Mach, D. M., and Stewart, M. F. (2003). Global frequency and distribution of lightning as observed from space by the Optical Transient Detector. *Journal of Geophysical Research: Atmospheres*, 108(D1):ACL 3475 4–1–ACL 4–15.
- Clark, A. J., Bullock, R. G., Jensen, T. L., Xue, M., and Kong, F. (2014). Application of Object-Based Time-Domain Diagnostics for Tracking Precipitation Systems in Convection-Allowing Models. *Weather and Forecasting*, 29(3):517–542.
- 3480 Coniglio, M. C., Hwang, J. Y., and Stensrud, D. J. (2010). Environmental Factors in the Upscale Growth and Longevity of MCSs Derived from Rapid Update Cycle Analyses. *Monthly Weather Review*, 138(9):3514–3539.
- Crane, R. K. (1979). Automatic Cell Detection and Tracking. *IEEE Transactions on Geoscience Electronics*, 17(4):250–262.
- 3485 Crum, T. D. and Alberty, R. L. (1993). The WSR-88D and the WSR-88D Operational Support Facility. *Bulletin of the American Meteorological Society*, 74(9):1669–1688.
- Daniels, J., Velden, C., Bresky, W., Genkova, I., and Wanzong, S. (2016). *Algorithm and Software Development of Atmospheric Motion Vector (amv) Products for the Future Goes-R Advanced Baseline Imager (abi)*.
- 3490 Dawe, J. T. and Austin, P. H. (2012). Statistical analysis of an LES shallow cumulus cloud ensemble using a cloud tracking algorithm. *Atmospheric Chemistry and Physics*, 12(2):1101–1119.
- Deierling, W. and Petersen, W. A. (2008). Total lightning activity as an indicator of updraft characteristics. *Journal of Geophysical Research: Atmospheres*, 113(D16).

- 3495 Del Genio, A. D. and Kovari, W. (2002). Climatic Properties of Tropical Precipitating Convection under Varying Environmental Conditions. *Journal of Climate*, 15(18):2597–2615.
- Dim, J. R. and Takamura, T. (2013). Alternative Approach for Satellite Cloud Classification: Edge Gradient Application. *Advances in Meteorology*.
- 3500 Dixon, M. and Wiener, G. (1993). TITAN: Thunderstorm Identification, Tracking, Analysis, and Nowcasting—A Radar-based Methodology. *Journal of Atmospheric and Oceanic Technology*, 10(6):785–797.
- Douglas, M. W., Maddox, R. A., Howard, K., and Reyes, S. (1993). The Mexican Monsoon. *Journal of Climate*, 6(8):1665–1677.
- 3505 Dubuisson, P., Giraud, V., Pelon, J., Cadet, B., and Yang, P. (2008). Sensitivity of Thermal Infrared Radiation at the Top of the Atmosphere and the Surface to Ice Cloud Micro-physics. *Journal of Applied Meteorology and Climatology*, 47(10):2545–2560.
- Durand, Y., Hallibert, P., Wilson, M., Lekouara, M., Grabarnik, S., Aminou, D., Blythe, P., Napierala, B., Canaud, J.-L., Pigouche, O., Ouaknine, J., and Verez, B. (2015). The flexible combined imager onboard MTG: From design to calibration. In *Sensors, Systems, and Next-Generation Satellites XIX*, volume 9639, page 963903. SPIE.
- 3510 Eastman, R. and Wood, R. (2018). The Competing Effects of Stability and Humidity on Subtropical Stratocumulus Entrainment and Cloud Evolution from a Lagrangian Perspective. *Journal of the Atmospheric Sciences*, 75(8):2563–2578.
- Elsaesser, G. S., Roca, R., Fiolleau, T., Del Genio, A. D., and Wu, J. (2022). A Simple Model for Tropical Convective Cloud Shield Area Growth and Decay Rates Informed by Geostationary IR, GPM, and Aqua/AIRS Satellite Data. *Journal of Geophysical Research: Atmospheres*, 127(10).
- Emanuel, K. A. (1994). *Atmospheric Convection*. Oxford University Press.
- 3515 Emde, C., Buras-Schnell, R., Kylling, A., Mayer, B., Gasteiger, J., Hamann, U., Kylling, J., Richter, B., Pause, C., Dowling, T., and Bugliaro, L. (2016). The libRadtran software package for radiative transfer calculations (version 2.0.1). *Geoscientific Model Development*, 9(5):1647–1672.
- Endlich, R. M. and Wolf, D. E. (1981). Automatic Cloud Tracking Applied to GOES and METEOSAT Observations. *Journal of Applied Meteorology and Climatology*, 20(3):309–319.
- 3525 Endlich, R. M., Wolf, D. E., Hall, D. J., and Brain, A. E. (1971). Use of a Pattern Recognition Technique for Determining Cloud Motions from Sequences of Satellite Photographs. *Journal of Applied Meteorology and Climatology*, 10(1):105–117.
- Evans, J. L. and Shemo, R. E. (1996). A Procedure for Automated Satellite-Based Identification and Climatology Development of Various Classes of Organized Convection. *Journal of Applied Meteorology and Climatology*, 35(5):638–652.

- Fan, J., Leung, L. R., Rosenfeld, D., Chen, Q., Li, Z., Zhang, J., and Yan, H. (2013). Microphysical effects determine macrophysical response for aerosol impacts on deep convective clouds. *Proceedings of the National Academy of Sciences*, 110(48):E4581–E4590.
- Fan, J., Wang, Y., Rosenfeld, D., and Liu, X. (2016). Review of Aerosol–Cloud Interactions: Mechanisms, Significance, and Challenges. *Journal of the Atmospheric Sciences*, 73(11):4221–4252.
- Farfán, L. M. and Zehnder, J. A. (1994). Moving and Stationary Mesoscale Convective Systems over Northwest Mexico during the Southwest Area Monsoon Project. *Weather and Forecasting*, 9(4):630–639.
- Farnebäck, G. (2003). Two-Frame Motion Estimation Based on Polynomial Expansion. In Bigun, J. and Gustavsson, T., editors, *Image Analysis*, Lecture Notes in Computer Science, pages 363–370, Berlin, Heidelberg. Springer.
- Feingold, G., Cotton, W. R., Kreidenweis, S. M., and Davis, J. T. (1999). The Impact of Giant Cloud Condensation Nuclei on Drizzle Formation in Stratocumulus: Implications for Cloud Radiative Properties. *Journal of the Atmospheric Sciences*, 56(24):4100–4117.
- Feng, Z., Dong, X., Xi, B., McFarlane, S. A., Kennedy, A., Lin, B., and Minnis, P. (2012). Life cycle of midlatitude deep convective systems in a Lagrangian framework. *Journal of Geophysical Research: Atmospheres*, 117(D23).
- Feng, Z., Hagos, S., Rowe, A. K., Burleyson, C. D., Martini, M. N., and de Szoeke, S. P. (2015). Mechanisms of convective cloud organization by cold pools over tropical warm ocean during the AMIE/DYNAMO field campaign. *Journal of Advances in Modeling Earth Systems*, 7(2):357–381.
- Feng, Z., Hardin, J., Barnes, H. C., Li, J., Leung, L. R., Varble, A., and Zhang, Z. (2022). PyFLEXTRKR: a Flexible Feature Tracking Python Software for Convective Cloud Analysis. *EGUphere*, pages 1–29.
- Feng, Z., Hardin, J., Barnes, H. C., Li, J., Leung, L. R., Varble, A., and Zhang, Z. (2023a). PyFLEXTRKR: a flexible feature tracking Python software for convective cloud analysis. *Geoscientific Model Development*, 16(10):2753–2776.
- Feng, Z., Houze, R. A., Leung, L. R., Song, F., Hardin, J. C., Wang, J., Gustafson, W. I., and Homeyer, C. R. (2019). Spatiotemporal Characteristics and Large-Scale Environments of Mesoscale Convective Systems East of the Rocky Mountains. *Journal of Climate*, 32(21):7303–7328.
- Feng, Z., Leung, L. R., Hardin, J., Terai, C. R., Song, F., and Caldwell, P. (2023b). Mesoscale Convective Systems in DYAMOND Global Convection-Permitting Simulations. *Geophysical Research Letters*, 50(4):e2022GL102603.
- Feng, Z., Leung, L. R., Liu, N., Wang, J., Houze Jr, R. A., Li, J., Hardin, J. C., Chen, D., and Guo, J. (2021). A Global High-Resolution Mesoscale Convective System Database Using Satellite-Derived Cloud Tops, Surface Precipitation, and Tracking. *Journal of Geophysical Research: Atmospheres*, 126(8):e2020JD034202.

- Field, P. R., Lawson, R. P., Brown, P. R. A., Lloyd, G., Westbrook, C., Moisseev, D., Miltenberger, A., Nenes, A., Blyth, A., Choularton, T., Connolly, P., Buehl, J., Crosier, J., Cui, Z., Dearden, C., DeMott, P., Flossmann, A., Heymsfield, A., Huang, Y., Kalesse, H., Kanji, Z. A., Korolev, A., Kirchgaessner, A., Lasher-Trapp, S., Leisner, T., McFarquhar, G., Phillips, V., Stith, J., and Sullivan, S. (2017). Secondary Ice Production: Current State of the Science and Recommendations for the Future. *Meteorological Monographs*, 58(1):7.1–7.20.
- Fiolleau, T. and Roca, R. (2013). An Algorithm for the Detection and Tracking of Tropical Mesoscale Convective Systems Using Infrared Images From Geostationary Satellite. *IEEE Transactions on Geoscience and Remote Sensing*, 51(7):4302–4315.
- Fu, Q. (1996). An Accurate Parameterization of the Solar Radiative Properties of Cirrus Clouds for Climate Models. *Journal of Climate*, 9(9):2058–2082.
- Fu, Q. (2015). RADIATION TRANSFER IN THE ATMOSPHERE | Cloud-Radiative Processes. In North, G. R., Pyle, J., and Zhang, F., editors, *Encyclopedia of Atmospheric Sciences (Second Edition)*, pages 13–15. Academic Press, Oxford.
- Fu, Q., Yang, P., and Sun, W. B. (1998). An Accurate Parameterization of the Infrared Radiative Properties of Cirrus Clouds for Climate Models. *Journal of Climate*, 11(9):2223–2237.
- Fueglistaler, S., Dessler, A. E., Dunkerton, T. J., Folkins, I., Fu, Q., and Mote, P. W. (2009). Tropical tropopause layer. *Reviews of Geophysics*, 47(1).
- Fujita, T. T. (1969). Present Status of Cloud Velocity Computations from the ATS I and ATS III Satellites. *Cospar Space Research*, IX.
- Fujita, T. T., Bradbury, D. L., Murino, C., and Hull, L. (1968). A Study of Mesoscale Cloud Motions Computed from ATS-I and Terrestrial Photographs. *SMRP Research Paper*, (71).
- Fujita, T. T., Fearl, E. W., and Shenk, W. E. (1975). Satellite-Tracked Cumulus Velocities. *Journal of Applied Meteorology (1962-1982)*, 14(3):407–413.
- Futyan, J. M. and Del Genio, A. D. (2007). Deep Convective System Evolution over Africa and the Tropical Atlantic. *Journal of Climate*, 20(20):5041–5060.
- Gasparini, B., Blossey, P. N., Hartmann, D. L., Lin, G., and Fan, J. (2019). What Drives the Life Cycle of Tropical Anvil Clouds? *Journal of Advances in Modeling Earth Systems*, 11(8):2586–2605.
- Gasparini, B., Sokol, A. B., Wall, C. J., Hartmann, D. L., and Blossey, P. N. (2022). Diurnal Differences in Tropical Maritime Anvil Cloud Evolution. *Journal of Climate*, 35(5):1655–1677.
- Gasparini, B., Sullivan, S. C., Sokol, A. B., Kärcher, B., Jensen, E., and Hartmann, D. L. (2023). Opinion: Tropical cirrus – From micro-scale processes to climate-scale impacts. *EGUsphere*, pages 1–47.

- 3610 Gasteiger, J., Emde, C., Mayer, B., Buras, R., Buehler, S. A., and Lemke, O. (2014). Representative wavelengths absorption parameterization applied to satellite channels and spectral bands. *Journal of Quantitative Spectroscopy and Radiative Transfer*, 148:99–115.
- 3615 Ge, J., Hu, X., Mu, Q., Liu, B., Zhu, Z., Du, J., Su, J., Li, Q., and Zhang, C. (2024). Contrasting characteristics of continental and oceanic deep convective systems at different life stages from CloudSat observations. *Atmospheric Research*, 298:107157.
- Goodman, S. J., Blakeslee, R. J., Koshak, W. J., Mach, D., Bailey, J., Buechler, D., Carey, L., Schultz, C., Bateman, M., McCaul, E., and Stano, G. (2013). The GOES-R Geostationary Lightning Mapper (GLM). *Atmospheric Research*, 125–126:34–49.
- 3620 Grant, L. D. and van den Heever, S. C. (2016). Cold pool dissipation. *Journal of Geophysical Research: Atmospheres*, 121(3):1138–1155.
- Gunshor, M. M., Schmit, T. J., Pogorzala, D. R., Lindstrom, S. S., and Nelson, J. P. (2020). GOES-R series ABI Imagery artifacts. *Journal of Applied Remote Sensing*, 14(3):032411.
- 3625 Han, L., Fu, S., Zhao, L., Zheng, Y., Wang, H., and Lin, Y. (2009). 3D Convective Storm Identification, Tracking, and Forecasting—An Enhanced TITAN Algorithm. *Journal of Atmospheric and Oceanic Technology*, 26(4):719–732.
- Handwerker, J. (2002). Cell tracking with TRACE3D—a new algorithm. *Atmospheric Research*, 61(1):15–34.
- 3630 Harrop, B. E. and Hartmann, D. L. (2016). The role of cloud radiative heating within the atmosphere on the high cloud amount and top-of-atmosphere cloud radiative effect. *Journal of Advances in Modeling Earth Systems*, 8(3):1391–1410.
- Hartmann, D. L. (2016). Tropical anvil clouds and climate sensitivity. *PNAS*, 113(32):8897–8899.
- Hartmann, D. L. and Larson, K. (2002). An important constraint on tropical cloud - climate feedback. *Geophysical Research Letters*, 29(20):12–1–12–4.
- 3635 Hartmann, D. L., Ockert-Bell, M. E., and Michelsen, M. L. (1992). The Effect of Cloud Type on Earth's Energy Balance: Global Analysis. *Journal of Climate*, 5(11):1281–1304.
- Hartung, D. C., Sieglaff, J. M., Cronce, L. M., and Feltz, W. F. (2013). An Intercomparison of UW Cloud-Top Cooling Rates with WSR-88D Radar Data. *Weather and Forecasting*, 28(2):463–480.
- 3640 Hayden, L., Liu, C., and Liu, N. (2021). Properties of Mesoscale Convective Systems Throughout Their Lifetimes Using IMERG, GPM, WWLLN, and a Simplified Tracking Algorithm. *Journal of Geophysical Research: Atmospheres*, 126(20):e2021JD035264.
- Heidinger, A. K. and Pavolonis, M. J. (2009). Gazing at Cirrus Clouds for 25 Years through a Split Window. Part I: Methodology. *Journal of Applied Meteorology and Climatology*, 48(6):1100–1116.

- Heidinger, A. K., Pavolonis, M. J., Calvert, C., Hoffman, J., Nebuda, S., Straka, W., Walther, A., and Wanzong, S. (2020). Chapter 6 - ABI Cloud Products from the GOES-R Series. In Goodman, S. J., Schmit, T. J., Daniels, J., and Redmon, R. J., editors, *The GOES-R Series*, pages 43–62. Elsevier.
- 3650 Heikenfeld, M., Marinescu, P. J., Christensen, M., Watson-Parris, D., Senf, F., van den Heever, S. C., and Stier, P. (2019). tobac 1.2: towards a flexible framework for tracking and analysis of clouds in diverse datasets. *Geoscientific Model Development*, 12(11):4551–4570.
- Held, I. M. and Soden, B. J. (2006). Robust Responses of the Hydrological Cycle to Global  
3655 Warming. *J. Climate*, 19(21):5686–5699.
- Hersbach, H., Bell, B., Berrisford, P., Hirahara, S., Horányi, A., Muñoz-Sabater, J., Nicolas, J., Peubey, C., Radu, R., Schepers, D., Simmons, A., Soci, C., Abdalla, S., Abellán, X., Balsamo, G., Bechtold, P., Biavati, G., Bidlot, J., Bonavita, M., De Chiara, G., Dahlgren, P., Dee, D., Diamantakis, M., Dragani, R., Flemming, J., Forbes, R., Fuentes, M., Geer, A., Haimberger, L., Healy, S., Hogan, R. J., Hólm, E., Janisková, M., Keeley, S., Laloyaux, P., Lopez, P., Lupu, C., Radnoti, G., de Rosnay, P., Rozum, I., Vamborg, F., Villaume, S., and Thépaut, J.-N. (2020). The ERA5 global reanalysis. *Quarterly Journal of the Royal Meteorological Society*, 146(730):1999–2049.
- Heus, T. and Seifert, A. (2013). Automated tracking of shallow cumulus clouds in large domain, long duration large eddy simulations. *Geoscientific Model Development*, 6(4):1261–1273.
- 3665 Heymsfield, A. J. and Miloshevich, L. M. (1993). Homogeneous Ice Nucleation and Super-cooled Liquid Water in Orographic Wave Clouds. *Journal of the Atmospheric Sciences*, 50(15):2335–2353.
- Higgins, R. W. and Shi, W. (2001). Intercomparison of the Principal Modes of Interannual and Intraseasonal Variability of the North American Monsoon System. *Journal of Climate*, 14(3):403–417.
- 3670 Hildebrandsson, H. H. (1887). Remarks concerning the nomenclature of clouds for ordinary use. *Quarterly Journal of the Royal Meteorological Society*, 13(62):148–154. \_eprint: <https://onlinelibrary.wiley.com/doi/pdf/10.1002/qj.4970136211>.
- Hill, P. G., Holloway, C. E., Byrne, M. P., Lambert, F. H., and Webb, M. J. (2023). Climate Models Underestimate Dynamic Cloud Feedbacks in the Tropics. *Geophysical Research Letters*, 50(15):e2023GL104573.
- Hodges, K. I. (1994). A General Method for Tracking Analysis and Its Application to  
3680 Meteorological Data. *Monthly Weather Review*, 122(11):2573–2586.
- Hodges, K. I. (1995). Feature Tracking on the Unit Sphere. *Monthly Weather Review*, 123(12):3458–3465.
- Hodges, K. I. and Thorncroft, C. D. (1997). Distribution and Statistics of African Mesoscale Convective Weather Systems Based on the ISCCP Meteosat Imagery. *Monthly Weather Review*, 125(11):2821–2837.

- Holloway, C. E., Wing, A. A., Bony, S., Muller, C., Masunaga, H., L'Ecuyer, T. S., Turner, D. D., and Zuidema, P. (2017). Observing Convective Aggregation. *Surveys in Geophysics*, 38(6):1199–1236.
- Hong, G., Heygster, G., Miao, J., and Kunzi, K. (2005). Detection of tropical deep convective clouds from AMSU-B water vapor channels measurements. *Journal of Geophysical Research: Atmospheres*, 110(D5).
- Hoose, C. and Möhler, O. (2012). Heterogeneous ice nucleation on atmospheric aerosols: A review of results from laboratory experiments. *Atmospheric Chemistry and Physics*, 12(20):9817–9854.
- Horner, G. and Gryspeerdt, E. (2023). The evolution of deep convective systems and their associated cirrus outflows. *Atmospheric Chemistry and Physics*, 23(22):14239–14253.
- Hoshen, J. and Kopelman, R. (1976). Percolation and cluster distribution. I. Cluster multiple labeling technique and critical concentration algorithm. *Phys. Rev. B*, 14(8):3438–3445.
- Houze, R. A. (2004). Mesoscale convective systems. *Reviews of Geophysics*, 42(4).
- Houze, R. A. (2014). Chapter 8 - Cumulonimbus and Severe Storms. In Houze, R. A., editor, *International Geophysics*, volume 104 of *Cloud Dynamics*, pages 187–236. Academic Press.
- Houze, R. A. (2018). 100 Years of Research on Mesoscale Convective Systems. *Meteorological Monographs*, 59(1):17.1–17.54.
- Hu, Y. X. and Stamnes, K. (1993). An Accurate Parameterization of the Radiative Properties of Water Clouds Suitable for Use in Climate Models. *Journal of Climate*, 6(4):728–742.
- Iacovazzi, R. and Wu, X. (2020). GOES-16 Advanced Baseline Imager visible near-infrared channel low-light signal-to-noise ratio. *JARS*, 14(2):026502.
- Ickes, L., Welti, A., Hoose, C., and Lohmann, U. (2015). Classical nucleation theory of homogeneous freezing of water: Thermodynamic and kinetic parameters. *Physical Chemistry Chemical Physics*, 17(8):5514–5537.
- Igel, M. R., Drager, A. J., and van den Heever, S. C. (2014). A CloudSat cloud object partitioning technique and assessment and integration of deep convective anvil sensitivities to sea surface temperature. *Journal of Geophysical Research: Atmospheres*, 119(17):10515–10535.
- Jeevanjee, N. (2017). Vertical Velocity in the Gray Zone. *Journal of Advances in Modeling Earth Systems*, 9(6):2304–2316.
- Jeevanjee, N. and Fueglistaler, S. (2020). Simple Spectral Models for Atmospheric Radiative Cooling. *Journal of the Atmospheric Sciences*, 77(2):479–497.
- Jeevanjee, N. and Romps, D. M. (2013). Convective self-aggregation, cold pools, and domain size. *Geophysical Research Letters*, 40(5):994–998.

- Jirak, I. L. and Cotton, W. R. (2007). Observational Analysis of the Predictability of Mesoscale Convective Systems. *Weather and Forecasting*, 22(4):813–838.
- Johnson, J. T., MacKeen, P. L., Witt, A., Mitchell, E. D. W., Stumpf, G. J., Eilts, M. D., and Thomas, K. W. (1998). The Storm Cell Identification and Tracking Algorithm: An Enhanced WSR-88D Algorithm. *Weather and Forecasting*, 13(2):263–276.
- Johnson, R. H., Rickenbach, T. M., Rutledge, S. A., Ciesielski, P. E., and Schubert, W. H. (1999). Trimodal Characteristics of Tropical Convection. *Journal of Climate*, 12(8):2397–2418.
- Jones, W. K., Christensen, M. W., and Stier, P. (2023a). A semi-Lagrangian method for detecting and tracking deep convective clouds in geostationary satellite observations. *Atmospheric Measurement Techniques*, 16(4):1043–1059.
- Jones, W. K., Stengel, M., and Stier, P. (2023b). A Lagrangian Perspective on the Lifecycle and Cloud Radiative Effect of Deep Convective Clouds Over Africa. *EGUsphere*, pages 1–25.
- Kalchbrenner, N., Grefenstette, E., and Blunsom, P. (2014). A Convolutional Neural Network for Modelling Sentences. *arXiv:1404.2188 [cs]*.
- Kanji, Z. A., Ladino, L. A., Wex, H., Boose, Y., Burkert-Kohn, M., Cziczo, D. J., and Krämer, M. (2017). Overview of Ice Nucleating Particles. *Meteorological Monographs*, 58(1):1.1–1.33.
- Kärcher, B. and Lohmann, U. (2002). A Parameterization of cirrus cloud formation: Homogeneous freezing including effects of aerosol size. *Journal of Geophysical Research: Atmospheres*, 107(D23):AAC 9–1–AAC 9–10.
- Kärcher, B. and Ström, J. (2003). The roles of dynamical variability and aerosols in cirrus cloud formation. *Atmospheric Chemistry and Physics*, 3(3):823–838.
- Keenan, T., Joe, P., Wilson, J., Collier, C., Golding, B., Burgess, D., May, P., Pierce, C., Bally, J., Crook, A., Seed, A., Sills, D., Berry, L., Potts, R., Bell, I., Fox, N., Ebert, E., Eilts, M., O'Loughlin, K., Webb, R., Carbone, R., Browning, K., Roberts, R., and Mueller, C. (2003). The Sydney 2000 World Weather Research Programme Forecast Demonstration Project: Overview and Current Status: Overview and Current Status. *Bulletin of the American Meteorological Society*, 84(8):1041–1054.
- Khain, A., Rosenfeld, D., and Pokrovsky, A. (2005). Aerosol impact on the dynamics and microphysics of deep convective clouds. *Quarterly Journal of the Royal Meteorological Society*, 131(611):2639–2663.
- Konduru, R. T., Kishtawal, C. M., and Shah, S. (2013). A new perspective on the infrared brightness temperature distribution of the deep convective clouds. *J Earth Syst Sci*, 122(5):1195–1206.
- Koop, T., Luo, B., Tsias, A., and Peter, T. (2000). Water activity as the determinant for homogeneous ice nucleation in aqueous solutions. *Nature*, 406(6796):611–614.

- Koren, I., Martins, J. V., Remer, L. A., and Afargan, H. (2008). Smoke Invigoration Versus Inhibition of Clouds over the Amazon. *Science*, 321(5891):946–949.
- Kroeger, T., Timofte, R., Dai, D., and Van Gool, L. (2016). Fast Optical Flow using Dense Inverse Search. arXiv.
- Laing, A. G. and Michael Fritsch, J. (1997). The global population of mesoscale convective complexes. *Quarterly Journal of the Royal Meteorological Society*, 123(538):389–405.
- Lakshmanan, V. and Smith, T. (2009). An Objective Method of Evaluating and Devising Storm-Tracking Algorithms. *Weather and Forecasting*, 25(2):701–709.
- Lakshmanan, V. and Smith, T. (2010). An Objective Method of Evaluating and Devising Storm-Tracking Algorithms. *Weather and Forecasting*, 25(2):701–709.
- Lakshmanan, V., Smith, T., Stumpf, G., and Hondl, K. (2007). The Warning Decision Support System—Integrated Information. *Weather and Forecasting*, 22(3):596–612.
- Leese, J. A., Novak, C. S., and Ray Taylor, V. (1970). The determination of cloud pattern motions from geosynchronous satellite image data. *Pattern Recognition*, 2(4):279–292.
- Li, J., Feng, Z., Qian, Y., and Leung, L. R. (2021). A high-resolution unified observational data product of mesoscale convective systems and isolated deep convection in the United States for 2004–2017. *Earth System Science Data*, 13(2):827–856.
- Liang, K., Shi, H., Yang, P., and Zhao, X. (2017). An Integrated Convective Cloud Detection Method Using FY-2 VISSR Data. *Atmosphere*, 8(2):42.
- Lilly, D. K. (1988). Cirrus Outflow Dynamics. *Journal of the Atmospheric Sciences*, 45(10):1594–1605.
- Lin, B., Wong, T., Wielicki, B. A., and Hu, Y. (2004). Examination of the Decadal Tropical Mean ERBS Nonscanner Radiation Data for the Iris Hypothesis. *Journal of Climate*, 17(6):1239–1246.
- Lindsey, D. T., Bikos, D., and Grasso, L. (2018). Using the GOES-16 Split Window Difference to Detect a Boundary prior to Cloud Formation. *Bulletin of the American Meteorological Society*, 99(8):1541–1544.
- Lindsey, D. T., Grasso, L., Dostalek, J. F., and Kerkmann, J. (2014). Use of the GOES-R Split-Window Difference to Diagnose Deepening Low-Level Water Vapor. *Journal of Applied Meteorology and Climatology*, 53(8):2005–2016.
- Lindzen, R. S., Chou, M.-D., and Hou, A. Y. (2001). Does the Earth Have an Adaptive Infrared Iris? *Bulletin of the American Meteorological Society*, 82(3):417–432.
- Liou, K.-N. (1992). *Radiation and Cloud Processes in the Atmosphere: Theory, Observation and Modeling*. Oxford University Press.
- Liu, H., Koren, I., and Altaratz, O. (2023). Observed decreasing trend in the upper-tropospheric cloud top temperature. *npj Climate and Atmospheric Science*, 6(1):1–8.

- Loeb, N. G., Doelling, D. R., Wang, H., Su, W., Nguyen, C., Corbett, J. G., Liang, L., Mitrescu, C., Rose, F. G., and Kato, S. (2018). Clouds and the Earth's Radiant Energy System (CERES) Energy Balanced and Filled (EBAF) Top-of-Atmosphere (TOA) Edition-4.0 Data Product. *Journal of Climate*, 31(2):895–918.
- Lucas, B. D. and Kanade, T. (1981). An iterative image registration technique with an application to stereo vision. In *Proceedings of the 7th international joint conference on Artificial intelligence - Volume 2*, IJCAI'81, pages 674–679, San Francisco, CA, USA. Morgan Kaufmann Publishers Inc.
- Luo, Z. and Rossow, W. B. (2004). Characterizing Tropical Cirrus Life Cycle, Evolution, and Interaction with Upper-Tropospheric Water Vapor Using Lagrangian Trajectory Analysis of Satellite Observations. *Journal of Climate*, 17(23):4541–4563.
- Maddox, R. A. (1980a). Mesoscale Convective Complexes. *Bulletin of the American Meteorological Society*, 61(11):1374–1387.
- Maddox, R. A. (1980b). Mesoscale Convective Complexes. *Bulletin of the American Meteorological Society*, 61(11):1374–1387.
- Marinescu, P. J., Heever, S. C. v. d., Heikenfeld, M., Barrett, A. I., Barthlott, C., Hoose, C., Fan, J., Fridlind, A. M., Matsui, T., Miltenberger, A. K., Stier, P., Vie, B., White, B. A., and Zhang, Y. (2021). Impacts of Varying Concentrations of Cloud Condensation Nuclei on Deep Convective Cloud Updrafts—A Multimodel Assessment. *Journal of the Atmospheric Sciences*, 78(4):1147–1172.
- Martin, P. P., Durand, Y., Aminou, D., Gaudin-Delrieu, C., and Lamard, J.-L. (2021). FCI instrument on-board MeteoSat Third Generation satellite: Design and development status. In *International Conference on Space Optics — ICSO 2020*, volume 11852, pages 125–140. SPIE.
- Massie, S., Gettelman, A., Randel, W., and Baumgardner, D. (2002). Distribution of tropical cirrus in relation to convection. *Journal of Geophysical Research: Atmospheres*, 107(D21):AAC 19–1–AAC 19–16.
- Masunaga, H. and L'Ecuyer, T. S. (2014). A Mechanism of Tropical Convection Inferred from Observed Variability in the Moist Static Energy Budget. *Journal of the Atmospheric Sciences*, 71(10):3747–3766.
- Masunaga, H. and Luo, Z. J. (2016). Convective and large-scale mass flux profiles over tropical oceans determined from synergistic analysis of a suite of satellite observations. *Journal of Geophysical Research: Atmospheres*, 121(13):7958–7974.
- Matsudo, C. M. and Salio, P. V. (2011). Severe weather reports and proximity to deep convection over Northern Argentina. *Atmospheric Research*, 100(4):523–537.
- McGarragh, G. R., Poulsen, C. A., Thomas, G. E., Povey, A. C., Sus, O., Stapelberg, S., Schlundt, C., Proud, S., Christensen, M. W., Stengel, M., Hollmann, R., and Grainger, R. G. (2018). The Community Cloud retrieval for CLimate (CC4CL) Part 2: The optimal estimation approach. *Atmospheric Measurement Techniques*, 11(6):3397–3431.

- McKim, B., Bony, S., and Dufresne, J.-L. (2024). Weak anvil cloud area feedback suggested by physical and observational constraints. *Nature Geoscience*, pages 1–6.
- Mecikalski, J. R. and Bedka, K. M. (2006). Forecasting Convective Initiation by Monitoring the Evolution of Moving Cumulus in Daytime GOES Imagery. *Monthly Weather Review*, 134(1):49–78.
- Mecikalski, J. R., Watts, P. D., and Koenig, M. (2011). Use of Meteosat Second Generation optimal cloud analysis fields for understanding physical attributes of growing cumulus clouds. *Atmospheric Research*, 102(1):175–190.
- 3845 Menzel, W. P. (2001). Cloud Tracking with Satellite Imagery: From the Pioneering Work of Ted Fujita to the Present. *Bulletin of the American Meteorological Society*, 82(1):33–48.
- Morel, C. and Senesi, S. (2002). A climatology of mesoscale convective systems over Europe using satellite infrared imagery. I: Methodology. *Quarterly Journal of the Royal Meteorological Society*, 128(584):1953–1971.
- 3850 Moreno-Ibáñez, M., Laprise, R., and Gachon, P. (2021). Recent advances in polar low research: Current knowledge, challenges and future perspectives. 73(1):1890412.
- Müller, R., Haussler, S., and Jerg, M. (2018). The Role of NWP Filter for the Satellite Based Detection of Cumulonimbus Clouds. *Remote Sensing*, 10(3):386.
- Müller, R., Haussler, S., Jerg, M., and Heizenreder, D. (2019). A Novel Approach for the 3855 Detection of Developing Thunderstorm Cells. *Remote Sensing*, 11(4):443.
- Mülmenstädt, J., Sourdeval, O., Delanoë, J., and Quaas, J. (2015). Frequency of occurrence of rain from liquid-, mixed-, and ice-phase clouds derived from A-Train satellite retrievals. *Geophysical Research Letters*, 42(15):6502–6509.
- Nicholson, S. E. (2009). A revised picture of the structure of the monsoon and land ITCZ 3860 over West Africa. *Climate Dynamics*, 32(7):1155–1171.
- Nicholson, S. E. (2018). The ITCZ and the Seasonal Cycle over Equatorial Africa. *Bulletin of the American Meteorological Society*, 99(2):337–348.
- Norris, J. R., Allen, R. J., Evan, A. T., Zelinka, M. D., O'Dell, C. W., and Klein, S. A. (2016). Evidence for climate change in the satellite cloud record. *Nature*, 536(7614):72–75.
- 3865 Nowicki, S. M. J. and Merchant, C. J. (2004). Observations of diurnal and spatial variability of radiative forcing by equatorial deep convective clouds. *Journal of Geophysical Research: Atmospheres*, 109(D11). eprint: <https://onlinelibrary.wiley.com/doi/pdf/10.1029/2003JD004176>.
- Núñez Ocasio, K. M., Evans, J. L., and Young, G. S. (2020). Tracking Mesoscale Convective Systems that are Potential Candidates for Tropical Cyclogenesis. *Monthly Weather Review*, 148(2):655–669.
- Orville, R. E. and Henderson, R. W. (1984). Absolute Spectral Irradiance Measurements of Lightning from 375 to 880 nm. *Journal of the Atmospheric Sciences*, 41(21):3180–3187.

- Park, J. M., van den Heever, S. C., Igel, A. L., Grant, L. D., Johnson, J. S., Saleeby, S. M., Miller, S. D., and Reid, J. S. (2020). Environmental controls on tropical sea breeze convection and resulting aerosol redistribution. *Journal of Geophysical Research: Atmospheres*, 125(6).
- Peters, J. M. and Chavas, D. R. (2021). Evaluating the Conservation of Energy Variables in Simulations of Deep Moist Convection. *Journal of the Atmospheric Sciences*, 78(10):3229–3246.
- Peters, J. M., Mulholland, J. P., and Chavas, D. R. (2022). Generalized Lapse Rate Formulas for Use in Entraining CAPE Calculations. *Journal of the Atmospheric Sciences*, 79(3):815–836.
- Peterson, M. (2019). Research Applications for the Geostationary Lightning Mapper Operational Lightning Flash Data Product. *J Geophys Res Atmos*, 124(17-18):10205–10231.
- Peterson, M. (2020). Removing solar artifacts from Geostationary Lightning Mapper data to document lightning extremes. *J Appl Remote Sens*, 14(3).
- Pinto, J. O., Grim, J. A., and Steiner, M. (2015). Assessment of the High-Resolution Rapid Refresh Model's Ability to Predict Mesoscale Convective Systems Using Object-Based Evaluation. *Weather and Forecasting*, 30(4):892–913.
- Plant, R. S. (2009). Statistical properties of cloud lifecycles in cloud-resolving models. *Atmospheric Chemistry and Physics*, 9(6):2195–2205.
- Prein, A. F., Feng, Z., Fiolleau, T., Moon, Z. L., Núñez Ocasio, K. M., Kukulies, J., Roca, R., Varble, A. C., Rehbein, A., Liu, C., Ikeda, K., Mu, Y., and Rasmussen, R. M. (2024). Km-Scale Simulations of Mesoscale Convective Systems Over South America—A Feature Tracker Intercomparison. *Journal of Geophysical Research: Atmospheres*, 129(8):e2023JD040254.
- Prein, A. F., Langhans, W., Fosser, G., Ferrone, A., Ban, N., Goergen, K., Keller, M., Tölle, M., Gutjahr, O., Feser, F., Brisson, E., Kollet, S., Schmidli, J., van Lipzig, N. P. M., and Leung, R. (2015). A review on regional convection-permitting climate modeling: Demonstrations, prospects, and challenges. *Reviews of Geophysics*, 53(2):323–361.
- Prein, A. F., Rasmussen, R. M., Wang, D., and Giangrande, S. E. (2021). Sensitivity of organized convective storms to model grid spacing in current and future climates. *Philosophical Transactions of the Royal Society A: Mathematical, Physical and Engineering Sciences*, 379(2195):20190546.
- Protopapadaki, S. E., Stubenrauch, C. J., and Feofilov, A. G. (2017). Upper tropospheric cloud systems derived from IR sounders: Properties of cirrus anvils in the tropics. *Atmospheric Chemistry and Physics*, 17(6):3845–3859.
- Proud, S. R. and Bachmeier, S. (2021). Record-Low Cloud Temperatures Associated With a Tropical Deep Convective Event. *Geophysical Research Letters*, 48(6):e2020GL092261.
- Punge, H. J. and Kunz, M. (2016). Hail observations and hailstorm characteristics in Europe: A review. *Atmospheric Research*, 176-177:159–184.

- Pérez, J. S., Meinhardt-Llopis, E., and Facciolo, G. (2013). TV-L1 Optical Flow Estimation. *Image Processing On Line*, 3:137–150.
- <sup>3915</sup> Raghuraman, S. P., Medeiros, B., and Gettelman, A. (2024). Observational Quantification of Tropical High Cloud Changes and Feedbacks. *Journal of Geophysical Research: Atmospheres*, 129(7):e2023JD039364.
- Ramanathan, V., Cess, R. D., Harrison, E. F., Minnis, P., Barkstrom, B. R., Ahmad, E., and Hartmann, D. (1989). Cloud-Radiative Forcing and Climate: Results from the Earth <sup>3920</sup> Radiation Budget Experiment. *Science*, 243(4887):57–63.
- Raut, B. A., Jackson, R., Picel, M., Collis, S. M., Bergemann, M., and Jakob, C. (2021). An Adaptive Tracking Algorithm for Convection in Simulated and Remote Sensing Data. *Journal of Applied Meteorology and Climatology*, 60(4):513–526.
- Riehl, H. and Malkus, J. S. (1958). On the Heat Balance in the Equatorial Trough Zone. <sup>3925</sup> *Geophysica*, 6(3–4).
- Rinehart, R. E. and Garvey, E. T. (1978). Three-dimensional storm motion detection by conventional weather radar. *Nature*, 273(5660):287–289.
- Roberts, R. D. and Rutledge, S. (2003). Nowcasting Storm Initiation and Growth Using GOES-8 and WSR-88D Data. *Weather and Forecasting*, 18(4):562–584.
- <sup>3930</sup> Roca, R., Fiolleau, T., and Bouniol, D. (2017). A Simple Model of the Life Cycle of Mesoscale Convective Systems Cloud Shield in the Tropics. *Journal of Climate*, 30(11):4283–4298.
- Rogers, R. R. (1979). *A short course in cloud physics / by R. R. Rogers*. Pergamon Press Oxford ; New York, 2d ed. edition.
- <sup>3935</sup> Romps, D. M. (2015). MSE Minus CAPE is the True Conserved Variable for an Adiabatically Lifted Parcel. *Journal of the Atmospheric Sciences*, 72(9):3639–3646.
- Romps, D. M. and Kuang, Z. (2010). Do Undiluted Convective Plumes Exist in the Upper Tropical Troposphere? *Journal of the Atmospheric Sciences*, 67(2):468–484.
- Rosenfeld, D. (1987). Objective Method for Analysis and Tracking of Convective Cells as <sup>3940</sup> Seen by Radar. *Journal of Atmospheric and Oceanic Technology*, 4(3):422–434.
- Rosenfeld, D., Lohmann, U., Raga, G. B., O'Dowd, C. D., Kulmala, M., Fuzzi, S., Reissell, A., and Andreae, M. O. (2008). Flood or Drought: How Do Aerosols Affect Precipitation? *Science*, 321(5894):1309–1313.
- Rosenfeld, D., Wolff, D. B., and Atlas, D. (1993). General Probability-matched Relations <sup>3945</sup> between Radar Reflectivity and Rain Rate. *Journal of Applied Meteorology and Climatology*, 32(1):50–72.
- Schmetz, J., Tjemkes, S. A., Gube, M., and van de Berg, L. (1997). Monitoring deep convection and convective overshooting with METEOSAT. *Advances in Space Research*, 19(3):433–441.

- 3950 Schmit, T. J., Griffith, P., Gunshor, M. M., Daniels, J. M., Goodman, S. J., and Lebair, W. J. (2016). A Closer Look at the ABI on the GOES-R Series. *Bull. Amer. Meteor. Soc.*, 98(4):681–698.
- Schmit, T. J. and Gunshor, M. M. (2020). Chapter 4 - ABI Imagery from the GOES-R Series. In Goodman, S. J., Schmit, T. J., Daniels, J., and Redmon, R. J., editors, *The GOES-R Series*, pages 23–34. Elsevier.
- 3955 Schröder, M., König, M., and Schmetz, J. (2009). Deep convection observed by the Spinning Enhanced Visible and Infrared Imager on board Meteosat 8: Spatial distribution and temporal evolution over Africa in summer and winter 2006. *Journal of Geophysical Research: Atmospheres*, 114(D5).
- 3960 Schulz, H. and Stevens, B. (2018). Observing the Tropical Atmosphere in Moisture Space. *Journal of the Atmospheric Sciences*, 75(10):3313–3330.
- Schumacher, C. and Houze, R. A. (2003). Stratiform Rain in the Tropics as Seen by the TRMM Precipitation Radar. *Journal of Climate*, 16(11):1739–1756.
- 3965 Schumacher, C., Houze, R. A., and Kraucunas, I. (2004). The Tropical Dynamical Response to Latent Heating Estimates Derived from the TRMM Precipitation Radar. *Journal of the Atmospheric Sciences*, 61(12):1341–1358.
- Seeley, J. T., Jeevanjee, N., Langhans, W., and Romps, D. M. (2019a). Formation of Tropical Anvil Clouds by Slow Evaporation. *Geophysical Research Letters*, 46(1):492–501.
- 3970 Seeley, J. T., Jeevanjee, N., and Romps, D. M. (2019b). FAT or FiTT: Are Anvil Clouds or the Tropopause Temperature Invariant? *Geophysical Research Letters*, 46(3):1842–1850.
- Seeley, J. T. and Romps, D. M. (2015a). The Effect of Global Warming on Severe Thunderstorms in the United States. *Journal of Climate*, 28(6):2443–2458.
- 3975 Seeley, J. T. and Romps, D. M. (2015b). Why does tropical convective available potential energy (CAPE) increase with warming? *Geophysical Research Letters*, 42(23):10,429–10,437.
- Seeley, J. T. and Romps, D. M. (2016). Tropical cloud buoyancy is the same in a world with or without ice. *Geophysical Research Letters*, 43(7):3572–3579.
- Seidel, S. D. and Yang, D. (2022). Temperatures of Anvil Clouds and Radiative Tropopause in a Wide Array of Cloud-Resolving Simulations. *Journal of Climate*, 35(24):8065–8078.
- 3980 Senf, F. and Deneke, H. (2017). Satellite-Based Characterization of Convective Growth and Glaciation and Its Relationship to Precipitation Formation over Central Europe. *Journal of Applied Meteorology and Climatology*, 56(7):1827–1845.
- Senf, F., Dietzsch, F., Hünerbein, A., and Deneke, H. (2015). Characterization of Initiation and Growth of Selected Severe Convective Storms over Central Europe with MSG-SEVIRI. *Journal of Applied Meteorology and Climatology*, 54(1):207–224.

- Senf, F., Klocke, D., and Brueck, M. (2018a). Size-Resolved Evaluation of Simulated Deep Tropical Convection. *Mon. Wea. Rev.*, 146(7):2161–2182.
- Senf, F., Lenk, S., Deneke, H., and Heinze, R. (2018b). High-resolution simulations of deep convective growth and Meteosat observations. 3990
- Sherwood, S. C., Webb, M. J., Annan, J. D., Armour, K. C., Forster, P. M., Hargreaves, J. C., Hegerl, G., Klein, S. A., Marvel, K. D., Rohling, E. J., Watanabe, M., Andrews, T., Braconnot, P., Bretherton, C. S., Foster, G. L., Hausfather, Z., von der Heydt, A. S., Knutti, R., Mauritzen, T., Norris, J. R., Proistosescu, C., Rugenstein, M., Schmidt, G. A., Tokarska, K. B., and Zelinka, M. D. (2020). An Assessment of Earth’s Climate Sensitivity Using Multiple Lines of Evidence. *Reviews of Geophysics*, 58(4):e2019RG000678.
- Sobel, I. (2014). An Isotropic 3x3 Image Gradient Operator. *Presentation at Stanford A.I. Project 1968*.
- Sokol, A. B. and Hartmann, D. L. (2020). Tropical Anvil Clouds: Radiative Driving Toward a Preferred State. *Journal of Geophysical Research: Atmospheres*, 4000 125(21):e2020JD033107.
- Sokol, A. B., Wall, C. J., and Hartmann, D. L. (2024). Greater climate sensitivity implied by anvil cloud thinning. *Nature Geoscience*, pages 1–6.
- Song, F., Feng, Z., Leung, L. R., Jr, R. A. H., Wang, J., Hardin, J., and Homeyer, C. R. (2019). Contrasting Spring and Summer Large-Scale Environments Associated with Mesoscale Convective Systems over the U.S. Great Plains. *Journal of Climate*, 4005 32(20):6749–6767.
- Steinacker, R., Dorninger, M., Wölfelmaier, F., and Krennert, T. (2000). Automatic Tracking of Convective Cells and Cell Complexes from Lightning and Radar Data. *Meteorology and Atmospheric Physics*, 72(2):101–110.
- 4010 Stephens, G., Winker, D., Pelon, J., Trepte, C., Vane, D., Yuhas, C., L’Ecuyer, T., and Lebsack, M. (2018). CloudSat and CALIPSO within the A-Train: Ten Years of Actively Observing the Earth System. *Bulletin of the American Meteorological Society*, 99(3):569–581.
- Stephens, G. L., Gabriel, P. M., and Partain, P. T. (2001). Parameterization of Atmospheric Radiative Transfer. Part I: Validity of Simple Models. *Journal of the Atmospheric Sciences*, 4015 58(22):3391–3409.
- Stevens, B., Acquistapace, C., Hansen, A., Heinze, R., Klinger, C., Klocke, D., Rybka, H., Schubotz, W., Windmiller, J., Adamidis, P., Arka, I., Barlakas, V., Biercamp, J., Brueck, 4020 M., Brune, S., Buehler, S. A., Burkhardt, U., Cioni, G., Costa-Surós, M., Crewell, S., Crüger, T., Deneke, H., Friederichs, P., Henken, C. C., Hohenegger, C., Jacob, M., Jakub, F., Kalthoff, N., Köhler, M., van Laar, T. W., Li, P., Löhnert, U., Macke, A., Madenach, N., Mayer, B., Nam, C., Naumann, A. K., Peters, K., Poll, S., Quaas, J., Röber, N., Rochetin, N., Scheck, L., Schemann, V., Schnitt, S., Seifert, A., Senf, F., Shapkalijevski, 4025 M., Simmer, C., Singh, S., Sourdeval, O., Spickermann, D., Strandgren, J., Tessiot, O.,

Vercauteren, N., Vial, J., Voigt, A., and Zängl, G. (2020). The Added Value of Large-eddy and Storm-resolving Models for Simulating Clouds and Precipitation. *Journal of the Meteorological Society of Japan. Ser. II*, 98(2):395–435.

4030 Stull, R. (2016). *Practical Meteorology: An Algebra-based Survey of Atmospheric Science*. AVP International, University of British Columbia.

Sullivan, S. C. and Voigt, A. (2021). Ice microphysical processes exert a strong control on the simulated radiative energy budget in the tropics. *Communications Earth & Environment*, 2(1):1–8.

4035 Sus, O., Stengel, M., Stapelberg, S., McGarragh, G., Poulsen, C., Povey, A. C., Schlundt, C., Thomas, G., Christensen, M., Proud, S., Jerg, M., Grainger, R., and Hollmann, R. (2018). The Community Cloud retrieval for CLimate (CC4CL) Part 1: A framework applied to multiple satellite imaging sensors. *Atmospheric Measurement Techniques*, 11(6):3373–3396.

4040 Takahashi, H., Lebsack, M. D., Richardson, M., Marchand, R., and Kay, J. E. (2019). When Will Spaceborne Cloud Radar Detect Upward Shifts in Cloud Heights? *Journal of Geophysical Research: Atmospheres*, 124(13):7270–7285.

Takahashi, H. and Luo, Z. (2012). Where is the level of neutral buoyancy for deep convection? *Geophysical Research Letters*, 39(15).

4045 Takahashi, H. and Luo, Z. J. (2014). Characterizing tropical overshooting deep convection from joint analysis of CloudSat and geostationary satellite observations. *Journal of Geophysical Research: Atmospheres*, 119(1):112–121.

Takahashi, H., Luo, Z. J., Stephens, G., and Mulholland, J. P. (2023). Revisiting the Land-Ocean Contrasts in Deep Convective Cloud Intensity Using Global Satellite Observations. *Geophysical Research Letters*, 50(5):e2022GL102089.

4050 Takahashi, H., Luo, Z. J., and Stephens, G. L. (2017a). Level of neutral buoyancy, deep convective outflow, and convective core: New perspectives based on 5 years of CloudSat data. *Journal of Geophysical Research: Atmospheres*, 122(5):2958–2969.

Takahashi, H., Protopapadaki, S., Stubenrauch, C., Luo, Z. J., and Stephens, G. L. (2017b). Relationships between Convective Strength and Anvil Development based on AIRS-CloudSat Joint Dataset.

4055 Taylor, J. W., Choularton, T. W., Blyth, A. M., Liu, Z., Bower, K. N., Crosier, J., Gallagher, M. W., Williams, P. I., Dorsey, J. R., Flynn, M. J., Bennett, L. J., Huang, Y., French, J., Korolev, A., and Brown, P. R. A. (2016). Observations of cloud microphysics and ice formation during COPE. *Atmospheric Chemistry and Physics*, 16(2):799–826.

4060 Taylor, S., Stier, P., White, B., Finkensieper, S., and Stengel, M. (2017). Evaluating the diurnal cycle in cloud top temperature from SEVIRI. *Atmospheric Chemistry and Physics*, 17(11):7035–7053.

Tecson, J. J. and Fujita, T. T. (1975). Cloud-motion Vectors over the Gate Area Computed by MCIDS and METRACOM Methods. *Satellite and Mesometeorology Research Project Research Paper*, (136).

- Thomas, C., Corpetti, T., and Mémin, E. (2010). Data Assimilation for Convective-Cell Tracking on Meteorological Image Sequences. *IEEE Transactions on Geoscience and Remote Sensing*, 48(8):3162–3177.
- Trapp, R. J., Diffenbaugh, N. S., Brooks, H. E., Baldwin, M. E., Robinson, E. D., and Pal,  
4070 J. S. (2007). Changes in severe thunderstorm environment frequency during the 21st century caused by anthropogenically enhanced global radiative forcing. *Proceedings of the National Academy of Sciences*, 104(50):19719–19723.
- Trenberth, K. E., Dai, A., Rasmussen, R. M., and Parsons, D. B. (2003). The Changing Character of Precipitation. *Bull. Amer. Meteor. Soc.*, 84(9):1205–1218.
- 4075 Tripoli, G. J. and Cotton, W. R. (1979). A Numerical Investigation of Several Factors Contributing to the Observed Variable Intensity of Deep Convection over South Florida. *Journal of Applied Meteorology*, 19(9):1037–1063.
- Tsakraklides, G. and Evans, J. L. (2003). Global and Regional Diurnal Variations of Organized Convection. *Journal of Climate*, 16(10):1562–1572.
- 4080 Ullrich, P. A. and Zarzycki, C. M. (2017). TempestExtremes: a framework for scale-insensitive pointwise feature tracking on unstructured grids. *Geoscientific Model Development*, 10(3):1069–1090.
- Ullrich, P. A., Zarzycki, C. M., McClenny, E. E., Pinheiro, M. C., Stansfield, A. M.,  
4085 and Reed, K. A. (2021). TempestExtremes v2.1: a community framework for feature detection, tracking, and analysis in large datasets. *Geoscientific Model Development*, 14(8):5023–5048.
- V. Hobbs, P. (1993). *Aerosol-Cloud-Climate Interactions*. Academic Press.
- van den Heever, S., Haddad, Z., Dolan, B., Freeman, S., Grant, L., Kollias, P., Leung,  
4090 G., Luo, J., Marinescu, P., Posselt, D., Rasmussen, K., Sai, P., Schulte, R., Stephens, G., Storer, R., and Takahashi, H. (2023). Tropical Convection through the Lens of the INCUS Mission. Vienna, Austria.
- Varble, A. (2018). Erroneous Attribution of Deep Convective Invigoration to Aerosol Concentration. *J. Atmos. Sci.*, 75(4):1351–1368.
- Vecchi, G. A. and Soden, B. J. (2007). Global Warming and the Weakening of the Tropical  
4095 Circulation. *Journal of Climate*, 20(17):4316–4340.
- Vizy, E. K. and Cook, K. H. (2019). Understanding the summertime diurnal cycle of precipitation over sub-Saharan West Africa: regions with daytime rainfall peaks in the absence of significant topographic features. *Climate Dynamics*, 52(5):2903–2922.
- Vondou, D. A., Nzeukou, A., Lenouo, A., and Mkankam Kamga, F. (2010). Seasonal  
4100 variations in the diurnal patterns of convection in CameroonNigeria and their neighboring areas. *Atmospheric Science Letters*, 11(4):290–300.
- Waitz, F., Schnaiter, M., Leisner, T., and Järvinen, E. (2022). In situ observation of riming in mixed-phase clouds using the PHIPS probe. *Atmospheric Chemistry and Physics*, 22(11):7087–7103.

- 4105 Wall, C. J. and Hartmann, D. L. (2018). Balanced Cloud Radiative Effects Across a Range of Dynamical Conditions Over the Tropical West Pacific. *Geophysical Research Letters*, 45(20):11,490–11,498.
- Wall, C. J., Hartmann, D. L., Thieman, M. M., Smith, W. L., and Minnis, P. (2018). The Life Cycle of Anvil Clouds and the Top-of-Atmosphere Radiation Balance over the 4110 Tropical West Pacific. *Journal of Climate*, 31(24):10059–10080.
- Wall, C. J., Norris, J. R., Gasparini, B., Smith, W. L., Thieman, M. M., and Sourdeval, O. (2020). Observational Evidence that Radiative Heating Modifies the Life Cycle of Tropical Anvil Clouds. *Journal of Climate*, 33(20):8621–8640.
- Walters, C. K. and Winkler, J. A. (2001). Airflow Configurations of Warm Season Southerly 4115 Low-Level Wind Maxima in the Great Plains. Part I: Spatial and Temporal Characteristics and Relationship to Convection. *Weather and Forecasting*, 16(5):513–530.
- Wang, C., Zheng, D., Zhang, Y., and Liu, L. (2017). Relationship between lightning activity and vertical airflow characteristics in thunderstorms. *Atmospheric Research*, 191:12–19.
- Wang, D., Jensen, M. P., D'Iorio, J. A., Jozef, G., Giangrande, S. E., Johnson, K. L., Luo, 4120 Z. J., Starzec, M., and Mullendore, G. L. (2020). An Observational Comparison of Level of Neutral Buoyancy and Level of Maximum Detrainment in Tropical Deep Convective Clouds. *Journal of Geophysical Research: Atmospheres*, 125(16):e2020JD032637.
- Wehr, T., Kubota, T., Tzeremes, G., Wallace, K., Nakatsuka, H., Ohno, Y., Koopman, R., Rusli, S., Kikuchi, M., Eisinger, M., Tanaka, T., Taga, M., Deghaye, P., Tomita, 4125 E., and Bernaerts, D. (2023). The EarthCARE mission – science and system overview. *Atmospheric Measurement Techniques*, 16(15):3581–3608.
- Weinzaepfel, P., Revaud, J., Harchaoui, Z., and Schmid, C. (2013). DeepFlow: Large Displacement Optical Flow with Deep Matching. pages 1385–1392.
- Weisman, M. L. (2015). MESOSCALE METEOROLOGY | Convective Storms: Overview. 4130 In North, G. R., Pyle, J., and Zhang, F., editors, *Encyclopedia of Atmospheric Sciences (Second Edition)*, pages 401–410. Academic Press, Oxford.
- Weiss, J. and Zeitler, J. (2008). Supercells of the Serranías del Burro. In *24th Conf. on Severe Local Storms*, volume 17A.4, Savanna, GA. American Meteorological Society.
- Westra, S., Fowler, H. J., Evans, J. P., Alexander, L. V., Berg, P., Johnson, F., Kendon, 4135 E. J., Lenderink, G., and Roberts, N. M. (2014). Future changes to the intensity and frequency of short-duration extreme rainfall. *Rev. Geophys.*, 52(3):2014RG000464.
- Williams, E. R., Geotis, S. G., Renno, N., Rutledge, S. A., Rasmussen, E., and Rickenbach, T. (1992). A Radar and Electrical Study of Tropical “Hot Towers”. *J. Atmos. Sci.*, 49(15):1386–1395.
- Williams, E. R., Weber, M. E., and Orville, R. E. (1989). The relationship between lightning type and convective state of thunderclouds. *Journal of Geophysical Research: Atmospheres*, 94(D11):13213–13220.

- Williams, M. and Houze, R. A. (1987). Satellite-Observed Characteristics of Winter Monsoon Cloud Clusters. *Monthly Weather Review*, 115(2):505–519.
- 4145 Wilson, J. W., Crook, N. A., Mueller, C. K., Sun, J., and Dixon, M. (1998). Nowcasting Thunderstorms: A Status Report. *Bulletin of the American Meteorological Society*, 79(10):2079–2100.
- Wilson, J. W., Ebert, E. E., Saxen, T. R., Roberts, R. D., Mueller, C. K., Sleigh, M., Pierce, C. E., and Seed, A. (2004). Sydney 2000 Forecast Demonstration Project: Convective Storm Nowcasting. *Weather and Forecasting*, 19(1):131–150.
- 4150 Wilson, J. W. and Schreiber, W. E. (1986). Initiation of Convective Storms at Radar-Observed Boundary-Layer Convergence Lines. *Monthly Weather Review*, 114(12):2516–2536.
- Woo, W.-c. and Wong, W.-k. (2017). Operational Application of Optical Flow Techniques to Radar-Based Rainfall Nowcasting. *Atmosphere*, 8(3):48.
- 4155 Wu, Q., Wang, H.-Q., Lin, Y.-J., Zhuang, Y.-Z., and Zhang, Y. (2016). Deriving AMVs from Geostationary Satellite Images Using Optical Flow Algorithm Based on Polynomial Expansion. *J. Atmos. Oceanic Technol.*, 33(8):1727–1747.
- Wulff, J. and Black, M. J. (2015). Efficient sparse-to-dense optical flow estimation using a learned basis and layers. In *2015 IEEE Conference on Computer Vision and Pattern Recognition (CVPR)*, pages 120–130.
- 4160 Wyser, K. (1998). The Effective Radius in Ice Clouds. *Journal of Climate*, 11(7):1793–1802.
- Xu, K.-M. and Emanuel, K. A. (1989). Is the Tropical Atmosphere Conditionally Unstable? *Monthly Weather Review*, 117(7):1471–1479.
- 4165 Yau, K., M. and Rogers, R., R. (1989). *A Short Course in Cloud Physics - 3rd Edition*. Butterworth-Heinemann.
- Zach, C., Pock, T., and Bischof, H. (2007). A Duality Based Approach for Realtime TV-L1 Optical Flow: 29th DAGM Symposium on Pattern Recognition. *Proceedings 29th DAGM Symposium "Pattern Recognition"*, pages 214–223.
- 4170 Zelinka, M. D. and Hartmann, D. L. (2010). Why is longwave cloud feedback positive? *Journal of Geophysical Research: Atmospheres*, 115(D16).
- Zhang, G. J. (2009). Effects of entrainment on convective available potential energy and closure assumptions in convection parameterization. *Journal of Geophysical Research: Atmospheres*, 114(D7).
- 4175 Zhang, X., van der A, R., Ding, J., Eskes, H., van Geffen, J., Yin, Y., Anema, J., Vagasky, C., L. Lapierre, J., and Kuang, X. (2023). Spaceborne Observations of Lightning NO<sub>2</sub> in the Arctic. *Environmental Science & Technology*, 57(6):2322–2332.
- Zhang, Y., Wistar, S., Piedra-Fernández, J. A., Li, J., Steinberg, M. A., and Wang, J. Z. (2014). Locating visual storm signatures from satellite images. In *2014 IEEE International Conference on Big Data (Big Data)*, pages 711–720.

Zinner, T., Forster, C., Coning, E. d., and Betz, H.-D. (2013). Validation of the Meteosat storm detection and nowcasting system Cb-TRAM with lightning network data &ndash; Europe and South Africa. *Atmospheric Measurement Techniques*, 6(6):1567–1583.

<sup>4185</sup> Zinner, T., Mannstein, H., and Tafferner, A. (2008). Cb-TRAM: Tracking and monitoring severe convection from onset over rapid development to mature phase using multi-channel Meteosat-8 SEVIRI data. *Meteorology and Atmospheric Physics*, 101(3):191–210.

Zipser, E. J. and Lutz, K. R. (1994). The Vertical Profile of Radar Reflectivity of Convective Cells: A Strong Indicator of Storm Intensity and Lightning Probability? *Monthly Weather Review*, 122(8):1751–1759.